GRAIN GROWTH IN HIGH MANGANESE STEELS

GRAIN GROWTH IN HIGH MANGANESE STEELS

By MADHUMANTI BHATTACHARYYA, B.E, M.TECH

A Thesis Submitted to the School of Graduate Studies in Partial Fulfillment

of the Requirements for the Degree of Doctor of Philosophy

DOCTOR OF PHILOSOPHY (2018)

Materials Science and Engineering

McMaster University, Hamilton, Ontario

TITLE: Grain Growth in High Manganese Steels

AUTHOR: Madhumanti Bhattacharyya, B.E (IIEST, Shibpur), M.Tech (IIT Kharagpur)

SUPERVISOR: Professor. Hatem. S. Zurob

NUMBER OF PAGES: xxvi , 260

Abstract:

The automotive industry, has been innovating in the field of materials development in order to meet the demand for lower emissions, improved passenger safety and performance. Despite various attempts of introducing other lightweight materials (Al, Mg or polymers) in car manufacturing, steel has remained as the material of choice till date due to its excellent adaptability to systematic upgradation and optimization in its design and processing. One of the outcomes is the development of second generation high Mn TWin Induced Plasticity (TWIP) steels with excellent strength-ductility balance suitable for automotive applications.

Cost effective high performance TWIP steel design is mostly based on its alloy design and advanced up and down stream processing methods (thermomechanical controlled processing (TMCP)) which can help achieve suitable microstructure to meet the property requirements. It has been observed that grain boundary migration (GBM) in austenite during high temperature TMCP stage dictates grain growth to control the final microstructure. This research work initially investigates the grain growth in Fe-30%Mn steel within a temperature regime of 1000-1200°C. Compared to conventional low Mn steel, austenite boundary mobility in Fe-30%Mn was found to be 1-2 orders of magnitude smaller. Atom probe tomography results showed no Mn segregation at austenite high angle grain boundaries (γ-HAGB) which rules out the effect of Mn solute drag on growth kinetics in Fe-30%Mn steels. Grain boundary character distribution (GBCD) study showed that the sample consists of two different population of grain boundaries. 50% of the grain boundaries are random HAGBs with high mobility. Remaining 50% are special in nature which introduce low mobility boundary/boundary segments in the global boundary network. The special boundaries are mostly in the form of Σ3 CSL boundaries or its variants like Σ9, Σ 27. These boundary/ boundary segments were introduced by the formation of annealing twins and their interactions with the random HAGBs. An attempt to investigate the effect of Mn on growth kinetics at 1200°C showed that Mn slows down growth kinetics up to 15 wt% predominantly by the formation of annealing twins. A qualitative study of the microstructures showed that as Mn concentration is increased from 1% to 15%, the annealing twin density increases resulting in Σ3 frequency to be 30%. The increased twinning frequency is attributed to the effect of Mn on lowering the stacking fault energy (SFE). Annealing twins, belonging to Σ3 CSL family, intersect the HAGBs resulting into twin induced boundary segments which possess very low mobility. In the light of this idea, slow grain growth in high Mn steel was attributed to the population of low

mobility boundaries. The proposed 'twin inhibited grain growth' model clearly points to the low mobility boundary/boundary segments to be the rate controlling factor during grain growth in high Mn steels. The effect of carbon on grain growth in Fe-30%Mn steel showed that the presence of carbon makes the growth kinetics faster by a factor of 4 and 6 at 1200°C and 1100°C respectively. Although, atom probe tomography results indicated that in presence of carbon, Mn segregation takes place at γ-HAGBs in Fe-30%Mn steel, solute drag does not appear to play a role as it was seen that with increase in Mn content beyond 1%, the solute effect of Mn in slowing down HAGB migration becomes weak. Also, abovementioned higher mobility values are obtained from the growth kinetics of Fe-30Mn-0.5C. This once again highlights the fact that effect of Mn in slowing down grain growth is due to the low mobility of twin/twin related boundaries or boundary segments.

Controlling grain growth has been commonly proposed to be accomplished through small addition (<0.1%) of microalloying elements (Nb, V and Ti) which can slow down GBM at high temperature by solute drag and at low temperature by precipitate pinning (Zener drag). This research work has also experimentally quantified the solute drag of Nb in a series of Fe- 30%Mn steels. Grain boundary mobility was estimated for various temperatures and niobium contents. An attempt was made to calculate the grain boundary mobility in presence of niobium using Cahn's solute drag model. This calculated mobility, when used in the proposed 'twin inhibited grain growth' model, the predicted growth kinetics which showed very good fit with the experimentally obtained growth kinetics in case of Fe-30Mn-0.03Nb and Fe-30Mn-0.05Nb steels at 1100°C. The effect of Nb solute drag, thus captured using Cahn's model, was shown to be slowing down only the HAGB migration in the microstructure, whilst the special boundary mobility was not affected by solute Nb.

Another attempt was made through grain boundary engineering (GBE) to control grain growth in Fe-30Mn-0.5C steel. Using different TMCP schemes, GBCD was modified to produce maximum frequency of special boundary. Preliminary studies on grain growth of single step-grain boundary engineered samples did show a significant lowering of grain size compared to a no-GBE sample after grain growth. However, the effect of iterative GBE didn't show any significant effect in controlling grain growth in spite of the fact that it increased Σ3 frequency to 64%. This probably indicates that the effect of GBE on grain growth by the formation of annealing twins/special low

mobility boundaries is a complicated process which might involve twin/special boundary morphology, annihilation kinetics and formation of grain clusters in the microstructure other than the formation of immobile special triple junctions through the intersection of twins/special boundaries with the random HAGBs.

ACKNOWLEDGEMENTS

First of all, I would like to thank my supervisor, Prof. Hatem S Zurob for his continuous support, guidance throughout my PhD and encouraging new ideas for the thesis. I learnt many valuable things from him especially not to give up until embracing the success. I will never forget his co-operation and friendly help in fixing leakage in furnaces, replacing gas cylinders and taking venture to cast model steels in induction furnace. I would also like to thank him for the patience he had during our weekly meetings when I used to come up with numerous ideas and questions. I will be ever grateful to him for providing ample financial support through research scholarships and other external scholarships.

I would also like to thank Prof. Gary Purdy, for not only being one of my committee members, but also for providing deep insights and suggestions to this thesis, comments on the write up and supporting me. I thank Prof. Gianluigi Botton for being one of my committee members and providing valuable suggestions to improve my microscopy skills and results. I express my gratitude to the external examiner, Prof. Douglas Boyd, for going through the thesis in great detail and providing valuable comments, suggestions, feedbacks and insightful questions for my thesis. I would like to thank Prof. Yves Brechet for many enriching suggestions and discussions during his visit to McMaster from France. I would also like to express my gratitude to Prof.S. Subramanian who helped me to get into the doctoral programme at McMaster University. His encouraging discussions in the field of steel research kept me motivated to keep exploring the beautiful power of microstructure of steel.

I thank School of Graduate studies, McMaster University and Department of Materials Science and Engineering for providing me TA support and financial support through graduate schcolarships and bursaries for my PhD studies. I would also like to thank Prof. Dmitri Malakhov for applauding my research work and encouraging me.

How can I forget my big time friend, Jim Garrett, who always helped me in fixing all possible problems related to my experimental set up. I will forever remember how he worked after hours to seal my samples, fire polishing the tubes, casting many finger ingots. I enjoyed all the discussions with Jim from how to change the gears in a bi-cycle, the Friday-the 13^{th}, to how to do glassblowing or cleaning iron in a flow of wet hydrogen. I am also grateful to Chris Butcher in

CCEM for his continuous guidance on microscopy, EBSD and metallography. I must express my sincere gratitude to Dr. Brian Langelier for carrying out all the atom probe experiments. His friendly behavior always made the complicated atom probe results understandable in so much of details. A big thanks to Dr. Xiang Wang for his immese patience to carry out all the TEM experiments with so much care. I would also like to thank Dr. Xiaogang Li, MSE lab for providing help and various ideas to try many different things in the lab. Thanks to Ed for fixing all the computer related issuses, especially, giving me an access to the server for working on Thermocalc. I appreciate all the help received from Dr. Thomas Garcin and Prof. Militzer from UBC, Dr. Fateh Fazeli, Dr. Colin Scott, Mike Attard, James Saragosa from Canmet Materials, Canada. I would also thank Prof.Goro Miyamoto, Tohoku University, Japan for helping to reconstruct the Austenite grain boundaries from the EBSD data of Fe-6Mn steel in such a short time.

Next I would like to thank my dear friend Dr. Kai Wang who always helped me during carrying out the experiments in our lab. I never saw him getting upset on failed experiments. Thanks to my colleagues, Dr. Hamid Azizi, Dr. Mark Fraser, Josh, Evan, Kohei for their valuable help during electropolishing, rolling, etching. I would also like to thank my friends in McMaster, Sayantee (Pekho), Tao, JB (Jayasree), Michelle, Aliyeh, Lynn, Minghe, Marie, Reena, Anand Bhaiya, Ameya whose company kept me cheerful during the worst and depressing time of my life. Also, continuous presence of Judy, Nick, Finnick, Nam-Nam, Oleg, Byangu, Cao-Cao and Bhetul as buddies is worth mentioning. Special thanks to Hamilton Street Railway (HSR) for their best service in commuting as I travelled the length and breadth of the city of Hamilton. I would like to extend my thanks to McMaster Outdoor Club and Arrive and Thrive group for giving me some of the best memories in McMaster. Special thanks to Cree, Jasmine, Mike and Connor for arranging those trips.

I thank my gurudev Swami Kripamayanandaji and Swami Satyabodhanandaji for inspring me and motivating me. Special thanks to Swami Sarvapriyanandaji and his inspiring lectures. I thank Prof. Eileen Schuller for her continuous support, encouragement and being a well wisher home away from home. I immensely thank my all time mentors Prof. Debjani Ganguly, Prof. Partha Pratim Chattopadhyay, Prof. Amitava Basu Mallick, Prof. Mainak Sengupta, Prof. Aparijita Sengupta, Prof. Chaitali Ray, Prof. S.B. Singh, Prof. K.K. Ray. Special thanks to Kaku and Kakima for their sumptous meals.

Finally, I thank the support from my family, Brother, Baromama, Chhotmama, Chhotokaku, especially my parents and ‘Pi(tchi)’ for their unconditional love and prayers that gave me the freedom and strength to pursue higher studies. A special thanks to my BABA who taught me how to win the battles of life. To the very end I want to dedicate this thesis to Goddess Sarada Ma and my Mom, who couldn’t chase her dreams to pursue PhD in astrophysics exploring the complexity of the universe through watching the galaxy sitting in an observatory.

Contents

Table of Figures

Table of Tables

1 Introduction:

Over the past two decades, steel has been proved to be one of the most well-known types of smart materials for enormous power of its microstructure. This came from myriad of ways in which its structure can be tailored by processing and proper designing of chemistry. One of the reasons of its stupendous dominance is its ability to adapt to changing environment with an excellent balance of the mechanical properties. And evolution of steel is probably a never ending process which gives a wide range of product basket used in various industrial sectors.

Recent awareness in the field of sustainable development has put into the demand of adoption of triple bottom line, meeting the needs economically, socially and environmentally. Therefore, robust, cost effective and ecofriendly design and manufacturing of steel structures are considered to be most important. During recent times of development, all the important industrial sectors emphasize for the best quality output in an economically viable and profitable way. Construction industries prefer high strength steels with smaller cross sectional area to curtail the material cost. At the end of 20^{th} century, vehicle producers realized that survival in the competitive market was centered upon the design of safe, light weight, aesthetically acceptable and competitive cost vehicles. In case of petroleum industry, transportation of large volume of oil and gas through different climatic condition has seriously demanded for high diameter pipelines with excellent mechanical properties.

In order to achieve the best quality steel for automotive applications, researchers introduced the concept of having a judicial balance in the strength and ductility. With the advent of advanced high strength steels (AHSS), the scope of improving properties increased manifold as it was found to have strength higher than the conventional high strength steels (HSS) alongwith excellent ductility (Figure 1.1). Because of their interesting microstructural features and significant work hardening rate,

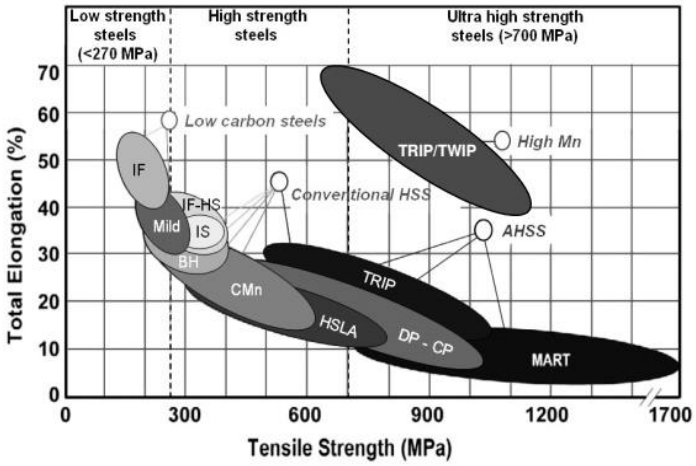

Figure 1.1. Strength-Ductility balance shown in banana curve for different types of steels (Phiu-on 2008)

austenitic steels have recently gained much attention of the materials engineers. This particular type of steel was found to have immense advantage of being applicable for manufacturing structural components of car body [Table 1.1]. Their introduction in making automobile parts has ensured vehicle weight reduction which has in turn lowered fuel consumption as well as air

Table 1.1. Motivational aspects of high Mn austenitic steel development (Phiu-on 2008)

Motivation/property	Potential use in automobiles
High strength	Lightweight design: reduction of sheet thickness
High formability	Components with complex geometries
High energy absorption	Safety: crash-relevant components
Cost reduction	Replacement of cost-intensive materials (stainless steels, Al and Mg) or cost-intensive processes (hot forming)

pollution (Dobrzański and Borek 2011). Owing to their excellent work hardening rate, high Mn steels can also be used for thinner gauge application including press formed parts with outstanding crashworthiness. Single phase austenitic microstructure with very low stacking fault energy is the key feature of one of the high Mn steels known as Twin Induced Plasticity (TWIP) steels. Application of high Mn TWIP steels in automobile part fabrication (Figure 1.2) is not only limited

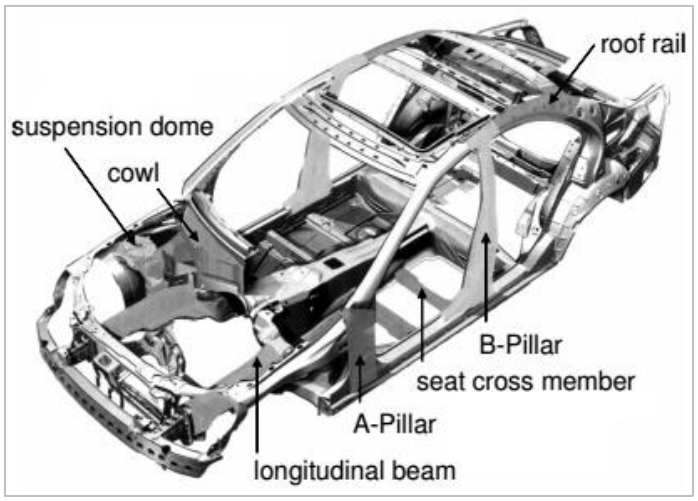

Figure 1.2. . Potential application of high Mn TWIP steels to make components of a medium-class limousine (Phiu-on 2008)

to structural reinforcement in its body-in-white (BIW), but also have aimed for making (Phiu-on 2008):

- parts related to collision like , longitudinal beam, cross member to protect passenger from front and side crashing
- parts for high safety use, e.g., cowl with very low deformability
- parts for other high strength parts, e.g, roof rail, A-pillar and B-Pillar etc.
- parts with high stretch flangeability , complex geometry and special properties e.g, suspension dome with good fatigue strength.

Through proper selection of chemistry and processing route, further development might be possible alongwith thorough understanding of the microstructure-property correlation. Special types of rolling treatment are particularly found to be responsible to bring changes in micro-scale along with chemistry. In ancient practice, the blacksmiths were only concerned about the macroscopic shape change. Following that, hot rolling of blooms came into practice with an objective of achieving dimensional precision and appearance. Further heat treatment was a mandate to achieve the desired microstructure resulting in high manufacturing cost. It was Domnanfvets Jernverk in Sweden in 1940, who first lowered the finish rolling temperature than the conventional one and realized that hot rolling can substantially be used to enhance

mechanical properties. In 1958, this type of hot rolling was termed as ThermoMechanically Controlled Rolling (TMCR) (Bai Qi 1993). Development of high Mn TWIP steel depends significantly on controlling the process parameters which in turn is governed by the presence of alloying elements.

Addition of microalloying elements to improve strength and toughness has been a common practice since a long time. In high Mn TWIP steels, effect of microalloying elements like niobium is not studied very well in particular to its effect on austenite grain boundary migration. Development of high Mn TWIP steels by TMCR inevitably requires an understanding of microstructure evolution with an emphasis on grain growth process which directly tailors the microstructure by creating annealing twins, altering their numbers and finally changing the crystallography of the austenite grain boundaries. Evaluation of grain growth kinetics with estimating the solute drag of Nb on austenite grain boundaries has been remaining one of the missing aspects in completing the microstructure-property correlation in high Mn TWIP steels. In addition to that, role of alloying elements like Mn, C on austenite grain boundary migration needs to be explored in a connection with their effect on the microstructure. This thesis primarily aims at evaluating austenite grain growth kinetics in a high Mn TWIP steel with a particular emphasis on quantifying Nb solute drag on austenite boundaries. The interaction of solute Nb with ferrite grain boundaries has been studied (Maruyama, Smith, and Cerezo 2003; Maruyama and Smith 2004). Also, some atom probe studies on solute Nb effect on prior austenite grain boundaries (PAGB) in very low Mn steel exist (Peter J Felfer et al. 2012). However for highly alloyed systems (high Mn Steels), solute Nb effect on γ-boundaries has not been explored. This study might be a break-through in this field of understanding solute drag under a wide regime of Mn content. In addition to this, effect of alloying elements (Mn, C) on grain boundary migration through highlighting their role in tailoring microstructure will also be explored. Segregation behavior of Nb with and without the presence of carbon will be studied experimentally. A correlation between stacking fault energy, Mn concentration and austenite boundary mobility will be presented which would encompass a big area to understand chemistry dependence of grain growth process. Understanding the role of twins on growth process will be partly explored and a preliminary model including the effect of annealing twins on growth process will be presented. Finally, a detailed description of the process and outcome of pursuing grain boundary engineering on high Mn TWIP steels will conclude the work leaving an opportunity for future research and application of

improving interfacial properties (corrosion resistance, creep strength) of these steels by changing their grain boundary character distribution.

2 Literature Review

2.1 High Manganese Steel (HMS) and microstructure tailoring:

In the year of 1882, Sir Robert Hadfield set a landmark in metallurgical history by introducing manganese steels. While visiting Paris exhibition four years ealier, he came across the research done by Terre Noire Company to successfully produce ferro-manganese with almost 80% Mn and small amount of carbon. There was a mention of detrimental effect of Mn beyond 3% in the company's pamphlet. His intention was to cast some very hard wheels for trams which was done with the addition of 13.76% Mn and 1.35% carbon to iron melt. The success of Hadfield's experimental attempt can be explained as he wrote in his diary "*Wonderfully tough*, even with a 16 lb. hammer [?] *hardly break it* . . . Not a *blow-hole in the wheel, sound as metal*. Really grand. Hurrah!!! " Further fine tuning of his experiments highlighted some important aspects like, addition of 12-14% Mn along with 1% carbon yields a material which is relatively soft but capable of being work hardened. Although, he proposed that this particular type of steel is next to impossible be machined commercially, his 'epoch-making' discovery of "Hadfield steels" is considered as the beginning of alloy steel era. His work was finally introduced to the scientific community in 1888 only after fixing some of the problems related to the casting of the steel. The first substantial utilization of Hadfield steels was done in 1892 in the form of casting an alloy steel in USA.

By 1897, the applicability of Manganese steel got widened as they were proved to be excellent candidate for abrasion resistant jaws of stone and ore crushing machinery, dredger-pins, mining wheels, paper pulp beaters and burglar-proof safes, war materials like tank treads and soldier's steel helmet (Geoffrey 1985). In 1929, a detailed study on the microstructure of Hadfield Steels was conducted by Hall and Krivobok separately. The key finding of their study came in the form of importance of heat treatment at 500°C followed by a quench which brings fully austenitic microstructure. In 1936, an empirical relationship was proposed by Tofaute and Linden to relate chemistry to austenite stability by the relation: wt% Mn +13wt%C $\geq$ 17. In 1935, Chevenard used

thermomagnetometry to study microstructure after plastic deformation at room temperature and formation of a hard phase was observed. After eight years, Troiano et al. found that deformation induced transformation products in Fe-Mn binary systems mainly come from two distinct modes: ε-martensite and α′ martensite formation. In 1950s, X-Ray diffraction studies revealed high work-hardening in Hadfield steels. Optical micrography proposed presence of planar defects in the form of mechanical twins which was later verified experimentally using TEM analysis (Bouaziz et al. 2011).

However, later research work on the high manganese steels revealed that presence of high amount of carbon (> 1%) results in poor weldability and machinability for thinner gauge application. In addition to that, around 15 % Mn was not sufficient to stabilize austenite as it leads to $\gamma \rightarrow \alpha'$ transformation when deformation is carried out. Following this, a modified grade of high Mn steels were designed where lowering of carbon content was balanced by increased Mn addition to ensure better stability of the austenite structure, no deformation induced martensite formation. This is the pathway which brought the new HMS

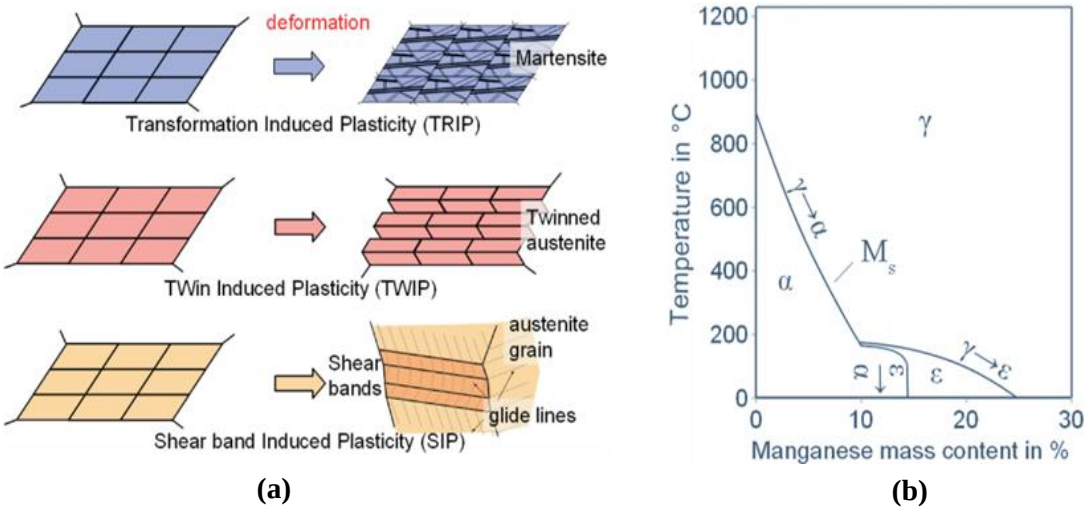

Figure 2.1.a) Schematic of deformation mechanisms involved in different HMS system, b) Fe-Mn binary phase diagram (note: α′martensite is denoted as α here) (Engl 2011)

(22-30%Mn and 0-0.6%C) into the steelmakers' world in 1970s (Scott et al. 2006; Ghasri Khouzani 2015). In mid-70's, Remy discovered the role of twins in retaining strain as dislocation pile-ups against twin boundaries. This resulted into excellent strength ductility balance even at sub-zero temperature in Fe-30Mn-5Al-0.5C steels (UTS 1200MPa with %Elongation 70). By then,

the utility of these high Mn steels in cryogenic application was strongly established by some other groups of scientists. Next step was taken by Japanese steel makers and Posco, Korea to publish first patent on high Mn steels. This resulted into the higher Mn steels (Fe-25Mn-1.5Al-0.5C-0.1N) capable of twinning at room temperature and thereby applicable for thinner section press formed parts in automobiles. In 1995, Posco published another set of patents on HMS which got acknowledged globally. In Europe, ThyssenKrupp was first to file a patent on HMS in collaboration with Düsseldorf Max Planck Institute. French steelmaker USINOR was next to file another patent. Since then, the scientific community took the interest to conduct research on development of high Mn Steels (Bouaziz et al. 2011).

The advantage of HMS is experienced through their higher work –hardening rate resulting from either formation of strain induced martensite (TRIP-effect) or twins (TWIP-effect). These steels are also known to offer kinematic strain hardening apart from dislocation hardening. A new concept of deformation mechanism in HMS is also introduced through formation of shear bands. In Figure 2.1.a, a schematic of different deformation mechanisms in HMS is depicted. Thermodynamic calculation of phase stability of HMS was done by many researchers. Among them, the most comprehensive study came after Schumann in the form of martensitic transformation diagram (Figure 2.1.b). It was indicated that Mn content upto 20% is not able to stabilize austenite resulting into unstable TRIP effects with the formation of either α' (α, in Schumann's diagram, Figure 2.1.b) or ε martensite. As the Mn content goes beyond 20%, single phase microstructure with stable γ is obtained as. Also, the Néel temperature of austenite which involves transition from paramagnetic to anti-ferromagnetic state is also increased (Phiu-on 2008). With lowering carbon content, $\gamma \rightarrow \varepsilon$ transformation is expected even in presence of 27% Mn according to the section of the Fe-Mn-C ternary diagram (Figure 2.2). Plastic deformation also has immense contribution to change the stability lines, e.g, the threshold of 27% is shifted to 33%.

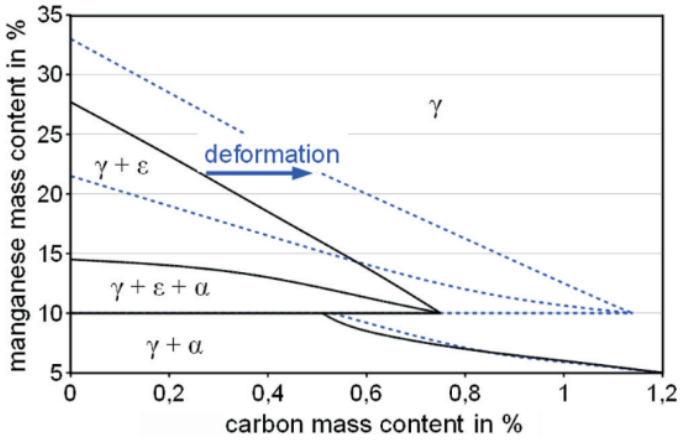

Figure 2.2. Fe-Mn-C ternary diagram with different phase maps sectioned at 298K (Engl 2011)

Increasing carbon content upto 0.8% lowers the ε martensite transformation with 17% Mn content. Effect of alloying elements is directly related to their relation with stacking fault energy (SFE) of the system which will be discussed next.

2.1.1 Stacking Fault Energy (SEF):

Depending on chemistry, new HMS shows a broad range of stacking fault energy values which dictates the type of deformation products like twins and HCP ε martensite. The final microstructure evolution is considered to be an interplay between metallurgical phenomena discussed in section 2.3 and the type –population of the abovementioned deformation products. Stacking fault is known to be a planar defect which consists of a region of imperfect sequencing of atoms. The ideal stacking sequence of {111} close packed planes in FCC is in the form of ABCABCA …This particular sequence can be altered in a number of ways. Insertion of an extra plane midway leads to the formation of ABCABACABC which is called an extrinsic stacking fault. Removal of a plane from the stack, in the form of ABCACABC, creates an intrinsic stacking fault which is favored by dissociation of a perfect dislocation into two Shockley-Partials according to following reaction:

$$\frac{a}{2}[01\bar{1}] \rightarrow \frac{a}{6}[11\bar{2}] + \frac{a}{6}[\bar{1}2\bar{1}] \qquad \text{…….. Eq 2.1}$$

Above reaction is energetically favored as energy of the dislocations is lowered by shortening the Burgers vectors of the partials. The partials, then, start to repel each other since elastic interaction prefers individual strain fields not to overlap. This is balanced by a shear force Γ, per unit length

of the partial dislocations to pull them together in order to minimize the fault area. SFE of a material usually dictates the magnitude of Γ. Under equilibrium condition, an adjusted separation distance, '*d*', is set between the partials which can be given in the following form:

$$d = \frac{\mu b^2}{4\pi\Gamma} \qquad \ldots\ldots\ldots\ldots \textit{Eq 2.2}$$

where, μ is the shear modulus, b being the Burgers vector. Above relation is indicative of the fact that lowering of SFE will increase the distance or the fault will be broadened (Ghasri Khouzani 2015).

Calculation of SFE was first made through electron theory of metals. Later on, in copper, SFE was measured by a variational method using central-force approximation. Next to that, a thermodynamic model was proposed for SFE calculation by Olsen et.al. A brief discussion of this model is given next. Introduction of a change or disturbance into the perfect crystal causes a change in its Gibbs free energy (ΔG). This change may be accounted in either form ΔG_{if} or ΔG_{vol}, Gibbs energy change according to interface and volume approach respectively, so, $\Delta G_{if} = \Delta G_{vol}$. For an area A and Γ^{∞} interfacial energy per unit area, we can write

$$\Delta G_{if} = A\Gamma^{\infty} \qquad \ldots\ldots\ldots\ldots \textit{Eq 2.3}$$

The volume approach leads to the Gibbs energy change to be in the form of

$$\Delta G_{vol} = V^{SF}\left(G_V^{SF} - G_V^{M}\right) + 2A\sigma \qquad \ldots\ldots\ldots\ldots \textit{Eq 2.4}$$

where, V^{SF} and $G_V{}^{SF}$ stand for the volume and Gibbs energy per unit volume of the stacking fault, $G_V{}^{M}$ is the Gibbs energy per unit volume of the matrix, σ is the interfacial energy per unit area of the phase boundary. Using above two equations in the relation $\Delta G_{if} = \Delta G_{vol}$ and then differentiating with respect to A, we get:

$$\Gamma^{\infty} = 2s\left(G_V^{SF} - G_V^{M}\right) + 2\sigma \qquad \ldots\ldots\ldots\ldots \textit{Eq 2.5}$$

where, '*s*' represents the interplanar spacing between close-packed planes lying parallel to the fault plane. Imbibing above concept and introducing molar Gibbs energy, stacking fault energy can be expressed as:

$$\Gamma_{SFE} = 2\rho(\Delta G^{\gamma\rightarrow\varepsilon}) + 2\sigma \qquad \ldots\ldots\ldots\ldots \textit{Eq 2.6}$$

In above equation, 'ρ' stands for molar surface density of close-packed {111} planes in FCC and molar Gibbs energy change is represented by $\Delta G^{\gamma \rightarrow \varepsilon}$. ρ can be calculated from:

$$\rho = \frac{4}{\sqrt{3}} \frac{1}{a^2 N} \qquad \ldots\ldots\ldots\ldots\ldots \text{Eq 2.7}$$

where, N is Avogadro's Number and a is the lattice parameter. Further sophisticated forms of stacking fault expressions can be found elsewhere (Ghasri Khouzani 2015; Phiu-on 2008; Scott et al. 2006; De Cooman, Chin, and Kim 2011; Curtze et al. 2011). The correlation between chemistry and SFE to govern stability of different phases is nicely depicted in Figure 2.3. It can be seen that the steels with SFE lower than 20mJ/m^2 are prone to undergo $\gamma \rightarrow \varepsilon$ phase transformation. Higher Mn steels with SFE higher than 20 mJ/m^2 have preference for mechanical twin formation in stable γ phase (Grassel, O., Kruger, L., Frommeyer, G., Meyer 2000) . This threshold value of SFE varies from one to the other research work.

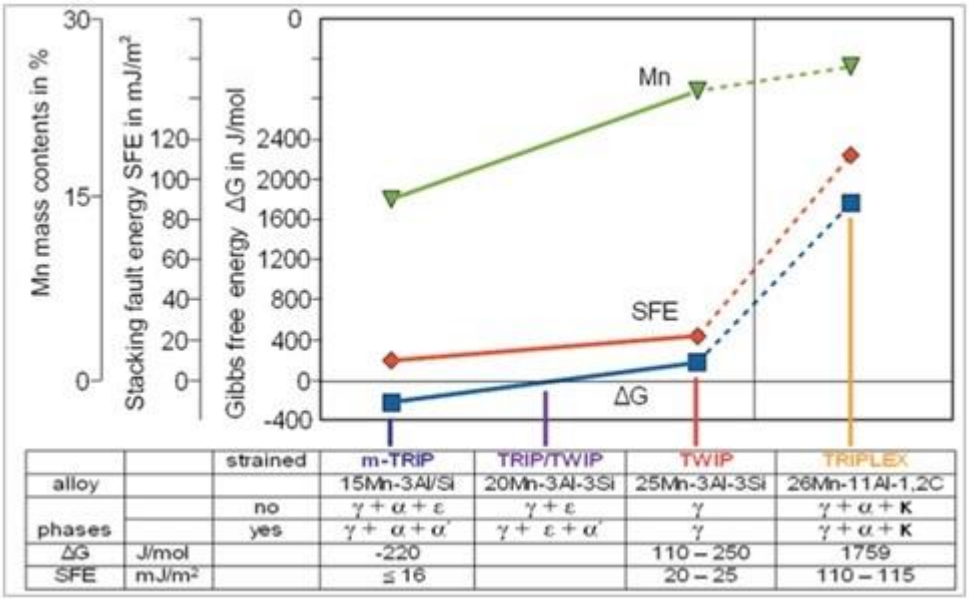

		strained	m-TRIP	TRIP/TWIP	TWIP	TRIPLEX
alloy			15Mn-3Al/Si	20Mn-3Al-3Si	25Mn-3Al-3Si	26Mn-11Al-1,2C
phases		no	$\gamma + \alpha + \varepsilon$	$\gamma + \varepsilon$	γ	$\gamma + \alpha + \kappa$
		yes	$\gamma + \alpha + \alpha'$	$\gamma + \varepsilon + \alpha'$	γ	$\gamma + \alpha + \kappa$
ΔG	J/mol		-220		110 – 250	1759
SFE	mJ/m²		≤ 16		20 – 25	110 – 115

Figure 2.3. Correlation diagram of various types of high Mn steels (Engl 2011; Grassel, O., Kruger, L., Frommeyer, G., Meyer 2000)

According to Allain et al., 18mJ/m^2 is the borderline value of SFE. They proposed that at SFE value 10 mJ/m^2, ε martensite formation starts and above 19mJ/m^2, mechanical twinning occurs (Allain et al. 2004). Dumay et al. proposed that below 18mJ/m^2 twinning is taken over by ε-martensite formation. In Fe-18Mn-0.6C-1.5Al system, SFE of 33mJ/m^2 was found to bring

twinning in austenite which was recently modified to be 30±10 mJ/m^2 by another researcher (De Cooman, Chin, and Kim 2011).

2.1.2 Factors affecting SFE:

SFE is primarily controlled by chemical composition and temperature. Some study has also found its dependence on austenite grain size. For constant chemistry, temperature has a direct proportionality with SFE. This can easily be related to equation 2.6 where the free energy for $\gamma \rightarrow \varepsilon$ transformation is a function of temperature. Allain et al. calculated temperature variation of SFE in Fe-22Mn-0.6C system taking into the magnetic and chemical contribution (equation 2.6) separately. The change in slope of the magnetic curve can be attributed to magnetic transition (Figure 2.4). Their calculated trend is in good agreement with experimentally measured temperature dependence of SFE in Fe-Mn-Cr-C system by Remy et al. (Allain et al. 2004; Remy 1977) .

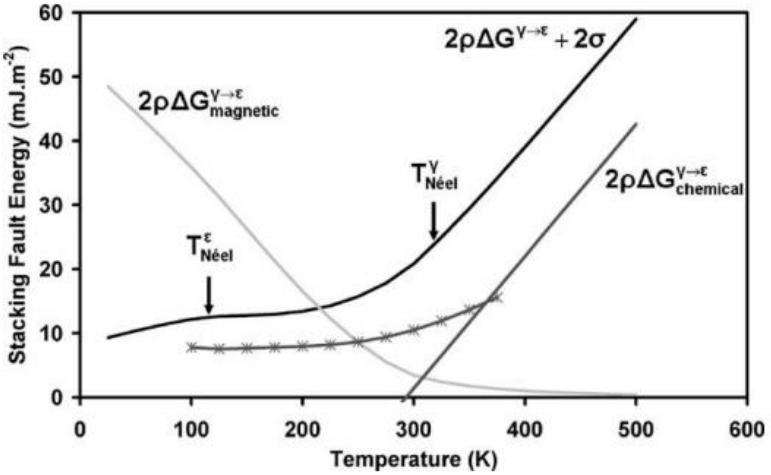

Figure 2.4. Temperature dependence of SFE modelled in Fe-22Mn-0.6C Steels considering the effect of chemical (dark grey) and magnetic contribution (light grey). A good agreement in the predicted value is shown by comparing Remy's experimentally measured (crossed)temperature dependence of SFE in Fe-20Mn-4Cr-0.5C steel (Allain et al. 2004)

A detailed study on temperature dependence of SFE in pure cobalt and different transitional alloys like Co-Ni, Co-Fe, Fe-Cr-Ni, Fe-Mn-Cr etc., silver and copper base alloys was performed by Remy *et al*. They measured the stacking fault node and ribbon dimensions on thin foils in a heating or

cooling stage of a TEM to determine SFE at different temperatures and justified their observation based on electron theory (Rémy, Pineau, and Thomas 1978).

Mn as an alloying element has immense effect on SFE (Figure 2.5.a). Around 13-14%, Mn has a

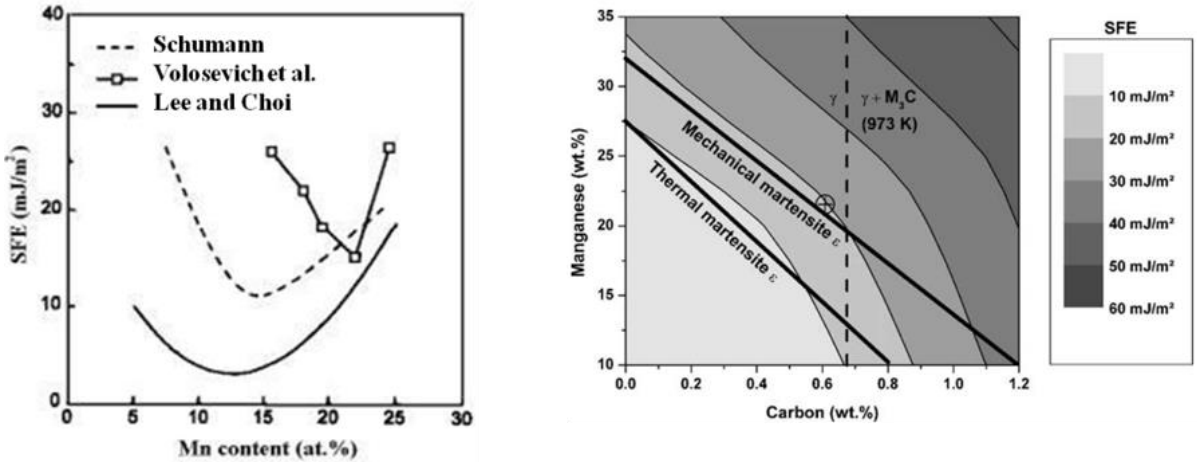

Figure 2.5. a) Dependence of SFE on Mn content in HMS (Ghasri Khouzani 2015), b) SFE map generated by different iso-SFE lines at 300K in C-Mn composition field (Allain et al. 2004)

lowering effect whilst beyond that value SFE increases with increase in Mn content. The minima seems to be different according to different approaches of study (Ghasri Khouzani 2015).

Carbon is considered to stabilize austenite and its effect on SFE was studied by several researchers. Experimentally determined SFE value of a range of austenitic stainless steel with carbon upto 0.91 wt% showed a linearly increasing relation. Some other researchers reported carbon insensitivity of SFE in austenitic stainless steel upto 0.29 wt% carbon (Brofman, PJ and Ansell 1978). A TEM study combined with EDS on Fe-22Mn-0.69 C showed that carbon increases SFE at higher concentration whilst decreases at lower concentration (Petrov 1993). Ambiguity in experimental outcomes regarding effect of carbon on SFE resulted into approaches based on thermodynamic modeling. Allain et al. considered the change in Gibbs free energy of each element during $\gamma \rightarrow \varepsilon$ transformation alongwith their mutual interactions and plotted iso-SFE lines on C-Mn field (Figure 2.5b) showing increase in SFE with increasing carbon content (Allain et al. 2004).This trend has recently got some confirmation from, ab initio simulation study (Ghasri Khouzani 2015).

Effect of Al on SFE was noticed as it increases SFE in high Mn Steels (1 wt% Al addition increases SFE by 5mJ/m^2) (Ghasri Khouzani 2015) and thereby lowers the chance of $\gamma \rightarrow \varepsilon$ transformation. Al addition also reduces strain hardening as dislocation cross-slip becomes easier. Density reduction because of Al results into light weight of high Mn steels. Similar effect of Nitrogen was noticed from X-Ray diffraction studies on Fe-20.24-22.57Mn-2-3Si-0.69-2.46 Al-0.01C where increased N and Al content was seen to suppress probability of stacking fault formation (De Cooman, Chin, and Kim 2011) by increasing SFE. Effect of silicon on SFE is two-fold. It increases SFE when its amount is less than 4% and the effect reverses at higher (>4%) Si content (Figure 2.6). Deviation of this finding happened when some researchers observed a drop in SFE of Fe-27Mn system after adding upto 2%Si (Dumay et al. 2008). The change of SFE with varying amount of different alloying elements was predicted by Dumay et al by using their thermochemical model. Their prediction is given in Figure 2.6. It can be seen that Copper follows the same trend as Al although former decreases Neel Temperature. A good agreement is noticed between experimentally measured trend and model predicted trend on effect of Chromium addition on SFE (Dumay et al. 2008).

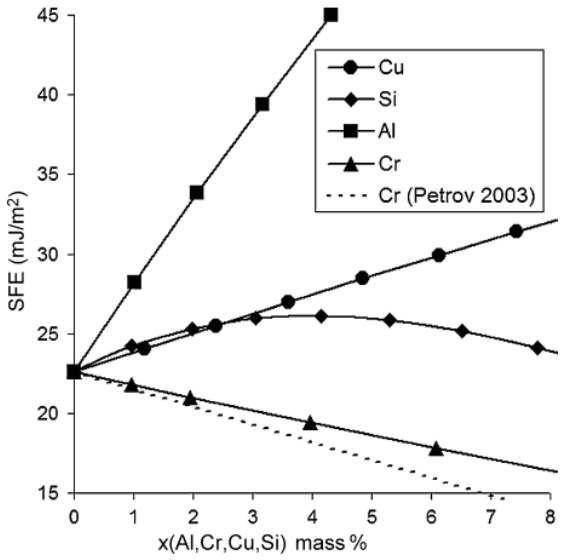

Figure 2.6. Effect of alloying elements on SFE of Fe-22Mn-0.6C system predicted from thermochemical model (Dumay et al. 2008)

Effect of grain size on SFE is explained through stability of austenite in microstructure. In 1998, Jun et al. investigated the change in martensite start (M_s) temperature with varying austenite grain size in Fe-18Mn alloy. An increase in M_s temperature indicates the likelihood of $\gamma \rightarrow \varepsilon$ transformation. The steel samples were austenitized within the temperature window of 700-

1100°C followed by room temperature water quenching (Figure 2.7.a). Grain size was found to be within 13-185 μm. A thermo-mechanical analyzer (TMA) was used to determine the M_s

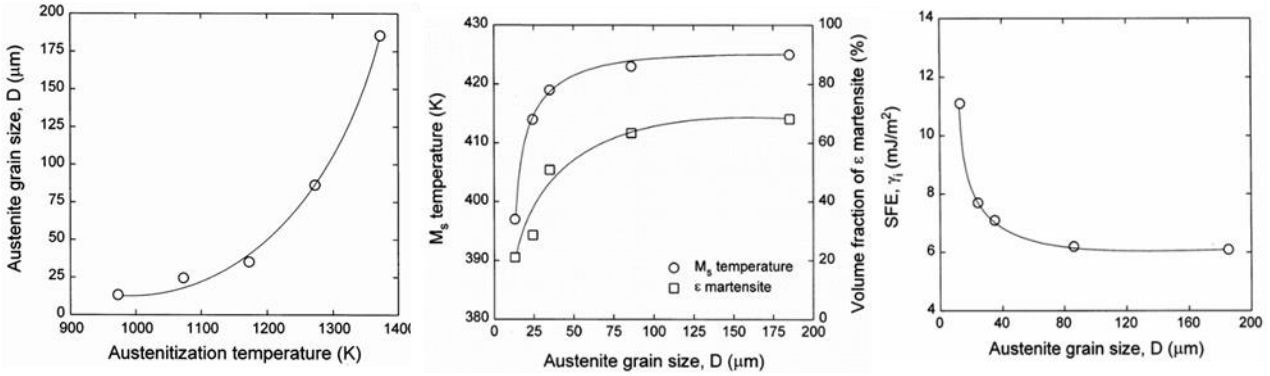

Figure 2.7. a) Temperature dependence of grain size, b) variation of M_S temperature and martensite fraction, c) Grain size dependence of SFE in Fe-18Mn alloy (Jun and Choi 1998)

temperature with a cooling rate of 3°C/min. Simultaneously, volume fraction of ε-martensite was measured using X-Ray diffractometer by calculating relative intensities of ε (10.1) and γ (200)plane. Figure 2.7.b shows inhibiting effect of grain refinement on γ → ε transformation. It is shown that upto grain size of 35 μm, both M_s temperature and volume fraction of ε-martensite increase steeply and gradually increases to saturation with further increase in grain size. This was explained in the light of free energy, ΔG*, of γ → ε transformation:

$$\Delta G^* = \Delta G^{\gamma \rightarrow \varepsilon} + \Delta G_{be} \qquad \ldots\ldots\ldots\ldots \textit{Eq 2.8}$$

where, ΔG_{be} is the change in free energy due to grain refining. Using above relation into equation 2.6 and SFE is calculated after obtaining ΔG_{be} by fitting data on drop in M_s value from Fe-15Mn system (Setsuo Takaki, Hideshi Nakatsu 1993).The dependence of SFE on grain size is, thereby, plotted as shown in Figure 2.7.c (Jun and Choi 1998). This trend of sharp decrease in SFE upto 35μm grain size and then transition to gradual drop is in good agreement with a similar study conducted on Fe-17.8Mn-0.47C alloy. Their explanation of change in SFE with grain size (Figure 2.8) was in the light of disequilibrium concentration of carbon retained in solid solution after quenching from low soaking temperature or smaller holding time to achieve fine grained austenite. Also the internal stress dependent dislocation dissociation might be responsible for SFE increase in small grain condition (Phiu-on 2008).

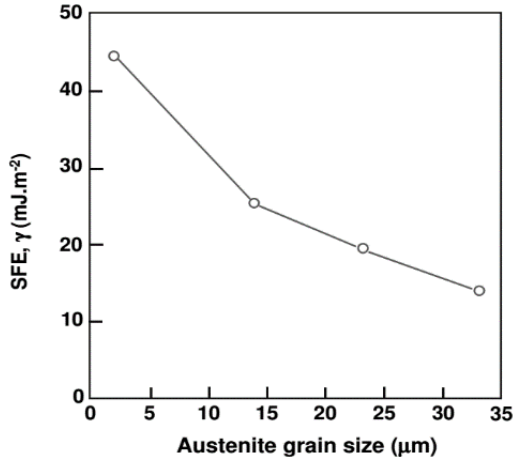

Figure 2.8. Experimentally determined SFE variation with respect to grain size in Fe-17.8Mn-0.47C alloys (Phiu-on 2008)

Further study on mechanical behavior of various high Mn steels was conducted by various authors (Ghasri Khouzani 2015; Phiu-on 2008; Scott et al. 2006; De Cooman, Chin, and Kim 2011; Bouaziz et al. 2011)

The development of high Mn steels requires an in-depth understanding of stability of the microstructure during thermomechanical processing. A few attempts have been made to understand recovery, recrystallization, precipitation strengthening and texture evolution in high Mn steels (Bouaziz et al. 2011; Scott et al. 2006; Momeni et al. 2014; Kang et al. 2010) . No such attempt to understand grain growth at high temperature in high Mn steel has been made till date. Also, after recrystallization the microstructure of high Mn steel is predominantly decorated with annealing twins. During grain growth, interaction between high angle austenite grain boundaries with the annealing twin boundaries dictate the growth kinetics. A detailed understanding of grain growth in presence of annealing twins is therefore important to elucidate austenite grain growth in any commercial microalloyed steels during roughing operation at very high temperature. Understanding stability of austenitic microstructure at high temperature might also be of interest for developing FCC materials for high temperature application (fusion reactor application) through grain boundary engineering process (Cole, Gelles and Hoyt 1992). During the installation of pipelines with bainitic microstructure, welding is an important processing. Understanding, austenite grain growth via studying γ- boundary migration in high Mn steels would present some analogy which can be adopted for the pipelines to control the γ- grain size during welding in the heat affected zone (HAZ).

From above discussion, it is clear that discovery of Hadfield steel has opened up a new horizon for the steel researchers which ultimately leads to a plethora of opportunities to developing advanced steels and processing techniques. The enormous effort put by modern day researchers and sophisticated techniques treading into the research arena will, no doubt, make Sir. Hadfield's expectations receive some good turnout in reality as he stated "the special question of steel alloys or combinations will be eventually found to possess considerable practical importance to the world at large, and perhaps be the means of eventually enabling our civil and mechanical engineers to design and carry out works of a magnitude which, notwithstanding the great strides made during the last few years, even at present are not possible" (Geoffrey 1985).

2.2 Thermo-mechanical Controlled Rolling (TMCR):

Implementation of hot rolling was done with the sole intent of changing shape, thickness of the material without paying attention to its final microstructure. Gradually, improvement in properties was achieved through strengthening which mostly came by increasing the level of alloying like, C, Mn, Cr, etc. This eventually posed a huge problem in terms of poor toughness, weldability and formability during their fabrication. In early 1950s, it was realized hot rolling process can be used in a controlled and judicious way to dictate the final microstructure (Bai Qi 1993). Before World War II, the most common practice for obtaining fine ferrite grain, was normalizing the Al-killed steel. After massive fracture failure of welded liberty ships and influenced by the work of Hall and Petch in 1950s, the new concept of controlling the rolling parameters was discovered. The urge developed from the necessity of increasing the notch toughness of shipbuilding and other structural steel grades. Some mills in Europe, by then, had already started practicing low-temperature hot rolling to achieve fine grain size. In 1959, some scientists discovered that small addition of niobium increased the strength after hot rolling. Great Lakes Steel was the first to commercially produce high strength Nb- bearing steels but with poor notch toughness. After this, it was realized that if the finish rolling temperature is lowered or total reduction at low temperature is increased to 30%, notch toughness of the Nb-bearing steels increases remarkably (Tanaka 1981). Finally in 1970s, controlled rolling was put into practice with small addition of Nb, Ti, Al and V to produce stronger steel grades using TMCR route. So TMCR can be considered as a sequential heating-deformation processes which transforms relatively simple materials into the one with extraordinary properties (Verlinden et al. 2007). Since last two decades, the scientific community

has meticulously started focusing on Nb-bearing steel research. In addition to that presence of high Mn along with Nb has particularly made the steel to be the newest field of research full of myriad scopes. Therefore, development of these steels through TMCR required a detailed understanding of the process and its role in microstructure evolution. Chronological development based on the understanding of softening and hardening phenomena occurring during TMCR has led to different types of TMCR process which will be discussed here.

2.2.1 Conventional Controlled Rolling (CCR):

Historically, this is the first type of controlled rolling practiced commercially (Figure 2.9). This involves control of all the four steps which is illustrated as follows.

2.2.1.1. Reheating - During this stage, the continuously cast slabs are reheated to relatively higher temperature, in the range of 1220-1260°C with carefully avoiding excessive austenite grain coarsening. The major objective of this step is to dissolve all the precipitates to take the microalloying

elements back into solid solution. The microalloying elements, in their solute form, control the grain size by retarding the grain boundary movement at high temperature. Reheating also makes microalloying elements available for downstream precipitation.

2.2.1.2. Roughing - This stage involves a number of heavy deformation passes (5-7) aiming to break the as-cast structure, reduce thickness and refine the as-reheated austenite. The deformation flattens the grains which once come out of the roll gap, quickly recrystallize into comparatively smaller grains. This is termed as static recrystallization which always occurs immediately after the deformation. Deformation conditions in terms of strain, strain rate and temperature if not chosen properly, may trigger incomplete static recrystallization resulting into bimodal grain size distribution. This duplex microstructure is undesirable in terms of toughness.

2.2.1.3. Finishing - This is the last series of deformation which is carried out at relatively low temperature regime to meet the final dimensions. This has enormous significance in microstructural evolution as it is conducted at a temperature which must be less than a particular temperature, called Recrystallization stop temperature (RST) or No Recrystallization Temperature (T_{NR}).

So, whatever strain is introduced gets accumulated and austenite grains are flattened. This is called pancaking of austenite. As microalloyed elements start precipitating out on the introduced dislocations, they pin them down. Eventually, softening specifically recrystallization is almost stopped. So the elongated grains attain the ratio (S_v) of grain surface to grain volume. This provides numerous nucleation sites for ferrite to form on cooling. During finishing, as strain accumulation happens due to the pinning action of the precipitates, additional potential nucleation sites are generated in the form of deformation or shear band which are found to be formed after more than 50% deformation (Bai Qi 1993). The resulting microstructure is extremely fine ferritic one suitable for attractive combination of good toughness and high yield strength.

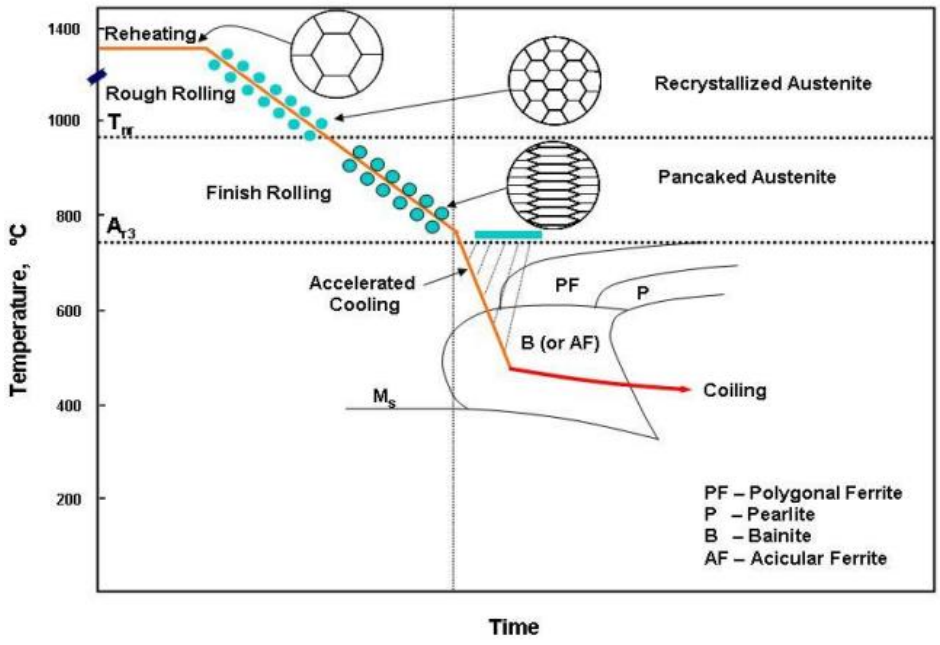

Figure 2.9. Schematic of TMCR process schedule with possible microstructure evolution (D. Bai, Cooke, Michael Ambrose Asante, and Dorricott 2004)

2.2.1.4. Cooling - The last stage of CCR is air or laminar cooling which is carried out below the austenite-to-ferrite transformation temperature (Ar_3). Phase transformation and interphase precipitation take place during this. Changing the cooling rate can change the final microstructure from ferritic to bainitic or martensitic as per requirement. Rapid cooling rate brings the Ar_3 temperature down broadening the strain accumulation regime. As the limitation of precipitation in austenite is increased, more microalloying elements remain in solution which on cooling gives

enhanced precipitation. Also, lowering Ar_3, limits the ferrite grain growth as they are formed at comparatively lower temperature.

2.2.2 Recrystallization Controlled Rolling (RCR):

In some specific products like heavy plates, thick-walled seamless tubes which cannot be finish rolled at lower temperature due to excessive rolling loads, TMCR is practiced in a modified form (Bai Qi 1993). This practice is called Recrystallization Controlled rolling (RCR). Here, to achieve finer grain size, recrystallization is carefully made to happen during comparatively high temperature finish rolling. Usually, the finishing temperatures are kept above 900°C which is higher than that employed in CCR. Usually, Ti-V based steels are rolled using this technique. RCR requires recrystallization to happen very fast because of smaller process window and prevention of grain growth following recrystallization. Compared to Nb, V makes recrystallization less sluggish .So, the first requirement is fulfilled by vanadium addition. On the other hand, Ti added is precipitated out as fine TiN particles during continuous casting and during rolling their fine distribution prevents grain coarsening. RCR is thus utilized to produce high quality thick microalloyed plates for shipbuilding, pipelines etc.

2.2.3 Dynamic Recrystallization Controlled rolling (DRCR):

Another type of modification is done in TMCR to process thin strips, rod or bar where there is not much time for recrystallization due to small inter-pass time. DRCR works on nucleation and growth of recrystallization during deformation. To ensure that, strain must exceed certain critical value so that recrystallization is so fast that once outside the roll gap, the grain refinement is achieved throughout the microstructure.

For our convenience, we will only consider the multipass deformation scenario in case of CCR. Proper utilization of TMCR to get best mechanical properties is only possible through a clear understanding of softening and hardening phenomena that occur during rolling. Recent development in the field of TMCR has immense contribution in making materials, especially FCC metals and alloys, resistant to intergranular degradation by modifying the crystallography of the grain boundaries in the microstructure. Specific combination of deformation and heating cycles, thereby, makes TMCR to be one of the most effective tools to successfully achieve grain boundary engineering (GBE). The purpose of TMCR is to obtain special boundaries by creating numerous

annealing twins. This, in particular, decreases the connectivity among the detrimental high angle grain boundaries and results in improved strength. However, due to some constraint, full commercialization of the process is yet not done. One of the reasons being lack of understanding on how TMCR actually brings the annealing twins and special boundaries into the microstructure. Some of the lab scale GBE processes seemed to be difficult for industrial scale implementation because of time and cost. Apart from grain refinement, TMCR, although showed a new pathway leading towards GBE, the field requires a huge body of comprehensive research work connecting morphological microstructure evolution to its crystallographic aspect. In *Table 2.1*, a comparison between conventional and controlled rolling parameters of a structural steel is given.

Table 2.1. Comparison of processing parameters during conventional and controlled rolling of a structural steel (Verlinden et al. 2007)

Hot rolling of a slab from 220 mm thick into a plate of 20 mm (0.12 wt% C, 1.4 wt% Mn, 0.025 wt% Nb)		
	Conventional	Controlled rolling
Reheating temperature	1200°C	1100°C
Number of passes in roughing mill	9	11
Temperature window for roughing	1100–1000°C	1050–950°C
Thickness after roughing	100 mm	67 mm
Time in between roughing and finishing mill	25 s	250 s
Start finishing rolling	1020–1000°C	800°C
Number of passes in the finishing mill	6	9
Exit temperature	1000–950°C	770°C
Cooling speed	0.8°C/s	8°C/s
Fracture appearance transition temperature (FATT)	−15°C	−85°C
Change in flow stress	0 (basis)	+50 MPa

Note: Typical reduction per pass: roughing: 5–13%; 'finishing': conventional 25–35% and controlled rolling 10–18%.

The next section deals with a basic review of the metallurgical phenomena directly contributing to microstructure evolution. A detailed discussion on application of TMCR in the field of GBE is given in section 2.10.

2.3 Basic Metallurgical Events during TMCR:

In this section individual processes of recovery, recrystallization, grain growth and precipitation are discussed in detail to build an understanding of microstructural evolution by TMCR.

2.3.1 Recovery:

The strain energy introduced in a material during deformation is mostly dissipated as heat energy. Only a very small amount (1%) remains as stored energy which is responsible for all the property changes due to generation of numerous crystalline defects like vacancies and dislocations. In practical situation, the point defects do not contribute much to the stored energy as they get annihilated at very low temperature. So, the stored energy depends on the introduced dislocation density. Multiplication of preexisting dislocations, their entanglement and even grain boundaries add a significant amount to the increased stored energy. This stored energy is found to be the driving force for recovery and recrystallization (Verlinden et al. 2007; Hatherly and Humphreys 2012)

The stored strain energy in a deformed material starts getting released by annihilation and rearrangement of dislocations. Recovery, therefore changes the microstructure prior to recrystallization by movement of dislocations without moving the High Angle Grain Boundary (HAGB). After this, a part of pre-existing properties is restored and the material is said to recover. Recovery softens the material by: formation of cells with highly tangled dislocation cell walls, annihilation of dislocations within cells, formation of subgrains and subgrain growth by the movement of Low Angle Grain Boundaries (LAGB) (Figure 2.10).

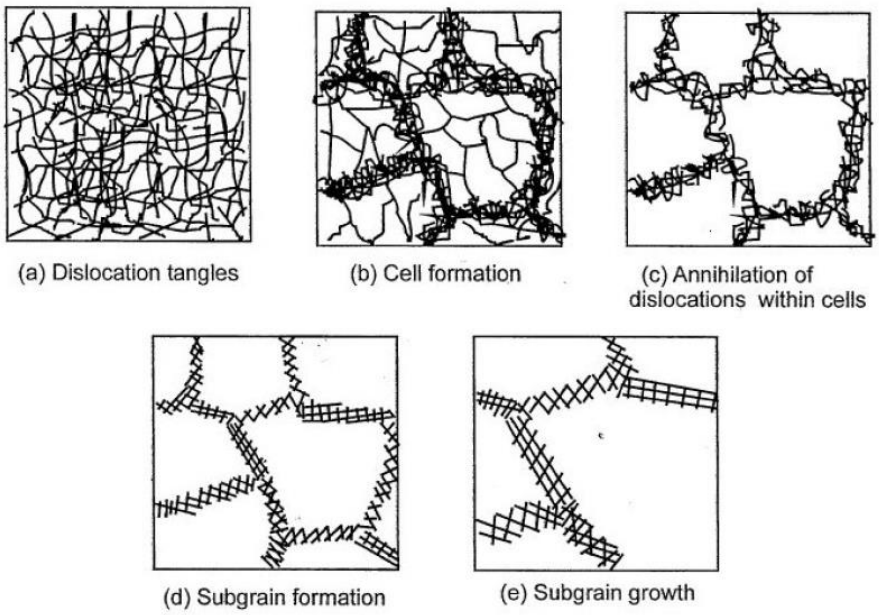

Figure 2.10. Sequential schematic of Recovery Process (Hatherly and Humphreys 2012)

In reality, a significant overlap of the sub steps of recovery may exist. Temperature, strain, strain rate and the addition of microalloying elements are the factors which usually affect recovery and depending on material one of them becomes rate controlling step. An increase in first three parameters accelerates where the last one makes recovery sluggish. Deformation of materials with high Stacking Fault Energy (SFE) at high temperature and strain may lead to greater rate of dislocation annihilation.

2.5.2.3 Measurement of Recovery- With the progress of recovery, the stored energy of the material is further reduced. So, any method that can measure the stored strain energy will be able to give a quantitative measure of recovery process. Direct methods of measuring recovery involves Differential Scanning Calorimetry (DSC) and X-ray diffraction (Verlinden et al. 2007). Measuring the changes in some physical and mechanical material properties such as electrical resistivity, stress, hardness and density give an indirect measure of recovery.

Due to continuously changing spatial distribution of dislocations in a high density network and high deformation temperature, recovery kinetics is measured exclusively through indirect estimation of global dislocation density as a function of time. Correlating the changes in other macroscopic material properties like electrical resistivity, hardness, density with microstructural changes is complicated and not very exact (Hatherly and Humphreys 2012). Phase transformation of austenite on cooling makes direct resistivity measurement impossible while high temperature measurements become erroneous due to high thermal scattering compared to weak recovery signal. Therefore, recovery is widely studied in microalloyed steel research using double-deformation and stress relaxation test (Yamamoto, Ouchi, and Osuka 1981). Both of these processes involve evolution of dislocation density or flow stress considering dislocation-dislocation interaction (Forest Hardening) given by the following equation:

$$\sigma = \alpha M \mu b \sqrt{\rho} \qquad \text{…….. } Eq\ 2.9$$

where, σ is flow stress, μ is the shear modulus, b is burgers vector, ρ is dislocation density, α is a constant of the order of 0.15 and M is the Taylor factor which is 3.1 for FCC material (Mecking and Kocks 1981). As significant contribution from recrystallization to softening process may mislead the exact estimation of recovered structure, the recovery studies are performed far below T_{NR} temperature or for very short duration above T_{NR} temperature.

A brief description of the recovery measurement methods is discussed next.

2.3.1.1.1. Double Deformation Test (DDT) - This test is done to measure the amount of softening occurring in between two consecutive deformation passes. Instead of going for conventional hardness measurement at room temperature where austenite phase does not exist anymore, tensile test is carried out at elevated temperature. The output can be used to calculate amount of softening the material has undergone through an interrupted two pass mechanical test. During the test, the material is heated to some higher temperature to get fully austenitic structure and cooled to some intermediate temperature where the first deformation pass is applied with certain amount of strain. The stress is then removed and the sample is held for some time (Figure 2.11. a). Following this holding time, the second deformation pass is given. The first deformation pass creates some defects and provides driving force for softening. The holding or the inter-pass time allows the material to soften and amount of softening is measured from the response of the material to the second deformation pass. The double deformation stress-strain curve (Figure 2.11. b) gives a measure of the softening ratio, *X*, following equation:

$$X = \frac{\sigma_{max} - \sigma_y}{\sigma_{max} - \sigma_{y_0}} \qquad \ldots\ldots\ldots\ldots \quad Eq\ 2.10$$

where, σ_{y_o} is the yield stress, σ_{max} is the maximum stress during the first deformation and σ_y is the yield stress in the second deformation. In reality, recovery, recrystallization and precipitation all contribute to the ratio, *X*. Therefore, it is a matter of paramount importance to filter out the individual effect of recovery to soften the material. A notable work of Yamamoto et al. explored probably the first and most convincing result in recovery study. They used metallography technique on deformed steel which was decarburized to rule out the possibility of precipitation. Microstructural observation revealed that below *X*=20%, recovery is the only factor to operate softening under their experimental conditions (Yamamoto, Ouchi, and Osuka 1981).

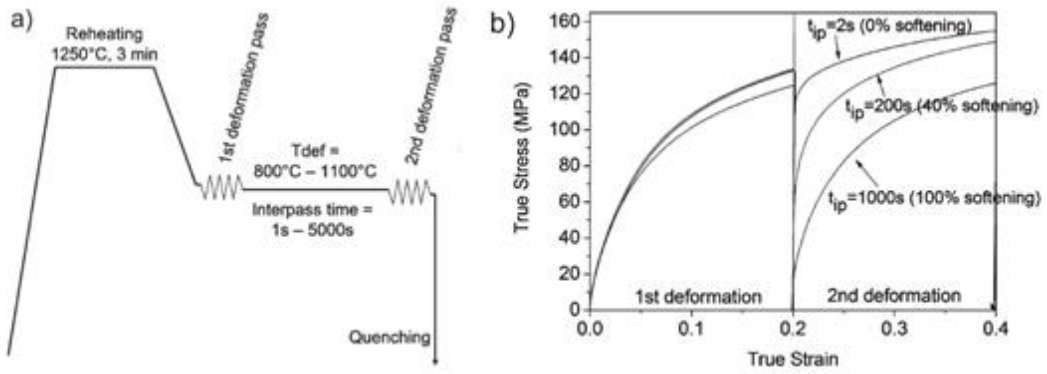

Figure 2.11. a) Schematic diagram of Double Deformation Test, b) True stress true strain graph generated from the test to calculate softening ratio (Vervynckt et al. 2010)

From the stress strain diagram obtained, a variety of methods are available to analyze them quantitatively e.g., back extrapolation method, mean flow stress and offset method. In addition to that, a cross check with the optical microstructure is necessary to confirm the softened volume fraction. The main drawback of this method (double deformation) is that it is quite tedious because of the fact that for every data point, a new sample is required which is to be given the same thermo-mechanical treatment.

2.3.1.1.2. Stress Relaxation Test (SRT) - This is a conceptually simple way to measure the recovery kinetics and used commonly in microalloying literature. Although, it had been used only to monitor onset of precipitation and estimate recrystallization fraction, Arieta and Sellar did an

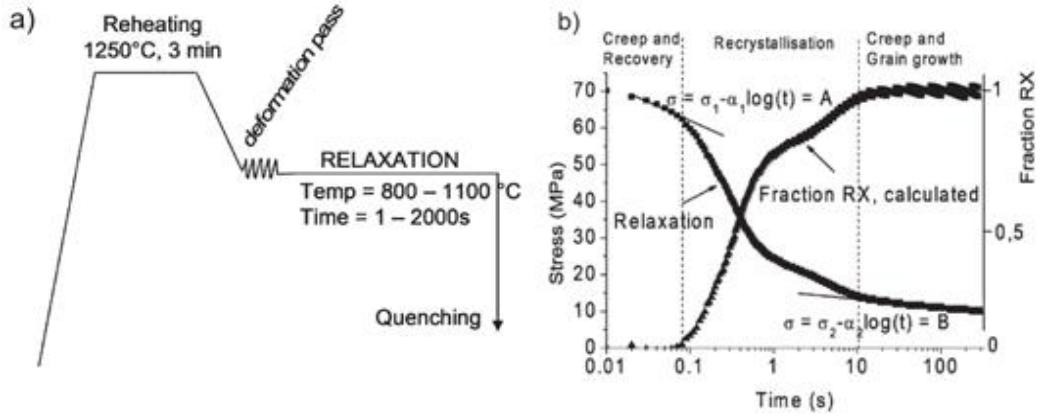

Figure 2.12. a) Schematic diagram of Stress Relaxation Test, b) Illustration of the analysis of a stress relaxation test (Vervynckt et al. 2010)

investigation of measuring recovery rate in presence of microalloying elements. Unlike Double Deformation Test, this test provides an opportunity to capture the complete softening kinetics with only one sample. The sample after being given the necessary heat treatment cycle is deformed. After a definite amount of strain at a given strain rate, the strain in the sample is fixed and changes in stress with temperature is recorded (Figure 2.12. a). This gives the progress of recovery. Utmost care should be taken during both the tests so that no second phase particles interfere with stress evolution. Though stress relaxation method looks simple and easy to implement yet it suffers from numerous drawbacks such as homogeneity of deformation, ageing during stress relaxation temperature sensitivity of the equipment.

2.3.1.2. Recovery Models - As recovery leads to softening, there is a gradual drop in the flow stress with time. Nature of this decay appears to attain logarithmic or power law kinetics (Hatherly and Humphreys 2012).

2.3.1.2.1. Logarithmic Law - According to Nes, this type of relationship seemed to be valid for recovery of all metals (single or polycrystal), high purity or commercial grades with heavy or small deformation. The kinetics study showed thermally activated cross slip or glide or solute drag may be the rate controlling step (Nes 1995). Friedel concluded (Friedel 2013) that flow stress drops logarithmically only in heavily strained FCC materials during low temperature annealing by thermally activated cross-slip as the mechanism. Microalloyed steels are found to follow this trend after being annealed at intermediate annealing temperature ($T_m/2$, m stands for melting point) (W. J. Liu and Jonas 1988; H. Zurob 2003). The form is given as:

$$\sigma = c_1 - c_2\, ln(t) \qquad \text{…….. Eq 2.11}$$

where c_1 and c_2 are some constants.

2.3.1.2.2. Power Law - This is given as

$$\sigma = c_3 - c_4 (t)^{-m} \qquad \text{…….. Eq 2.12}$$

where c_3 and c_4 are some constants.

A further improvement was done during recovery study of Al-Mg alloys. It was found that flow stress drops in moderately deformed system following Friedel's model logarithmically. This decay in flow stress due to dislocation rearrangement and annihilation is measured by correlating it with

bulk strain. The relation between microscopic motion of dislocations with macroscopic plastic strain was given by Orowan's law (Gondet et al. 2003)

$$M\dot{\varepsilon} = b\rho\bar{V} \qquad \text{…… Eq 2.13}$$

where M is Taylor factor, $\overline{V}$ is the average dislocation speed, b is burgers vector and Combining equations 2.12 and 2.13, Verdier et.al proposed the most accurate form of rate law for recovery kinetics study by the following equation (Verdier, Brechet, and Guyot 1998):

$$\frac{d\sigma}{dt} = -\frac{64\sigma^2 v_d}{9M_T^3\alpha_T^2 E_5}\, exp(-\frac{U_a}{R_g T})sinh(\frac{\sigma V_a}{k_b T}) \qquad \text{…… Eq 2.14}$$

In this equation, σ_e is the effective contribution of dislocations to flow stress, U_a is activation energy and V_a is activation volume required for recovery process to occur. v_d is Debye frequency, E_Y is Young's modulus and α_T is same as defined in Equation 2.9. It was found that value of U_a lies within a range of activation energy of pipe diffusion to self-diffusion (Nes 1995). The activation volume is the measure of how much free space available for the dislocations to move without getting locked by other dislocation (jogs for screw dislocation movement) or some pinning center (solute atom, second phase particle). This is calculated as $L.b^2$ where L is the activation length that changes inversely with dislocation density. L usually varies between 20-40b. It was found prior deformation changes the activation length by tightening the cell-walls. The only drawback of using above equation is its high sensitivity to dislocation density. For, subgrains with relatively low dislocation density, less accurate results are predicted (Hatherly and Humphreys 2012).

2.3.2 Recrystallization:

Amongst all the softening mechanism occurring during TMCR, probably recrystallization is the most important one to evolve the final microstructure. The deformed material recovers through annihilation and rearrangement of dislocations and reduces a part of the stored strain energy. Recovery ends up with the formation of sub-grains or cell structures with comparatively less dislocation density than in the just deformed material. When those sub-grains start growing, after certain critical radius it sets the platform for recrystallization. Formation of new set of strain free grains by the movement of high angle grain boundary replacing the old grains with higher

dislocation density typifies recrystallization process. As the boundary moves from low to high dislocation density region, there is a drastic reduction in overall dislocation density which leads to a decrease in yield strength of the material and increased ductility. Those strain-free grains nucleate and then grow consuming the entire deformed structure.

Among all other parameters, strain, strain rate, temperature and initial grain size control the process the most. Smaller initial grain size, higher strain, strain rate and temperature increase the rate of recrystallization. Industrially, recrystallization is very important not only to restore ductility required for further processing (Doherty et al. 1997), but also to tailor the final microstructure by controlling the grain size and hence the overall toughness of the material.

Depending on the nature of the nucleation and growth of strain-free grains, recrystallization can be classified as follows:

1. Static Recrystallization – The nucleation and growth of recrystallized grain take place once the deformation is over. To get recrystallization started, there must be more than a certain amount (~8% in case of Ni) of deformation which acts as driving force.
2. Dynamic Recrystallization – When the above driving force attains certain high value in terms of greater deformation, the time required for nucleation of recrystallization, i.e., incubation time is decreased. So, the nucleation followed by growth of the recrystallization nuclei occurs inside the roll gap during the deformation.
3. Meta-dynamic Recrystallization – This is somewhat midway between the first two where the nucleation happens during the deformation while the following growth mechanism operates after the deformation is over.

Once again it is worth mentioning that for our convenience, we shall only consider the first case and all recrystallization discussions will be limited only to static recrystallization.

2.3.2.1. Measurement of Recrystallization- An excellent description of recrystallized fraction is possible by direct measurement using quantitative optical microscopy. Using proper etching technique and special expertise, it is possible to quantify recrystallization volume fraction and rate by measuring the prior austenite grain size. The only disadvantage of this method is most of the commercial steels do not retain austenitic microstructure at room temperature. In case of phase transformation to martensite on quenching, roughly measured prior austenite grain size can give some idea of recrystallization volume fraction. But, in case of ultra-low carbon steels, where

austenite transforms to ferrite on quenching, it is very difficult to reveal the prior austenite grain boundaries (PAGB). Despite having some potential usage, as reviewed by Orsetti Rossi and Sellars, the above technique suffers from some error and has limited use in the microalloying literature (Doherty et al. 1997).

An alternative way to quantify recrystallization is through measuring flow stress restoration at high temperature where austenite is a stable phase. Usually, Double Deformation Test and Stress Relaxation Tests are carried out to measure softening due to recrystallization. Although, there are many methods to distinguish the effect of recrystallization from that of recovery, all of them have certain drawbacks. Due to lack of other techniques, quantification of recrystallization from flow stress measurement continues to be a common practice.

2.3.2.2. Stages of Recrystallization –

2.3.2.2.1. Nucleation - To describe recrystallization process, nucleation of the recrystallized grain should be modeled accurately. Since a long time, much emphasis was given on the growth part as nucleation is found to be over before the recrystallized fraction getting detected. Due to that, it was a common practice to start calculation with a parameter which gives an estimation of number of already formed nuclei. These already formed nuclei put the concept of 'site-saturation'. But, as nuclei formation depends on dislocation density difference which usually exists throughout the process of recrystallization, there is possibility of nucleation to happen once recrystallization has started.

Exhaustive x-ray diffraction (XRD) work (Lauridsen et al. 2003) showed both the concepts of nucleation to happen before and during recrystallization to be realistic. A critical nuclei size of 1 micron has been considered and it was shown that 80% of nucleation occurs before the material has recrystallized 10% which is a close assumption to site saturation, but the remaining 20% of the nuclei forms much later. Figure 2.13 supports that site saturation is not the only case as we see nucleation does take place at later stage of recrystallization due to dislocation density difference.

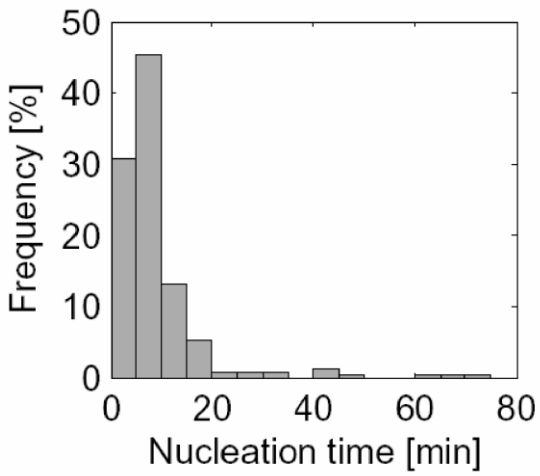

Figure 2.13. Distribution of nucleation times determined from 244 growth curves by 3-d X-ray diffraction (Lauridsen et al. 2003)

In microalloying literature, various mechanisms have been considered for nucleation to happen, and theories like Classical Nucleation, Particle Stimulated Nucleation (PSN), Strain Induced Boundary Migration (SIBM), Subgrain growth and coalescence, etc. are most common. Recent investigations into the nucleation mechanism have emphasized SIBM to be the dominant mechanism at lower range of strain during high temperature deformation of microalloyed steel (Lauridsen et al. 2003; H S Zurob, Dunlop, and Brechet 2006). The concept of site saturation has directed to the use of Avrami equation to calculate the overall kinetics of recrystallization and that is why nucleation by SIBM was mostly overlooked. Moreover, according to Humphreys (Humphreys 2004), the length scale of observing growth process of recrystallization is in the range of detection using microscopy which is not possible in the case of nucleation. That is why physically based modeling of nucleation process got neglected somehow.

It was Beck and Sperry, in 1950, who were investigating grain boundary movement in high purity aluminum. What they found is a special type of boundary migration taking place only in strain-hardened material leading to increase in grain boundary area (Beck and Sperry 1950). The kinetics of SIBM was first analysed by Bailey and Hirsch in recrystallized copper. The idea adopted was the formation of a stable nucleus only possible when the subgrain size distribution contains some subgrains which attain the critical size (Bailey and Hirsch 1962). For them, the driving force *G(t)* for subgrains to grow to form a viable nuclei should balance the capillary force, where $\frac{2\gamma_{SE}}{r(t)}$,

where γ_{SE} is the surface energy and *r(t)* is the size of the subgrain. Nucleation will take place when the following criterion will be fulfilled,

$$r_c(t) > \frac{2\gamma_{SE}}{G(t)} \qquad \ldots\ldots\ldots\ldots \text{ Eq 2.15}$$

where, $r_c(t)$ is time dependent critical radius which depends on dislocation density.

This concept was further re-established with sound explanation by Humphreys, 2004, where it was found that a strain energy gradient across the boundary can initiate SIBM which acts as recrystallization front. This front can move as a bulged boundary adjacent to several subgrains (Figure 2.14. a) or single subgrain (Figure 2.14. b). A further detailing of these two cases was done by Bate et. al and Hurley et al separately.

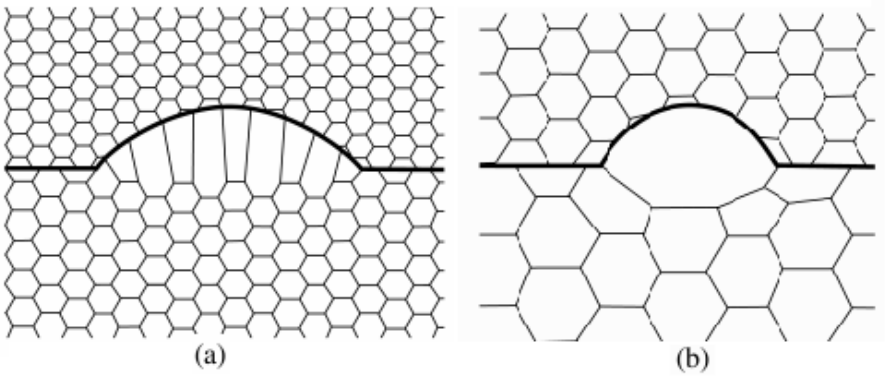

Figure 2.14. a) Multiple Subgrain SIBM, b) single subgrain SIBM (Humphreys 2004)

Multiple subgrain SIBM usually takes place in case of materials with poorly developed dislocation cell structure and large dislocation density gradient (Bate and Hutchinson 1997). On the other hand, single subgrain SIBM is likely to occur in well-recovered structures. While studying growth rates of SIBM in aluminum, they found that an incubation time for nucleation is needed which supports the necessity of recovery to happen for the onset of SIBM (Lauridsen et al. 2003).

Extending this idea, Zurob et al modeled recrystallization nucleation (H S Zurob, Dunlop, and Brechet 2006). They incorporated Bailey–Hirsch criterion to calculate the critical size of a nucleus. The fraction of subgrains larger than critical nuclei is calculated considering Rayleigh type distribution of subgrain size (Hansen, Vander Sande, and Cohen 1980; M Militzer, Hawbolt, and Meadowcroft 2000; Rehman and Zurob 2013).

The analytical value of the fraction is given as:

$$f(t) = exp\left(-\frac{\pi}{4}\chi_c(t)^2\right) \qquad \text{…… Eq 2.16}$$

where χ_c is the critical normalized subgrain size.

The final nucleation rate is formulated considering only the subgrains near HAGB to form recrystallization nuclei by SIBM. The final form of time evolution of nucleation is given by equation 2.16.

$$\frac{dN}{dt} = \frac{df}{dt}\frac{S_V}{A_{nucl}}F_n(t) \qquad \text{…… Eq 2.17}$$

where, S_V is the deformed grain boundary area per unit volume, A_{nucl} is the average area of viable nucleus and $F_n(t)$ gives a measure of area left for nuclei to form near grain boundary.

A more clear pictorial representation of Zurob's model was introduced by his co-workers (Rehman and Zurob 2013).The formation of hemispherical nuclei from the subgrains near HAGB by SIBM was assumed to occur inside a shell near HAGB (Figure 2.15. a). This ends up with site saturation when new hemispherical nuclei consume the whole shell and growth starts as the recrystallization front (dotted line) approaches to the center (Figure 2.15. b).

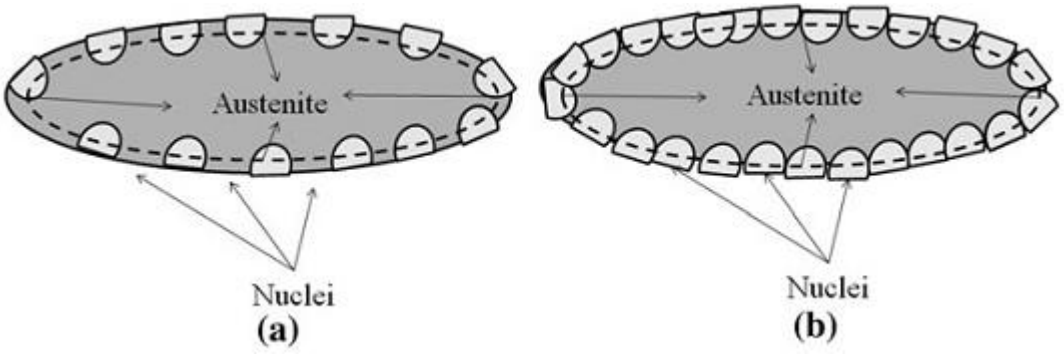

Figure 2.15. Schematic of Nucleation of recrystallization nuclei in deformed austenite by SIBM (Rehman and Zurob 2013)

In a recently published recrystallization model (Bäcke 2010), it was assumed that the size of sub-grain is proportional to the mean free distance of the dislocation slip. Low angle boundary energy and sub-grain misorientation both were found to be a function of the dislocation density which decreases as recovery progresses. Eventually, a certain critical value of the ratio of recovered

dislocation density to the original deformed dislocation density is achieved when nucleation was assumed to start.

2.3.2.2.2. Growth - As most solid-state transformation kinetics follow a sigmoidal plot of fraction transformed vs time, experimental evidences show the same trend for recrystallization. Overall, recrystallization kinetics is therefore expressed using classical Johnson-Mehl-Avrami-Kolmogorov (JMAK) model. While considering recrystallized fraction calculation, JMAK model is based on the consideration that nucleation and growth happen isotropically at all points without any impingement. This is called Extended Volume concept which makes the JMAK equation of the form as follows (Hatherly and Humphreys 2012):

$$X_{ext} = \int_0^t V(t)\dot{N}dt \qquad \text{…… Eq 2.18}$$

where, X_{ext} is the extended recrystallized fraction,$\dot{N}$ is the nucleation rate (assumed constant) and *V(t)* is the volume of the single recrystallized grain. JMAK model deviates from reality by the fact that it does not rule out the possibility of phantom nucleation in already transformed matrix and hindrance due to impingement of growing nuclei. For randomly distributed nuclei, the actual recrystallized fraction X_{act} is corrected using following equation:

$$X_{act} = 1 - exp(-X_{ext}) \qquad \text{…… Eq 2.19}$$

Combining the above two equations and replacing volume by $4\pi(\mathrm{r})^3/3$ and replacing radius by velocity* time, one obtains:

$$X = 1 - exp\left(-\frac{4\pi}{3}\int_0^t \dot{N}(vt)^3 dt\right) \qquad \text{…… Eq 2.20}$$

Now in the most common formulation of the above equation nucleation rate and growth velocity are assumed to be constant. Consequently the above equation simplifies to:

$$X = 1 - exp\left(-\frac{\pi}{3}\dot{N}v^3t^4\right) \qquad \text{…… Eq 2.21}$$

The above equation is the simplified JMAK equation which strictly assumes constant nucleation and growth rates and random distribution of nuclei. This is a serious limitation as nuclei do form at specific locations like grain boundary, twins etc. As nucleation and growth rates are usually assumed to be constant hence the two values are clubbed up together in one variable. Consequently the above equation simplifies to:

$$X = 1 - exp(-Kt^n) \qquad \text{…… Eq 2.22}$$

where, K is constant and n are commonly referred to as JMAK exponent. Conventionally, Avrami constants are not calculated separately but are calculated by fitting the JMAK equation to the experimentally obtained recrystallization kinetics data due to which any physical meaning is difficult to derive from the values of those constants. As such Avrami constants are at best quasi-physical parameters.

In the limiting case of site-saturation, the above equation can be similarly derived where all nuclei will be formed before the start of recrystallization. This assumption will lead to an exponent value of 3. JMAK exponent will lie in between 3 and 4 when nucleation decreases at a finite rate (Hatherly and Humphreys 2012). Experimentally derived JMAK exponents can have values less than 3 also because of the fact that the growth rates and dimensionality can change during recrystallization.

Some other parameters like grain size can also make JMAK exponent vary. While measuring recrystallization kinetics in a cold worked copper, Hutchinson et.al found that final grain size has a significant effect (Figure 2.16. a, b) on exponent value. In case of fine grain, more randomly distributed nuclei near grain boundary are there leading to n value near 3. A further decrease in the exponent value is observed in case of coarse grained material where nuclei are non-randomly distributed making the exponent deviating further from the constant 'n' value (Hutchinson, Jonsson, and Ryde 1989).

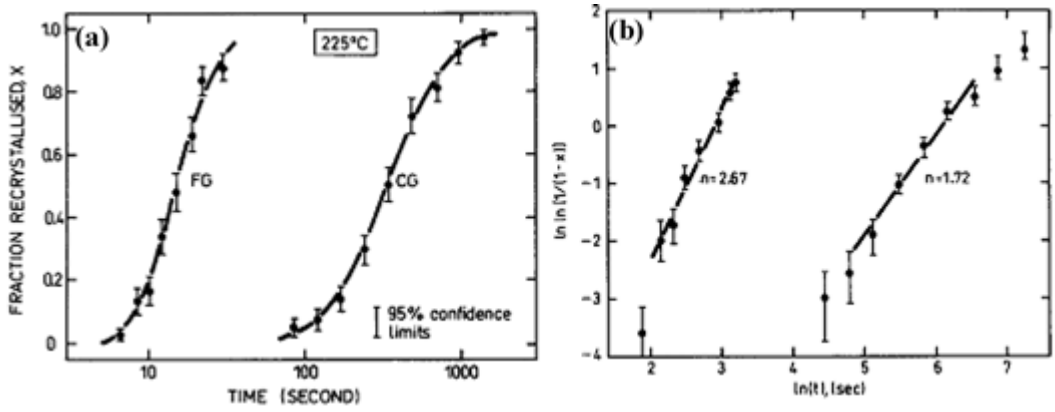

Figure 2.16. a) Recrystallized volume fraction as function of annealing time of copper at 225°C cold rolled 93% having fine grain (FG) and coarse grain (CG), b)Determination of JMAK exponent (Hutchinson, Jonsson, and Ryde 1989)

Considering the nature of nucleation rate and dimensionality of growth, JMAK exponent keeps changing. As nucleation rate usually varies with time in reality leading to site-saturation a

hypothetical case, JMAK exponent is decreased. In addition to that, growth of recrystallized grain can get constrained due to sample geometry or microstructural change making it sensitive to dimensionality resulting in the JMAK exponent being a non-integer and varying with time (Table 2.2).

Table 2.2. Theoretically calculated JMAK exponent (Hatherly and Humphreys 2012)

Growth dimensionality	Site saturation	Constant nucleation rate
3-D	3	4
2-D	2	3
1-D	1	2

The drawback of the consideration in JMAK model was modified in the next generation models considering the exponent as function of time to give a better fit to experimental data. But, this purely empirical approach came to be invalid for cases where the exponent is already defined and further physical interpretation of the model became impossible.

Next, in 1990, Sellars proposed another empirical equation to calculate the time for 50% recrystallization given by the equation as follows:

$$t_{0.5RX} = 2.5 * 10^{-19} {D_0}^2 \varepsilon^{-4} \, exp\left(\frac{300000}{RT}\right) \qquad \ldots\ldots\ldots \text{ Eq 2.23}$$

where, D_0 is initial austenite grain size. This equation is valid for carbon manganese steels (Sellars 1990). Similar equations have been proposed for micro-alloyed steels. These equations, in past two decades are immensely popular with researchers studying the relative effects of influential parameters.

Yoshie et al. modified the original JMAK equation replacing time with dislocation density thus allowing the use of single equation for predicting the recrystallization kinetics in successive rolling passes (Yoshie et al. 1987). In 1991, Medina et al. carried out torsion studies on a variety of composition both that of micro-alloyed and carbon manganese steels to estimate the constants used in Sellar's equation (Medina and Fabregue 1991). Sun et al. realized that physically-based models are too complicated to develop and hence used Sellar's empirical models to compare

recrystallization kinetics between steels having different chemistries and processing conditions (Sun and Hawbolt 1997).

In 2001, Sellars' equation was applied to determine recrystallization kinetics in steels of different chemistries and processing conditions where the effect of Nb as microalloying element to control boundary mobility was observed in both solute form and as precipitate (S. Cho, Kang, and Jonas 2001). This was further improved by the application of Finite Element Method (FEM) to correlate microstructure evolution with flow stress using equation 2.9 (J. R. Cho et al. 2005). These models were proved to be capable enough to predict complete microstructure evolution for their robustness to calculate recrystallization in industrial continuous cooling and multi-pass scenarios.

The next improvement was made by capturing another parameter which always interferes with recrystallization. In 2005, Gomez et al. summarized the approaches to calculate Zener Drag to incorporate the pinning effect of microalloyed precipitates during HAGB migration. They presented three models such as- Rigid Boundary Models (RBM), Flexible Boundary Model (FBM) and Sub Boundary Model (SBM). They concluded that the best reasonable estimate of pinning force is given by FBM which assumes that an infinitely flexible boundary can interact with any particle of radius '*r*' until it is fully pinned (Gomez, Medina, and Valles 2005).

Zurob et al. implemented the effect of precipitation on recrystallization kinetics calculation by capturing the time-dependent boundary mobility and dislocation density term (H S Zurob, Brechet, and Purdy 2001). The idea inherited from Humphreys, 1997 (Humphreys 1997a, 1997b) was that growth part in recrystallization happens by the growth of an individual subgrain. The rate is quantified as driving force times boundary mobility while the driving force is reduced by Zener Drag term to consider the precipitate pinning effect on recrystallization. At the same time, effect of recovery on recrystallization was also taken into account (H S Zurob et al. 2002) by introducing time dependent dislocation density term. And the final expression to calculate recrystallized fraction takes the following form:

$$X(t) = 1 - exp\left(-N_{rex}\int_0^t \Psi(t)M(t)G(t)dt\right) \qquad \ldots\ldots\ldots \text{ Eq 2.24}$$

where, N_{Rex} is the number of recrystallization nuclei, $M(t)$ is the boundary mobility, $G(t)$ is the driving force and $\psi(t)$ is a factor used to capture the effect of precipitation on nucleation. $\psi(t)$ equals unity when sub-grain size becomes greater than the inter-precipitate distance.

Pereda et al. developed a model using Avrami equation and Sellars' equation to predict growth of recrystallized nuclei for multi pass rolling and under non isothermal conditions from single pass isothermal models (Pereda, Rodriguez-Ibabe, and López 2008). They used the following equation to develop the growth model:

$$X = 1 - exp\left(-ln\,2\left(\frac{t}{t_{0.5X}}\right)^{n}\right) \qquad \ldots\ldots\ldots \text{ Eq 2.25}$$

In connection to their another contribution, (Fernández et al. 2000) time for 50% recrystallization was calculated considering the drag effect of solute niobium ,([Nb]) by following equation:

$$t_{0.5X} = 9.92 * 10^{-11} D_0 \varepsilon^{-5.6 D_0^{-0.15}} \dot{\varepsilon}^{-0.53} exp\left(\frac{18000}{RT}\right) exp\left[\left(\frac{275000}{T} - 185\right)[Nb]\right] \qquad .. \text{ Eq 2.26}$$

To be applicable for a wide range of conditions, exponent 'n' was modified as:

$$n = 155 exp\left(-\frac{56485}{R_g T}\right) \qquad \ldots\ldots\ldots \text{ Eq 2.27}$$

These equations were strictly valid for isothermal single pass rolling. To extend it for non-isothermal conditions Pereda et al. used additivity principle where in the temperature was discretized in small isothermal steps and corresponding recrystallized fraction was calculated in each steps and later on added. To calculate for multi-pass deformation schedules effective grain sizes were calculated at end of each pass and the corresponding recrystallized fraction and was used as an input for the next pass (Pereda, Rodriguez-Ibabe, and López 2008).

Most recent development added to recrystallization kinetics model is by Backe (Bäcke 2010). Adopting the concept of Humhreys (Humphreys 1997a, 1997b), a physically based growth model was proposed. It was shown that growth rate of sub-grains will be proportional to subgrain boundary mobility, driving force and the sum of vacancy concentration in the deformed and recrystallized zone. This model is more accurate and realistic as net driving force used in it is the stored energy of deformation reduced by the Zener pinning force and solute drag forces.

2.3.3 Grain Growth:

Growth of the fine recrystallized grains is an area of utmost importance to study. The deformed material releases the strain energy stored inside it by recovery and recrystallization. The outcome is an almost homogeneous distribution of fine grains. Although, the energy of the system is

lowered to a great extent, the increased grain boundary area increases the free energy of structure. There is a considerable potential for the recrystallized grains to grow during the delay time between end of rough rolling and start of finish rolling while processing through TMCR. The driving force for grain growth is the energy stored in the form of grain boundaries and is usually two orders of magnitude less than that for static recrystallization (Hatherly and Humphreys 2012).

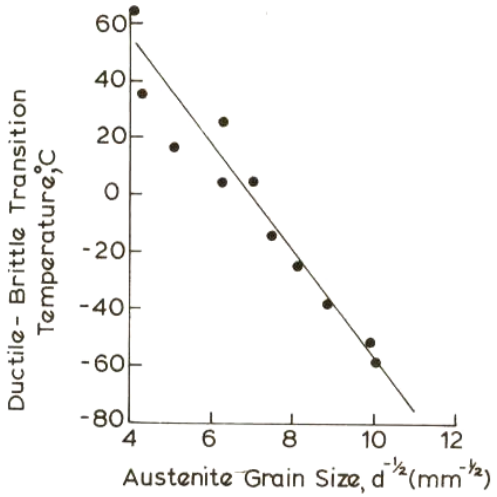

Figure 2.17. Effect of grain size on Ductile-Brittle-Transition-Temperature (Gladman, McIvor, and Pickering 1972)

The urge to explore grain growth kinetics came from the dependence of mechanical behavior on grain size. Gas or oil transmission pipelines usually require to be designed to operate at high pressure with enhanced toughness over a wide range of temperature. Without increasing the thickness of the pipe walls it leads to high installation cost, a judicial balance of strength and ductility is maintained to withstand high operating pressure and contrasting variables of land climatic conditions (Stalheim, Barnes, and Mccutcheon 2006). The microalloyed steels used for manufacturing pipelines are therefore carefully designed to balance between high yield strength and improved low temperature fracture toughness. This requires utmost care to control the grain size as with increase in grain size, the ductile to brittle transition temperature (DBTT) gradually increases (Figure 2.17). The material becomes more prone to fracture as crack arresting HAGB are reduced in number. A good understanding of grain growth is therefore one of the significant areas to control microstructure during TMCR of Microalloyed Steels.

Many notable research works have been done to study grain growth in single phase alloys. It was seen that microalloying elements have tremendous effect on grain growth. Post recrystallization

grain growth may be divided into two types, normal grain growth and abnormal grain growth or secondary recrystallization. Normal grain growth is a continuous process in which the microstructure coarsens

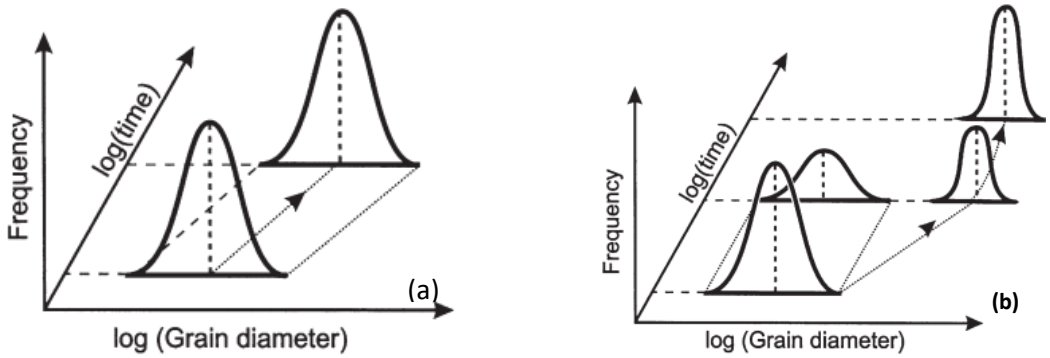

Figure 2.18. Grain size distribution change shown schematically during a) normal grain growth, b) abnormal grain growth (Hatherly and Humphreys 2012)

uniformly. After sometime, the system reaches a quasi-stationary state with invariant form of grain size distribution (Figure 2.18. a). Usually the range of both grain sizes and shapes is narrow and the distribution is independent of time and scale. On the other hand the central mechanism of abnormal grain growth is size difference between grains. This discontinuous process rapidly increases size difference over time as few larger grains grow consuming the smaller grains leading to bimodal grain size distribution (Figure 2.18. b) (Verlinden et al. 2007; Hatherly and Humphreys 2012; M Hillert 1965). Eventually, large grains impinge and the process again gets back to normal grain growth. Due to precipitate unpinning of boundaries, presence of strain gradients, inhibition from free surface, abnormal grain growth is supposed to take place. There are four main factors that affect grain growth. The first one is temperature which directly governs mobility of high angle grain boundaries (HAGB) by which grain growth occurs. For smaller driving force, grain growth kinetics becomes faster at higher temperature. The second factor is the presence of solute atoms and/or second phase particles. This will be discussed in the solute drag section (section 2.8) and Zener drag will be mentioned in brief in section 2.6. Next factor controlling grain growth is specimen size. It was observed that if the sample thickness is less than the size of growing grains, further growth is stopped. The grains, then, continue to grow in only one direction diminishing the driving force. A practical example of this is thermal etching, where free surface of the sample stunts the growth of the grains intersecting the surface and gradually develops grooves slowing

down grain growth further. The final and most important factor controlling grain growth is the presence of certain non-random texture which makes the grain growth kinetics sluggish through introducing low energy-low angle grain boundaries (LAGB) in the microstructure (Hatherly and Humphreys 2012). A detailed discussion of theories of grain growth will be given in section 2.6.

Apart from above discussed phenomena, two other important events take place during TMCR. One of them is precipitation of microalloying elements. This has immense influence in microstructure evolution during the finish rolling stage. The objective of the current thesis partly lies on exploring the effect of solute niobium on grain boundary migration during grain growth. This is the reason why a detailed discussion of the precipitation process, its kinetics and models to predict precipitation are not discussed. Also, the other important phenomenon occurring during TMCR is annealing twin formation that changes grain boundary character distribution (GBCD). A detailed description of twin formation mechanism will be given in section 2.9.

2.4 Grain boundary- description and classification:

Cost effective high performance material design has been one of the overgrowing interests of the scientists which requires a very strong understanding of microstructure-property correlation. In polycrystalline materials, microstructure evolution is a complex phenomenon which requires understanding of grain boundaries that separate regions of different crystallographic orientation but of the same phase. This section is a review to explore some of the basic aspects related to the description and classification of grain boundaries.

2.4.1 Description of a Grain boundary:

Grain boundaries are reported as longest, non-equilibrium crystal defects between two grains where the atoms have a compromising situation than their position at grain interior. Evolution in the research field of structure and properties of grain boundaries from amorphous cement theory (by Rosenhain-Ewen, 1912), Coincidence site lattice model (by G. Friedel 1920 and Kronberg-Wilson 1949) as a “conceptual phase” to bicrystal theory led to the introduction of “discovery phase” due to advent of several computational and experimental techniques. Being a surface separating two regions of different crystallographic orientations, it can be described crystalloprahically (Watanabe 2011). If we consider AB to be a boundary between two grains 1 and 2 (Figure 2.19. a), in order to describe

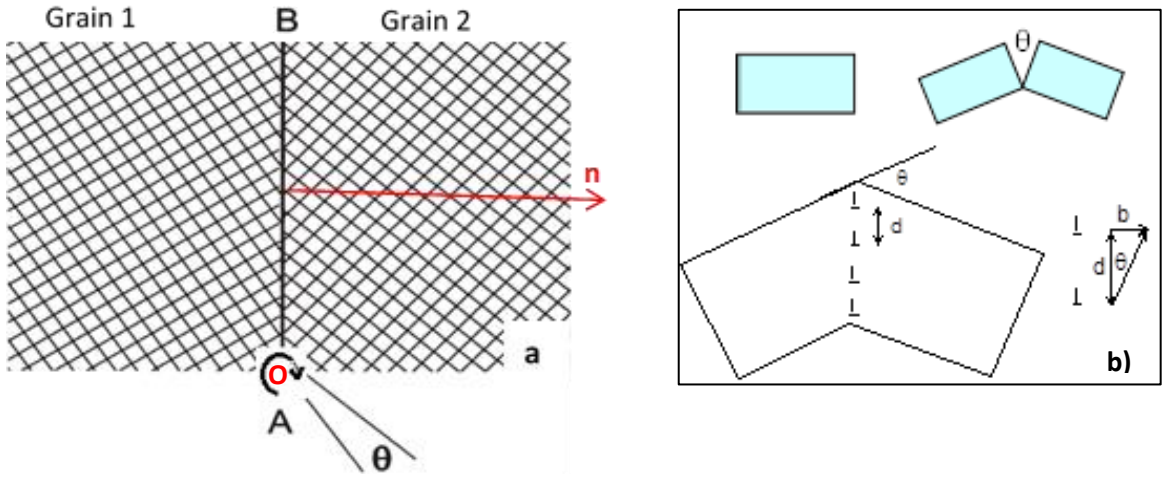

Figure 2.19.a) Schematic of a grain boundary separating two grains of misorientation θ about an axis perpendicular to the plane of the whole figure (Hatherly and Humphreys 2012), b) Creation of a bi-crystal

it exactly, we need eight degrees of freedom (DOF). Of them, 5 are independent macroscopic and 3 are microscopic. According to bicrystal model, a cut through a single crystal followed by a tilt of the two halves, generate a wedge shaped gap between them (Figure 2.19. b). If we consider a cubic crystal with an edge dislocation, the part on both sides of the extra half plane is tilted. This is very similar to the tilted halves in the imaginary operation to construct a grain boundary from a single crystal. Grain boundary DOFs are described in terms of misorientation of the two crystals and the spatial orientation of the grain boundary plane. If we consider a normal to define a grain boundary plane, it can also be considered as a vector whose orientation can be described with respect to a co-ordinate system with the help of three direction cosines, Cosα, Cosβ and Cosδ where α, β and δ are the angles between the vector and the axes. As we know, $Cos^2\alpha+Cos^2\beta+Cos^2\delta = 1$, so we need only two of those to describe the orientation of the vector as well as normal to the grain boundary plane. Thus, 2 DOFs are associated with spatial orientation of the grain boundary plane. Apart from that, misorientation between the two crystals can be defined by the angle of rotation, hence, 1 more DOF and the axis (again can be considered to be a vector with 2 DOFs) about which the rotation is executed. This is known as angle-axis pair representation of orientation relationship in the Rodrigues-Frank space. In brief, 5 DOFs come like, 2 to specify the unit vector normal to the interface, 2 to specify the axis of rotation and 1 to specify angle of rotation (right handed in Figure 2.19. b). In addition to these 5 macroscopic DOFs, there are also 3 microscopic parameters in terms of translational vector representing rigid body rotation of the two

grains either parallel or perpendicular to grain boundary plane to generate equilibrium atom structures at grain boundary (Lejcek 2010).

Based on above discussion, grain boundaries can be described by the notation $\theta^0[h_0k_0l_0],(h_{n1}k_{n1}l_{n1})$, i.e., angle-axis pair and boundary normal with respect to one grain. To make it more accurate, sometimes the contribution from grain 2 to define grain boundary plane is also included as $\theta^0[h_0k_0l_0],(h_{n1}k_{n1}l_{n1})/(h_{n2}k_{n2}l_{n2})$. As several combinations of orientation are possible, grain boundaries can be categorised based on the relation between the 5 DOFs. If the rotation axis and grain boundary normal are considered to be 'o' and 'n', then for the condition of ($o \parallel n$), the boundary is referred as pure twist boundary (Figure 2.20. a). In this special case, the grain boundary plane is clearly defined and independent of the rotation angle. For the condition of ($o \perp n$), tilt boundaries are generated with the rotation axis within the grain boundary plane. For a range of rotation angle, a series of grain boundary planes are possible. In case of mirror symmetry between grain 1 and 2, the boundary is called symmetrical tilt boundary (Figure 2.20. b). All other configurations are called asymmetrical tilt boundaries Figure 2.20. c). Grain boundaries which do not fulfill either of the criteria of the first two classes are termed mixed or random grain boundaries and consist of mixed twist and tilt components.

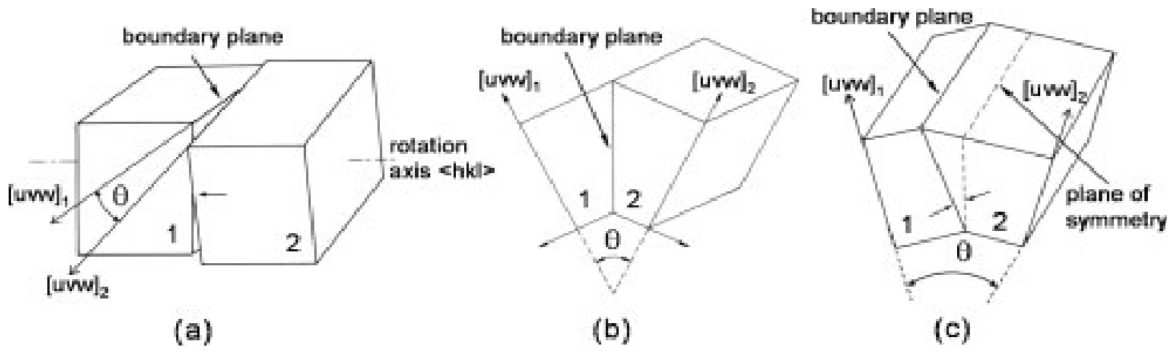

Figure 2.20. Schematic of different types of grain boundary a) twist grain boundary, b) symmetrical tilt boundary and c) asymmetric tilt boundary (Gunter Gottstein and Shvindlerman 2009)

The above discussion can be summarized based on boundary plane indices and twist angle as:

$\{h_1k_1l_1\}=\{h_2k_2l_2\}$, twist angle =0 indicative of symmetric tilt boundary (STB)

$\{h_1k_1l_1\}\neq\{h_2k_2l_2\}$, twist angle =0 indicative of asymmetrical tilt boundary (ATB)

$\{h_1k_1l_1\}=\{h_2k_2l_2\}$, twist angle $\neq 0$ indicative of twist boundary (TWB)

$\{h_1k_1l_1\} \neq \{h_2k_2l_2\}$, twist angle $\neq 0$ indicative of general boundaries.

2.4.2 Grain boundary Geometry measurement:

Measurement of grain boundary geometry is possible using one of the several techniques such as X-Ray diffraction, transmission electron microscopy (TEM) diffraction using selected area diffraction (SAD) or convergent beam electron diffraction (CBED). However, the most convenient method of grain boundary identification and measurement is electron back scattered diffraction (EBSD). When the electron beam hits the 70° tilted sample, diffraction patterns in the form of bands are generated. This is a characteristic of the sample crystal structure and known as a Kikuchi pattern (Figure 2.21. a). These are nothing but intersection of the diffracted electrons from lattice planes with the phosphor screen.

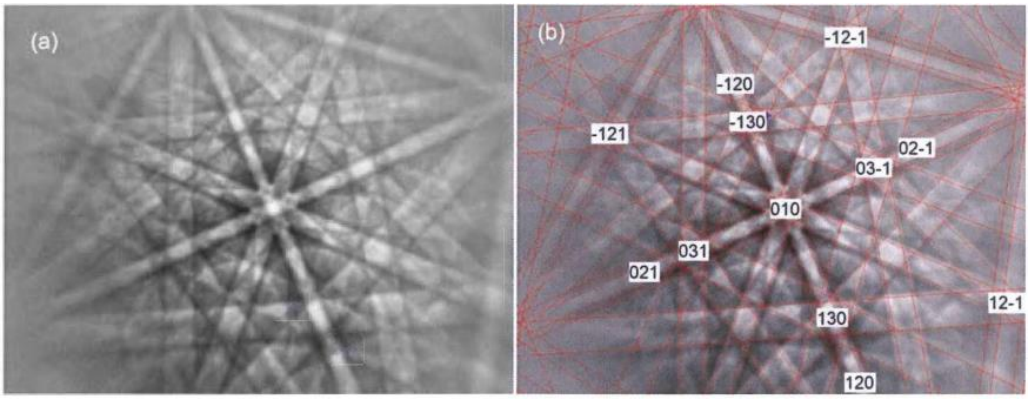

Figure 2.21. a) raw Kikuchi pattern obtained from diffraction, b) pattern indexed as that of an FCC system

The angles between three sets of bands are measured and compared with the ones made by different crystallographic planes in that particular crystal system for indexing (Figure 2.21. b). A detailed description of this method will be discussed in experiment part of this thesis. EBSD diffraction can also give information about lattice parameter, phase identification, orientation of the lattice etc. Also, the orientation difference between two points can be detected and based on if this exceeds a user-defined threshold, the position of a grain boundary is confirmed. From the orientation data of two points sitting on either side of the grain boundary, misorientation of the grain boundary can be determined to assign a boundary its exact type, e.g., CSL, HAGB, etc.

2.4.3 Crystallographic Classification of Grain boundaries:

Earlier, it was believed that grain boundary structure is amorphous. Later on the concept was replaced by the idea that grain boundary is composed of region of 'good and bad fit'. This idea was extended further in dislocation models of grain boundary structure. Based on numerous theoretical and experimental evidences, next phase of interface science proved that grain boundary is also crystalline (Lejcek 2010). The difference in magnitude of atomic misfit across grain boundary plane results into different internal structure of it. Based on this, we can classify the grain boundaries into two broad types, viz., Low Angle Grain Boundary (LAGB) and High Angle Grain Boundary (HAGB). Apart from this, a new concept based on atom coincidence gives rise to a new type, known as 'CSL' boundary.

2.4.3.1 Low Angle Grain Boundary (LAGB):

When the spatial orientation of the two adjacent crystals does not differ largely (<15°), the interface between them is called an LAGB. An LAGB is completely comprised of an array of dislocations (with same Burgers vector, ***b*** (Figure 2.22. a)) as mentioned in the bi-crystal model.

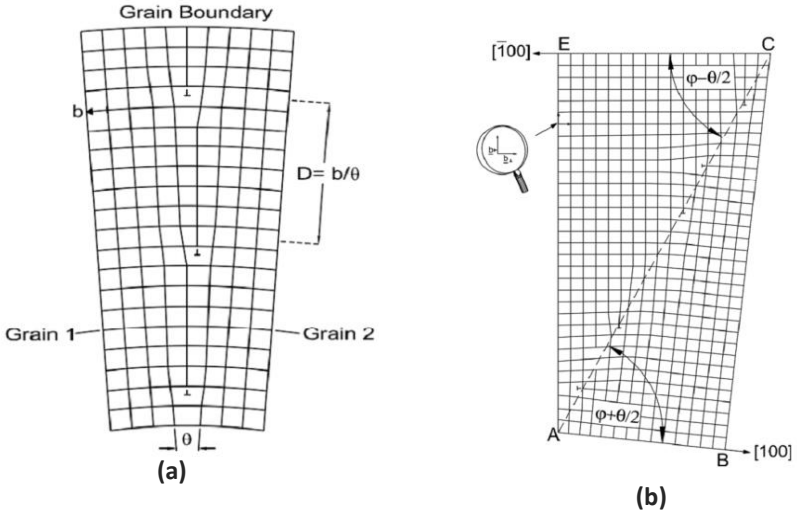

Figure 2.22. a) Dislocation model of a symmetric LAGB, b) asymmetrical tilt boundary structure (Gunter Gottstein and Shvindlerman 2009)

The number of dislocations per unit length in the grain boundary, 1/D, increases with the misorientation angle θ, which can be given by a simple trigonometry as, 1/D= θ/b. Situation becomes more complex when the increase in misorientation leads to the introduction of another array of non-parallel edge dislocations in case of an asymmetrical twist boundary. The number of

dislocations of this second set increases with increasing deviation. This ultimately leads to the formation of a new symmetrical tilt boundary, perpendicular to the original one, made up of dislocations of second array. The number of dislocations in both the arrays can be measured in terms of θ and φ (inclination angle) (Gunter Gottstein and Shvindlerman 2009). The energy of the boundary (γ_s) can be calculated considering the dislocation model as

$$\gamma_S = \gamma_0 \theta (A - \ln \theta) \qquad \text{…….. Eq 2.28}$$

where, $\gamma_0 = Gb/4\pi(1-\nu)$, $A = 1+\ln(b/2\pi r_0)$ and r_0 is the dislocation core radius , usually considered as 1-5 times Burgers vector (Hatherly and Humphreys 2012). As misorientation increases, more and more edge dislocations can be introduced in the tilt boundary leading to increase in the γ_s value upto some θ. With this, the distance, d, between the edge dislocations is also decreased leading to overlap of the strain field of the dislocations. Beyond this point, dislocation theory fails to predict boundary structure. The upper limit of successful application of this model is 13-15° which corresponds to $d \approx 4|b|$. Experimental validation of this transition range came from a study on contact angle measurement of grain boundary trace at free surface of bismuth. Another evidence from migration studies of planar boundaries in aluminium also showed 13.6° to be the transition angle (Lejcek 2010). However, beyond 15°, overlapping results into decrease in the energy per dislocation line as well as low energy of the boundary. Hence, thermodynamically a material prefers to have same number of dislocations in few numbers of boundaries with high θ value.

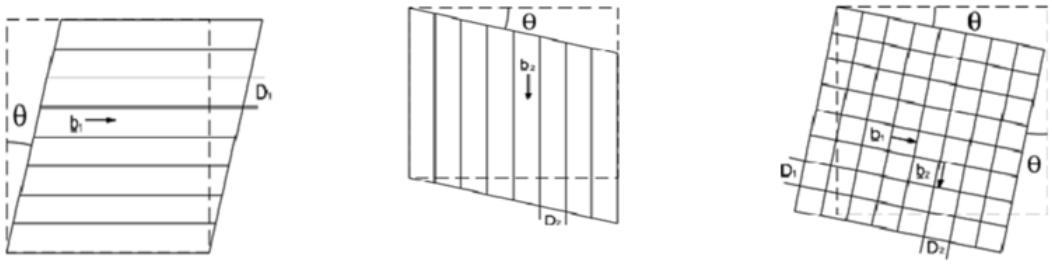

Figure 2.23. Formation of low angle twist boundaries (Gunter Gottstein and Shvindlerman 2009)

Similar to the above, the twist boundaries are generated with screw dislocations which have to appear normal to each other in two sets in order to have a rotation.

Based on the orientation of the dislocation's Burgers vectors, we can again classify the grain boundaries into two categories. The boundary which contains dislocations with Burgers vector

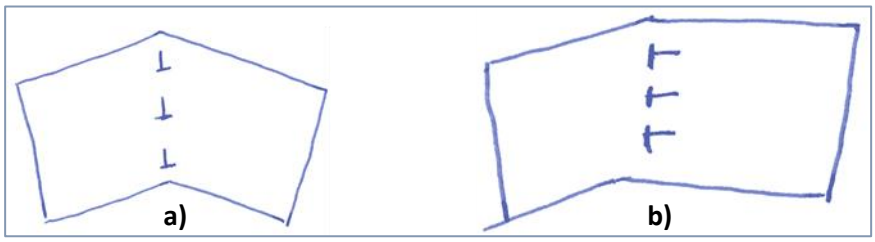

Figure 2.24.Schematic of a) Glissile boundary, b) Sessile grain boundary

perpendicular to (or away from) the boundary plane is called glissle interface (Figure 2.24. a). Here, translation of interface can be possible by normal slip without any diffusion. It is worth to mention that in case of martensitic transformation, this type of interface is required. For the edge dislocations with Burgers vector on the boundary plane, diffusion must occur in order to move the interface. This type of boundary is called a sessile boundary (Figure 2.24. b).

2.4.3.2 High Angle Grain Boundary (HAGB):

For misorientation angle higher than 15°, the dislocation cores tend to overlap which destroys the identity of individual dislocation as a crystal defect. Thus, the dislocation model fails to predict the specific grain boundary energy variation with misorientation. Grain boundary energy measurements show no further change with increasing θ, in contrast to the dislocation model which would predict an energy decrease for high-angles of rotation (Figure 2.25. a). So, some special geometric treatment to describe the boundaries with misorientation more than 15° became important. The concept of HAGB structure to be an undercooled liquid was proved to be misleading as some defined atomic structures were noticed in them. The island model proposed by Mott and modified by Gifkins assumed HAGB structure to be made of perfectly crystalline islands floating in an undercooled medium. This model failed for deviation in atom behavior

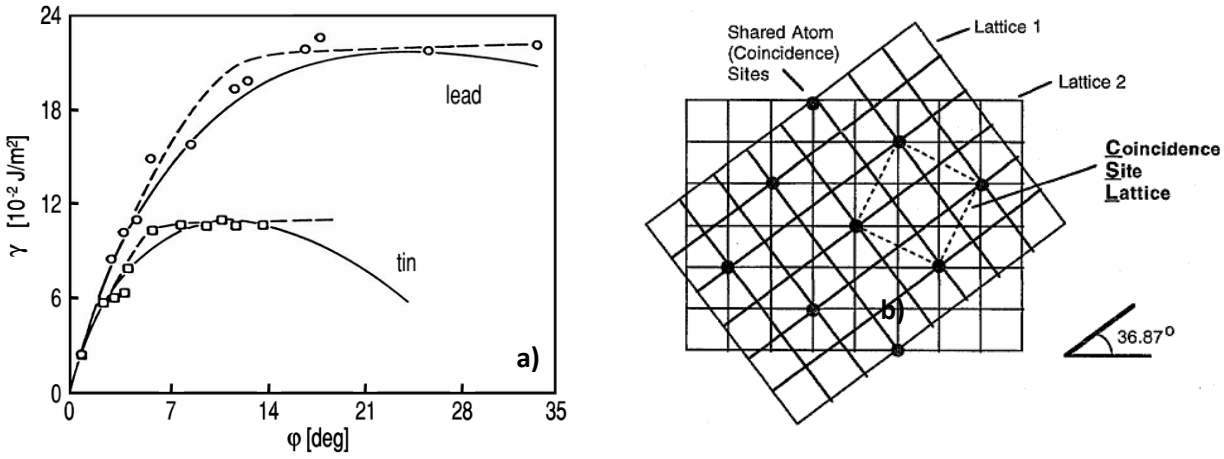

Figure 2.25. a) Dependence of specific grain boundary energy with misorientation (lines are dislocation model calculated and points and dashed lines are experimental results) (Gunter Gottstein and Shvindlerman 2009), b) Schematic representation of a CSL boundary with Σ=5 (Aust 1994)

from single to cluster atom model.

Another approach to classify HAGBs is on the basis of structural units. Using systematic computer modelling, grain boundaries in FCC crystals were demonstrated using a structural unit model which considers repetition of a fixed number of structural units to describe HAGB structure (Figure 2.26). Basis of these units were assumed to be seven types of convex polyhedral-tetrahedron, regular octahedron, pentagonal bipyramid, tetragonal dodecahedron, capped prism, capped archimedian prism and icosahedron. Majority of grain boundaries are considered to be made up of combination of structural units (structural unit ⎪A.A⎪ from delimiting {013} and

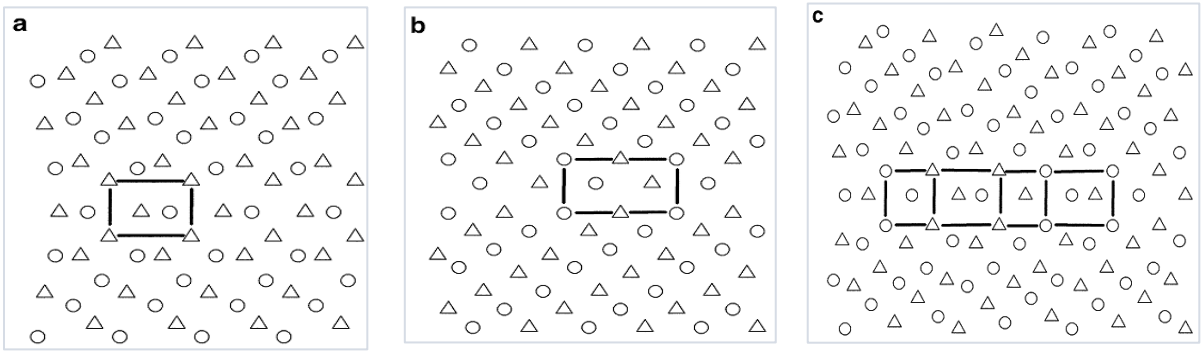

Figure 2.26. Computer simulated symmetrical tilt boundary for a) {013}, b) {024} and {037} boundary planes with different structural units (Lejcek 2010)

$\left|B.B\right|$ from delimiting {024} boundaries form another structural unit $\left|AB.AB\right|$ of {037} boundary in a bcc lattice as in Figure 2.26).

The delimiting grain boundaries which contain single structural unit are called singular boundaries and the ones with combination of structural units are called general grain boundaries with very high energy. The third type of grain boundaries are just an energetically transitional ones between the above two and termed as vicinal boundaries. Their structure is made of unit of the nearest singular boundary with an additional array of secondary grain boundary dislocations (Lejcek 2010).

2.4.3.3 Coincidence Site Lattice (CSL) boundary:

A thermodynamic point of view led to a new way to describe grain boundaries. The positions of the atoms inside the crystal correspond to a condition when the material attends minimum free energy state. Maintaining periodicity of the atoms even in the boundary region thus gets energetically favoured. It was found that for certain misorientation angles there is a perfect matching between the two crystals where HAGBs allow the crystallographic planes to continue from one to the other grain. Thus, atoms in the grain boundary coincide with ideal (minimum free energy position) positions (Figure 2.25. b) that belong to both adjacent crystals. The pattern formed by those coincidence points is called coincidence site lattice (CSL). The idea of CSL to correlate with boundary structure was first introduced in 1949 by Kronberg and Wilson. So, the central idea rotates around formation of a theoretical superlattice (by rotation of two lattices) with a number of overlapping atomic sites. CSLs are just patterns with high density of coincidence points where grain 1 and 2 gain a lot of coherency. The proportion of coincident sites is given by a quantity called, $1/\Sigma$ .To quantify the CSL size with respect to the elementary cell, relative volume is expressed in terms of the parameter Σ as follows:

$$\sum = \frac{volume\ of\ \ elementary\ cell\ of\ \ CSL}{volume\ of\ \ elementary\ cell\ of\ \ crystal\ lattice} \qquad \ldots\ldots\ldots\ldots\ldots \quad Eq\ 2.29$$

This parameter defines how similar the CSL and the crystal lattice are. The larger the value of Σ, the smaller the number of coincidence sites in the grain boundary and vice versa. So, a $\Sigma 5$ CSL boundary will have higher energy than a $\Sigma 3$ because, in the former only 1 in 5 lattice points are in coincidence. Σ value is not associated with a particular boundary plane. It is just an orientation

relationship that gives the coincidence. The boundary plane can be anywhere between the two crystals and that boundary will always have $1/5^{th}$ of the lattice points coincident if $\Sigma=5$. This concept can be extended to the LAGBs also when $\Sigma=1$, because all the lattice points, except those occupied by the dislocations, are in coincidence. For high Σ boundaries, we can expect more impurity segregation as less number of coincident points lead to more empty space, i.e., free-volume.

Each $\sum$ value corresponds to one or more specific lattice misorientations that meet its necessary geometric conditions. Some of the very first $\sum$ configurations are listed in Table 2.3.

Table 2.3. Description of CSL boundary as per angle-axis concept (D. Drabble 2010)

Σ Value	Misorientation Angle, θ	Misorientation Axis, UVW	Allowable Deviation, v_m*
3	60°	<111>	8.67°
5	36.87°	<100>	6.71°
7	38.21°	<111>	5.67°
9	38.94°	<110>	5.00°
11	50.48°	<110>	4.52°
13a	22.62°	<100>	4.16°
13b	27.80°	<111>	4.16°
15	48.19°	<210>	3.87°

* based on the Brandon criterion

In reality, exact CSL configuration might not be achieved. In that case, the deviation from exact CSL misorientation is accommodated through introducing an array of dislocations. While calculating this deviation, a matrix operation is used where rotation of an exact CSL matrix (R_{CSL}) and the boundary of concern generates a deviation matrix (R_M) according to the relation expressed as $R_M = R \cdot R_{CSL}^{-1}$. The deviation angle which is obtained from diagonal elements of matrix R_M, gives the maximum allowable limit to still satisfy particular CSL criterion. Several researchers have attempted to calculate this limit, e.g. Brandon's, Deschamp's, Ishida & McLean's and Palumbo's criteria. The basic idea of all of them was based on Read and Shockley relationship (P. K. Lin 1998). Of them, the most commonly used Brandon's criterion empirically relates, maximum allowable deviation, v_m, and $\sum$ as:

$$v_m = \frac{15}{\sum^x} \qquad where,\ x=1/2 \qquad \ldots\ldots\ldots\ldots \ Eq\ 2.30$$

As a comparison, Palumbo's criterion allows a maximum of 6° deviation for ∑3 boundaries (x =5/6) whereas Brandon's criterion allows 8.67°, in McLean's criterion, x=1, in Deschamp's criterion, x=2/3 (Lejcek 2010).With successful implementation of EBSD in grain boundary characterization, CSL model has become the most convenient and popular one. This is because CSL model relies on misorientation across boundary concept which can be directly applied to EBSD data set. EBSD software can thus identify the boundary CSL value and length fractions can be determined from that which is the theme of measuring grain boundary character distribution (GBCD) during grain boundary engineering (GBE). Identification of annealing twins is also possible using CSL approach. However, CSL model has a drawback as it considers one of the 5 degrees of freedom, misorientation. That is why it is an incomplete way to describe boundary unless it is being coupled with boundary plane information for fully being applied to predict bulk properties (D. Drabble 2010). On another note, ∑-value can also be evaluated from the Miller indices of the symmetrical tilt boundary in cubic lattice according to:

$$\sum = \delta(h^2 + k^2 + l^2) \qquad \ldots\ldots\ldots\ldots \ Eq\ 2.31$$

where, δ=1 if (h^2+ k^2+ l^2) is odd and δ =1/2 if (h^2+ k^2+ l^2)is even, as in cubic systems, all ∑-values are odd (Lejcek 2010).

Due to improved property, these boundaries are sometimes also called as special boundaries. In bicrystal studies, it was found that energy and mobility of a grain boundary is a function of its ∑-value. Compared to HAGBs, low-∑ boundaries have lower diffusivity, lower susceptibility to solute segregation, higher intergranular degradation resistance which is attributed to lower free volume associated with these boundaries for more coincidence lattice points. As an exception, not all low CSL boundaries are special ones as also boundary plane inclination plays important role to predict its behavior.

2.5 Grain Boundary Motion:

One of the key factors in microstructure evolution in a cold worked metal during annealing is the migration of low angle grain boundaries (LAGBs) and high angle grain boundaries (HAGBs) which has been the subject of extensive studies since many years. In particular, LAGB motion takes place during the recovery stage when newly formed subgrains grow followed by nucleation

of recrystallization. By contrast, HAGB movement occurs during primary recrystallization followed by growth of the recrystallized structure. The movement of a boundary in the direction of the normal to its tangent plane is defined as Grain Boundary Motion/Migration (GBM). Despite having profound influence on microstructure evolution, there is not enough information about the mechanism behind it except some preliminary results from molecular dynamics and high resolution TEM studies. This is mainly due to processes occurring at the atomic level at a very high speed and temperature and under conditions far from equilibrium making it extremely difficult to study experimentally or theoretically. This section aims at reviewing the proposals made on GBM followed by factors affecting the motion.

2.5.1 Concept of Grain Boundary Mobility:

Under certain driving force P, a moving boundary with velocity V, maintains its movement with the assumption that velocity is directly proportional to the driving force. This leads to the relationship, V=MP. The proportionality constant M is known as boundary mobility. It is kind of a measure of the ability of a grain boundary to migrate. Mobility is usually dependent on temperature and is usually expressed in the form of an Arrhenius type relationship as follows:

$$M = M_0 exp\left(-\frac{Q}{RT}\right) \qquad \text{…….. } Eq\ 2.32$$

where, Q is the activation energy for boundary movement, M_0 is the pre-exponential factor, R is universal gas constant. Measurement of mobility is one of the most difficult tasks since many years. Mostly, because of various factors like impurity, experiment condition, intrinsic mobility measurement is quite cumbersome. Indirect measurement of boundary velocity under certain driving force is the commonest way to calculate mobility. Sometimes bicrystals of controlled geometry or as-cast substructure with known driving force are used to perform mobility measurement studies. Also, the mobility of a boundary in deformed and un-deformed material may vary as in the former one dislocation interaction might change its mobility. It is worth to mention that mobility and velocity are interchangeably used specially under the condition of constant driving force. In that case, measured velocity can be assumed to be proportional to boundary mobility (Hatherly and Humphreys 2012).

2.5.2 Mechanism of Grain Boundary Migration:

The mechanism of boundary migration is mainly an atomistic process which is governed by a number of variables like boundary structure (which is also a function of misorientation and boundary plane), temperature, type and magnitude of the force acting on the boundary and most importantly point defects like solutes and vacancies. In brief, the boundary motion can be divided into two different types. Climb and glide of constituting dislocations help to migrate the low angle boundaries which can be described in the light of dislocation theory. On the other hand, constant transfer of atom in and out of the boundary plane from the adjacent grain is the key process to move high angle boundaries. This is can be elucidated using thermally activated atomic jump models. Migration of high angle boundaries is also possible through movement of their special structural parts like steps, ledges or grain boundary dislocations. Sometimes diffusionless shuffle of group of atoms (in case of diffusionless phase transformations), combined sliding –migration also occurs to aid HAGB migration (Hatherly and Humphreys 2012). In the following subsections, a detailed discussion of migration mechanism of different types of grain boundaries will be given.

2.5.2.1 Low Angle Grain Boundary motion:

Under this category we will first discuss the motion of symmetrical tilt boundaries which are composed of a planar array of edge dislocations with common Burgers vector (Bainbridge, Choh, and Edwards 1954). These boundaries can readily move if stress is applied on them. Their mobility is found be a strong function of temperature and misorientation. In zinc crystals, the motion of symmetrical tilt boundaries were measured in a special type of experimental set up using travelling microscope. The temperature dependence of boundary mobility strongly suggests that a thermal activation process was present to dictate the motion (Figure 2.27. a) and the activation energy was calculated to be approximately 21,500 cal/mole. As the misorientation increases, the dislocation densities also increase which result into slow migration of the boundaries (Figure 2.27. b). This is attributed to the interference of the dislocations as they increase in number with increased misorientation (Bainbridge, Choh, and Edwards 1954). Another interesting study on the migration of planar symmetrical <111> and <112> tilt boundaries in very high purity aluminium under small

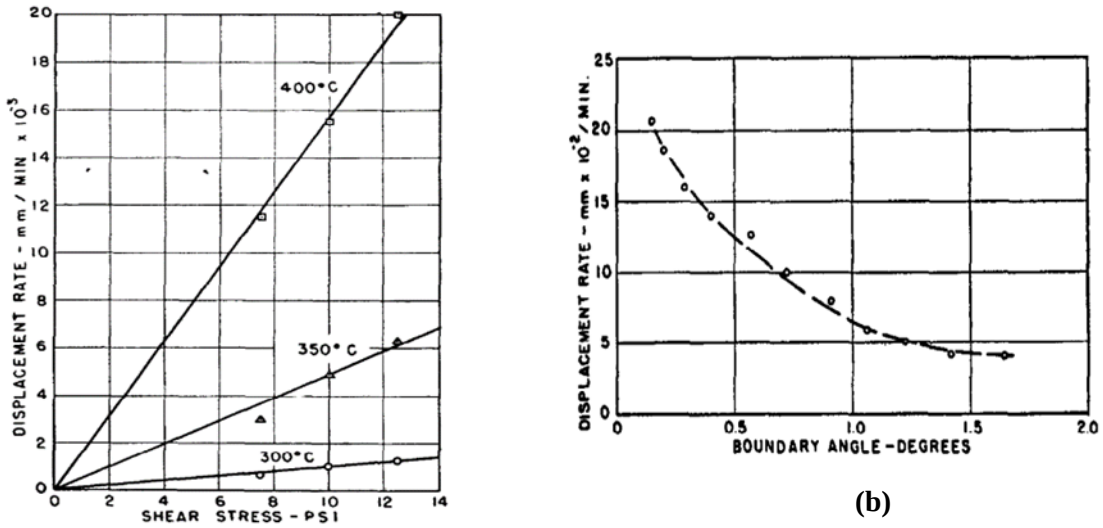

Figure 2.27. a.) Effect of stress and temperature on a 2° edge dislocation boundary, b) effect of misorientation on the mobility (expressed as displacement-rate) of a symmetrical tilt boundary in zinc crystal at 350°C under constant shear stress of 9.19 psi (Bainbridge, Choh, and Edwards 1954)

shear stresses revealed a sharp transition in mobilities when the misorientation is around 14°. Some other features noticed are like, low angle boundary mobilities remain fairly constant with changing misorientation, activation enthalpy for the migration is close to that required for self-diffusion (making it a dislocation climb controlled process) and there is a strong temperature dependence (Hatherly and Humphreys 2012).

For its low magnitude, general LAGB motion is almost impossible to investigate before recrystallized grains consume the whole structure (Huang and Humphreys 2000b, 2000a). An outstanding work by Huang et al. (Huang and Humphreys 2000b) successfully investigated migration of LAGBs with a huge range of misorientaion (2°-5° and more than 5°) using cube oriented crystals. Some of the aspects of the LAGB motion were concluded from a series of work by several researchers as a) LAGB migration takes place under a steady driving pressure with a constant mobility at a particular annealing temperature, b) bulk diffusion controls the LAGB motion, 3) LAGBs with higher misorientation move faster than that with low misorientation (Huang and Humphreys 2000b). A few experimental evidences showed that recrystallized grains

grow at a very sluggish rate especially because its boundary orientation with the matrix is small. In a bicrystal experiment, it was found that activation energy for migration of LAGBs is higher than that for HAGBs. Another bicrystal study on high purity zinc and aluminium also proved similar aspect of activation energy in addition to the fact that medium angle boundaries move faster with increased misorientation. In the same study by Huang *et. al*., they also observed that the activation energy for boundary migration is a function of misorientation upto 14° after that it pretty much remains constant (Figure 2.28. a). Similar experimental findings were obtained in mobility studies of LAGBs in 99.98% pure aluminium (Hatherly and Humphreys 2012).

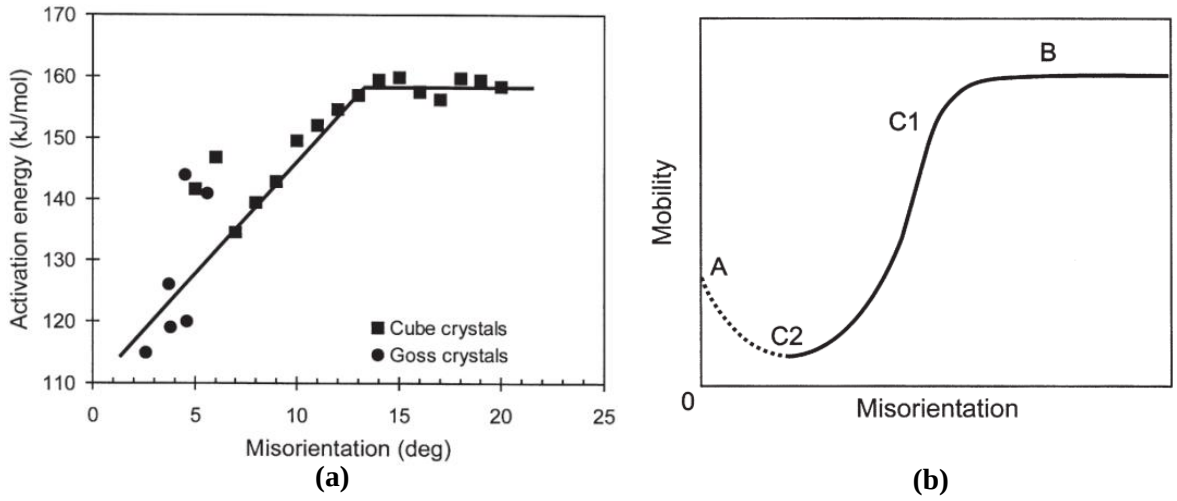

Figure 2.28. a) Dependence of activation energy for LAGB migration with misorientation (Huang and Humphreys 2000b), b) Possible Mobility –misorientation relationship for a range of LAGBs (Hatherly and Humphreys 2012)

The variation of activation energy with misorientation (Figure 2.28. a) strongly suggests climb of dislocations comprising LAGBs to be the operative mechanism with lattice diffusion of solutes to be the rate controlling step.

As was mentioned before, LAGB migration generally requires dislocation climb process. This seems to be the rate controlling step. Furu, Ørsund, and Nes 1995 expressed mobility of LAGBs according to following equation considering its dependence to its structure and energy as:

$$M = \frac{CD_S b}{kT} \qquad \ldots\ldots\ldots \text{ Eq 2.33}$$

where, C is a constant of the order of unity, is the coefficient of self-diffusion, b is the Burgers vector of the dislocation comprising the boundary, T is the temperature. This relation in particular

doesn't highlight the dependence of mobility on misorientation, θ. It was next taken into account so that the whole regime of misorientation dependence of mobility can be estimated.

If it is considered that a subgrain boundary is bowing to a radius of curvature R_{sub}, the pressure (P) due to this curvature is given by

$$P = \frac{2\gamma_s}{R_{sub}} \qquad \ldots\ldots\ldots \text{Eq 2.34}$$

where, γ_s is the boundary energy which is related to misorientation according to Read and Shockley as $\gamma_s \sim c_1 Gb\theta$ (C1 is a small constant). If we apply the Einstein relation for GBM, the velocity is expressed as follows:

$$V_{LAGB} = \frac{dR_{sub}}{dt} = \frac{2M\gamma_s}{R_{sub}} = \frac{2c_1 MGb\theta}{R_{sub}} \qquad \ldots\ldots\ldots \text{Eq 2.35}$$

Now three different ranges of misorientation angle will be considered to calculate mobility.

Case I, ($\boldsymbol{\theta \rightarrow 0}$) - For LAGBs, θ is very small where the effect of single dislocation is dominant. Upon bowing to a radius of R_{sub}, the force imposed on the dislocation line, $\boldsymbol{F}$, is given as

$$F = \frac{Gb^2}{2R_{sub}} \qquad \ldots\ldots\ldots \text{Eq 2.36}$$

Under low angle i.e., less number of dislocations, the vacancy supersaturation is negligible and the velocity with which the dislocations climb can take place is given by

$$V_c = D_s c_j \left(\frac{Fb}{kT}\right) \qquad \ldots\ldots\ldots \text{Eq 2.37}$$

where, c_j is the concentration of the jogs and D_s is the self-diffusion coefficient. As the dislocations are independent, the climb velocity will determine the LAGB motion and we can write $V_{LAGB} = V_c$. Combining above four equations, we can write:

$$V_{LAGB} = \frac{2c_1 MGb\theta}{R_{sub}} = \frac{D_s C_j Gb^3}{2kTR_{sub}} \qquad \ldots\ldots\ldots \text{Eq 2.38}$$

Or,

$$M = \frac{D_s C_j Gb^2}{4c_1 kT\theta} \qquad \ldots\ldots\ldots \text{Eq 2.39}$$

It is clear from above equation that, LAGB motion gets sluggish with increased misorientation. This trend is shown by the initial dotted line or region A ($\theta < 1°$) in Figure 2.28. b . So, within this range

a) climb of individual dislocations seems to be a dominant mechanism
b) v=M.P is valid
c) M has an inverse relationship with θ.

Case II, (θ >15-20°) – This is the case for a general high angle boundary which will be discussed in the next section for HAGB motion.

Case III, the intermediate case- This transitional regime is one of the most important ones as this mostly corresponds to recovery phase of deformed matrix. It is also very difficult to analyze.

C1 (medium angles) -A little increase in θ value corresponding to C1 (Figure 2.28. b) (θ =5-20°) shows -an increase in the mobility which is due to change in the mechanism from climb to atom transfer over a distance '***h***' which is the spacing between the dislocations of '*b*' Burgers vector ($\theta = b/h$). This transfer can be imagined to be diffusion of atom through a membrane of thickness '***h***'. As θ increases, due to more number of dislocations, *h* decreases and *M* increases. So, $M \propto \theta$.

C2 (low to medium angles) -The region C2 (2°-5°) is a clear transition between region A and C1. The mechanism of boundary movement is not too clear here. Two factors always contradict within this region

a) *M* and θ will be inversely related according to case I.
b) With increased θ, the vacancy source-to-sink distance, '*h*' will decrease which in turn increase the mobility by enhanced climb rate as discussed in case C1.

In summary the whole mobility regime can be divided as shown in Figure 2.28. b:

Region A (dotted as no experimental data is available within this very low angle range (θ<1°), only computed)

Region B (related to HAGBs)

Region C1 (related to boundaries within 5°-20° misorientation, $M \propto \theta$)

Region C2 (related to boundaries within the range 2°-5°)

Further, experimental data are required to enhance the understanding of the LAGB migration mechanism (Hatherly and Humphreys 2012) .

2.5.2.2 High Angle Grain Boundary motion:

When the misorientation increases to such an extent that the dislocation cores overlap, we land up with HAGBs in the microstructure. The dominant mechanism for the HAGB motion is thought to be thermally assisted jump of atoms across the boundary. The activation energy is close to that for boundary diffusion. The Einstein relation is considered to remain valid with M being independent of θ. The model of HAGB migration considers a series of detachment of atoms from regular lattice sites like A or B (Figure 2.29. a) to the more disordered region of boundary, say, C by thermal activation followed by reattachment to the normal lattice sites again. Thus, there is a flux of atoms moving from both the grains towards each other. Under the steady state condition, the net flux is zero and the boundary is static. However, under the condition of HAGB migration, net atom flux

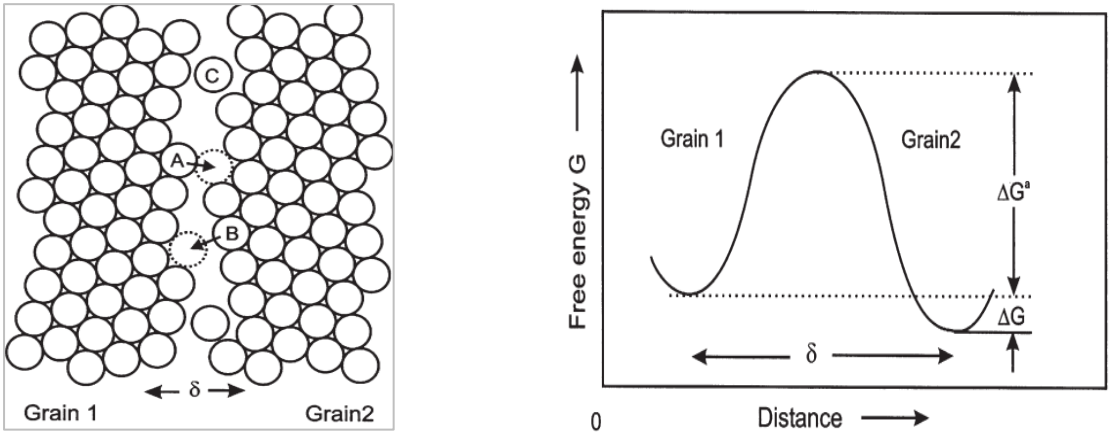

Figure 2.29. a) HAGB migration mechanism by single atom jump, b) thermodynamics of atom jump across HAGBs (Hatherly and Humphreys 2012)

will be higher opposite to the boundary motion. There are some factors that may alter the mechanism like single or group activation of atoms, spatial distribution of the atoms after the detachment and probability of having preferential sites for attachment-detachment.

When the consideration is limited to the activation of a single atom for HAGB migration, Turnbull proposed a theory for that. His early model considered the boundary region to have certain volume of thickness δ (Figure 2.29. a) which is much broader than lattice spacing of atoms (δ>>b). If the boundary moves from right to left due to a free energy difference, ΔG, we can assume that a net atom flux to exist towards right. This detachment from parent lattice needs some thermal assistance and an activation energy ΔG^a is essential for crossing the energy hump (Figure 2.29. b). If atomic

vibration frequency is ν_0, then the no. of times the atom might acquire this energy per second is given by $\nu_0 exp(-\Delta G^a/kT)$. If there are 'n' number atoms capable to jump per unit area of HAGB, total number of jumps per second from a grain is $n\nu_0 exp(-\Delta G^a/kT)$. There comes another two factors which are Grain boundary structure dependent factor A_J and accommodation factor A_A which determine the preferred detachment and attachment sites respectively. Considering all these, the effective atomic flux from grain 1 to 2 will be $A_J A_A\, n\nu_0 exp(-\Delta G^a/kT)$ and the same for grain 2 to 1 will be $A_J A_A\, n\nu_0 exp(-\Delta G^a+\Delta G/kT)$. We can express the net flux as follows:

$$J = A_J A_A n\nu_0 \, exp\left(-\frac{\Delta G^a}{kT}\right)\left(1 - exp\left(\frac{-\Delta G}{kT}\right)\right) \qquad \text{…….. Eq 2.40}$$

Now, the boundary velocity V_{HAGB} can be can be expressed in terms of lattice spacing 'b' as

$$V_{HAGB} = J\frac{b}{n} = A_J A_A \nu_0 b \, exp\left(-\frac{\Delta G^a}{kT}\right)\left(1 - exp\left(\frac{-\Delta G}{kT}\right)\right) \qquad \text{…….. Eq 2.41}$$

Considering the driving force ΔG for HAGB migration to be small during softening compared to high value during phase transformation, the exponential series expansion leads to the velocity equation as given in equation 2.42.

$$V_{HAGB} = A_J A_A \nu_0 b \, exp\left(-\frac{\Delta G^a}{kT}\right)\left(\frac{-\Delta G}{kT}\right) \qquad \text{…… ……. Eq 2.42}$$

Substituting $\Delta G^a = \Delta H^a - T\Delta S^a$ and ΔG=P, the driving pressure, the above equation gives the mobility expression as:

$$M_{HAGB} = \frac{A_J A_A \nu_0 b}{kT} exp\left(-\frac{\Delta H^a}{kT}\right) exp\left(\frac{\Delta S}{k}\right) \qquad \text{……. Eq 2.43}$$

Some shortcomings of in terms of diffusion mode, determination of the parameters A_J and A_A, activation enthalpy for atomic jump made the model a very general one which is taken into account in the later theories.

The first theory that considered HAGB motion to take place by movement of islands of atoms detaching from one grain to the boundary region and attachment of the same type of group from

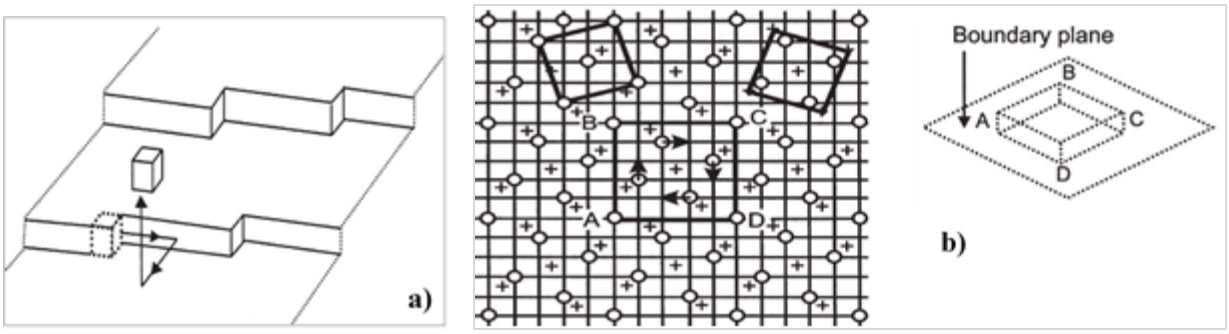

Figure 2.30. a) Step models of HAGB migration (Hatherly and Humphreys 2012), b) Boundary defect model of migration for highly ordered Σ5 [001] twist HAGB (Gunter Gottstein and Shvindlerman 2009).

boundary to another grain was considered by Mott. The activation of islands led to high ΔH^a value which was proved to be due to impurity content. New group models were then developed where it was proposed by HRTEM studies that HAGB migration takes place by movement of steps or kinks in HAGBs (Figure 2.30. a) (Gleiter 1969b). The movement occurs by addition or removal of atoms from the steps followed by short distance diffusion. This is kind of similar process that occurs during crystal growth from vapour phase and ledge movement mechanism is also observed during phase transformation where interphase boundaries move. Gleiter calculated boundary velocity for the driving force available during annealing to be

$$v = bv_0\psi exp\left(\frac{\Delta G^a}{kT}\right)\frac{P}{kT} \qquad \text{..... Eq 2.44}$$

This equation resembles equation 2.42 except there is a factor 'ψ' which incorporates the step configurations in a boundary of thickness 'δ' through the following equation:

$$\psi = \frac{c}{\delta}\left(1 + \frac{b}{\delta}\left(\frac{1}{f_1} - \frac{1}{f_2}\right)\right) \qquad \text{..... Eq 2.45}$$

where, f_1 and f_2 are the functions related to the step density on the lattice on both sides of the boundary which also links misorientation and boundary planes to mobility, *b* is the Burgers vector, *c* is a constant (Hatherly and Humphreys 2012).

The next improvement in understanding came by recognising grain boundary steps and intrinsic boundary dislocations to have similar effect on HAGB migration. It was shown when the intrinsic dislocations with steps in their cores move, the HAGB migration takes place. These boundary defect models for migration mechanism also consider glide of boundary dislocations and collective

defect movement to result into combined migration and sliding of HAGBs (Hatherly and Humphreys 2012). Another factor was considered that affects boundary migration is influence of capillary forces at high temperature. This leads to jerky motion with very high migration rate without changing the boundary dislocation structure for local cooperative shuffling of atoms (Figure 2.30. b) which was demanded to be most convincing mechanism than movement of boundary dislocations. The first planes of grain 1 is denoted by 'O' symbols and of grain 2 is denoted by '+'. The left one in Figure 2.30. b is a view along [001] with vectors indicating atomic shuffles in grain 1 to displace the boundary by a/2 and to produce a ledge shown on right (Hatherly and Humphreys 2012).

2.5.2.3 Factors affecting HAGB migration:

As stated earlier, this discussion will include the factors affecting GBM in brief. Temperature is the first thing which can alter the GBM. It is seen that the mobility and temperature has an Arrhenius type of relationship (Equation 2.31). In case of alloys, more than one apparent activation energy are found to be operational over a range of temperature. A change in mobility and activation energy is sometimes evidenced at very high homologous temperature. This is due to change in the boundary structure and operating mechanism. Aust and Rutter performed some experiments on high purity lead where it was observed at higher temperature that the special boundaries lost their mobilities due to change in grain boundary character. Orientation of boundary plane as well as that of the adjacent grains also play vital role on migrating a boundary. In many studies on recrystallization of lightly deformed aluminum or copper, grains with higher misorientation (20°-40°) exhibited fast grain growth. The coincidence boundaries with low $\sum$ value ($\sum$=3) show lower mobilities than some other coincidence boundaries ($\sum$=7, 13, 17, 19 etc.). In connection to orientation of grain boundaries, there is a significant effect of small amount of solute atoms on GBM. It is believed that solute atoms constantly move with the boundary imparting a drag force when their concentration is very high. The boundary velocity relative to the diffusivity of the solutes decides the drag on the boundary (Cahn 1962). And there also comes a combined effect of temperature and solute drag. As can be seen from Figure 2.31. a, 20ppm addition of iron to gold, activation energy decreases as the temperature is lowered. At high temperature, the activation energy was observed to be closed to that of very high purity materials. A smooth transition peak was also observed in case of activation energy with increased solute content leading to slow

boundary movement. In Figure 2.31. b, a clear correlation between increase in solute content and decreased mobility is somehow a clear indication that due to presence of solute activation energy

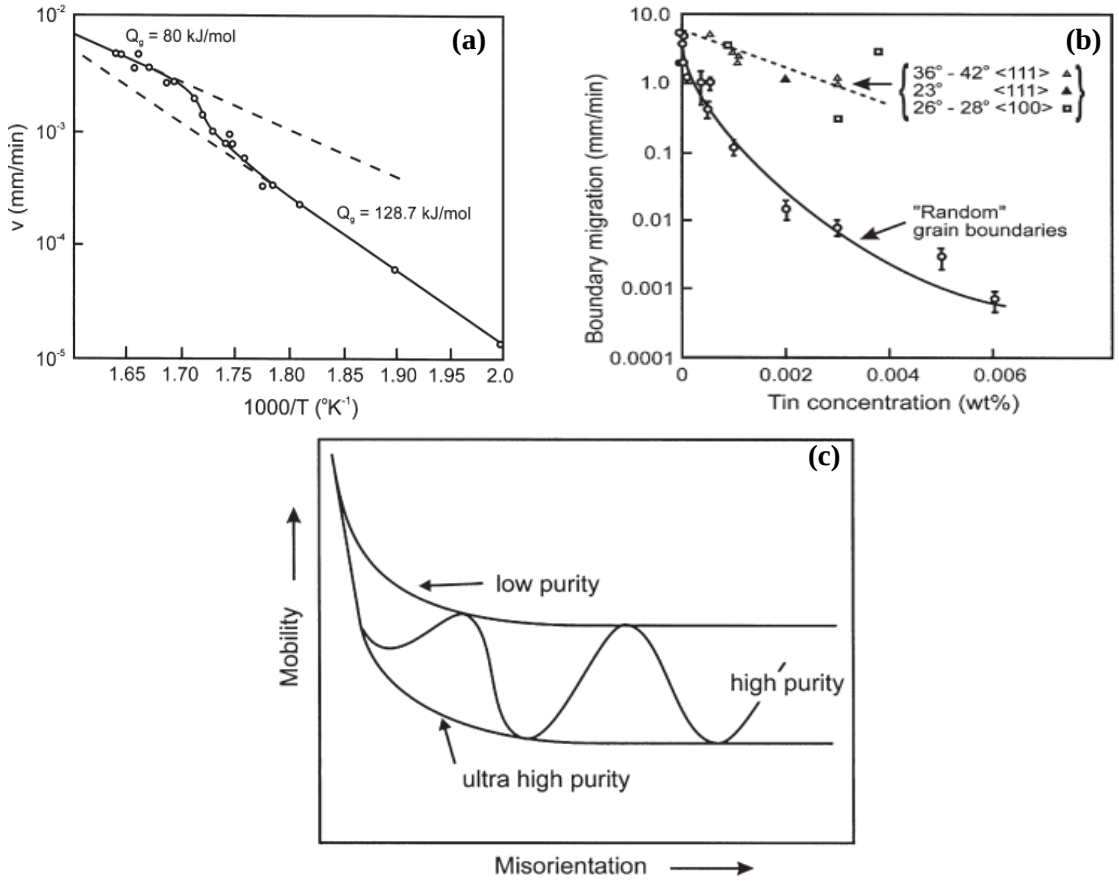

Figure 2.31.a) Temperature dependence of migration velocity of a 30°<111> tilt boundary in gold (Hatherly and Humphreys 2012), b) effect of solute (tin) addition on boundary migration in zone-refined lead at 30°C (Aust and Chalmers 1970), c) a schematic diagram depicting impurity level and orientation dependence of boundary mobility (Hatherly and Humphreys 2012)

for boundary migration increases.

Solute segregation is happened to be a strong function of the boundary structure. Therefore, at low impurity concentration, mobility of special (∑) and high angle boundaries are similar. But, at high impurity concentration, HAGBs are more affected than special boundaries as the former one embraces more solute because of its higher free volume. The dependence on orientation and impurity level of boundary mobility can only be found within a short window of impurity content and is given in Figure 2.31. c. For the purest and low purity materials, mobility doesn't depend on orientation reflecting that no structure dependence is involved. With normal materials with high purity, mobility again becomes a function of orientation follows Reed-Hill relationship based on

certain low energy configuration (G Gottstein and Shvindlerman 1992). A vacancy flux or supersaturation was found to enhance the mobility of HAGBs in a copper single crystal during recrystallization which was left exposed to neutron radiation. The radiation was responsible for generation of Frank vacancy loops which increases the free volume of the boundary while being swept away and makes the GBM faster by making atom transfer process more convenient. Same evidence was observed during grain growth of ion bombarded thin films of gold, germanium and silicon etc., sintering of copper wires and alumina. The second phase particles can also impede GBM by imparting Zener drag which is a factor of boundary coherency, particle morphology, volume fraction and size (Hatherly and Humphreys 2012). Recently, groove dragging effect on GBM is also introduced elsewhere (Gunter Gottstein and Shvindlerman 2009).

2.6 Theories of Grain Growth:

Post recrystallization grain growth of materials although seems to be a relatively simple process, over past few decades many of its aspects has still been remaining unexplored. It is generally accepted that grain growth happens to further minimize the free energy by reducing the interface area. The driving force for grain growth to happen is usually two orders of magnitude less than that during recrystallization and appears to be as 10^{-2} MPa. At low temperature, the rate of grain growth decreases as it also gets hindered by the presence of solute atoms and second phase particles. Two main criteria should be satisfied by grain structures in order to grow. One is to maintain volume conservation which is possible if all grains have good connectivity among them through shared surfaces. The second criterion is force balance must be maintained, i.e., surface tensions between neighboring grains must be under equilibrium. After meeting above two conditions, grains grow resulting in an inherent distribution of grain sizes with substantial decrease in total free energy of the system (Lechuk 2000). Technologically, importance of grain growth is not only limited to bulk polycrystalline materials used in sub-zero application, transformer cores, thinner gauge application, but also to the development of electronic devices through controlling grain growth of thin films, oxides and semiconductor films etc. This brings the necessity of generating comprehensive database through complete understanding of the fundamentals of grain growth (Hatherly and Humphreys 2012).

It is customary to take a close look into the mechanism of grain growth proposed by a number of researchers before describing the models. It started during 1920, when Carpenter and Elam used a tin alloy containing 1.5 % antimony to study grain growth in single crystal. They captured the positions of a grain boundary after heating and cooling as an impression of line on the surface of the sample. The gist of their findings is as follows:

a. Grain growth occurs solely due to grain boundary migration not by coalescence of neighboring grains.
b. Boundaries migrate in a discontinuous manner and the rate varies during subsequent heating stages with a possibility of changing the direction of migration
c. Two opposing phenomena can be possible in a single grain when its one side may grow and migrate into the neighboring grain and another side gets consumed by its adjacent grain simultaneously.
d. The shrinking of a grain as it gets consumed by its neighbor doesn't take a long time.

This observation is further modified in 1928 using the same system and technique by Sutoki, who observed that migration of a curved grain boundary is preferred to its center of curvature. Sutoki's observation was further confirmed by Harker and Parker, in 1945 and furthermore some special correlation of grain growth with grain morphology was established using statistical technique as: "Where grain boundaries in a single phase metal meet at angles different from 120 degrees, the grain included by the more acute angle will be consumed, so that all angles approach 120 degrees " (Burke and Turnbull 1952).

2.6.1 Grain growth models:

Theoretical and experimental approaches result into many well established grain growth models. In addition to that some statistical, topological and deterministic approaches to model grain growth was also made. In this sections different types of models will be discussed in brief.

2.6.1.1 Empirical and theoretical models:

In 1948, Beck et al. attempted to model the grain growth kinetics in aluminium-magnesium alloys and 70-30 brass. The grain sizes obtained under normal grain growth regime during isothermal annealing experiments fitted the following power relationship:

$$D_g = C_0 t^n \qquad \ldots\ldots\ldots\ldots \text{Eq 2.46}$$

where, D_g is the average grain size for a given holding time t, C_0 and n are independent of grain size but varies with annealing temperature and composition of the material. Above equation was experimentally valid especially within the condition of initial grain size being smaller than that of growing grains. Equation 2.46 was modified by the same researchers to accommodate the deviation observed at shorter annealing time. They proposed a modified one as follows:

$$D_g{}^{1/n} - D_i{}^{1/n} = ct \qquad \ldots\ldots\ldots\ldots \text{Eq 2.47}$$

Where D_i is the initial grain size (Lechuk 2000).

Predicted from reaction rate theory, grain boundary movement is directly proportional to the net pressure on it in absence of interactions with solute atoms. And the growth rate can be expressed as

$$V = MP \qquad \ldots\ldots\ldots\ldots \text{Eq 2.48}$$

where, V is the velocity at which HAGB migrates, P is the net pressure which acts as driving force. M, the proportionality constant, is known as mobility of HAGBs which details the mechanism of migration and is assumed to be independent of driving force. In 1951, Turnbull derived an expression for mobility in solute free case termed as intrinsic mobility (M_i) which takes the form of following equation (Turnbull 1951):

$$M_{pure} = \frac{\delta D_{GB} V_m}{b^2 RT} \qquad \ldots\ldots\ldots\ldots \text{Eq 2.49}$$

where δ is the grain boundary thickness, D_{GB} is the grain boundary self-diffusion co-efficient, V_m is the molar volume, b is the Burgers vector, T is temperature in absolute scale, R_g is universal gas constant. Having found the pre-exponential factor to be weakly depending on temperature, above equation can be expressed as an Arrhenius type relationship:

$$M = M_0 exp\left(-\frac{Q}{RT}\right) \qquad \text{…….. Eq 2.50}$$

where, M_0 is a constant and Q is the activation energy for thermally activated atom movement. It will be shown later on that the intrinsic mobility calculated by Turnbull was modified by next generation researchers. Finally, in 1952, the grain growth kinetics was deduced by Turnbull considering the global driving force (P) to be influenced by the boundary curvature. Considering two principal radii of curvature to be R_1 and R_2 of a boundary whose energy is γ_{gb}, the driving force can be expressed as follows:

$$P = \gamma_{gb}\left(\frac{1}{R_1} + \frac{1}{R_2}\right) \qquad \text{…….. Eq 2.51}$$

Considering a spherical grain of radius R, we can apply $R_1 = R_2 = R$ to above equation and rewrite as:

$$P = \frac{2\gamma_{gb}}{R} \qquad \text{……. Eq 2.52}$$

Another set of assumptions were made as γ_{gb} being constant for all boundaries and the radius of curvature R is proportional to the average radius ($\bar{R}$) of an individual grain. Thus equation 2.52 is modified as:

$$P = \frac{\alpha\gamma_{gb}}{\bar{R}} \qquad \text{…….. Eq 2.53}$$

where, α is a geometric factor.

Combining equation 2.53 and equation 2.49, the final grain growth rate can be expressed in terms of rate of change of radius as follows:

$$\frac{dR}{dt} = M\left(\frac{\alpha\gamma_{gb}}{\bar{R}}\right) \qquad \text{…….. Eq 2.54}$$

Integration of above equation results in

$$\bar{R}_f^2 - \bar{R}_i^2 = 2\alpha M\gamma_{gb}t \qquad \text{…….. Eq 2.55}$$

where , R_i is initial grain radius and R_f is the final radius after time *'t'*. The above equation can be written in a more general form of

$$\bar{R}_f^n - \bar{R}_i^n = ct \qquad \text{…….. Eq 2.56}$$

Where, *c* is a constant and *n* is termed as grain growth exponent which is 2 theoretically. The experimentally observed value of n was observed to be well above 2 and a function of temperature and composition. Generally a trend of lower 'n' value with increase in temperature is obtained. Even for ceramics, the measured grain growth exponent exhibited similar range of values. The explanation for this deviation from theoretical value is given by Burke and Turnbull as:

- Under certain situation, the mobility is a function of the velocity of a boundary making equation 2.48 to be invalid, e.g., in the very low or high velocity regime boundary velocity is not linearly related to driving force and presence of solute drag. In some cases structural modifications of HAGB result in lower n values. Particular mode of grain boundary migration always leads to n value between 1- 4 in ceramics.
- Influence of limiting grain size which was accommodated in equation 2.48 according to Grey and Higgins as:

$$V = M(P - C) \qquad \text{..... Eq 2.57}$$

where, C is a constant for particular material which can be considered to be either similar to Zener

Table 2.4. Experimentally determined grain growth exponent 'n' in high purity material under isothermal condition (Hatherly and Humphreys 2012)

Metal	Exponent n	Reference
Al	4	Gordon and El Bassyoumi (1965)
Fe	2.5 (varies with T)	Hu (1974)
Pb	2.5	Bolling and Winegard (1958)
Pb	2.4	Drolet and Gallibois (1968)
Sn	2.3	Drolet and Gallibois (1968)

pinning term that accounts for a limiting grain size in two-phase material or solute clusters dragging boundaries back to its motion. A number of experimental studies have been performed in quest of determining exact value of *'n'* for a variety of materials (Hatherly and Humphreys 2012), as listed in Table 2.4 lists them up.

2.6.1.2 Statistical Models:

In 1965, a statistical approach was used by Hillert (based on the idea of Hillert and Feltham) to model grain growth kinetics considering the behavior of single grain in an environment of grains with various sizes. He assumed spherical or circular grains of radius '*r*' whose grain boundary velocity is inversely proportional to its radius of curvature. In addition to that Hillert introduced the concept of critical grain size R_{crit}, such that grains larger than this size will continue to grow and less than that will exhibit shrinkage. He implemented the concept of particle coarsening by Ostwald ripening in a distribution of second phase particles to calculate growth rate. The rate equation as proposed by Hillert takes the following form:

$$\frac{dR}{dt} = \alpha M \gamma_{gb} \left(\frac{1}{R_{crit}} - \frac{1}{R} \right) \qquad \text{…… Eq 2.58}$$

where α =1/2 for a two-dimensional array and 1 for three-dimensional array of grains, R_{crit} is critical grain size which changes over time according to following equations:

$$\frac{d\left(R_{crit}^2\right)}{dt} = \frac{\alpha M \gamma_{gb}}{2} \qquad \text{…… Eq 2.59}$$

$$\frac{d(R_{crit})}{dt} = \frac{\alpha M \gamma_{gb}}{4R_{crit}} \qquad \text{…… Eq 2.60}$$

For 2-D case, Hillert showed that $\bar{R} = R_{crit}$ and for any particular grain size distribution in 3-D case, $\bar{R} = 8/9 R_{crit}$ which finally leads to parabolic grain growth. Hillert's model can also be used to predict grain size distribution in 3-D and it was shown that initial grain size distribution containing no grain larger than 1.8 $\overline{R}$ will show normal grain growth and the grain size distribution will be self –similar. On the other hand presence of grain larger than 1.8 $\overline{R}$ in the grain size distribution will result in abnormal grain growth. The value for 2-D case was calculated to be 1.7 $\overline{R}$. Another way of expressing this limited grain size was $1.6R_{crit}$ for 3-D and $1.7R_{crit}$ for 2-D system (M Hillert 1965). This approach was similar to the one taken by Feltham, in 1957, considering a log-normal and time dependent normalized grain size distribution. The final expression accordingly took the form of equation 2.61.

$$\frac{dR^2}{dt} = cln\left(\frac{R}{\bar{R}}\right) \qquad \text{…… Eq 2.61}$$

where, *c* is a constant and parabolic kinetics was obtained considering $R = R_{max} = 2.5\,\bar{R}$ (Hatherly and Humphreys 2012).

Louat proposed his random walk theory, in 1974, to explain grain growth in the light of diffusional process. He considered that the boundary segments undergo random motion leading to parabolic grain growth. The final grain size distribution predicted by his theory came as a Rayleigh distribution which is close to the distribution obtained experimentally. Later, the author developed the model further clarifying some of the physical assumptions which it was criticized for ignoring. In 1987, the concept of random walk and curvature driven grain growth concept were combined into a single statistical model by Pande. To summarize, the statistical models are based mostly on **mean field** concept that determines the nature of a boundary or grain in an environment representing average of the surrounding. Feltham's and Hillert's models considered the temporal cum spatial evolution of grain size and are considered as **drift models**. On the other hand, grain face undergo changes by diffusion and Louat's model is considered to be a **diffusion model** (Hatherly and Humphreys 2012).

2.6.1.3 Topological model:

The topological aspect of grain growth was first reviewed by Smith in 1952. His statement was "**Normal grain growth results from the interaction between the topological requirements of**

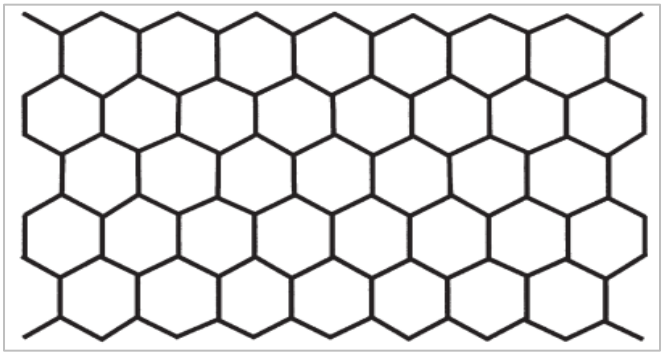

Figure 2.32. Most stable arrangement of grains in the pattern of 2-D array of regular hexagons (Hatherly and Humphreys 2012)

space-filling and the geometrical needs of surface tension equilibrium".

Introduction of grain topology led to the idea of most stable grain structure arrangement to be an array of regular hexagons (Figure 2.32) which satisfies above criteria of space-filling and equilibrium boundary tension. Any arrangement other than this bee-hive structure exhibits grain

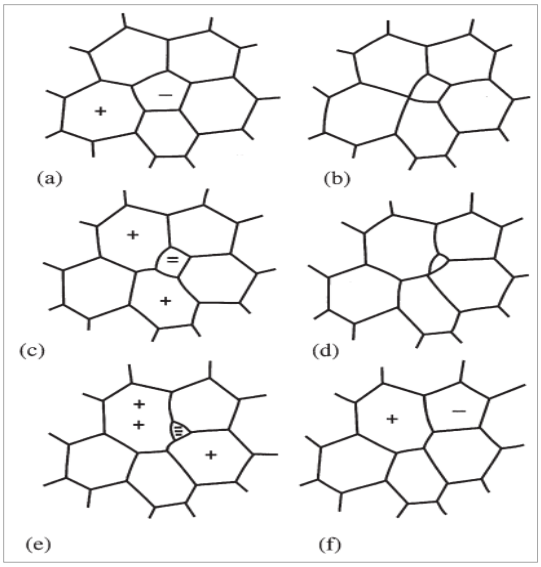

Figure 2.33. Sequence of grain growth introduced in a 2-D array of grains due to insertion of a grain with less or more than 6 sides (Hillert 1965)

growth as it is an unstable one. An example is given in Figure 2.33. Introduction of a 5-sided polygon requires one of its neighboring hexagons to be a 7-sided one to maintain average number of sides per grain according to the Euler's equation (Figure 2.33. a). The force balance requirement leads to the grain boundary angle to be 120° which is achieved by attaining a curvature at the boundary which initiates curvature driven grain towards the center of curvature (Figure 2.33. b) to minimize surface energy. Thus the "5-7" pair can be considered as an imperfection that starts grain growth in the 2-D array (M Hillert 1965). Following this, any grain with sides n > 6 will exhibit growth because it has concave sides and grains with sides < 6 will shrink because of their convex sides. Thus, the 5-sided grain in figure 2.6.2.a forms a 4-rayed vertex (Figure 2.33. b) which results into a 4-sided grain after decomposing into two 3-rayed vertices (Figure 2.33. c). In a similar manner, the grain eventually becomes a 3-sided one (Figure 2.33. e) and disappears leaving one 5-sided grain next to a 7-sided grain (Figure 2.33. f).

In 1952 Von Neumann and in 1956 Mullins, proposed a new equation for growth kinetics as a rate of change of grain area (d*A*) for a 2-D cell with '*n'* sides and area '*A*' based on force balance which is given as follows:

$$\frac{dA}{dt} = c(n-6) \qquad \ldots\ldots\ldots\ldots \text{ Eq 2.62}$$

Above equation can also be expressed in the form of conventional grain radius form as

$$\frac{dR}{dt} = \frac{c(n-6)}{2R} \qquad \text{..... Eq 2.63}$$

where, '*R*' is the radius of grain.

2.6.1.3.1 Defect model:

Based on topological concept of grain growth. Hillert also proposed that presence of a defect in the form of polygonal grains with side not equal to 6 will continue the process of simultaneous growth- shrinkage. This leads to the decrease in the number of neighbors for any shrinking grain. The defect thus sweeps through the array in steps where number of grains is decreased by one after every step is complete. Hillert formulated grain growth rate to be directly proportional to the number of defects per grain, *c* and inversely proportional to the time, *a* taken by the defect to complete one step or to complete the shrinkage of a normal sized grain to zero. This is expressed as follows:

$$-\frac{dN}{dt} = \frac{cN}{a} \qquad \text{..... Eq 2.64}$$

where, ***N*** is the number of grains. The relation between ***N*** and root mean square grain size is given by

$$N * R^2 = constant \qquad \text{..... Eq 2.65}$$

Assuming a constant distribution function, any mean value of *R* can be chosen by wisely varying the constant in the equation 2.65. Introducing R_{cr}, equation 2.64 can be rewritten as:

$$\frac{2dR_{cr}}{cr} + \frac{dN}{N} = 0 \qquad \text{..... Eq 2.66}$$

Combining equations 2.64 and 2.66, we get,

$$\frac{d(R_{crit})}{dt} = -\frac{R_{cr}}{2N} \cdot \frac{dN}{dt} = \frac{1}{2} R_{cr} \cdot \frac{c}{a} \qquad \text{..... Eq 2.67}$$

Now, in a 2-D distribution of grains or cells, more than one defect can be present and it is reasonable to consider that they co-operate in the shrinkage process. Above equation can be modified accordingly as:

$$\frac{d(R_{crit})}{dt} = -R_{cr}^2 \cdot \sum_p \frac{c_p}{a_p} \qquad \text{..... Eq 2.68}$$

where, c_p is the concentration of grains with number of neighbors 6-p and a_p is the time taken by such a grain to disappear. Neumann-Mullins equation and equations 2.48 and 2.52 were applied to estimate the value of a_p considering n = 6-p as:

$$\frac{dR}{dt} = -\frac{pM\gamma_{gb}}{6R} \qquad \ldots\ldots\ldots\ldots \text{ Eq 2.69}$$

Considering shrinkage in the limit criterion while integrating above as the grains shrink from R_{cr} to 0, we get

$$a_p = -\frac{6}{Mp\gamma_{gb}}\int_{R_{cr}}^{0} RdR = \frac{3R_{cr}^2}{Mp\gamma_{gb}} \qquad \ldots\ldots\ldots\ldots \text{ Eq 2.70}$$

Finally combining equations 2.68 and 2.70, another form of parabolic growth kinetics equation is obtained as follows:

$$\frac{dR_{cr}^2}{dt} = \frac{1}{3}M\gamma_{gb}\sum_p p \cdot c_p \qquad \ldots\ldots\ldots\ldots \text{ Eq 2.71}$$

As long as the number of defects remains constant, parabolic nature is maintained for grain growth (M Hillert 1965). This model was later extended in three dimensions by Morral and Ashby in 1974 by introducing an array of 14-sided polyhedral with defects as 13 and 15 sided grains (Hatherly and Humphreys 2012).

2.6.1.3.2 The Rhines and Craig analysis:

This approach also introduces role of topology in grain growth. Rhines and Craig proposed that the simultaneous shrinkage-growth (Figure 2.33) of defective grains (side ≠6) will not only affect the neighboring grains but also the farther grains will also be influenced through the alteration of the topological attributes (vertices, faces, edges, shape etc.) of the neighboring grains. Two new factors were introduced by them. The first one was **sweep constant**, Θ, which represents number of grain lost after unit volume of material is swept out by the grain boundaries. This parameter is difficult to measure experimentally as it keeps changing. The second parameter introduced was **structural gradient**, ζ, which is simply a product of **surface area per unit volume** (S_V) and **curvature of surface per grain** (m_V/N_v). Using these factors, they proposed the rate of loss of grains and the volume compensation (net gain) after each lost grain ($\bar{V}$) was considered to be distributed on average among the remaining grains (N_v). They finally found a linear relationship

between net increased volume due to shrinkage ($\bar{V}$) and time which in turn gives, $R \propto t^{1/3}$, i.e. grain growth exponent, *n* to be 3. This deviation posed an open question to the researchers regarding the grain shape anisotropy aspect in addition to consideration of topology (Hatherly and Humphreys 2012).

2.6.1.3.3 The Abbruzzese-Heckelman-Lucke model:

This model also considered topological aspects by introducing parameters correlating number of sides of a grain ($\overline{n_i}$) to its size (r_i). Experimentally they found

$$\overline{n_i} = 3 + r_i \qquad \text{..... Eq 2.72}$$

Also, the mean grain size ($\overline{r_n}$) was correlated to number of grain sides as:

$$n = 6 + \frac{3(\overline{r_n} - 1)}{\xi^2} \qquad \text{..... Eq 2.73}$$

where, ξ was declared as a correlation coefficient with a value of 0.85. This particular model finally leads to a parabolic grain growth equation similar to Hillert's one (Hatherly and Humphreys 2012).

2.6.1.4 Other Models:

Apart from statistical models, some "deterministic" or "vortex" models of grain growth also do exist. Statistical approach does not accommodate the fact that growth happens when a grain is surrounded by smaller grains and the same shrinks if the neighborhood contains grain larger than it. Hunderi et al. proposed a linear soap bubble model where a bubble, i, in a cluster is assumed to be in contact with i-n to i+n bubbles with n being a factor of relative bubble size. The pressure gradient between the bubbles result in mass transfer and a growth equation of the bubbles in 2-D was formulated which resembles Hillert's parabolic law. In recent time, frequently used deterministic models are the ones mainly based on equation of motion and Monte-Carlo simulation methods. In the first approach, the initial grain structure is fixed and the grain growth is allowed by the movement of vertices, sides governed by specific equations. Like, boundary motion is set to be curvature driven only after adjusting boundary angle at triple junctions to 120° to maintain equilibrium. Several iterations of this two-step process is applied for all grain boundaries and

growth behavior is modelled. In the Monte-Carlo simulation techniques, shrinkage of a grain in 2-D is considered to be governed by following equation:

$$A - A_0 = -ct \qquad \ldots\ldots\ldots \text{ Eq 2.74}$$

where, A_0 is the initial grain size and c is a constant. The above equation results in a parabolic relationship between grain radius and time and a liner dependence of velocity on driving force. However, the grain growth exponent, calculated from above method appears to be 2.44 after an initial transient which was attributed to topological factors. Over time, driving force dropped as the movement of vertices of the computer generated grain structure alters the curvature. This is the reason for deviation of grain growth exponent to higher value. Later on, large number of grain arrays were included in the simulation and they were run for long duration. This includes the steady state grain growth and is free from the effect of initial grain structure. Thus, a final grain growth exponent close to 2 was obtained in 2-D (Hatherly and Humphreys 2012).

2.7 Grain Boundary Segregation (GBS):

Grain boundary segregation (GBS) has been studied extensively for its strong influence on microstructure evolution. Segregation of solute atoms to grain boundaries strongly alters its physicochemical properties causing fracture in grain boundaries during tempering, creep embrittlement, stress relief cracking in welded joints, grain boundary corrosion, hydrogen embrittlement etc. in polycrystalline engineering materials. This also alters grain boundary mobility which influences boundary diffusivity and also the softening kinetics. Even in other applications like thin film conductors in recent microelectronic devices, doped solid electrolytes in high temperature electrochemical devices, boundary segregation of solutes plays an important role. GBS, thus being the common denominator for all the above issues, needs to be studied quantitatively to control the problems predictably and also to use it as a strengthening tool by decorating with solute atoms to tailor the microstructure.

2.7.1 Method of segregation study:

Being an internal interface with local excess volume, grain boundaries are associated with high Gibbs energy which is thermodynamically preferred to be lowered in many ways. On the other hand, the energy gradient from the grain interior to the grain boundary results in a force (dU/dx)

on each solute atom by the boundary. This interaction leads to an excess of solute atoms in the vicinity of the grain boundary called solute segregation. There has been a plethora of techniques available to quantify GBS in terms of various parameters. A list of them with brief description will be discussed in this section.

2.7.1.1 Energy Approach:

This method solely works upon measuring the grain boundary energy as a function of solute concentration and is indeed an indirect method. This uses the concept of the absolute grain boundary energy to be related to the surface energy which is a function of the dihedral angle formed due to intersection of surface and grain boundary tension lines (Hondros 1965).

Using X –ray interferometry, several grain boundary grooves were measured to determine the dihedral angle as well as the boundary energy. Using Gibbs adsorption theorem, the segregation of an element could be measured following the equations $d\mu = RTd(\ln X)$ and $d\gamma = -\sum_i \tau_i d\mu_i$, where μ is the chemical potential of the i^{th} component. The effect of segregation obtained from above study was plotted as shown in Figure 2.34.

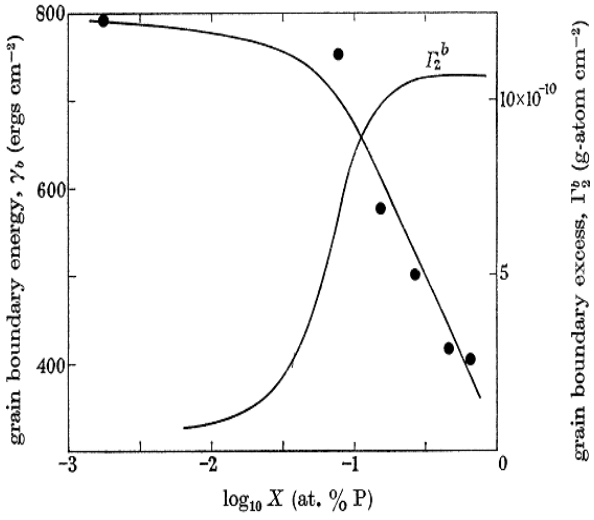

Figure 2.34. Grain boundary segregation of phosphorous at 1450°C in δ-iron measured through absolute grain boundary energy measurement (Hondros 1965)

2.7.1.2 Spectroscopic Techniques:

With the advent of new surface spectroscopic technique, quantitative estimation of GBS has become more accurate with a sound understanding of the fundamentals. A brief description of the available spectroscopic techniques will be given in the following part.

2.7.1.2.1. Auger Electron Spectroscopy (AES) - This technique is primarily used for materials with weak grain boundaries suffering from intergranular failure. The interface to be studied is

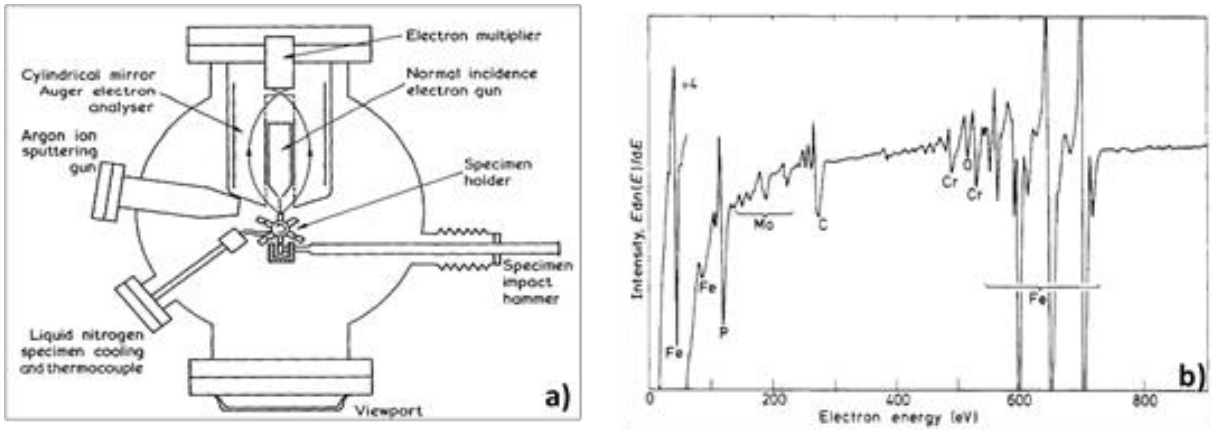

Figure 2.35. a) AES apparatus set up for GBS measurement of fractured surface, b) Auger electron spectrum from temper brittle, 3Cr-0.5Mo Hinkley Point turbine rotor (Hondros and Seah 1977)

exposed by fracturing the specimen, *in situ*, in the ultra high vacuum (UHV) chamber of the AES apparatus (Figure 2.35. a). A focused electron beam of energy 1-30 KeV is used to bombard a core electron of the elements present at the interface leaving an inner shell vacancy which is filled by the electrons of higher energy level with emission of some energy which is in turn abosorbed by another outer shell electron making it come out of the system as an Auger electron with some kinetic energy. This energy level depends upon the atom type. Auger electrons emitted are captured as small peaks at the characteristics superimposed upon a large secondary electron backgroud. Thus, suitable areas of the fractured surface can be imaged by rastering focussed electron beam. Auger electron map of each element (Figure 2.35. b) with a spatial resolution of 1 μm gives point quantitative analyses of the GBS level.

The map showed a 1000 time more enrichment of phosphorus in the grain boundary of the turbine rotor which was susceptible to temper brittleness. This surface technique is suitable for light elements with the exception of H and He. Another advantage is the ability to raster the beam over

the area of interest which specially used to make a scanning electron micrograph of the surface microstructure. Although, the information obtained comes from top few atomic layers, a depth composition profile can also be obtained by combining AES with layer by layer sputtering of the surface by inert gas ion bombardment. However, this technique has some limitations like necessity of exposing the surface by fracturing, inaccuracy due to surface contamination etc. (Hondros and Seah 1977; Seah 1980).

2.7.1.2.2. Wavelength Dispersive X-ray Spectroscopy (WDS) - In materials like non-oriented silicon steels, GBS can be measured using electron probe micro analysis by wavelength dispersive X-ray Spectroscopy (EPMA-WDS). This technique also works on fracturing and exposing the interfaces but the sample can be fractured ex situ as WDS is not sensitive to surface contamination. This method of measurement has certain advantages like convenient specimen preparation and large area available from interface to analyse. The relative intensity (I/I_{Std}) measurement is done to determine interface concentration of the segregants. The quantification for Sn segregation measurement in a silicon steel sample is based on the following equation:

$$\frac{I}{I_{std}} = \frac{\int_{\rho z=0}^{\infty} F(\rho Z)\varphi(\rho Z)d\rho Z)}{\int_{\rho z=0}^{\infty} F_{Std}(\rho Z)\varphi_{Std}(\rho Z)d\rho Z)} \qquad \ldots\ldots\ldots\ldots \text{ Eq 2.75}$$

where, I and I_{Std} are the intensities of segregant L_α line measured on the GB facets of the specimen and on the standard material (pure solute) respectively, z (cm) is the depth, ρ (g/cm^3) is the mass per unit volume, ρz (g/cm^2) is the mass thickness (i.e. the mass per unit area of a layer of thickness z), F(ρz) and $F_{Std}(\rho z)$ are the weight fraction of Sn in the sample and the standard material (pure Sn), respectively. φ(ρz) and $\varphi_{Std}(\rho z)$ are dimensionless functions that describe the distribution of

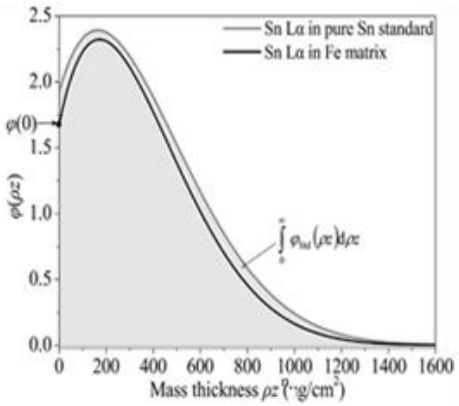

Figure 2.36. Quantification of Segregation using integrated intensity after MSG model (Yang et al. 2015)

the Sn L_α line emerging intensity as a function of depth for 20 kV primary electrons for silicon steel and pure Sn (Yang et al. 2015) as can be seen in Figure 2.36. Finally the GBS of Sn can be determined from mass per unit grain boundary area, X_{WDS} by the relation, $X_{WDS}= 2(\mu- \mu_{bulk})$, where μ is the total concentration inside the X-ray analyzed volume during WDS experiment and μ_{bulk} is the theoretical concentration from the bulk contribution for the same analyzed volume. The factor 2 is included to consider the Sn atom to be shared on both sides of the fracture surface. The quantified result of WDS (i.e. X_{WDS}) is expressed as the mass thickness (ng/cm^2), i.e. the mass per unit area of a layer with a certain thickness.

2.7.1.2.3. Secondary Ion Mass Spectroscopy (SIMS) - This technique is another way to quantify GBS with higher degree of sensitivity to the segregating elements. Measurement is done from surface in a layer-by-layer manner. Bombarding surface with primary ion beam excites the atoms of the interface and they emit secondary electrons which characterises the chemical composition of the interface. A mass spectroscope collects the time-of-flight information for all the secondary ion signals and analyses them. This method is particularly useful in studying interaction amongst co-segregating elements. Despite having some advantages like hydrogen detection, detection sensitivity up to parts per billion (ppb) level and ability to provide information regarding interface chemical structure , SIMS has not been used frequently for some shortcomings which is mostly due to bigger spot size of the primary ion beam (Lejcek 2010).

2.7.1.2.4. Other Techniques – Some other spectroscopic techniques are X-ray photoelectron spectroscopy (XPS), ion scattering spectroscopy (ISS or low-energy ion scattering, LEIS), Rutherford backscattering spectroscopy (RBS), Mössbauer spectroscopy, secondary neutron mass spectroscopy (SNMS), glow discharge optical emission spectroscopy (GDOES), etc. In some studies, impedance spectroscopy was used to measure conductivity for measuring boundary solute coverage and also co-segregation of Si and Ca in sintered ZrO_2 stabilized by Y_2O_3 and CaO (Aoki et al. 1996).

2.7.1.3 Spectroscopic Techniques:

Without fracturing the sample, GBS quantification can be possible by microscopic techniques. This is mostly classified into two broad categories. The brief description is given below.

2.7.1.3.1. Analytical Electron Microscopy (AEM)- This imaging method is a combination of high resolution microscopic techniques (HRTEM, STEM) for obtaining images with high spatial resolution with tools like energy dispersive X-ray (EDX) analysis or electron-energy loss spectroscopy (EELS) for local composition analysis. Thin foil specimen is used with particularly grain boundaries oriented normal to the surface to image the boundary structure and analyse its chemical structure. This method has the advantage of measuring layers of segregation, precipitate and inclusion check at the interfaces by X-Rays and electron diffraction. But, again the sample preparation for this is quite cumbersome and this technique is insensitive to analyse elements with atomic number below 10 (Lejcek 2010).

2.7.1.3.2. Atom Probe Field Ion Microscopy (APFIM)- This technique of GBS measurement is the most recent one which analyses intact grain boundaries by combining time-of-flight mass spectroscopy with field ion microscopy. The grain boundary of interest is chosen and lift up from the sample by milling with Focussed Ion Beam (FIB) forming ultimately a needle-like sample with sharp but round tip (Figure 2.37. b).

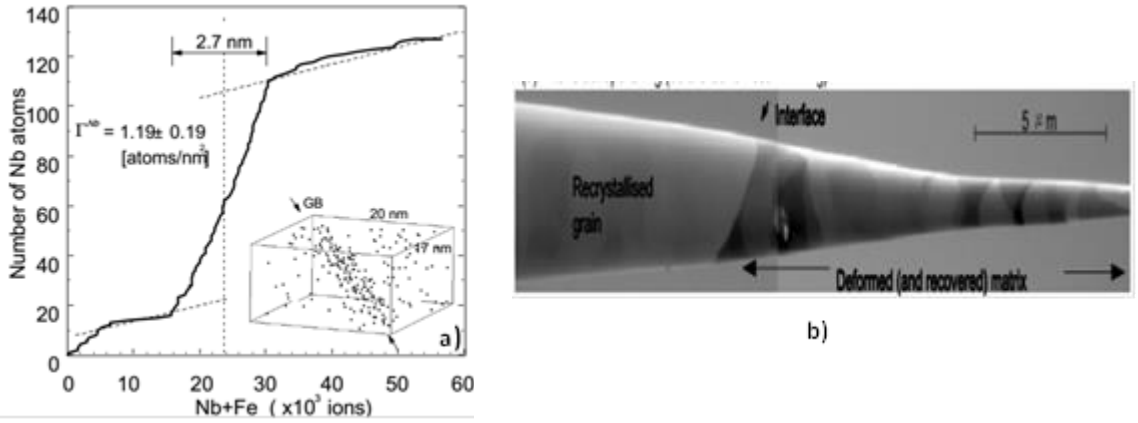

Figure 2.37. a) Ladder diagram of Nb across a sub-grain boundary with misorientation of 10° in a Fe-0.09Nb alloy, b) FIB image of atom probe tip before milling (Maruyama and Smith 2004)

The atoms situated at the top of the tip are desorbed by field evaporation technique and projected into a mass spectrometer. Thus, the mass of the field-desorbed atoms is given with almost near atomic spatial resolution. These field-desorbed atoms in a given mass range can be used to reconstruct image of the tip in an atomic level by suitable gating the channel plate image intensifier used in a field-desorption microscope for imaging. Thus the atoms segregating at the grain boundaries can be imaged and a concentration profile across the boundary can be obtained. APFIM

technique has many advantages like near atomic resolution, crystallographic information about the boundary structure, a faster, standardless analysis of all elements, etc. But, sample preparation technique is complicated as probability of having the grain boundary sitting near the tip is very low. In addition, exposure of the needle tip to high electric field for evaporation leads to fracture of the sample (Hondros and Seah 1977; Lejcek 2010).

A recent development came in the form of 3D Atom probe or 3D tomography where field evaporation of the layers from the tip is done and the detector captures all the atoms evaporated at the same time and using a 3D reconstruction technique, distribution of the solute atoms in grain boundary in a small volume is obtained with resolution in the scale of 0.5 nm. This technique was used to measure interaction of Nb and Mo with high angle grain boundaries (HAGB) in ferrite by some researchers. Using Langmuir-McLean isotherm, the segregation enthalpy of the solute Nb and Mo are measured by determining Gibbs energy of segregation (Maruyama and Smith 2004; Maruyama, Smith, and Cerezo 2003). Due to near atomic spatial resolution, width of the GBS was also obtained from a ladder diagram of the solutes (Figure 2.37. b) which is an estimate of variation of grain boundary excess of Nb across the boundary. Using the same technique, difference in the GBS of Nb at ferrite-ferrite HAGBs and prior austenite HAGBs was studied by some other researchers (Peter J Felfer et al. 2012).

Apart from all the above mentioned experimental techniques, some theoretical ways to study GBS are also there which mostly works on simulating grain boundary structure and energetics with solute atom in the module of a pure material. One of these is quantum mechanical approaches based on first principles to solve independent electronic Schrödinger equation of a many-electron system. Instead of considering wave nature, another approach of density functional theory was also used to study the interface structure and GBS. The other theoretical approach is based on simulations based on molecular mechanics (Lejcek 2010).

2.7.2 Models for Grain Boundary segregation:

Due to the number of incomplete bonds in any interface, its free energy is higher and to attain stability a system tries to minimize it. Being an interface, grain boundaries try to low its energy by interacting with solute atoms as a coupled atomic and electronic relaxations occur there. This results into an atmosphere of solutes strongly modifying the grain boundary (GB) behaviour as

well as bulk material properties. To understand the phenomenon of grain boundary segregation (GBS), it is imperative to focus on the thermodynamic description of the same. To start, the models derived from classical thermodynamics will be dealt with. These were mostly validated by Auger electron spectroscopy (AES). Although, the initial development of these approaches was made to predict segregation at random boundaries in polycrystals, later on it was extended to GBS at well characterized boundary in a bicrystal.

2.7.2.1. Gibbs Adsorption Isotherm: The fundamental characteristic of a surface from thermodynamic point of view is its energy *'γ'* which indicates the reversible work done to create unit area of surface while the bicrystal growing by equilibrium transport of components i=1,2,…*N* from the surrounding under constant temperature (T), volume(V) and chemical potentials (μ_i). Under the consideration of a hypothetical system consisting of two regions 1 & 2 of uniform properties up to a plane called the dividing surface, any thermodynamic property of the system can be expressed in the form as follows:

$$\Phi^s = \Phi - (\Phi^1 + \Phi^2) \qquad \ldots\ldots\ldots \text{ Eq 2.76}$$

where, ϕ is the thermodynamic property of the total system and ϕ^1 and ϕ^2 are the same of the two regions. So the thermodynamic property of the real system over and above the hypothetical system is termed as interfacial excess properties ϕ^s. This above Gibbsian convention has an exception while expressing the volume of the system which is considered as $V=V^1+V^2$ indicating the interfacial excess volume, V^s, to be zero (Wynblatt and Chatain 2006). This might sound contradictory with the consideration of grain boundary as a free volume. Geometrically, some researchers (Gunter Gottstein and Shvindlerman 2009) interpreted this as the transition layer between two regions in the form of two-dimensional dividing surface. The internal energy of region or grain 1 can be written as

$$dE^1 = \left(\frac{\partial E^1}{\partial S^1}\right)_{V^1 n_i^1} ds^1 + \left(\frac{\partial E^1}{\partial V^1}\right)_{S^1 n_i^1} dV^1 + \left(\frac{\partial E^1}{\partial n_i^1}\right)_{S^1 V^1 n_i^1 \neq i} dn_i^1 \qquad \ldots\ldots\ldots \text{ Eq 2.77}$$

or,

$$dE^1 = Tds^1 + PdV^1 + \sum_i \mu_i^1 dn_i^1 \qquad \ldots\ldots\ldots \text{ Eq 2.78}$$

where, T is the temperature, *P* is the pressure, and μ_i^1 is the chemical potential of component '*i'* in grain 1. Above is the standard expression for the internal energy of a single uniform phase

containing more than one component. Following equation 2.78, the internal energy for grain 2 can also be expressed as

$$dE^2 = Tds^2 + PdV^2 + \sum_i \mu_i^2 dn_i^2 \qquad \ldots\ldots\ldots \text{ Eq 2.79}$$

As stated above while discussing the surface energy of a grain boundary which doesn't have any volume, the internal energy expression will look like following:

$$dE^s = Tds^s + \gamma dA + \sum_i \mu_i^s dn_i^s \qquad \ldots\ldots\ldots\ldots \text{ Eq 2.80}$$

Rearranging, equations 2.77, 2.78, 2.79 and 2.80 according to 2.76, we obtain

$$dE = T(ds^1 + ds^2 + ds^s) - P(dV^1 + dV^2) + \sum_i \mu_i (dn_i^1 + dn_i^2 + dn_i^s) + \gamma dA \qquad \ldots\ldots \text{ Eq 2.81}$$

Or,

$$dE = Tds - PdV + \gamma dA + \sum_i \mu_i dn_i \qquad \ldots\ldots\ldots\ldots \text{ Eq 2.82}$$

The above equation is used to relate change in internal energy of a system containing grain boundaries using thermodynamic first principle. Integrating equation2.80, gives rise to

$$E^s = TS^s + \gamma A + \sum_i \mu_i n_i^s \qquad \ldots\ldots\ldots\ldots \text{ Eq 2.83}$$

Redifferentiation of equation 2.83 gives,

$$dE^s = Tds^s + S^s dT + \gamma dA + Ad\gamma + \sum_i (\mu_i dn_i^s + n_i^s d\mu_i) \qquad \ldots\ldots\ldots\ldots \text{ Eq 2.84}$$

Comparing above equation with equation 2.80, we get,

$$dE^s = S^s dT + Ad\gamma + \sum_i n_i^s d\mu_i \qquad \ldots\ldots\ldots\ldots \text{ Eq 2.85}$$

Equation 2.85 can be re-written as

$$d\gamma = -s^s dT - \sum_i \tau_i d\mu_i \qquad \ldots\ldots\ldots\ldots \text{ Eq 2.86}$$

where, terms normalized by grain boundary area , s^s and Γ_i are specific surface excess entropy and number of moles of component i. Equation 2.86 is known as **Gibbs adsorption equation** which relates the variation in γ with changes in T and μ_i. At constant temperature, for a two –component system, the Gibbs adsorption equation gives:

$$d\gamma = -\tau_1 d\mu_1 - \tau_2 d\mu_2 \qquad \ldots\ldots\ldots \text{Eq 2.87}$$

Applying Gibbs-Duhem equation, $n_1^1 d\mu_1 + n_2^1 d\mu_2 = 0$ and ignoring the solvent's chemical potential, equation 2.87 can be rewritten as:

$$\frac{d\gamma}{d\mu_2} = \left(\tau_1 \frac{n_2^1}{n_1^1} - \tau_2 \right) \qquad \ldots\ldots\ldots\ldots \text{Eq 2.88}$$

In the case of interfaces between a condensed phase and a vapor phase, the difference in density across the interface makes it possible to select the position of the Gibbs dividing surface so as to make one of the adsorption terms vanish. By choosing the position of the dividing interface so that $\Gamma_1 = 0$ which is indicated by $\Gamma_{2,1}$, relative adsorption, equation 2.88 becomes,

$$\frac{d\gamma}{d\mu_2} = -\tau_{2,1} \qquad \ldots\ldots\ldots\ldots \text{Eq 2.89}$$

Substituting the chemical potential μ_i by the activity a_i as, $\mu_i = \mu_i^0 + RT\ln a_i$, where, μ_i^0 is the standard chemical potential. For both ideal solution and dilute solution, we can write after differentiating the chemical potential expression as, $d\mu_2 = RT\, d(\ln X_2)$, and using that in equation 2.88, we get,

$$\frac{1}{RT}\frac{d\gamma}{d\ln X_2} = -\tau_{2,1} \qquad \ldots\ldots\ldots\ldots \text{Eq 2.90}$$

The above expression quantifies segregation of species 2 and relates the change of the interfacial energy 'γ' with the molar fraction X_2. This is the most commonly used form of Gibbs adsorption isotherm for a dilute binary system. Despite the simplicity and having been applied to predict segregation of phosphorous in γ-iron etc., some limitations like complicated measurement of surface energy variation with composition, indirect measurement of $\Gamma_{2,1}$, unknown relationship between $\Gamma_{2,1}$ and μ_2, Gibbs approach had limited usage. This is when there came a new approach from the viewpoint of statistical thermodynamics to complement Gibbsian shortcomings (Wynblatt and Chatain 2006; Priester 2012).

2.7.2.2. Langmuir-McLean's Model: This approach was the first to quantify segregation specifically at the grain boundaries while the previous one was just for a generic free surface case. A monolayer presentation of grain boundary was chosen for this model with a regular solution

consideration. The total free energy was assumed to have contributions from non-zero enthalpy of mixing and entropy of mixing. The random distribution of solute in bulk and GBs, the total entropy for the ideal solution takes the following form:

$$S_{id} = -R\left[n^s x^s \ln x^s + n^s (1-x^s) \ln(1-x^s) + Nx \ln x + N(1-x) \ln(1-x) \right] \quad \ldots\ldots\ldots \text{ Eq 2.91}$$

where, x^s and x are the atom fractions, n^s and N are the numbers of solute atoms segregating in the monolayered interface and the bulk, respectively. This ideal solution approximation results into composition in the interface as:

$$\frac{x^s}{1-x^s} = \frac{x}{1-x} \exp\left\{ -\frac{\Delta H_{seg}}{RT} \right\} \quad \ldots\ldots\ldots\ldots \text{ Eq 2.92}$$

where ΔH_{seg} is the enthalpy of segregation. This x^s is not analogous to Γ and their relation is $\Gamma = (x^s\text{-}x)/\sigma$, where σ is the area per mole at the interface. The driving force for segregation was, therefore, assumed to come from bulk strain energy, ΔE_{el}, which arises due to misfit strain around the solute atoms located in the bulk. Thus an exchange of a solute atom with a solvent atom at the surface is governed by $\Delta H_{seg} = -\Delta E_{el}$. This expression is formally equivalent to the Langmuir isotherm for the adsorption of an element on a free surface and therefore referred as Langmuir-McLean's model (Wynblatt and Chatain 2006).

2.7.2.3. Seah-Hondros Model: The extension of above model of GBS for interstitial solute atoms was done by Seah and Hondros. Here, the segregation sites at the GBs were assumed to be saturated being occupied by solvent atoms. The maximum fraction at saturation is given by

$$X^{0GB} = \frac{N_{\text{int}}^{GB}}{N_{\text{int}}^{GB} + n_{subst}^{GB}} \quad \ldots\ldots\ldots\ldots \text{Eq 2.93}$$

Finally considering a sold solubility limit of solute S in the matrix as X_s*, the segregation equation becomes,

$$\frac{X_S^{GB}}{X^{0GB} - X_S^{GB}} = \frac{X_S}{X_S^*} exp\left(-\frac{\Delta G_S}{RT}\right) \quad \ldots\ldots\ldots\ldots \text{ Eq 2.94}$$

where, X denotes the mole fraction of solutes and a coverage factor balances the interstitial and substitutional atom contribution (Priester 2012).

2.7.2.4. The Defay and Prigogine Model: This model computes the equilibrium composition of a liquid surface applying regular solution model. A solid like model of liquid was chosen with nearest neighbour bond description to calculate the enthalpy of the system. This model also considers the interface to be a single plane. The segregation takes place according to

$$\Delta H_{seg} = (\gamma_B - \gamma_A)\sigma + 2\omega\left[z^l(x - x^s) + z^v(x - \frac{1}{2}) \right] \qquad \ldots\ldots\ldots\ldots \text{ Eq 2.95}$$

where, γ is the surface energies of pure form of components A and B, ω is the regular solution parameter expressing difference between the A-B and (A-A)+ (B-B) bond energies. The terms z^l and z^v are the numbers of in-plane bonds and half of the out-of-plane bonds of an atom in the surface plane, so that total number of atoms in direct neighborhood becomes $z = z^l + 2z^v$ (Wynblatt and Chatain 2006).

2.7.2.5. The Wynblatt and Ku Model: The accurate description of GBS in binary alloys was given by considering both chemical and elastic contributions to calculate enthalpy of segregation. This combined effect on heat of segregation was somehow neglected in the models of McLean and Defay. So the Wynblatt *et.al* model is expressed as

$$\Delta H_{seg} = (\gamma_B - \gamma_A)\sigma + 2\omega\left[z^l(x - x^s) + z^v(x - \frac{1}{2}) \right] - \Delta E_{el} \qquad \ldots\ldots\ldots\ldots \text{ Eq 2.96}$$

The elastic energy term is further given according to continuum linear elastic formalism by Friedel. The above model indicates that there are three parameters that influence GBS as the surface energy driving force, interatomic interaction driving force and elastic strain energy. The last two terms will be zero in case of an ideal solution. It is important to mention the signs of the above three factors dictate the GBS. Negative contributions to the heat of segregation increase the value of x^s .i.e., aids in segregation. Being always positive, the ΔE_{el} part always favours solute segregation. The surface energy difference between solute and solvent can be negative or positive. So, the smaller surface energy component (here, B is solute) will have the tendency to segregate. Similarly, a positive ω will accelerate segregation. So, the all the three factors altogether control the GBS according to their signs (Wynblatt and Chatain 2006).

2.7.2.6. Lee-Aaronson Model: Further modification of the above model was done by considering structural and energy anisotropy effect of surface. Although, this issue was considered partially in

the model of Defay *et. al.*, their model was valid for only the atoms of the first plane of the interface. Any (hkl) plane atoms may also have broken bonds from deeper atom planes. A multilayer consideration by Lee and Aaronson which is valid for any atom with incomplete bonding at any surface orientation in an FCC crystal. This excludes the restriction of segregation only to monolayered structure of interfaces (Wynblatt and Chatain 2006).

2.7.2.7. Fowler and Guggenheim's Model: This model considers the interaction between the solute atoms which is expressed by a Fuller term ($2z\omega_{ij}X_S^{GB}/X^{0GB}$) where the ratio between two atom fractions is expressed in Seah-Hondros Model as coverage factor. For a binary solid solution where the solute may be localised on the site i or j of the boundary, $\omega=A[\varepsilon_{ij}-0.5(\varepsilon_{ii}+\varepsilon_{jj})]$. A is the Avogadro number ε_{ij}, ε_{ii} and ε_{jj} are the pair potentials between atoms in the sites i and j. The segregation equation is expressed as:

$$\frac{X_S^{GB}}{X^{0GB}-X_S^{GB}}=\frac{X_S}{1-X_S}\exp\left\{-\frac{(\Delta H_{seg}+2z\omega_{ij}X_S^{GB}/X^{0GB}}{RT}\right\} \qquad \text{…….. } Eq\ 2.97$$

In above expression, a positive ω means repulsive interaction between solute atoms at GB to be predominant which increases the heat of segregation and thereby lowers the extent of segregation than that in absence of interaction and in its progressive decrease with X_S^{GB} increase (Priester 2012).

Some other modifications are also made to the regular solution based models which assume ideal random mixing and random distribution of energy. Several attempts have been made at different times to introduce more realistic entropy descriptions. Recently, a new concept of free energy expansion method was also introduced to model surface segregation (Wynblatt and Chatain 2006). Other models by Guttmann *et.al.* for studying segregation in a three component system with interaction between the segregants and site competition effects, Mean field approximation model, Luthra and Briant model are also common (Lejcek 2010).

2.8 Solute Drag:

From the discussion on grain boundary structure, the concept of free excess volume associated with HAGBs came into the picture. As, grain boundaries are considered to be region of higher Gibbs energy, compared to the lattice interior, thermodynamically the system will tend to reduce

the excess energy by various ways. One of them is interaction of solute atoms with grain boundaries. If this favors the Gibbs energy minimization, local redistribution of solute atoms occur at the grain boundary which is known as equilibrium solute segregation. This results into formation of solute atmosphere around the boundary. Segregation phenomenon has been realized to have enormous importance on metallurgical properties of materials. In 1894, segregation of solute elements (P, S, As) was first correlated with grain boundary brittleness of iron (Priester 2012). In 1956, Lücke and Detert found that addition of 0.01% of manganese or iron in high purity aluminum has huge effect on HAGB migration. Mn makes recrystallization kinetics sluggish by a factor of 10^{12} and iron by 10^{16}. Under the presence of driving force, when the HAGB migration takes place, these segregating solute atoms tend to impart a force which acts opposite to the direction of boundary motion. This has been known as solute drag effect. As grain boundary migration dictates bulk properties of a material through microstructure evolution, the effect of solute atoms on moving boundaries has become a research area of growing interest for more than 50 years.

Experimentally, solute drag effect was first quantified in high purity aluminium by Lücke, Masing, and Nölting and Detert- Lücke, in copper by Smart and Smith in mid 50's. The highlight of their studies can be summarized as follows (Lücke and Detert 1957):

i) The significant drop in recrystallization rate by 10^{16} is solely due to the solute form of the impurity elements.

ii) Initially, the rate drop was slow as impurity addition is increased but becomes very fast once the concentration goes beyond 0.01% since the recrystallization mechanism gets changed. This critical limit of 0.01% seems to have no connection with the solubility limits. It may remain within the range of solid solubility

iii) Impurity affects both the nucleation stage of recrystallization and grain growth in a similar extent which is indicative of a common elementary process involved behind this phenomenon.

iv) The impurity effect was found to be less prominent when extent of deformation was smaller

v) A contradictory observation of reduced activation energy of recrystallization with impurity addition was also reported in most of the cases

vi) They suggested that effect of impurity came through their interaction with boundaries, not from the difference in deformed conditions between pure and impure metals. This was evidenced that during grain growth and secondary recrystallization, impurity also retards the kinetics although no deformation strain is present.

The type of interaction that an impurity atom undergoes with a moving grain boundary is mostly elastic in nature. For the size difference (atomic radius, *r*) of the solute (impurity) atom from the solvent atom, an elastic stress field is created around it when at the undisturbed lattice interior. To lower the strain energy associated with the stress field, solute atoms prefer to be into the grain boundary rather than grain interior. Therefore, it is evident the extent of size difference between solvent and solute atom dictates the magnitude of the stress field resulting in no elastic interaction if the solute atom has the same size as solvent atom. An example of this was observed during recrystallization of copper where an increase in recrystallization temperature was observed with increasing size difference of the alloying elements. Addition of nickel (r=1.24Å) to copper matrix (r = 1.24Å) does not increase the recrystallization temperature. But addition of Co (r = 1.26Å), Fe (r = 1.27Å), Ag (r = 1.44 Å), Sn (r = 1.58Å), etc. increases recrystallization temperature by 15°C, 15°C, 80°C and 180°C respectively. A correlation between this increase in recrystallization temperature and valency difference of the solute- solvent was also highlighted by Smith. Later on it was realized that the influence of size difference is more pronounced than that in valencies from experimentally obtained recrystallization temperature values in 40% rolled aluminum with 0.01% impurity addition (Lücke and Detert 1957).

Transfer of solute atom to boundary region leads to decrease in energy which was, initially, calculated using linear elastic theory. In the light of Cottrel's dislocation formula, the release in energy can be written as:

$$V = \frac{4}{3} r^3 G \frac{1+\sigma}{1-\sigma} \eta \qquad \text{…… Eq 2.98}$$

where, *G* stands for shear modulus, σ is the Poisson's ratio (0.33 for Al) and *r* is the solvent atom's radius. η can be expressed as

$$\eta = \left| \frac{r - r_F}{r} \right| \qquad \text{…… Eq 2.99}$$

where, r_F is the radius of the foreign (solute) atom.

The energy release can also be computed from the aspect that transfer of atom to grain boundary region decreases the strain energy associated with the stress field as:

$$V = 8\pi r^3 G\eta^2 \qquad \ldots\ldots\ldots\ldots \textit{Eq 2.100}$$

The calculated value of *V* from both equations 2.98 and 2.100, with η =0.1 was ~ 3000 cal/mole (considering G_{Al}= 2.7x10^{11} dyn/cm^2, r_{Al} =1.43x10^{-8}cm) which was later on questioned as it was formulated based on linear elastic theory. Also, the decrease in grain boundary energy itself for having the solute atoms in it was not considered in the calculation. Later on when the boundary energy reduction by one solute atom was calculated, its value came somewhat less than *V* indicating correct prediction of the order of magnitude of *V* by above equations. The solute-boundary interaction also has an electronic part which has still remained unexplored for the electronic state of boundary being unknown. However, it is clear from the above discussion that solute –boundary interaction is the reason behind formation of solute atmosphere in the grain boundary although the nature of the interaction force was not considered by Lücke *et al* (Lücke and Detert 1957).

A more detailed investigation on the theory of solute drag in dilute solution was done independently by Cahn in 1962 (Cahn 1962) and Lücke and Stüwe in 1963. In 1971, Lücke and Stüwe extended Cahn's theory for high solute concentration using Fermi-statistics whilst the previous approaches were based on Boltzmann-statistics (Lücke and Stüwe 1971). Also they assumed stress field of atomic dimensions unlike previous models where extended stress field of the grain boundary was considered. After this, the famous CLS (Cahn-Lücke -Stüwe) theory came into the picture which interpreted solute drag as a 'force' exerted by solutes on the boundary. One of the other popular solute drag theories was after Hillert and Sundman (Mats Hillert and Sundman 1976) where the Gibbs energy dissipation equality of boundary motion to solute diffusion was considered. Next, a detailed description of these two approaches will be discussed.

2.8.1 Cahn-Lücke -Stüwe (CLS) Model:

This continuum model is based on variation of interaction energy (*E*) between solute atoms and the moving boundary with distance (*x*) of an atom from the midpoint of the boundary (Cahn 1962). A triangular interaction energy profile was chosen to interpret diffusion of solute atoms towards the boundary and final solute concentration at the boundary (Fig 2.38.a). Also, the boundary was

represented by an interaction energy E(x) and diffusion coefficient D(x) considering solute diffusion occurring as the boundary starts to migrate.

As the change in chemical potential (where, μ = kT ln C(x)+E(x)+ const.) is considered to drift the solute diffusion towards the boundary, the flux of atoms can be expressed as (Fick's first law taken into account):

$$-J = \frac{DC}{kT}\frac{\partial \mu}{\partial x} = D\frac{\partial C}{\partial x} + \frac{DC}{kT}\frac{\partial E}{\partial x} \qquad \ldots\ldots\ldots\ldots \text{ Eq 2.101}$$

where, the expression of μ is substituted in $\partial\mu/\partial x$ and D is only a function of x.

Applying Fick's second law, the change in solute concentration can be given written as:

$$\frac{\partial C}{\partial t} = D\frac{\partial^2 C}{\partial x^2} + \left[\frac{\partial D}{\partial x} + \frac{D}{kT}\frac{\partial E}{\partial x}\right]\frac{\partial C}{\partial x} + \frac{1}{kT}\left[\frac{\partial D}{\partial x}\frac{\partial E}{\partial x} + D\frac{\partial^2 E}{\partial x^2}\right]C \qquad \ldots\ldots\ldots\ldots \text{ Eq 2.102}$$

When the boundary moves with a constant velocity, no accumulation of solute is expected leading to the solute profile reaching a steady-state condition for which

$$\frac{\partial C}{\partial t} = -V\frac{\partial C}{\partial x} \qquad \ldots\ldots\ldots\ldots \text{ Eq 2.103}$$

And for steady state, equation 2.102 can be re-written as:

$$D\frac{\partial^2 C}{\partial x^2} + \left[\frac{\partial D}{\partial x} + \frac{D}{kT}\frac{\partial E}{\partial x}\right]\frac{\partial C}{\partial x} + \frac{1}{kT}\left[\frac{\partial D}{\partial x}\frac{\partial E}{\partial x} + D\frac{\partial^2 E}{\partial x^2}\right]C = 0 \qquad \ldots\ldots\ldots\ldots \text{ Eq 2.104}$$

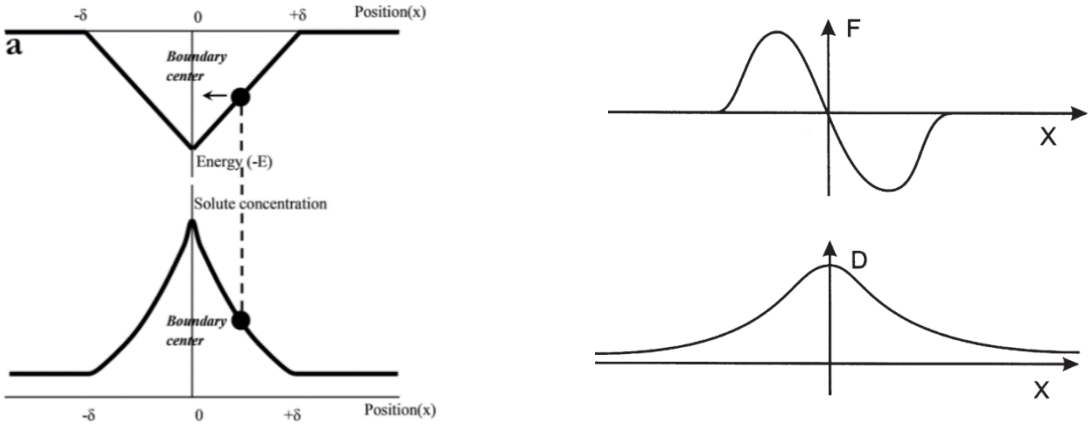

Figure 2.38. a) Solute interaction energy profile (top) across the boundary for the case E(x)<0 indicating segregation (arrow means attraction of solutes to boundary) of solute at grain boundary resulting in concentration profile shown at the bottom (Qiu 2013), b)Represents the interaction force F(x) profile of a solute segregating at the boundary (top) and diffusivity (D(x)) profile of the solute in the boundary region (Hatherly and Humphreys 2012)

Equation 2.104 is the diffusion equation combined with interaction energy which on solving yields

$$C = C_0 V\, exp\left\{-\frac{E(x)}{kT} - V\int_{x_0}^{x}\frac{d\eta}{D(\eta)}\right\} * \int_{-\infty}^{x} exp\left\{\frac{E(\xi)}{kT} + V\int_{x_0}^{\xi}\frac{d\eta}{D(\eta)}\right\}\frac{d\xi}{D(\xi)} \qquad \ldots\ldots\ Eq\ 2.105$$

where, C_0 is the matrix composition which is same as the one trailing the boundary at steady state. Above equation highlights that the concentration profile at a point 'x' is influenced by the boundary segment which has not yet moved past the point. However, equation 2.105 is not valid for V≤0. For stationary boundary (V=0) above equation represents singularity in solution and accordingly we have:

$$C = C_0\, exp\left[-\frac{E(x)}{kT}\right] \qquad \ldots\ldots\ldots\ Eq\ 2.106$$

Above equation based on Boltzmann-statistics indicates equilibrium segregation profile of the solute atoms (Figure 2.38. a (bottom)) around a stationary boundary and it is symmetric. Also, the interaction force and diffusivity profiles are given in Figure 2.38. b. Upto now, the discussion just has shown how the segregation of solute atoms is thermodynamically possible at an interface.

Now, each solute atom exerts an interaction for 'F' which can be written as (-dE/dx) on the boundary. Usually the tendency of a solute atom to segregate to the boundary becomes higher as its solubility drops. So, the interaction force also varies from one to another solute-solvent combination. Also, this can vary for moving and stationary boundaries as the former has larger free volume. Upon integrating over all the atoms segregated near boundary region, total force by the solutes on the boundary or the 'solute drag' can be written as:

$$P_d = -N_v \int_{-\infty}^{+\infty}(C - C_0)\frac{dE}{dx}\,dx \qquad \ldots\ldots\ldots\ Eq\ 2.107$$

Here, N_v is the number of atoms per unit volume. To integrate above equation one must solve equation 2.105 for some specific limiting cases.

High velocity case: when the boundary velocity is very high, the diffusion of solute atom is still slower. Solute atoms can no longer keep up with the boundary and the grain boundary breaks away from its atmosphere, the pressure- velocity relationship is given by

$$P_d = \frac{V}{M} + \frac{C_0}{\alpha \dot{V}} \qquad \ldots\ldots\ldots\ Eq\ 2.108$$

where, M is the intrinsic mobility, α' is a constant defined as α/β^2. The expression for is $(\beta^2 = (\alpha k T \delta) / (2N_V E_0^2 D)$. Constant α will be discussed in detail for low velocity case.

Low velocity case: In the case of low boundary velocity, the relationship between the driving pressure P_d for GBM and boundary velocity V was approximately as:

$$P_d = \frac{V}{M} + \alpha C_0 V \qquad \text{…….. Eq 2.109}$$

In this expression the constant α depends on several parameters of the model and can be expressed as

$$\alpha = \frac{\delta N_v (k_B T)^2}{E_b D_{cross}} \left(sinh\left(\frac{E_b}{kT}\right) - \frac{E_b}{kT} \right) \qquad \text{…….. Eq 2.110}$$

where, δ is the grain boundary width (~*1 nm*), N_v is the number of atoms per unit volume, E_b is the solute-boundary binding energy (20 kJ/mol) (H. Zurob 2003; Menyhard, Yan, and Vitek 1994). D_{cross} is the cross- boundary diffusion coefficient approximated as per segregation profile study

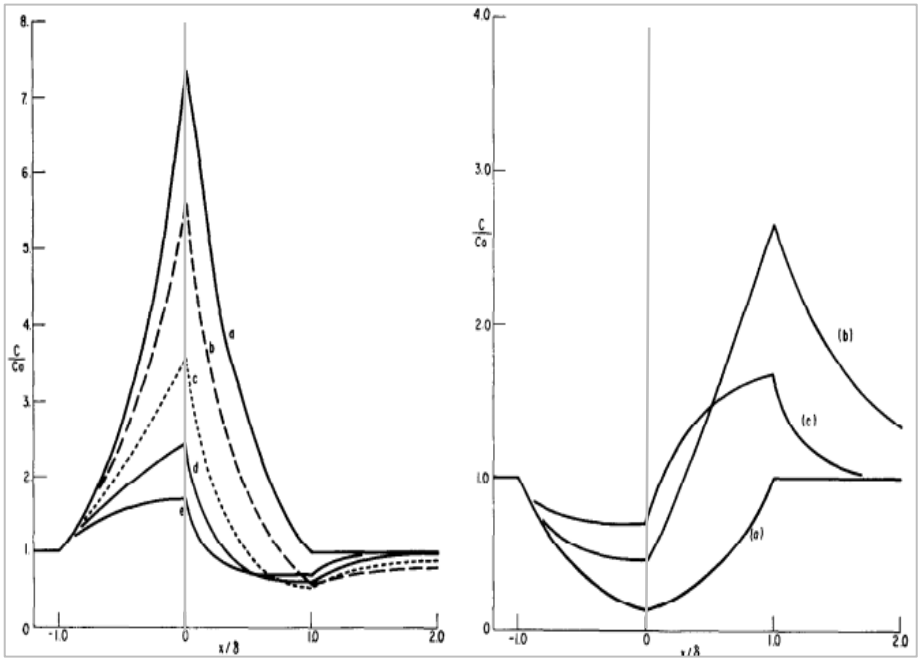

Figure 2.39. a) solute concentration profiles for different boundary velocities (a<b<c<d<e) at E(x)<0 indicating segregation b) solute concentration profiles for different boundary velocities (a<b<c) at E(x)>0 indicating de-segregation, resulting in a step function for the high velocities e and c in b and c respectively (Cahn 1962)

(H. Zurob 2003; Maruyama, Smith, and Cerezo 2003). D_{cross} is considered to be twice the bulk diffusion coefficient of solute in austenite (H S Zurob et al. 2002; Subramanian et al. 2013). In case of Nb microalloyed steel, D = 2*[0.000083 exp (-266,500 /R_gT)] m^2/s (Hatem S Zurob et al. 2005). Most of the constants are not well known t0 date due to lack of reliable experimental data. Therefore, some approximated values are taken from the literature. So as to discuss the output of Cahn's model, a constant diffusion profile is selected and based on triangular energy profile (Figure.2.39.a), probable solute concentration is computed for E < 0 ((Figure.2.39.a) and E > 0 (Figure.2.39.b). It is important to notice that for V=0, symmetric profile indicates balanced pulling and pushing at the boundary. From the figures above, the position of boundary as indicated by red line suffers drag force everywhere throughout its length under both the conditions of segregation and de-segregation. It is worth repeating that on the right side of the boundary the concentration change occurs so rapidly that it never imparts solute drag on the boundary (Cahn 1962).

Under the presence of driving force, as the boundary starts to migrate, the concentration profile

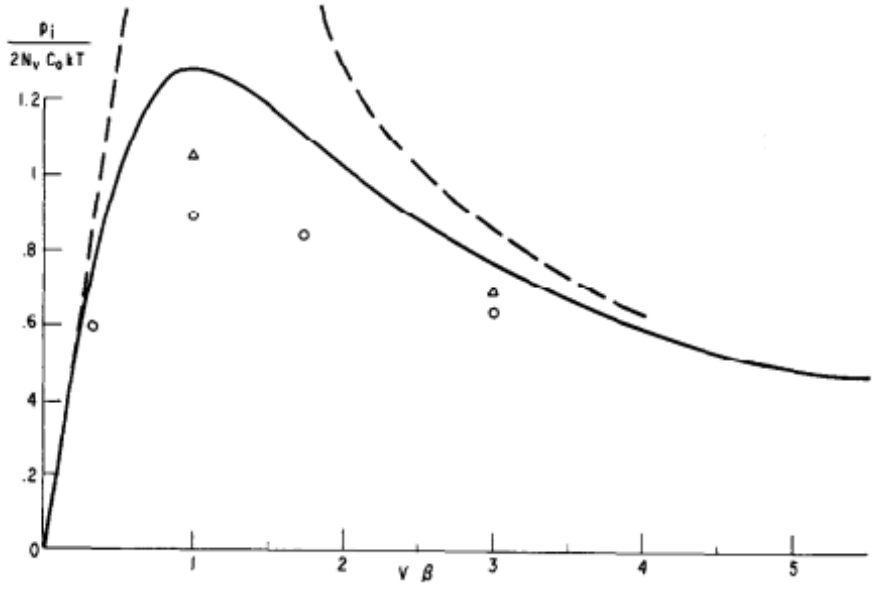

Figure 2.40. Solute drag pressure on the boundary for different velocities. Dotted lines are separately calculated from equations 12 and 15 in Cahn's original work. Circles stand for E<0 and triangles for E>0 case (Cahn 1962)

gradually becomes asymmetric resulting in a drag pressure as shown in Figure 2.40 which is calculated from the complex forms of equations 2.108 and 2.109 given as equation 12 and 15 in Cahn's original work (Cahn 1962). It is clear that solute drag starts to build the moment boundary

migration begins and reaches maxima for specific boundary velocity at an intermediate value and gradually comes down as the boundary moves faster under high driving force. Then the solute atoms can no longer keep up with the moving boundary. It is worth mentioning that for low velocity regime, second term in equation 2.109 is dominant and for high boundary velocity the first term of equation 2.108 is dominant. Finally these two equations combined in CLS model to give expression for solute drag as (Hatherly and Humphreys 2012)

$$P_d = \frac{V}{M} + \frac{\alpha C_0 V}{1+\alpha\alpha' V^2} \qquad \ldots\ldots\ldots\ldots \quad Eq\ 2.111$$

Dependence of solute drag on boundary velocity leads to a new equation of motion for the grain boundary given as:

$$V = M(P - P_d) \qquad \ldots\ldots\ldots\ldots \quad Eq\ 2.112$$

Using above equation, CLS theory emphasized on variation of solute drag with boundary velocity reaching a maximum value at intermediate velocity as shown in Figure 2.41. a. This also indicates

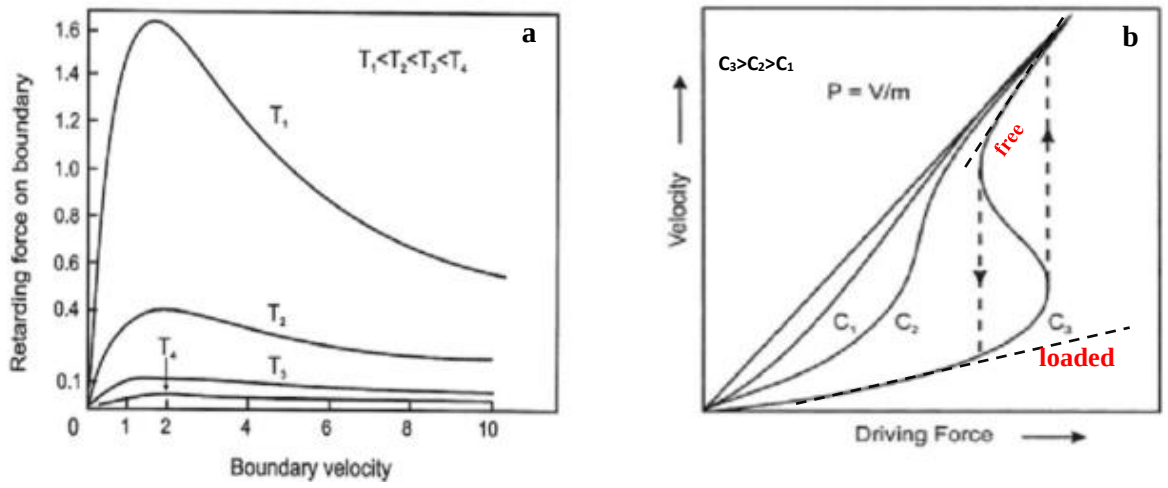

Figure 2.41. a) Variation of solute drag with boundary velocity (V) and Temperature , b) Predicted grain boundary velocity as a function of driving force for different solute concentration where C1<C2<C3 . (Lücke and Stüwe 1971)

that at high temperature solute drag effect is negligible as under these conditions the solute segregation to the grain boundary decreases according to equation 2.106. The effect of solute concentration on boundary velocity was also studied as shown is Figure 2.41. b. For low concentration, the curve is continuous, and there is only a small deviation from the straight line corresponding to a system without any solute. This implies that the solute atoms cannot keep up

with the migrating interface after it breaks away from its impurity atmosphere. For high solute concentrations the curve has two branches and velocity will change discontinuously from one branch (loaded) of the curve to the other (free) and vice versa at some critical driving force as indicated by the dashed line in Figure 2.41. b (Lücke and Stüwe 1971). It is worth-noting that the transition velocity is not same for the two jumps. The relationship between boundary velocity and driving force at intermediate velocities is very difficult to calculate (Hatherly and Humphreys 2012).

The above concept was implemented to model solute drag effect on recrystallization by Zurob et al. (H S Zurob, Dunlop, and Brechet 2006) and Dunlop et al. (Dunlop et al. 2007) by capturing the mobility term in presence of Nb as solute using the following equation:

$$M_{HAGB} = \left(\frac{1}{M_i} + \alpha C_{Nb}\right)^{-1} \qquad \ldots\ldots\ldots\ldots \text{ Eq 2.113}$$

M_i is the intrinsic mobility of the high angle grain boundaries which will be experimentally measured in this research work and will be used to calculate α to determine binding energy of Nb with HAGBs. Cahn's solute drag model will be used to interpret the results obtained in the grain growth studies in current thesis to compare calculated binding energy with the one obtained from atom probe analysis in a non-dilute system. Cahn's approach was claimed to be invalid as a continuum approach by Lücke and Stüwe and the reason for that was the boundary thickness was assumed to be within two atomic distances. An atomistic approach considering the boundary structure in a two-phase scenario was then introduced by Lücke and Stüwe (Lücke and Stüwe 1971).

2.8.2 Hillert's model:

Previous idea of modelling solute drag was in the light of force acting on the boundary by solute elements. Hillert stated that "*the work put into the movement of a boundary in order to overcome the solute drag, must dissipate by the diffusion of the solute taking place as a result of the boundary movement. It should thus be possible to evaluate P as* $\Delta G_m/V_m$ *where* ΔG_m *is the dissipation of free energy due to diffusion when boundary passes through a volume containing one mole of atoms*". His model was applicable to both grain and interphase boundaries. More interestingly Hillert's model boils down to previous CLS (Cahn-Lücke-Stüwe) treatment at low solute content whilst its validity spans over a broad range of solute content for both ideal and regular solutions.

Hillert's treatment was formulated for the case of a binary system made up of solvent ("A") and solute ("B") where the mobilities of both the components are the same. Under this condition, inter-diffusion is favored because of the difference in chemical potentials. Note that in his formulation Hillert used "G" to express chemical potential instead of μ. The mutual diffusion flux can be written as:

$$-J_A = J_B = -\frac{D}{RTV_m} x_A x_B \left(\frac{d(G_B - G_A)}{dy}\right) \qquad \text{…….. Eq 2.114}$$

where, x stands for mole fraction, V_m is the molar volume and the term within bracket is the driving force for interdiffusion. The product of this driving force and flux gives the rate of Gibbs energy (G) dissipation and we can write:

$$\frac{dG}{dt} = -\int_V J_B \cdot \frac{d(G_B - G_A)}{dy} dV \qquad \text{…….. Eq 2.115}$$

Above will be applied to an infinitely long volume element with its cross section 'A' being parallel to the migrating boundary of velocity v. Then free energy dissipation (ΔG_m) for a short interval Δt on passing 1 mole of element by the boundary can be calculated as in equation 2.116:

$$\Delta G_m = \left(\frac{dG}{dt}\right) \cdot \Delta t = -\frac{V_m}{v} \int_{-\infty}^{+\infty} J_B \cdot \frac{d(G_B - G_A)}{dy} dy \qquad \text{…….Eq 2.116}$$

where, $\Delta t = V_m/Av$ and $dV = Ady$. According to the definition of solute drag given by Hillert, ($\Delta G_m/V_m$) is the measure of solute drag. So, three equivalent forms of solute drag equation with flux (J), Gibbs energy (G) and inter-diffusivity (D) can be formulated as :

$$P = -\frac{1}{v} \int_{-\infty}^{\infty} J_B \cdot \frac{d(G_B - G_A)}{dy} \cdot dy \quad (in\ form\ of\ J, G) \qquad \text{…….. Eq 2.117}$$

$$P = \frac{1}{vRTV_m} \int_{-\infty}^{\infty} D x_A x_B \left[\frac{d(G_B - G_A)}{dy}\right]^2 \cdot dy \quad (in\ form\ of\ G, D) \qquad \text{…….. Eq 2.118}$$

$$P = \frac{RTV_m}{v} \int_{-\infty}^{\infty} \frac{J_B^2}{D x_A x_B} \cdot dy \quad (in\ form\ of\ D, J) \qquad \text{…….. Eq 2.119}$$

For stationary state, local concentration is comparable to local flux and we can write

$$\frac{\partial x_B}{\partial t} = -v \frac{\partial x_B}{\partial y} \qquad \text{…….. Eq 2.120}$$

Applying Ficks' second law to interdiffusion of A and B, we obtain:

$$-\frac{\partial x_A}{\partial t} = \frac{\partial x_B}{\partial t} = V_m \frac{\partial J_B}{\partial y} = \frac{\partial x_B}{\partial y} \cdot v \qquad \text{…….. Eq 2.121}$$

Or

$$-\frac{dJ_A}{dx_A} = \frac{dJ_B}{dx_B} = \frac{v}{V_m} \qquad \ldots\ldots\ldots \text{ Eq 2.122}$$

Upon integrating equation 2.122, we obtain:

$$-J_A = J_B = \frac{v}{V_m}(x_B - x_B^0) = -\frac{v}{V_m}(x_A - x_A^0) \qquad \ldots\ldots\ldots \text{ Eq 2.123}$$

Here, x_A^0 and x_B^0 are the equilibrium concentration far away from the boundary. Using above, two more forms of solute drag equation can be expressed as:

$$P = -\int_{-\infty}^{\infty} \frac{(x_B - x_B^0)}{V_m} \cdot \frac{d(G_B - G_A)}{dy} \cdot dy \quad (in\ form\ of\ x, G) \qquad \ldots\ldots\ldots \text{ Eq 2.124}$$

$$P = \frac{RTv}{V_m}\int_{-\infty}^{\infty} \frac{(x_B - x_B^0)^2}{Dx_A x_B} \cdot dy \quad (in\ form\ of\ x, D) \qquad \ldots\ldots\ldots \text{ Eq 2.125}$$

To get some output of drag force, the input should be through some parameter which is known. Therefore, the term containing G_B and G_A in the integrand is chosen and applying Henry's law in dilute solution ($G_B = {}^0G_B(y) + RT\ln x_B$ and $G_A = {}^0G_A(y) + RT\ln x_A$), it can be written for dilute or ideal solution that:

$$\frac{d(G_B - G_A)}{dy} = \frac{d({}^0G_B - {}^0G_A)}{dy} + \frac{RT}{x_A x_B}\frac{dx_B}{dy} \qquad \ldots\ldots\ldots \text{ Eq 2.126}$$

Using above equation in equation 2.124, we can write the final form of the solute drag equation as:

$$P = -\int_{-\infty}^{\infty} \frac{(x_B - x_B^0)}{V_m} \cdot \frac{d(\Delta^0 G)}{dy} \cdot dy \qquad \ldots\ldots\ldots \text{ Eq 2.127}$$

where, $\Delta^0G = ({}^0G_B - {}^0G_A)$ and the second part of equation 2.126 vanishes because of similar composition at upper and lower limit. It is to be noted that in most of the equations governing solute drag (equations 2.118, 2.119, 2.125) the positive sign of the integrand indicates free energy dissipation by diffusion. The flexibility of Hillert's model came through having different forms of the solute drag expression which can be conveniently applied for high velocity (equation 2.118) and low velocity (equation 2.119) case ultimately merging it with the expression obtained from CLS approach in dilute case. Another advantage of this model is its applicability to whole composition range assuming any thermodynamic property model for the binary system.

To discuss the output of the model, it should be mentioned that Hillert's assumption of energy profile was a square-well function (Figure 2.42. a) to give constant properties inside which changes

as one moves outward the boundary. Based on that, different zones of the boundary are shown in Figure 2.42. a. Composition profile of the solute as calculated from equation 2.123 is given in Figure 2.42. b for three different velocities of the boundary in the order of $v_1<v_2<v_3$. It is evident as the velocity increases, center of gravity of the solute profile lags behind the boundary and total amount of segregation at the boundary drops. At the same time, a depletion in solute also takes place in zone 4 at the transition region in the grain which gradually decreases to reach equilibrium with increasing velocity to v_3. In Figure 2.42. c, integrand in the solute drag equation 2.125 is being shown across the boundary. It is important to compare the role of different zones of boundaries with increasing velocity. Drag is centered inside the boundary for low velocity (curve

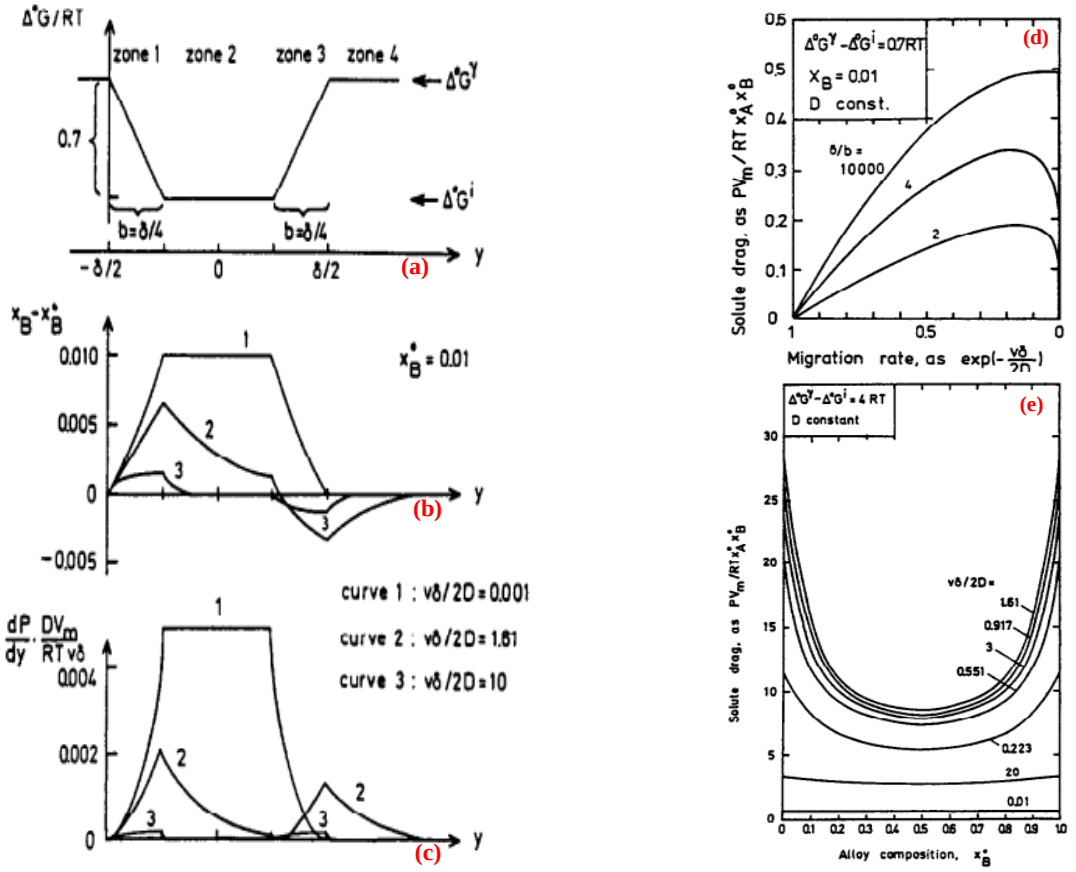

Figure 2.42. Assumed a) energy profile of the boundary with four distinct zones, b) calculated solute profiles for three different velocities, c) integrand from equation 2.125 to calculate solute drag, d) variation of solute drag with migration rate for different zones in the boundary, e) composition dependence of solute drag for different boundary velocities given by the term vδ/2D (Mats Hillert and Sundman 1976)

1, in Figure 2.42. c).With increasing velocities (2, 3), the two sides of the boundary and the spike of solute offer the drag (curve 2, in Figure 2.42. c). At very high velocities, the spikes diminish and only the sides of the boundary impart solute drag. The calculated drag force with increasing boundary velocity indicates (Figure 2.42. d) that the drag increases as the boundary migration gets faster leading to an asymptotic form at some velocities thus creating a contrast in prediction compared to CLS model by the absence of maxima in drag. The variation of solute drag is also calculated for the whole range of solubility indicated by, $\mathbf{PV_m/RTx^0_Ax^0_B}$, resulting in the symmetric type of variation shown in Figure 2.42. e. The drag curve for high and low velocities are based on equations 2.118 and 2.119 respectively whose detailed derivation is given in (Mats Hillert and Sundman 1976). A detailed description of the drag contribution from four distinct zones are also given under segregation and desegregation scenario by Hillert in his model considering constant inter-diffusivity. Even extension of the ideal solution case to a regular solution using an interaction parameter yields symmetric solute drag curves for whole range of binary composition.

Some of most important criticisms of the two popular solute drag models include: applicability of continuum model for 1nm width grain boundary to come up with concentration profiles as shown in Figure 2.39 instead of using an atomistic approach, assumption of flat boundary during migration instead of considering the additional degrees of freedom added from their non-flat nature during movement, ignoring the effect of solutes on intrinsic boundary mobility, etc. (Qiu 2013). Based on the criticisms above, the concept of attachment of the solvent atom to a growing grain and effect of solute to dictate the attachment kinetics was proposed to be the cause of retarding boundary migration by solutes. With more solute content in bulk, lower temperature and higher mobility of the solute atom, there will be more interference with solvent atoms during the attachment process. However, these new ideas still have only got good acceptance only by Molecular Dynamics (MD) simulation studies of solute drag on interphase boundaries, Kinetic Monte Carlo (KMC) on migrating boundaries and Phase Field Crystal (PFC) simulation study of boundary motion.

2.9 Annealing Twins:

In 1926 Carpenter and Tamura proposed annealing twin formation mechanism which was related

closely to the atomic arrangement of the metals and alloys during their growth. Certain specific crystallizing forms (FCC, tetrahedral cubic) of the metals were revealed to be associated with annealing twin formation. Sufficient experimental evidences were given in their original paper on twinning in different crystal systems (Carpenter, H . C . H . , Tamura, S. 1926). This was the foundation for understanding the formation mechanism based on atomic slips on close packed planes. Since then the topic has not been settled as much attention was not paid due to economic reason (it was myth that annealing twins don't control the most common and important mechanical properties like other features as dislocations, precipitates etc.) (Meyers, M.A., McCowan 1984). With the intent of designing future generation functional and structural materials, subsequently a focus was nucleated to investigate the annealing twins in metals and alloys. Different approaches have been formulated with strong experimental and computer simulation data to elucidate/illustrate the mechanism by which the annealing twins are formed. For this review, the discussions will be limited to only face centered cubic (FCC) systems although annealing twins are common in some other crystal structures.

2.9.1 Morphology of Annealing Twins:

Annealing twins are special and interesting features in FCC metals and alloys with low or medium stacking fault energy (SFE). Copper, nickel, lead and their alloys, austenitic stainless steels, high Mn steels (HMS) are the most commonly occurring systems to exhibit annealing twins in their microstructure. Some ceramics (TiO_2), minerals (anorthite) and intermetallics with $L1_2$ structure (Ni_3Al, Zr_3Al, $(Fe, Co, Ni)_3V$) also exhibit parallel sided annealing twins. Most surprisingly, germanium (Ge) and silicon (Si) are the systems which exceptionally show annealing twins unlike other BCC metals.

In FCC metals, they are mostly visible under optical and transmission electron microscopy. The two dimensional (2-D) morphologies revealed are the result of traces formed by the intersection of the twins with sectioning planes. Based on different plane positions, a given annealing twin can give rise to different morphologies. The most commonly encountered morphologies, either or combination of 4 types, are given in Figure 2.43. a. Annealing twins in FCC systems usually

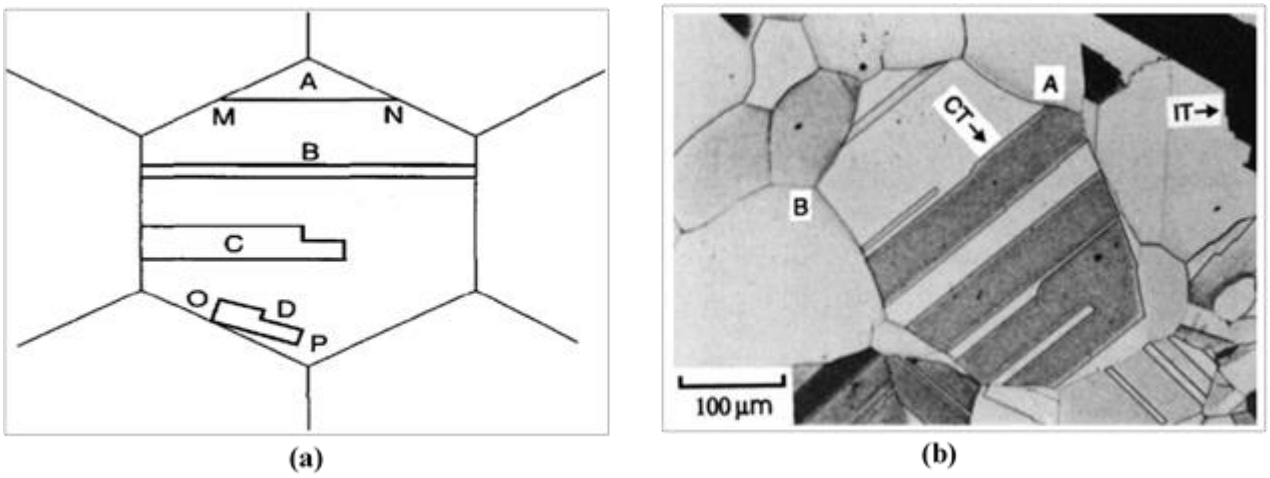

Figure 2.43. a) Most common two dimensional morphologies of annealing twins observed in FCC systems (Mahajan 1997) b) Microstructure of 70:30 Brass annealed showing annealing twins (Yuan Jin 2014)

present as lamellae bounded by {111} planes named as coherent twin boundaries (CT) and at their two ends are steps terminated by incoherent twin boundaries (IT). The 4 common types are i) one sided or corner twin (A) having MN as coherent boundary, ii) complete parallel-sided twin (B) which traverse whole grain, iii) incomplete parallel-sided twin (C) which ends inside the grain and iv) central twin (D) which is completely embedded inside grain.

Apart from that, for family of octahedral (111) planes, a single grain is capable to have four variants of twins in it. It is important to highlight that real morphologies of twins in 3-D can only be revealed by the reconstruction of microstructures from serially sectioned planes (Meyers, M.A., McCowan, 1986, Jin 2015). In addition to above 4 morphologies, another form known as atypical

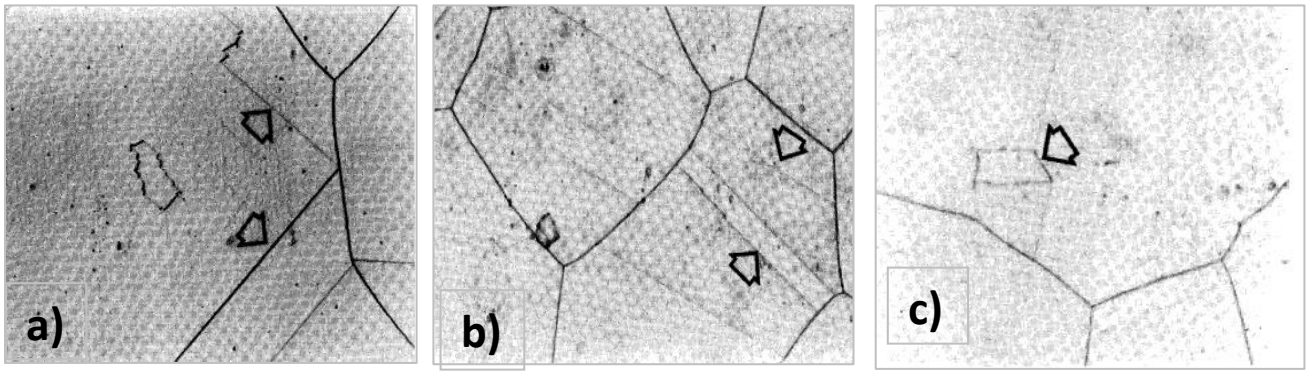

Figure 2.44. Atypical twins (Meyers, M.A., McCowan 1984)

twins is also revealed. These can have two coherent boundaries forming a “quadruple” point at a general high angle grain boundary (HAGB) (Figure 2.44. a) or a parallel twin inside a broader one at approximately 13° (Figure 2.44. b) and a grain interior twin offsetting a one-sided twin (Figure 2.44. c). The mechanism behind the formation of these three types of atypical twins is still not clear (Meyers, M.A., McCowan 1984).

2.9.2 Crystallography of Annealing Twins:

The annealing twinning occurs in the FCC matrix on a particular plane where the stacking sequence changes to form a mirror symmetry (ABCABC …. to ABCA**B**ACBACBA.. if B is the twin plane). This particular plane or the mirror plane is the coherent twin boundary which is a

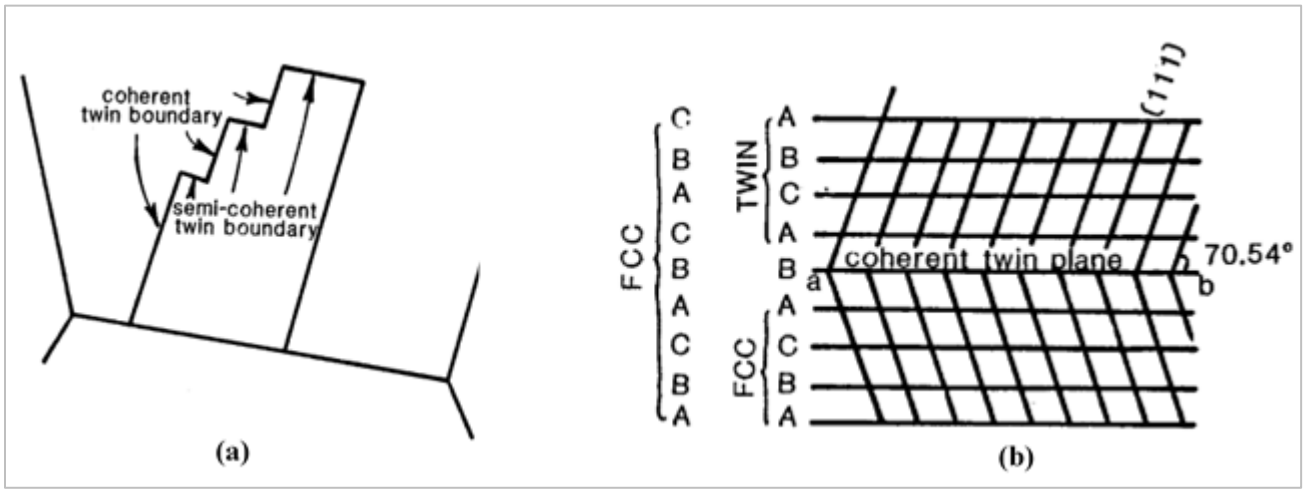

Figure 2.45. Different parts of annealing twin boundaries, b) Atomic stacking structure of a coherent twin boundary (Meyers, M.A., McCowan 1984)

symmetric (111) boundary. The coherent twin boundary and the family of (111) plane in two grains make an angle of 70.54°(Figure 2.45. b).

At the coherent boundary plane, the stacking takes the form A**B**A which resembles a three layer structure having hexagonal close packed structure (HCP). Therefore, the free energy difference between this three-layer HCP structure formed and parent FCC matrix can be considered as the interfacial energy of coherent boundary which is roughly half the stacking fault energy (SFE) of the material. Experimental measurements of the dihedral angle between the coherent twin and grain boundaries on a section were obtained. These values were corrected for different sectioning planes using the width of boundary plane projections. Another way of describing the orientation

relationship of twinned region with parent matrix is 60° rotation about <111> axis, where the plane perpendicular to rotation axis is the coherent twin boundary plane. In CSL terminology, coherent boundaries are designated as ∑3 boundaries indicating one in every 3 atoms has a coincidence point giving rise to good matching of atoms at the boundary plane. This leads to low energy and low mobility of these coherent twin boundaries (Valerie Randle 2004).

For an incomplete twin, the coherent boundary ends at incoherent or semi coherent twin boundaries which also seem to have specific orientations according to different researchers. The formation of these boundaries can be described in the light of two models. According to Oblak and Kear, the incoherent boundary was pictured as an array of dislocations (Frank partials) which create a twin configuration as shown in Figure 2.46. a. Another model by Meyers and Murr proposed the incoherent boundaries to be made up of Shockley partials which are oriented perpendicularly (Figure 2.46. b) if compared to the dislocations in previous model. The arrangement is such that the matrix stacking sequence is changed at the mirror plane (C, with no dislocation) to twin sequence. For both the cases, the total Burgers vector will be zero to ensure no strain associated with an annealing twin. This model deals with dislocation dipoles in the array making an angle of 45° with each other or with other dipoles to minimize strain energy. Also the dislocations in Meyers' model are glissile making the incoherent boundary mobile unlike coherent ones. From CSL point of view, these boundaries are ∑3 boundaries with {112} planes. Although, these ∑3s have higher free volume and energy compared to the coherent ones, these are still lower than the average free volume associated with HAGBs (Valerie Randle 2004).

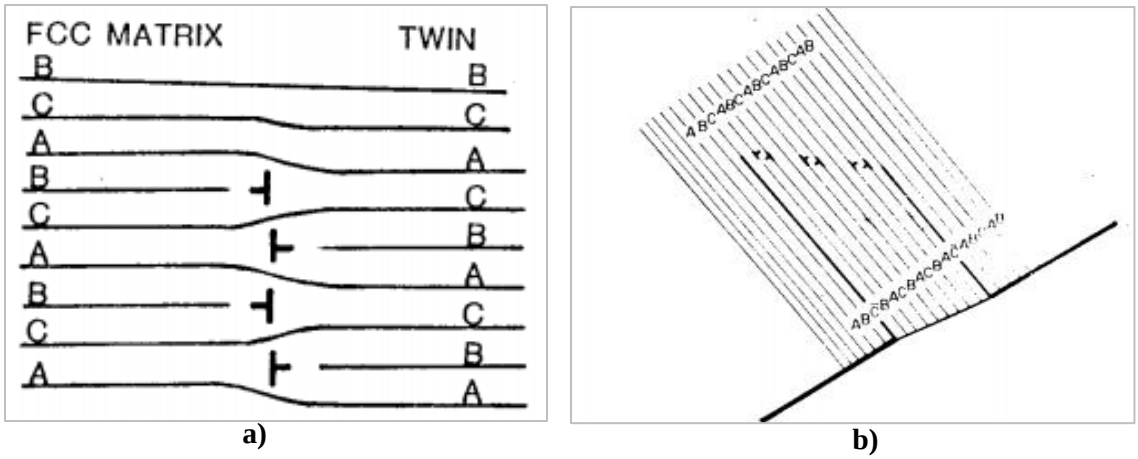

Figure 2.46. Models for the formation of Incoherent twin boundaries after a) Oblak and Kear, b) Meyers and Murr.(Meyers, M.A., McCowan 1984; Meyers and Murr 1978)

2.9.3 Theories of Annealing twin Formation:

Based on an organized body of work dedicated to explore the underlying mechanism of annealing twin formation, it can be said that there mainly exist four distinct schools-of thought which individually encompasses several similar approaches. A few of them only, till date, allow theoretical predictions of twin density supported by experimental validation (Meyers, M.A., McCowan 1984) (Table 2.5).

Table 2.5. Models proposing annealing twin formation categorized into 4 distinct groups

Growth Accident Model	Carpenter and Tamura (1926), Burke (1950), Fullman and Fisher (1951), Gleiter (1969), Pande (1996), Mahajan (1997)
Grain Encounter	Burgers (1946,1949), Nielsen (1967), Kurzydlowski (1991)
Stacking Fault Packets at Migrating Grain Boundaries	Dash and Brown (1963)
Grain Boundary Dissociation	Meyers and Murr (1978) , Goodhew (1979), Kopezky (1983)

2.9.3.1 Growth Accident Model:

Carpenter and Tamura were the first to build the foundation of the growth accident concept behind annealing twin formation. They proposed that during grain growth, a wrong atomic slip followed by rearrangement of the following atoms on the closest packed plane can minimize the energy of the system by forming annealing twins. This concept was further developed by Burke when he observed in alpha brass the twins appear, one boundary at a time, at the grain corners during their growth. Next modification in the growth accident model was done by Fullman and Fisher in the light of thermodynamic free energy minimization. (Fullman and Fisher 1951). An annealing twin formation will only be favored if the following condition is satisfied:

$$A_{A'B}\,\gamma_{A'B} + A_{A'C}\,\gamma_{A'C} + A_t\,\gamma_t < A_{A'B}\,\gamma_{AB} + A_{A'C}\,\gamma_{AC} \quad \text{..... } Eq\ 2.128$$

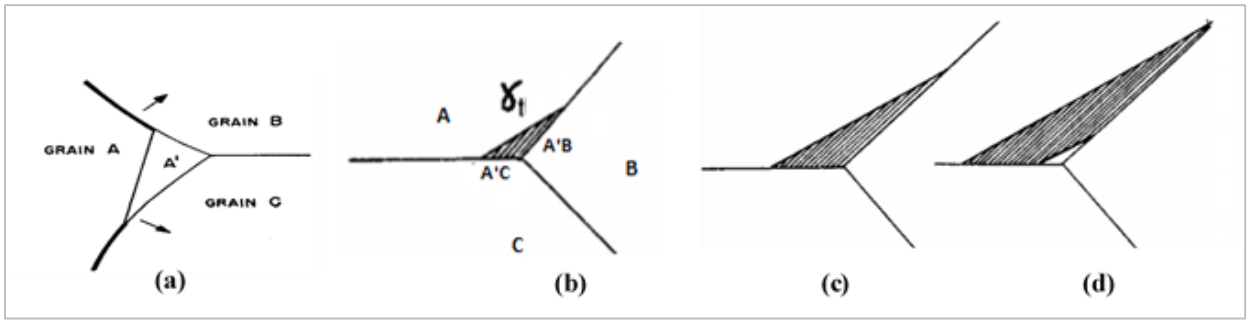

Figure 2.47. a), b) Preferential twin formation based on thermodynamic free energy minimization, c) sequential growth of the annealing twin with grain boundaries moving from left to right, d) Second growth accident forming another coherent twin boundary to make the twin complete-parallel sided (Fullman and Fisher 1951; Meyers, M.A., McCowan 1984)

A and γ represent the area and the interfacial free energy, respectively, *t* subscript stands for coherent twin boundary. In reference with Figure 2.47. a, the bold lines indicate HAGB with higher interfacial energy which are not yet modified by twinning. According to above relationship, A/A' interface (Coherent twin boundary) formation will be favored if the twin modified HAGB segments A'/B and A'/C are energetically less than the original pure HAGB segment A/B and A/C. Due to migration of HAGBs, annealing twins first form as a single sided corner one (Figure 2.47. a, b) maintaining the energy minimization criterion. The twin keeps growing as the HAGBs move and by another independent growth accident the other coherent boundary of the twin forms (Figure 2.47. c, d). Although, common FCC microstructures contain not only corner twins, but also other types of twins, above model aptly explains the corner twin formation mechanism which is prevalent in aluminium (Meyers, M.A., McCowan 1984).

Gleiter further advanced the model in the light of ledge formation by atomic movement during grain boundary migration (Gleiter 1969a). This was backed by TEM observations which showed in FCC systems the grain boundary planes are made up of steps of {111} planes. It was found that close to melting point ($0.9T_m$) these steps may disappear. As new atoms join the step, the grain boundary moves forward resulting in a growing grain. The mechanism which helps to form new {111} planes in growing grain which are parallel to the {111} steps influence the formation of annealing twins. TEM observation shows the new {111} planes of the growing grain may form by either growth spirals or 2-D nucleation on the close packed plane of the growing grain. However,

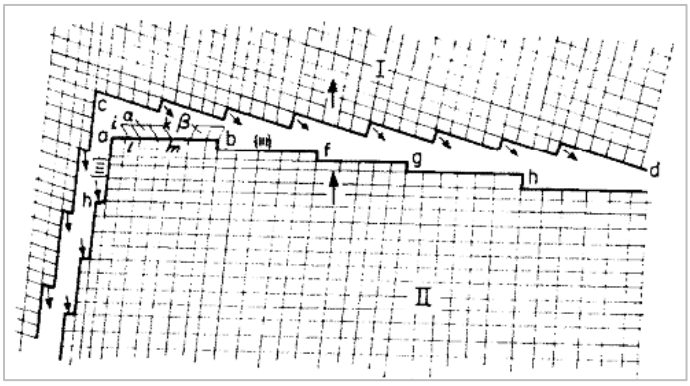

Figure 2.48.Model showing two dimensional nucleation of annealing twins on close packed plane (ab) of grain boundaries moving from II to I (Gleiter 1969a)

based on TEM observations, the spiral mechanism was proved to be less feasible than the second one. In two dimensional nucleation model (Figure 2.48), annealing twins are formed at the boundary between a growing grain (grain II) and a shrinking grain (grain I) due to faulted stacking of atoms that prefer to leave grain I to join the growing grain (II). This atomic migration is considered to be a curvature driven process. After reaching the close packed planes (ab, bf, fg, etc.) of the growing grain (Figure 2.48), atoms can give rise to change in stacking sequence. If the ab plane is considered to be a B layer and the underlying plane assumed to be A, then atoms joining grain II can take atom positions pertaining to A or C. If the atoms take the C position, then normal ABC sequence is continued and normal FCC matrix keeps growing. On the other hand, if the atoms position on A stacking, an ABA layer is formed which leads to a twin formation only if the subsequent atomic stacking follows normal 3 layer FCC stacking sequence. This gives finally the form ABC ABA CBA.. and the annealing twin nucleation becomes successful. So, the atomic stacking while deviating from normal FCC sequence to a wrong sequence of ABA, the first layer of twin forms. The twin gradually grows as the faulty stacking nucleus becomes bigger due to atoms joining the edges. The probability of finding a {111} plane to be nucleation site for coherent twin boundary was given by Gleiter as

$$p = exp\{\frac{-\frac{Q}{kT}+ln(\Delta G/kT}{(\frac{\pi\varepsilon^2h^2}{Q\gamma_{tb}}-1)}\} \qquad \ldots\ldots\ldots \text{Eq 2.129}$$

where, T is the temperature in Kelvin, Q is the activation energy for grain boundary migration, ΔG is the critical free energy for the fault twin nucleus to form on {111} plane facets, ε is the energy of the steps at the boundary , h is the height of the twin nucleus and γ_{tb} is the coherent twin

boundary energy. The above equation can be used to calculate twin density and dependence on temperature within certain range and grain size (considering $\Delta G=\beta/D$, β is constant for the material).

The next generation model of twin formation was after Pande et al. where twin density prediction during grain growth was formulated (Pande, Imam, and Rath 1990). The semiempirical model assumed that twin nucleation and growth occurs due to HAGB migration and grain size determines the twin density. If a grain of initial size D and twin density (No. of twins/grain) N_G increases to D+ΔD and $N_G + \Delta N_G$, then $\Delta N_G \propto \Delta D^*$ F. F is the driving force expressed as F= γ_g /D, where γ_g is the HAGB energy. Considering, $N_G = N_L * D$, where N_L is the no. of twin intersections per unit of length traversed, the final form of Pande's model took a form as follows:

$$N_L = \frac{1}{D} K \gamma_g ln \frac{D}{D_0} \qquad \ldots\ldots\ldots \text{Eq 2.130}$$

where D_0 is the critical grain size below which no twinning is feasible, *K* is a constant. The model got validated with several experimental data from different FCC alloy systems

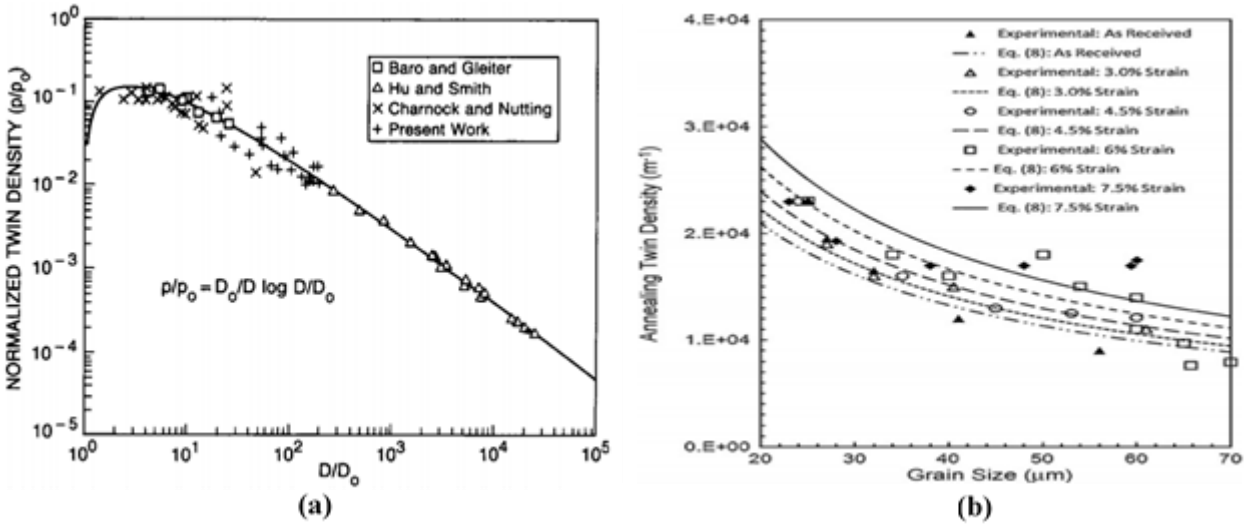

Figure 2.49. a) Grain size dependence of annealing twin density (Pande, Imam, and Rath 1990), b) Annealing twin density calculated from equation 2.130 and plotted against grain size (Cahoon, Li, and Richards 2009)

(Figure 2.49. a) where a normalized grain size was taken.

Later on this model was improved by Cahoon *et. al.* by incorporating stored energy into driving force to strain induced boundary migration (SIBM). Then the twin density can be predicted as:

$$N_L = \frac{C}{\gamma}\left(\frac{4\gamma_{gb}}{D}(1 + As^2)\right) ln\frac{D}{D_0} \qquad \ldots\ldots\ldots\ldots \text{ Eq 2.131}$$

In this equation, C is a dimensionless constant, γ is the stacking fault energy, *s* is the plastic strain introduced through cold working, A is dimensionless material constant with a value ≈ 70. The value of s^2 is equated to $Ee^2/2$, where *e* is the residual elastic strain energy and E is the elastic modulus. The model got a good agreement with experimental data obtained (Figure 2.49. b) on SIBM (Cahoon, Li, and Richards 2009).

An atomistic approach was made next by Mahajan et al. to illustrate annealing twin formation. The model assumed that formation of annealing twins on migrating boundaries which have {111} steps takes place during curvature driven grain growth. In Figure 2.50. a, the HAGB segment PQRS can move to the right only if the step MNRQ moves up (in a direction parallel to (111) step) and generates new {111} planes via Shockley partial loops below each step. Thus the coherent twin boundary formed moved to the left (fig b) (Mahajan et al. 1997) .

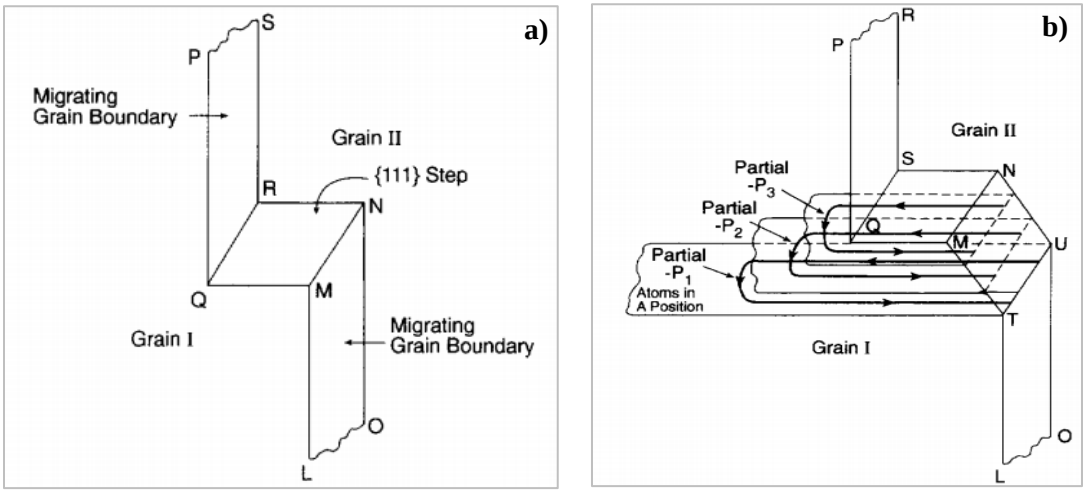

Figure 2.50. Atomistic model of annealing twin formation through formation of Shockley partials (Mahajan et al. 1997)

Most recently, a huge amount of *in-situ* EBSD work by Jin et al. was able to capture annealing twin formation mechanism in 99.995% pure Nickel. They observed that during recrystallization twin density increases while during grain growth it comes down. The factors responsible were migration velocity, boundary curvature (Y. Jin et al. 2014) and tortuosity (B. Lin 2015). In their atomistic model, it was shown (Figure 2.51) that for the convex boundaries moving away from the

center, it is feasible to nucleate a coherent twin boundary. In case of concave boundaries moving towards their centers will give rise to Shockley partials (marked by red 'x' in fig d) to form twins. This is an energetically unfavourable situation which is prevalent during grain growth to have decrease in twin density (Y. Jin et al. 2014).

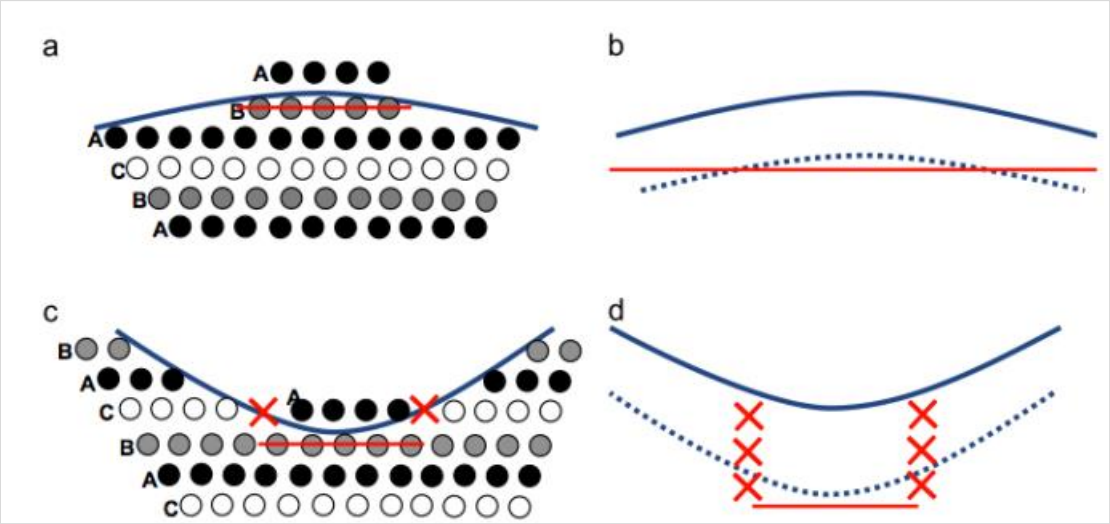

Figure 2.51. Effect of boundary curvature on the formation of annealing twins according to growth accident theory occurring at site A (instead of C) on a {111} facet in case of a) Convex boundary, c) concave boundary with the ABC stacking sequence in the growing crystal, twin formation (thick read line) behind the migrating b) convex , d) concave interface. Red crosses indicate the Shockley partials inevitable for ITB formation to facilitate twin nucleation only at concave interfaces (Y. Jin et al. 2014)

2.9.3.2 Grain Encounter Model

This model was proposed based on the fact that in a population, any two grains distantly spaced can have twin orientation (hatched grains in Figure 2.52). Upon grain growth, the boundaries migrate through grains in between them and eventually face each other forming a single coherent twin boundary. This leads to energy minimization of the whole system. The probability of occurrence of such a preferential phenomenon was calculated by Nielsen himself and a value of once in every 16,000 grain interaction was found (1/16,000).This is very realistic in the case of heavily cold worked and annealed systems where billions of encounters occur per cubic millimeter

to produce recrystallized microstructures (Nielsen 1967).

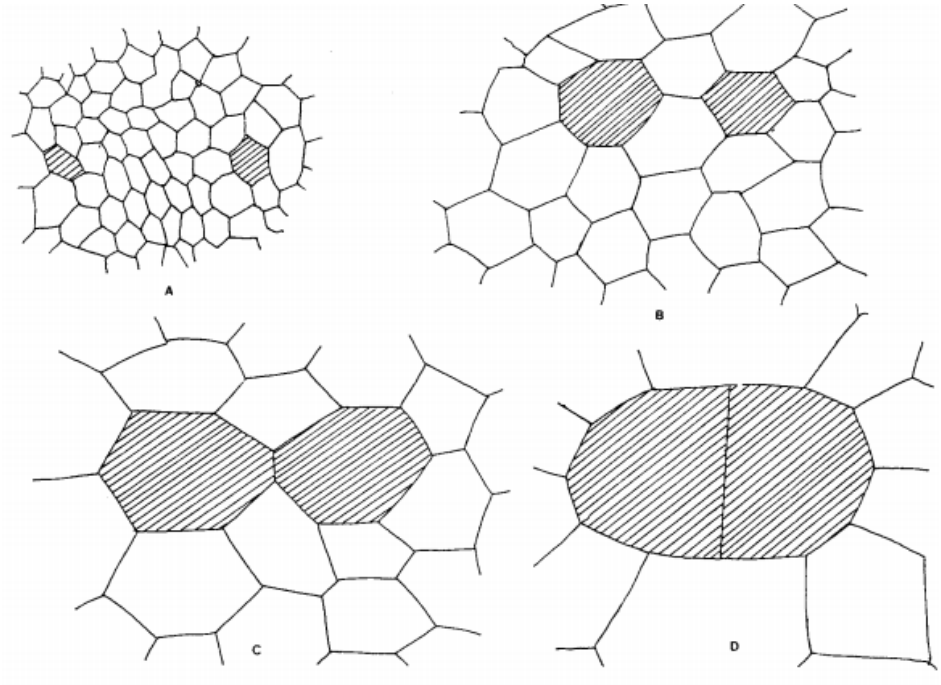

Figure 2.52. Formation of Annealing twins by grain encounter mechanism (Meyers, M.A., McCowan 1984)

2.9.3.3 Stacking Fault Packets at Migrating Grain Boundaries:

Abundance of annealing twins in low stacking fault energy (SFE) FCC systems was well known to be connected with grain boundary migration during post deformation recrystallization. Following the category of interface controlled process, annealing twins form by comparatively less complex mechanism unlike other diffusionless transformations (e.g., martensitic transformation, deformation twinning). Post cold work annealing leads to the movement of HAGBs under the driving force of stored energy from lower to higher dislocation density of the matrix according to Bailey-Hirsch criterion (Hatherly and Humphreys 2012) . During this migration, annealing twins were seen to be nucleated and growing on the dislocation free side of the HAGBs (Figure 2.53. a). In 1963, Dash and Brown, made an outstanding study on partially recrystallized 78%Ni-Fe alloy using thin foil transmission electron microscopy (TEM) technique (Dash, S., Brown 1963). Their study uncovers the nucleation as well as growth of annealing twins in the light of stacking fault formation and their glide into the strain free side of the migrating HAGBs.

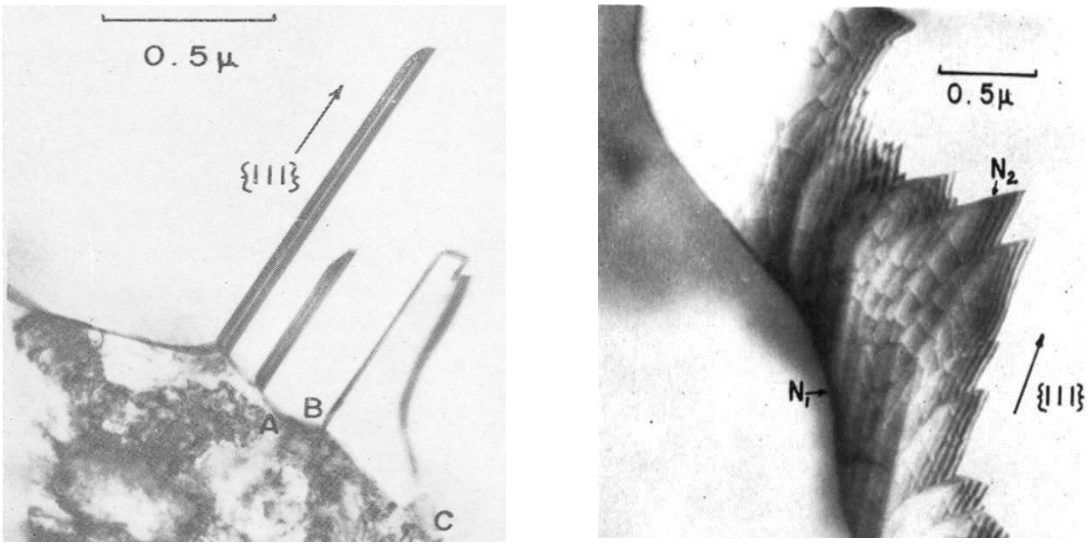

Figure 2.53. a) Nucleation of annealing twins in low strain energy matrix behind migrating HAGBs, b) TEM observation of stacking fault packets formed in layers (Dash, S., Brown 1963)

Although the favourable dislocation configuration at the migrating HAGBs that results in formation of stacking faults was not possible to be identified, different morphologies of stacking faults from simple layered to complex arrayed appearance were seen under TEM of the thin foils. These single stacking fault or faults in a form of thin packets act as nuclei. After this, the annealing twins grow by different mechanisms: a) lengthening of the twins as the HAGB keeps migrating to left (Figure 2.54.b), b) non-coherent twin boundary moving towards right (Figure 2.54. c) and c) thickening of the twins as packets of stacking faults join next to each other in a direction normal to the {111} twinning planes (Figure 2.53. b, Figure 2.54. b, d). During the HAGB migration to highly deformed matrix, a new stacking fault or a group of them nucleates by glide process from the HAGB once it emits a partial dislocation from it. These contiguous stacking faults, also known as micro-twins, are the twin thickening units. This way only non-coherent twin boundary area is increased (N_2 in Figure 2.53. b) which was shown to be balanced by a partial dislocation through replacing the HAGB segment by low energy N_1 (Dash, S., Brown 1963).

The whole nucleation and growth process is assumed to be thermodynamically favored by the lowering of the energy of the parent HAGB by lowering the curvature of the twinned segment on it. Their calculation showed that, under equilibrium conditions, $E_{BC} = 0.93E_{AB}$, where E is the HAGB energy. The nucleation criterion is given as $2/\pi(E_{BC}-E_{AB})+E_n < 0$ restricted to $n \neq 1$, *n* being the no. of stacking faults. The partial dislocations interact with the faults to mainly lower the non-coherent boundary energy. The calculation also showed that during the edgewise growth of the

annealing twins, HAGB energy term dominates over the absolute twin boundary energy which ultimately makes the net energy decrease per unit movement of the annealing twins to be the driving force for twin growth (Dash, S., Brown 1963).

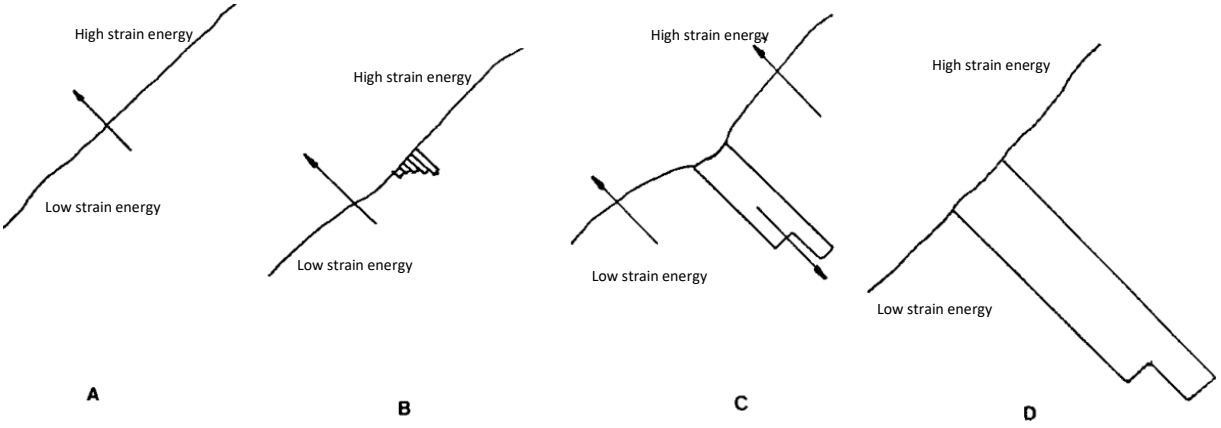

Figure 2.54. Schematic of twin nucleation and growth process behind a migrating HAGB during recrystallization (Meyers, M.A., McCowan 1984)

Dash & Brown model ultimately nullified the connection of pole mechanism to annealing twin formation as partial dislocation of non-identical Burger vectors are favored to ensure zero strain at the twin-matrix interface and lowest possible non-coherent boundary energy. Later on, High Voltage Electron Microscopy (HVEM) studies also revealed annealing twin formation due to moving HAGBs during recrystallization according to Dash & Brown model. In a 96% cold rolled specimen of high purity nickel, annealing twin formation was observed under a 500KV electron microscope with a heating stage. This in-situ recrystallization study is another strong evidence of formation of annealing twins behind migrating HAGBs during recrystallization (Meyers, M.A., McCowan 1984).

2.9.3.4 Grain Boundary Dissociation:

Compared to all other existing theories, this model doesn't require HAGB migration as one of the criteria for annealing twin nucleation in the FCC systems. The 'popping-out' of annealing twins from the HAGB was first proposed by Meyers and Murr (Meyers and Murr 1978). Later in a gold bicrystal experiments using TEM, grain boundaries of certain misorientation (specific coincidence sites) were observed to dissociate to give rise to annealing twins (Goodhew 1979). Meyers's model has two distinctive stages viz, initiation and propagation.

During the initiation, nucleation of annealing twins may take place under two different scenarios. If there exists a twin orientation between two grains, the grain boundary separating them is a high energy or High Angle Grain Boundary (HAGB) due to its random angle of inclination (Meyers and Murr 1978). To attain equilibrium this HAGB prefers to rotate to a new position equivalent to

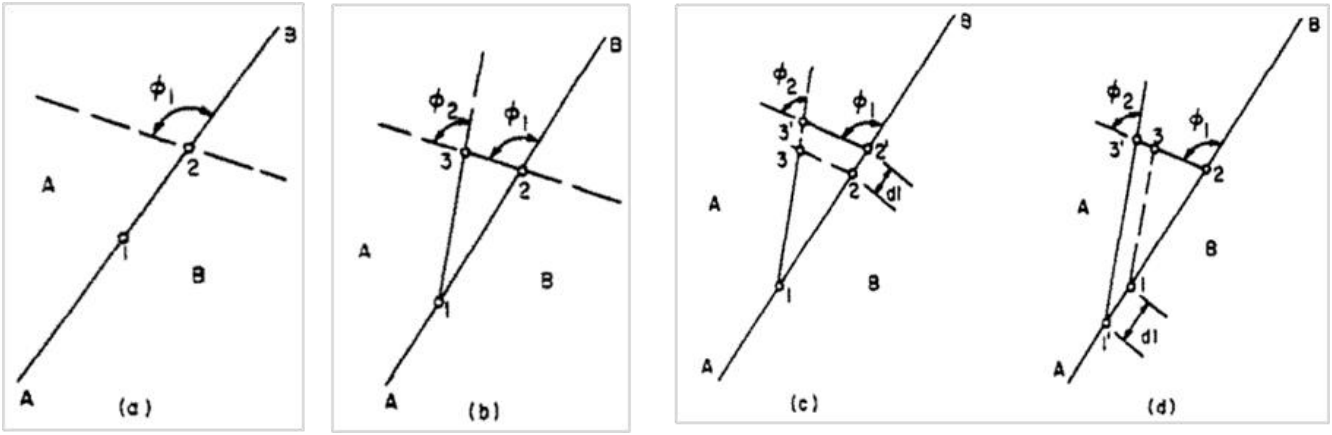

Figure 2.55. Schematic of Twin nucleation and growth process between two grains of twin orientations. a) HAGB segment before initiation stage, b) Dissociation of HAGB into coherent and non-coherent segments, growth of twin nucleus by dislocation movement from original HAGB to the nascent c)non-coherent twin boundary, d) at the edge l of the twin. (Meyers and Murr 1978)

that of a coherent twin boundary (CTB) for convenient inclination. This results into splitting of the boundary $\overline{12}$ into a non-coherent segment $\overline{13}$ and coherent segment $\overline{23}$ (Figure 2.55. b) following the thermodynamic criterion of, $(\gamma_{ntb}A_{ntb} + \gamma_{ctb}A_{ctb}) < \gamma_{gb}A_{gb}$,where γ_{ntb}, γ_{ctb}, γ_{gb} stand for energy of non-coherent, coherent and HAGB, and A stands for area. For small twin nuclei, above criterion is easy to achieve as also energy of the coherent segment is very low. This segment $\overline{13}$ is assumed to be created by movement of dA amount of area by $\overline{23}$ distance by either dislocation or vacancy migration and notably no HAGB migration is required. So, to summarise, the partial dislocations emanating and gliding out from the HAGB and lead to the formation of the twin nuclei- even during recovery. It is worth to mention during this initiation stage, the twin boundaries created don't achieve the ideal coincidence configuration. During growth, rotation of non-coherent boundaries to exact coincidence configuration takes place. Once the nucleus is formed, partial dislocation transport from the existing HAGB to the newly formed twin boundaries results into twin thickening (Figure 2.55. c, d).

Another scenario is when the two neighbouring grains are at random orientation but prefers to have the HAGB between them to be replaced by a special boundary. This leads to decomposition of the original HAGB into coherent, non-coherent boundaries and a special boundary segment substituting the original one. The driving force for this is obviously energy minimization through replacing the high energy segment by special boundary with low energy.

A better understanding of the propagation of twins was done using three dimensional depiction of microstructure. It is seen that the twin traverses the AB boundary completely with 123 and

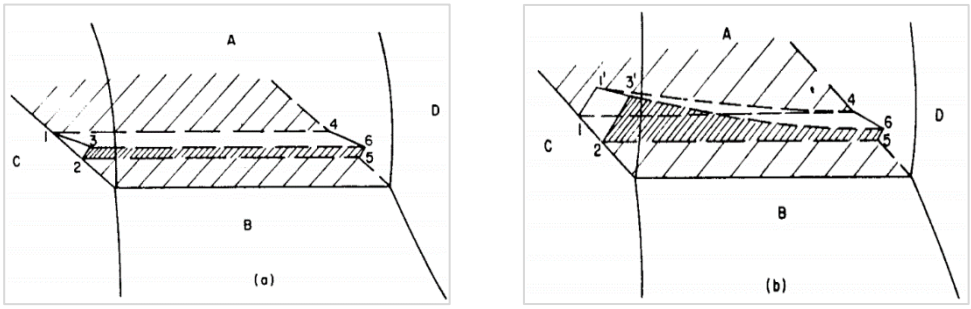

Figure 2.56. a) Three dimensional representation of small triangular twin nucleus appearing as ledge type of structure in HAGB plane, b) Emergence of the parallel sided twin partially grown from HAGB (Meyers and Murr 1978)

456 faces in contact with grain C and D respectively (Figure 2.56. a). Here, 1463 and 2365 planes represent coherent and non-coherent twin boundaries in the trace. A part of AB plane, gets substituted by low energy special boundary 1254. The movement of 1463 helps to propagate the twin into the grain away from HAGB. Overall reduction of interfacial energy acts as the driving force for the propagation. To attain this, non-coherent boundary plane (1'3'64) rotates from its nucleation inclination to meet the nearest 'special boundary' configuration. The net energy reduction ensure formation of the low energy coherent boundary planes 11'4 and 23'65 (Figure 2.56. b).

Goodhew observed dissociation of grain boundaries to be favourable when the misorientations lie within 2° of coincidence or special configurations. In a series of gold bicrystal, the boundaries which are close to ∑9, ∑11 and ∑99 (∑ is the reciprocal density of coincident sites throughout the lattice) orientations, the reactions observed are listed below as:

$$\sum 9 \rightarrow \sum 3 \; - \; \sum 3 \qquad \text{…….. Eq 2.132}$$

$$39.0° \rightarrow 109.5° - 70.5°$$

$$\sum 11 \rightarrow \sum 3 - \sum 33 \qquad \text{…….. } Eq\ 2.133$$

$$50.5° \rightarrow 70.5° - 20.0°$$

$$\sum 99 \rightarrow \sum 3 + \sum 33 \qquad \text{…….. } Eq\ 2.134$$

$$50.5° \rightarrow 70.5° - 20.0°$$

However, the first reaction is the most energetically favourable and is seen to be predominant as it leads to coherent and non-coherent ∑3 both of low energy. Exception prevails for reaction 2 where ∑33 (20° [110]) boundaries are formed being a lower energy one compared to ∑11. Dissociation of ∑99 was seen to have a frequency less than 60% (Goodhew 1979).

2.9.3.5 Other Mechanisms of Annealing twin formation:

Some other notable observations were done primarily on recrystallization twin formation. In α-brass, three annealing twins were observed at 2000x magnification within a small recrystallized grains. Similarly annealing twins were found to form during recrystallization in nickel and partially recrystallized copper. In heavily deformed bronze, annealing twins influence the change in texture during recrystallization by forming second generation twins (Meyers, M.A., McCowan 1984).

In a modified growth accident model, it was proposed that twins nucleate where a (111) plane becomes tangent to the boundary surface. This results in energy minimization by setting the coherent boundary length zero (b). As the coherent boundary of low energy advances, as shown in Figure 2.57 (c) and (d), its length increases. To compensate, another coherent boundary is formed by a second fault accident (Figure 2.57.e). The migrating HAGB will exert tension (indicated by arrow in Figure 2.57.f) on the coherent twin boundary resulting into detachment of the twin from the HAGB. The complete detachment (Figure 2.57.g) results in freeing of the HAGB which keeps migrating during recrystallization. As the tangency criterion is not met any more due to change in curvature of the HAGB, an additional set of twin lamellae will not nucleate anymore (Meyers, M.A., McCowan 1984). However, non-parallel twins may form if the contact angle ‘α’ (Figure 2.57. c) exceeds 70.54°.

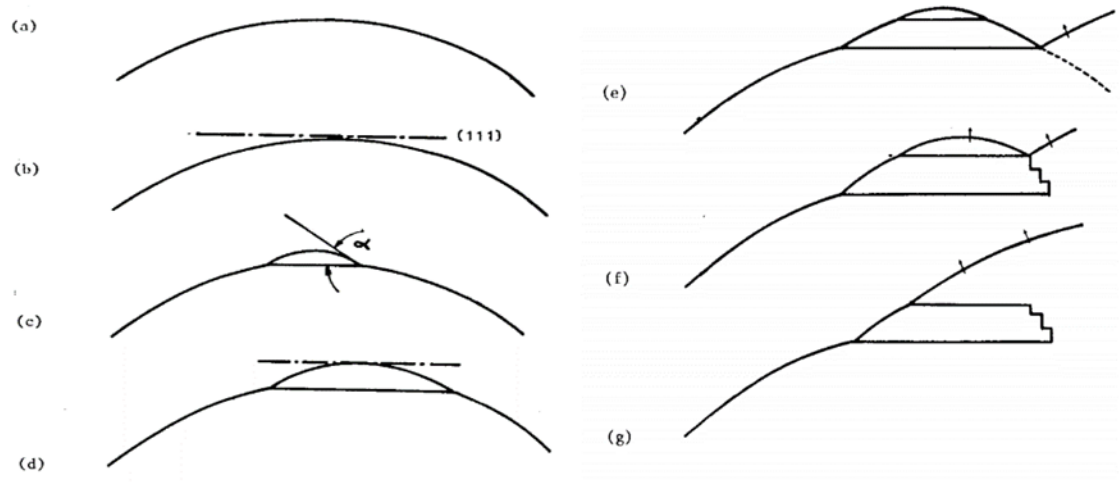

Figure 2.57. Formation of annealing twin based on tangency criterion between migrating HAGB and (111) according to modified growth accident model (Meyers, M.A., McCowan 1984)

2.9.4 Annealing Twin Quantification:

Among various techniques used by different researchers, 4 distinct methods to quantify annealing twins in a microstructure are most well-known. They are listed below as:

i) **Twins per grain (N_G):** The number of annealing twin boundaries per grain is measured on a polished cross section. This method, somewhat represents, twin content in each grain by illustrating twinning frequency of individual grains. Electron back scattered diffraction (EBSD) maps are used to determine N_G using the following formula:

$$N_G = \frac{N_2 - N_1}{N_1}$$

where, N_1 and N_2 are the number of grains without and including annealing twin boundaries ($\sum 3$) respectively. This method of quantification is strongly dependent on individual grain size. So, its application is limited to microstructures with individual grains of similar size and N_G can only be compared between microstructures of very close average grain sizes (Yuan Jin 2014).

ii) **Twins per area:** The number of annealing twins per unit area of the cross section is considered here.

iii) **Twin Density (N_L):** This is defined as the number of twin boundary intercepts per unit

length of a line. This, being independent of grain size, gives an absolute measurement of twin content and frequently used during microstructure evolution to measure twin density. N_L can also be measured from EBSD maps using the following formula:

$$N_L = \frac{L_{TB}}{S_{rex.g}} \times \frac{2}{\pi}$$

where, L_{TB} is the length of the twin boundary and $S_{rex.g}$ is the area of the corresponding recrystallized grain (Yuan Jin 2014; B. Lin 2015).

iv) **Twin Boundary Fraction:** This is given by two different ways of quantification, twin fraction by length (f_L) and by number (f_N). They are expressed as:

$$f_L = \frac{L_{TB}}{L_{HAGB}}$$

$$f_N = \frac{N_{TB}}{N_{HAGB}}$$

where, L_{TB} and L_{HAGB} stand for total length of all twin boundaries (TB) and all high angle grain boundaries (HAGB) and similary N_{TB} and N_{HAGB} indicate number of TBs and HAGBs respectively.

None of the above is an actual indictor of twin content, rather they indicate relative proportions in the global boundary network. Therefore, f_L and f_N are predominantly used

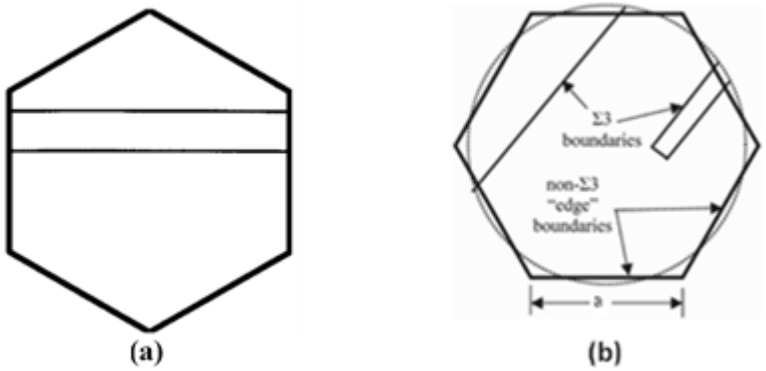

Figure 2.58. a) Schematic illustration of a complete parallel sided twin within a 2-D hexagonal grain touching two HAGBs at two ends (Valerie Randle 2002), b) Representation of a 2D regular hexagonal grain with its equivalent circle of radius 'r' (Schuh, Kumar, and King 2005)

To classify materials in terms of their grain boundary network related properties (Yuan Jin 2014; B. Lin 2015). It has been found by some researchers (M Kumar, Schwartz, and King 1999; V Randle, Rios, and Hu 2008) that the length fraction is higher than number fraction. This ensures that the interface length covered by the low energy annealing twins is longer than that by the normal HAGBs resulting in energy minimization. The relation between f_L and f_N was first calculated by Randle in PE16, a nickel-based superalloy system (Valerie Randle 2002). It was shown for a complete parallel sided twin (2 twin boundaries) in a hexagonal grain with 'a' as each side length, from Figure 2.58. a, length of each twin boundary can be calculated as 2 cos30°a =1.732a.

total interface area = (2 TBs +6/2 HAGBs(each side being shared between two hexagonal grains))

= (2 *1.732a+ 6a / 2)

=6.464a

Therefore, the length fraction for 2TBs/grain $= \frac{2*1.732a}{6.464a} = \underline{0.536}$

This indicates maximum f_L for the case of 2 TBs per grain with the TBs making 90° with HAGB which is seen to occur commonly in a microstructure under equilibrium.

On the other hand, the number fraction (f_N) calculation was performed as follows:

Total no. of interfaces = 2 TBs + 6 HAGBs = 2+ (6/2) = 5

Total no. of twin interfaces = 2

Number fraction for 2TBs/grain = 2/5 =$\underline{0.4}$

This leads to the relation between f_N and f_L to be as $f_N = 0.75f_L$ for 2 TBs per grain. Similarly, $f_N = 0.68f_L$ for 1 TB , $f_N = 0.0.79f_L$ for 3 TBs, $f_N = 0.82f_L$ for 4 TBs per grain was also calculated. This difference was seen to increase with no. of twins per grain. This discrepancy between is mostly attributed to some non-ideal twin morphologies like incomplete parallel sided twins, intersecting twins, corner twins, etc. (Valerie Randle 2002).

Further modification of Randle's model was done by Kumar et al., to take care of the morphological variability of annealing twins in the microstructure. A regular hexagonal grain of side length 'a' can be represented with an equivalent circular grain of same area when the relation between radius (r) and the hexagon side length (a) is $r = \frac{\sqrt{3}}{\pi}a$ (Figure 2.58. b). This model thus considers a complete-parallel sided twin in hexagonal grain to be lying on any of the chords of the

equivalent circle. The average length of the twin boundary is calculated as:

$$L_{TB} = 2r\int_0^1 \sqrt{1-x^2}\,dx = 2\frac{\sqrt{3}}{\pi}a\frac{\pi}{4} \approx 1.53a \qquad \text{…… Eq 2.135}$$

where, x is an integration variable relating the equivalent circle perimeter. This leads to f_L to be 2*1.53a/6.464a =0.475. According to Kumar's model, the relation between f_N and f_L came as f_N= 0.84f_L. Equation 2.135 reasonably approximated the effect from different morphologies and it was found that the value predicted for half-way parallel sided twins is very close to the ideal case (Schuh, Kumar, and King 2005).

v) 2D vs 3D quantification: Recent advancements in electron microscopy have enhanced morphological characterization of microstructures in three dimensions (3D). Serial sectioning followed by EBSD mapping has uncovered the differences between 2D and 3D values of f_L, N_L and N_G. The reconstructed microstructure using 117 2D maps obtained at a slicing distance of 0.25 mm and step size of 0.25μm shows some difference in the values as given in Table 2.6.

Table 2.6. Twin quantification in 2D and 3D (Yuan Jin 2014)

	3D microstructure	1st layer	117th layer
N_L (mm^{-1})	75	60	70
N_G	0.88	0.5	0.53
f_L	0.203	0.18	0.22

N_L in 3D was calculated using the relation $N_L = \frac{1}{2}\frac{S_{twin}}{V}$, where S_{twin} is the area of the annealing twin and V is the volume of the microstructure. Also, for f_L calculation in 3D area fraction of twin boundaries is considered. As twin morphology changes through thickness number of twin boundaries measured on 2D section changes and this results in significant difference in N_G values in 2D and 3D (Yuan Jin 2014; B. Lin 2015).

Based on relative merits and demerits, the techniques to quantify annealing twins should be exploited based on the final application. To sum up, f_N and f_L are highly sensitive to grain size and can only illustrate relativeness of twin content in global boundary network. Although, N_G has strong dependence on grain size, both types of twin density N_L and N_G should be used to measure twin content during microstructural evolution.

2.9.5 Annealing twins and microstructure:

There has been limited research work correlating annealing twins with various microstructural aspects as well as processing history. One of the notable works was by Pande et al. (Pande, Imam, and Rath 1990). In 99.9% pure nickel, grain growth experiments were carried out in the temperature range of 750-1200°C. It was found that the annealing twin width increases as grains become larger (Figure 2.59. a). Although the effect of processing route (amount and direction of cold work) was not investigated, it was estimated that twin width becomes roughly one third of the average grain size. This relationship was indicative of consecutive twin nucleation and annihilation process

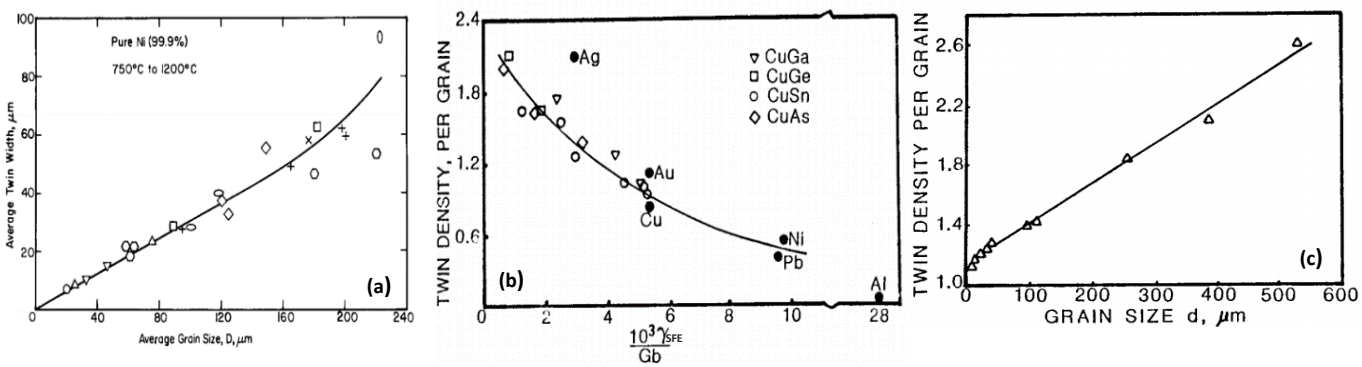

Figure 2.59. (a) Correlation between annealing twin width and grain size in 99.9% pure Ni (Pande, Imam, and Rath 1990), b) correlation between annealing twin density (N_G) and stacking fault energy for a constant grain size of 50 μm in a series of FCC metals and alloys, (c), grain size dependence of twin density per grain in Cu-15at%Zn alloy (Meyers, M.A., McCowan 1984)

due to HAGB migration during grain growth. Also, high temperature annealing results in wider twins. In terms of annealing twin density, it was found to be mostly governed by grain size once a particular grain size is achieved by any combination of annealing time and temperature. Another study revealed that twin density increases with extent of cold work (as dislocation density increases) in OF copper (99.95%) and Cu-Al alloys (96.9% Cu-3%Al), whereas it remains constant for 99% nickel. Also, smaller initial grain size, lower stacking fault energy were seen to result into higher annealing twin density (Gindraux and Form 1973). In a series of FCC systems, twin density was experimentally measured in terms of number of twin boundaries per grain (N_G) and it was compared with respective stacking fault energy values for constant grain size of 50 μm. Similar to Form's observation, it was found that twin density decreases as the stacking fault energy 'γ_{SFE}' increases (Figure 2.59. b).

The analytical expression of the plot is given as:

$$Z_r = 2.25 \exp(-\frac{165\gamma_{SFE}}{Gb})$$

where, Z_r is change in annealing twin density, G is shear modulus and b is the Burgers vector. Also, the change in annealing twin density was experimentally measured in Cu-15at%Zn system where it was found to exhibit a linear and directly proportional relationship with grain size (Figure 2.59. c). There has been found a significant increase in twin density from 1.2 to 2.6 twins per grain when grain size increased from 30 μm to 540 μm. Similarly, twin density increased with grain size in Fe-C alloys during annealing in austenitic range (950-1050°C) and in cold rolled Ni-200 alloys during annealing in the range of 800-1100°C (Meyers, M.A., McCowan 1984).

From all above observations, it was realized that a robust model capturing twin generation from recrystallization to grain growth including intermittent twin annihilation (in a shrinking grain) is of utmost importance to elucidate the effect of annealing twins in microstructure evolution.

2.10 Grain Boundary Engineering:

During mid 80's, a group of scientists extended their understanding of grain boundary structure into practice by proposing a technique to form strong and ductile polycrystals through controlling the population and crystallography of grain boundaries in the microstructure (Watanabe 1984). Grain boundaries had already been known to have tremendous influence on physical, chemical and most importantly mechanical properties in polycrystalline materials. In relation to the investigation of embrittlement phenomenon, it was observed that crack propagation is favored along intrinsically weak high angle random boundaries. By changing the boundaries to their best possible crystalline and morphological structure, geometry and number, polycrystalline materials of relatively simple composition can be turned into a material with extraordinary properties. At the advent, this was mostly known as 'grain boundary design'.

It must be mentioned that the coincidence site lattice model proposed by Kronberg and Wilson during their secondary recrystallization study in copper and the impurity segregation study in pure lead by Aust led to the idea of controlling grain boundary structure to attain specific configurations far from randomness which is the foundation of grain boundary engineering (W. G. Wang 2007). The first implementation of this idea was done by Aust and Rutter to improve stress corrosion

cracking resistance in nuclear materials. Since then the topic became popular under the name 'grain boundary engineering' (GBE) which depicts nothing but engineering the microstructure by manipulating the population of certain types of grain boundaries in the global boundary network. This was somehow interesting as previous approaches to strengthen material was limited to only length scale control (domain size, grain size) or introduction of second phase etc.

Initial efforts of grain boundary engineering were limited to changing the misorientation distribution function (MDF) by specific thermo-mechanical processing, thin film deposition techniques and solidification processes. With the development in the field of electron microscopy, it became convenient to examine and characterize interfacial structures. A significant progress in the field of GBE was through the advent of electron back scatter diffraction (EBSD) technique which was the key tool for orientation imaging microscopy (OIM).

2.10.1 Chronological depiction of GBE studies:

This should start with two significant works in early 1990s. Lin et al. (P. Lin et al. 1995) first aimed at evaluating the potential effect of "grain boundary design and control" (GBCD) on

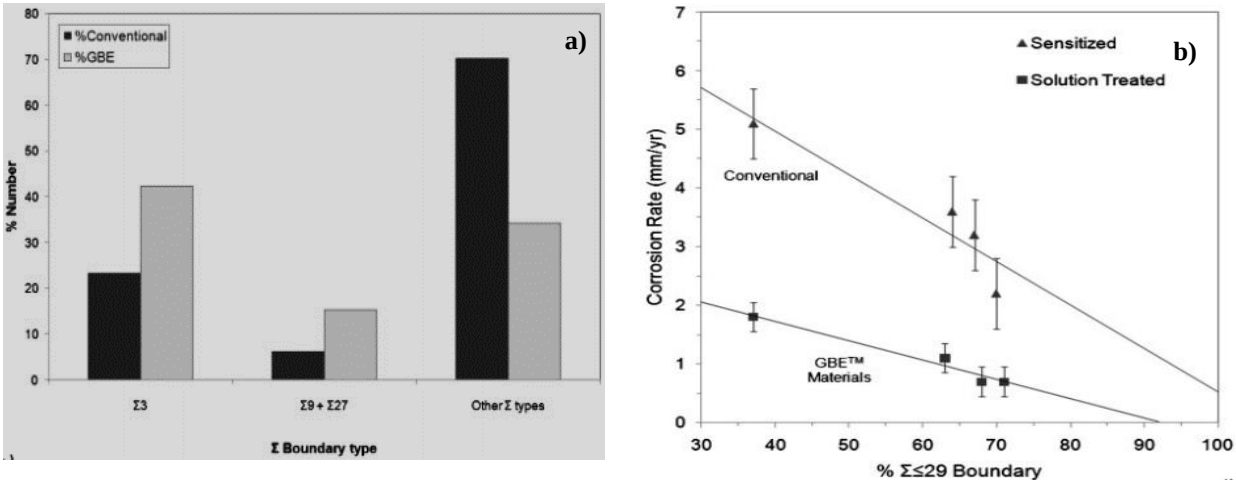

Figure 2.60. a) Comparison in the special boundary (∑≤29) fraction between conventionally processed and GB Engineered alloy 600 (Valerie Randle 2010) b) Effect of special boundary fraction on intergranular corrosion susceptibility under both solution annealed and sensitized condition (P. Lin et al. 1995)

boundary related properties like sensitization and intergranular corrosion resistance in Alloy 600, a nickel based austenitic alloy, which is predominantly used at elevated temperatures, e.g. nuclear reactors, aerospace applications. They were able to achieve a significant increase in the percentage

of low ∑ boundaries (compared to one in conventionally processed alloy 600) through some patented thermomechanical treatments (Figure 2.60. a). It was revealed that low stacking fault energy of the alloy makes it amenable to twinning. Thus, most of the HAGBs are replaced in part by twin related segments or $\sum 3^n$ boundaries (n=1, 2, 3). Effect of this is reflected in Figure 2.60. (b), as a decreased corrosion rate with increased fraction of special low∑ (∑≤29) boundaries in the grain boundary engineered alloy (GBE^{TM}). Even for the conventional material, induced susceptibility to corrosion through sensitization got an attenuating effect as the special boundary fraction increases. This was attributed to less likelihood of solute segregation and precipitation in low CSL (low ∑) boundaries because of their highly ordered structure. Their findings somewhat laid the foundation of transferring the knowledge of interface science to interface engineering through GBE.

Randle and co-workers studied effectiveness of GBE to create low ∑ special boundaries in high purity nickel samples by doing low to moderate cold rolling followed by annealing. Correlation between GBCD and texture, importance of special triple junctions (TJ) in microstructure were some of the important findings (Thomson and Randle 1996, 1997). Next to this, high temperature application superalloys came into the picture with the sole intent of increasing their weldability and resistance to hot corrosion, fatigue and creep. Iron and nickel based superalloys were engineered using a series of deformation followed by recrystallization annealing between 975-1200°C. This thermo-mechanical process is patented by Ontario Hydro, Toronto, Canada. A significant increase in the special boundary (∑≤29) frequency from 10-20% to 50-70% was achieved which showed good thermal stability after prolonged exposure to service temperature of 850°C. Simultaneously, due to less disordered structure, increased fraction of low ∑ boundaries also increased weldability 50-times and improved corrosion, creep and fatigue resistance by 50 %, 90% and 50% respectively, as compared to the conventionally manufactured counterparts. This ensures GBE to be the most effective way to increase longevity, reliability, manufacturing and servicing cost of superalloy components for high temperature use (Lehockey, Palumbo, and Lin 1998). Was et al. also found in alloy 600 that two or three step rolling (2-5%) followed by annealing for 1-20 hours within a temperature window of 890-940°C increased special boundary fraction two timescompared with the solution annealed specimens which in turn reduced the creep rate by factor of 10-30 (Was, Thaveeprungsriporn, and Crawford 1998).

A two-step rolling followed by a special two-stage heat treatment successfully replaced the random boundaries in oxygen free electronic (OFE) copper where up to 85% of low ∑ boundaries were observed in Grain boundary character distribution (GBCD) (King and Schwartz 1998). Application of GBE was extended for battery application by Lehockey et al when significant improvement in battery life was achieved through increasing special boundary fraction. A patented

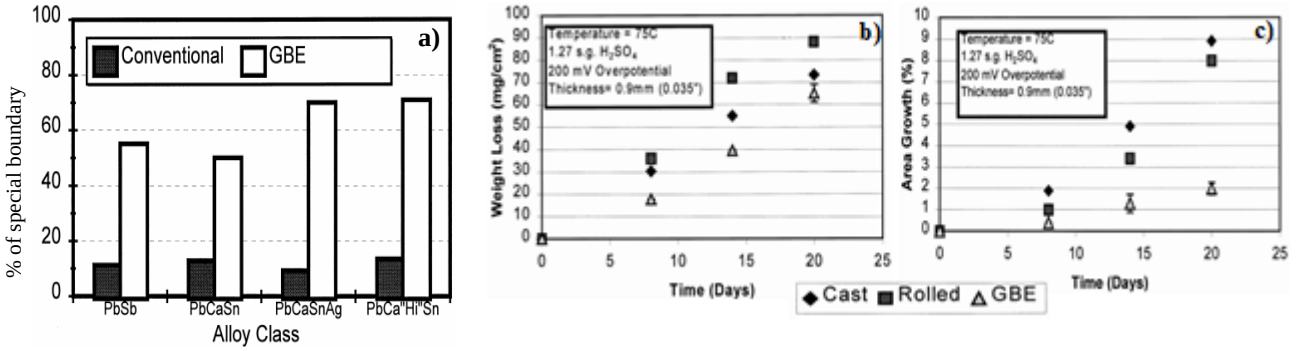

Figure 2.61.a) Increased fraction of special boundaries achieved through GBE in a series of positive Pb-acid battery grids, effects of special boundary opulence in improving battery life by decreasing b) rate of weight loss, c) rate of grid growth (Lehockey 1999)

thermo-mechanical treatments were applied to a series of commercially important grid alloys. This results in an increase in the special boundary fraction from 12% in conventional (cast and rolled) material to nearly65% in GBE alloy (Figure 2.61. a). This results in an improvement in delaying weight loss by 16% and resistance to growth rate by 75% (Figure 2.61. b, c) (Lehockey 1999). Lee et al. were able to engineer Pb- based alloys to introduce up to 91% special boundaries in the GBCD which improved the service life of the Pb batteries. It was found that large amount of cold rolling although destroys CSL boundary in Ni-base alloys, actually favors special boundary formation in Pb-base alloys (D. S. Lee, Ryoo, and Hwang 2003).

Application of GBE to various material systems includes 304 stainless steel (Shimada et al. 2002; Thaveeprungsriporn, Sinsrok, and Thong-Aram 2001; Tsurekawa, Nakamichi, and Watanabe 2006; B. R. Kumar et al. 2007; Fang et al. 2008; Wasnik et al. 2002), 316 (Owen and Randle 2006; Michiuchi et al. 2006; Zhang et al. 2016), alloy 600 (Telang et al. 2016; Sunil Kumar et al. 2013; Li and Tin 2014) , alloy 825 (Bai et al. 2017), alloy 800 (D. J. Drabble, Bishop, and Kral 2011; Akhiani et al. 2015), brass (S. Y. Lee et al. 2003), electronic application (T. Chuang et al. 2013, 2014), Hastealloy (X. Wang et al. 2016), Ni-based alloys (Y. Jin et al. 2014; Gao et al. 2005)

Table 2.7. Summarized tabulation of remarkable GBE work (Valerie Randle 2004)

No.	Material	Treatment (reduction (%)/temperature (°C)/time)	Strain or recrystallisation anneal	Number of iterations	Grain size (μm)	Number or length statistics	CSL start (%)	Σ3 (%)	Σ9 (%)	LAB (%)	CSL maximum (%)	Property or attribute	Refer
1	Alloy 600	25/1025/18 min	R	4	–	*N*	43	–	–	–	62	Triple junctions	[32]
2	Alloy 600	5/890/16 h+3/890/20 h+ 2/936/11 h, etc.	S	(3+)	330, 35	–	–	(20–33)	–	–	26–40	Creep	[33]
3	Alloy 600	–	–			–	–	43 45	1 8	2 2	47 54	Cracking	[34]
4	Alloy 600	5–30/900–1050/2–10 min	R	3–7 5	<30	*N*	–	46 47 67	5 10 7	3 2 0	63 71 68	Intergranular corrosion	[3]
5	Alloy 600	4 C precipitation treatments, then 3/925/7.5 min	S	3	35 s	*N*	–	–	–	2–6	64–70 (29–43)	Intergranular corrosion	[35]
6	Alloy 600	20/1000/15 min	R	7	–	*N* *L*	25	34	18	–	65	Triple junctions	[36]
7	Steel 304	5/927/72 h	S	1	31	–	–	–	–	–	87	Intergranular corrosion	[37]
8	Steel 304	3/950/10 min	S	3	34	–	34	50	–	–	57	Energy	[38]
9	Ni	–	R	–	200	–	–	50	7	1	66	Triple junctions, ductility	[39]
10	Ni alloy	20/1050/1 h	R	4	74	*L*	21	34	2	–	41	Cracking	[40]
11	Ni alloys (2)	(1) 1079/40 h, 1079/100 h (2) 954/40 h, 954/100 h, 1010/2 h (precipitate dissolution)	–	1 (2)	255 559	*L*	46 41	65 58	1 1	–	69 64	Cracking	[41]
12	Cu	30/350–400/10 min	R	3	125 s 50	*N* *L*	20	31	21	4–7	63	Triple junctions	[36]
13	Cu	6/344/8 h + 532/14 h 6/275/14 h + 375/7 h 6/225/14 h + 325/6 h 6/325/6 h	S	(2) (2) (2) 1	10 s	–	70	44 67 63 61	5 9 9 10	43 3 2 2	–	Statistics	[42]
14	Brass	25/665/5 min	R	5	20–54	*N*	–	34	8	–	42	Ductility	[43]
15	Brass	3/700/23 h 2/595/21 h 1/700/1 h 4/700/95 h	S	(4)	28 s 154	*N*	50	32			40	Ductility	[44]
16	Brass (2 phase; a-alpha b-beta)	20/680/20 min	R	4	>1000 s	–	–	67a	–	5a 67b	78a 73b	Statistics	[45]
17	Pb alloy	–	–	–	–	–	12	–	–	–	57–66	Intergranular corrosion	[4]
18	Pb alloy	30/270/10 min 30/270/10 min 30/270/10 min	R	3 3 2	25–60	*L*	–	12 39 64	<1 8 26	63 9 5	79 61 96	Statistics	[46]
19	Pb alloy	–	–		–	–		56	12	5	71	Intergranular corrosion, ductility	[47]

and many other (Watanabe and Tsurekawa 1999; Watanabe 1993; Lo, Shek, and Lai 2009; Tan, Allen, and Busby 2013; M Kumar, Schwartz, and King 2002; Schlegel, Hopkins, and Frary 2009).

Apart from the works mentioned above, there has been a vast body of research on the application of GBE and correlation of GBCD to many microstructural parameters which is beyond scope to be discussed in detail in this section. A brief description of all significant GBE work is given in Table 2.7 (Valerie Randle 2004).

2.10.2 Key features of GBE:

Discussion from previous section highlights one common feature pertaining to the successful application of GBE. It was clear that certain types of materials which are capable to generate large number of ∑3 boundaries through combination of deformation – annealing are the ones selected for GBE. This indicates mostly the metals and alloys which have low to medium stacking fault energy (SFE) and thereby annealing twins are formed frequently in them. As twinning occurs, its interaction with HAGB results in regeneration of a new or existing boundary with highly ordered structure. This leads to increase in non-random boundaries in the network which is the key objective of GBE. FCC metals and alloys with low SFE are the materials of interest for GBE as profuse twinning is common in them. Some of the other requirements include grain boundary geometry (misorientations, plane inclination etc.), stability of grain boundary structure and configuration (Watanabe 1984), GBCD, $\sum 3^n$ boundary interaction, HAGB network connectivity and percolation threshold. Following subsections are designed with the intent of highlighting the aspects of the above features that dictates 'twinning-related' GBE in FCC materials.

2.10.2.1 Grain boundary Description:

A detailed discussion on grain boundary has already been presented in section 2.4. It is well known that five independent parameters or degrees of freedom (DOF) are used to describe grain boundary geometry. There happens to be significant influence of grain boundary structure (geometry) on its property. Systematic bicrystal studies were done to explore some of them. It was found that higher misorientations increases grain boundary energy. Grain boundary plane inclination also controls grain boundary energy. In a molecular dynamics simulation study, it was shown that if the grain boundary plane deviates further from (111) and misorientation axis is neither parallel nor perpendicular to the plane, those ∑3 boundaries have very high mobility compared to ∑3s with boundary plane as exact (111). This was for the case of a mixed boundary. In case of symmetric

∑3, i.e., a twin, they are immobile because there is not much deviation in the boundary plane. Also, ∑7 twist boundary was found to be less mobile than its mixed component (Janssens et al. 2006).

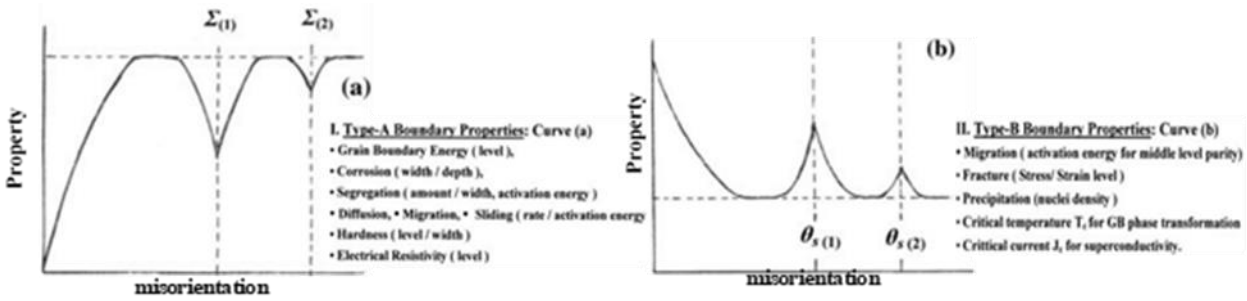

Figure 2.62. Structure dependent activity of a) higher-energy, b) lower-angle/lower-energy and special high angle/ low energy boundaries (Watanabe 2011)

In the domain of GBE, misorientations is the only requirement until now to bring change into the boundary structure. Structure dependent properties of grain boundaries with respect to misorientations was studied using bicrystals. It was evident that low energy boundaries have strong structure dependence of their properties as shown in Figure 2.62. a, b (Watanabe 2011).

2.10.2.2 Special boundaries (∑3^n):

The key outcome of GBE is the generation of boundaries which, according to the CSL model, can be considered as low ∑ boundary. Of them, ∑3^n boundaries are the most dominant ones. Twinning during annealing causes the generation of the ∑3 boundaries in FCC metals and alloys. ∑3 boundaries can be divided into five distinct categories (Valerie Randle and Davies 1999; D. Drabble 2010):

i> symmetrical tilt boundary (STB) on {111} plane - coherent twin boundary (CTB) (energy <0.02 J/m^2)

ii> asymmetrical tilt boundary (ATB) on planes line {110},{411}(energy 0.02-0.6 J/m^2)

iii> symmetrical tilt boundary on {112}- incoherent twin boundary (ITB) (energy 0.54 J/m^2)

iv> three twist boundaries (energy > 0.6 J/m^2)

v> boundaries with irrational planes.

This is why annealing twins are known as subset of ∑3 interfaces. The corresponding energy values are calculated by atomistic simulations in copper. {111} CTBs are mostly reliable exhibiting special properties as they have large extent of free volume (this principal intrinsic

property dictates boundary behavior). In contrast to that, ITBs and other ∑3s with special boundary planes (tilt, twist or low index) have higher free volume. But, the free volume associated with random HAGBs is significantly higher than that related to any ∑3 boundary. Consequently, the energy of STB is $1/50^{th}$ time that of HAGB and ITB energy is although higher than STB energy, still small compared to HAGB. As for example, the measured energies of CTB, ITB and HAGB in 304 stainless steel came as 19, 209 and 835 mJ/m^2 respectively (D. Drabble 2010). In terms of mobility, for highly ordered structure, CTBs are immobile while ITBs move very fast. It was also observed in austenitic stainless steels that only CTBs are resistant to inter-granular stress corrosion cracking (IGSCC). In contrast, all were found to be crack resistant in nickel aluminide ribbons (Valerie Randle 2004). However, it was evident that almost all types of ∑3 boundaries contain at least one low index plane which makes them special compared to HAGBs.

These boundaries are known to have different roles during different stages of GBE. During, first GBE step, dislocations and other defects pile up at the twin boundaries and that is how ∑3 boundaries retain strain in the lattice. During the second iteration, new defects are added to the retained mass which leads a higher driving force for grain boundary migration. This leads to movement of incoherent ∑3s, ∑9 (generated from ∑3) through the matrix annihilating some of the existing annealing twins. This ensures no more strain retention during next strain iteration. During the annealing after third iteration, the driving force is not that high as was after second iteration since no retained strain is available. The migration velocity of the boundaries is perfect for nucleation of fresh annealing twins. This is how ∑3 boundary frequency increases with generation of some twinning related low energy boundaries (∑9, 27) replacing the HAGBs. TEM observation of dislocation substructures in GBEd copper sample showed direct evidence of strain retention at twins(Valerie Randle 2010).

Other special boundaries commonly occurring during GBE are ∑5, ∑7, ∑9, ∑27, etc. all of which contribute to disconnect the HAGB network connectivity.

2.10.2.3 Grain Boundary Character Distribution (GBCD), Connectivity and Percolation:

One of the important aspects of GBE is the extent and type of special boundaries generated into the microstructure of the FCC polycrystalline materials by selective thermo-mechanical processing. So, this frequency of occurrence and type of special boundaries is known as grain boundary character distribution (GBCD). This along with grain boundary energy distribution (GBED) is used to study global boundary network (Yuan Jin 2014). In FCC polycrystalline materials, GBCD is primarily dominated by $\sum 3$ boundaries (Schuh, Kumar, and King 2005). Before the introduction of EBSD, grain boundary characters were analyzed using electron channeling patterns (ECP) which gave the orientation information. Materials from grain size 5μm to 10mm were used for this. Recent trend of using EBSD has made it easier to characterize the grain boundaries by measuring the misorientation across it. Effect of the type of fabrication process on GBCD was found to be important in polycrystalline materials. A normal iron polycrystal sintered at 700°C was found to have less frequency of low angle boundaries than its counterpart which was rolled and sintered. Although the fraction of CSL boundaries was similar. In some alloys (α Fe-3%Si), the frequency of low angle and CSL boundaries both increased with decreasing annealing temperature as well as grain size (Watanabe 1984). It is worth mentioning that all above techniques rely on data from a 2D section of plane. So, to determine GBCD of the bulk polycrystal, advanced 3D imaging techniques like 3D X-ray diffraction (3DXRD), 3D microscopy using Focused Ion Beam (FIB) (to do serial sectioning) +EBSD , it is possible to generate the complete boundary network distribution of the bulk sample in 3D (Yuan Jin 2014; Rohrer et al. 2004).

GBCD also is a measure of how well the random boundaries are connected to form a network. Connectivity study has somehow broadened the research to study the topological nature of the global boundary network. This, in particular, is of paramount importance as interfacial phenomena like diffusion, intergranular corrosion, Coble creep etc. happen when the weak random HAGBs are very well connected. So, compared to having crystallographic information of individual boundary, it is more meaningful to study the continuity of the boundary network. This can be illustrated incorporating the triple junctions in the microstructure where the branching of the boundaries occurs. So, a triple junction, with two special boundaries, will efficiently attenuate crack propagation compared to one with all random or one random boundary(/ies). Existing methods to study connectivity are as follows:

a) ***Neutral twin method-*** This is the oldest concept of measuring boundary connectivity where the coherent twin boundaries are excluded from the calculation as they directly don't interfere with the random boundary connectivity. The effective special boundary fraction is calculated based on the following equation:

$$f_{sp}^{eff} = f_{\sum 1} + f_{\sum 3}^{eff} + f_{3<\sum<29} \qquad \ldots\ldots\ldots \text{ Eq 2.136}$$

where the second term on the right hand side ignores the coherent parts known as neutral twins.

$f_{\sum 3}^{eff}$ is obtained from $f_{\sum 3}^{eff} = -\frac{f_{\sum 27}+f_{\sum 9}}{2} \pm \sqrt{\left(\frac{f_{\sum 27}+f_{\sum 9}}{2}\right)^2 - 2\left(f_{\sum 1}f_{\sum 9} + f_{\sum 1}f_{\sum 27} - f_{\sum 27} - f_{\sum 9}\right)}$

This leads to better estimation of crack depth measurement (D. Drabble 2010).

b) ***Triple junction distribution:*** Initially the focus of GBE was to modify the misorientations distribution function (MDF) to increase the special boundary fraction. Later on this has been analyzed from the perspective of the triple junctions the boundaries are related to. Kumar et al. has classified the triple junctions based on number of special boundaries as 0, 1, 2 or 3 CSL ones (M Kumar, Schwartz, and King 1999). The objective of this approach was to determine the GBCD improvement effect on spatial connectivity of the grain

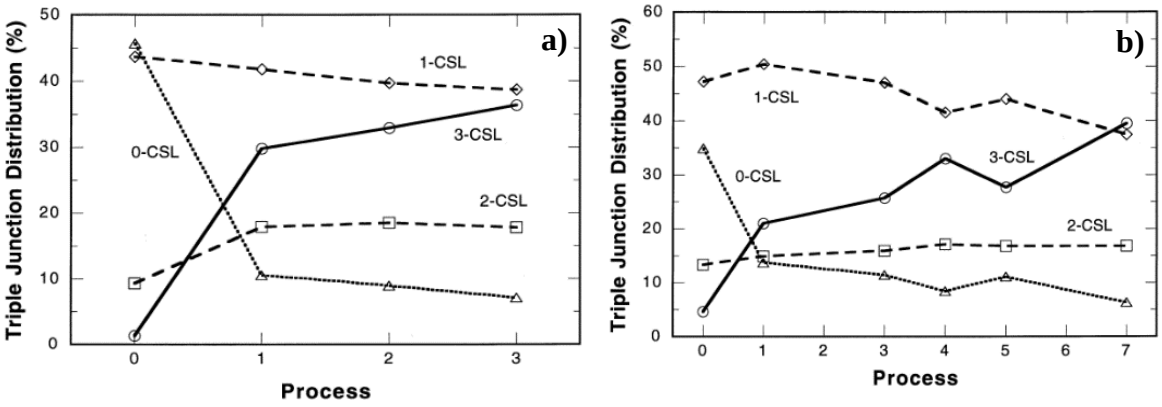

Figure 2.63. Experimentally determined triple junction distribution (TJD) in sequentially strain recrystallized a) ofe-copper (annealed at 400°C),b) Inconel 600 (annealed at 1000°C) (M Kumar, Schwartz, and King 1999)

boundaries. Through selective thermo-mechanical processing of OFE-copper and commercially pure Inconel, fraction of 0-CSL triple junctions were noticeably decreased to approximately 5%. Simultaneously, 2 and 3-CSL fractions levelled off and increased respectively (Figure 2.63. a, b)). The levelling of is due to the fact that if the two boundaries are of CSL class, then the reaction between them will make the third one a CSL as well. Due to twinning and its interaction with HAGBs, 3-CSL fraction is increased. However, this approach has a limitation as it doesn't predict correctly those special boundaries which are a part of the original HAGB network compared to the special ones which are located within the HAGBs (D. Drabble 2010).

c) ***Percolation Theory:*** This concept is built on the idea of percolation dynamics and cluster mass analysis where all similar type of interconnected boundaries form the cluster. So, using this approach, special boundary fractions can be related to uninterrupted path length through which interfacial phenomena can happen. Accordingly, it was also predicted that a crack can only propagate if 65% (excluding the 3-CSL ones) of the triple junctions impart no barrier. Conversely, to break the continuous interconnected path for interfacial phenomena to happen, the percolation threshold happens according to the relation, $f_{2CSL}/f_{(1-3CSL)} \geq 0.35$, i.e, continuous flow along interface is arrested if more than 35% triple

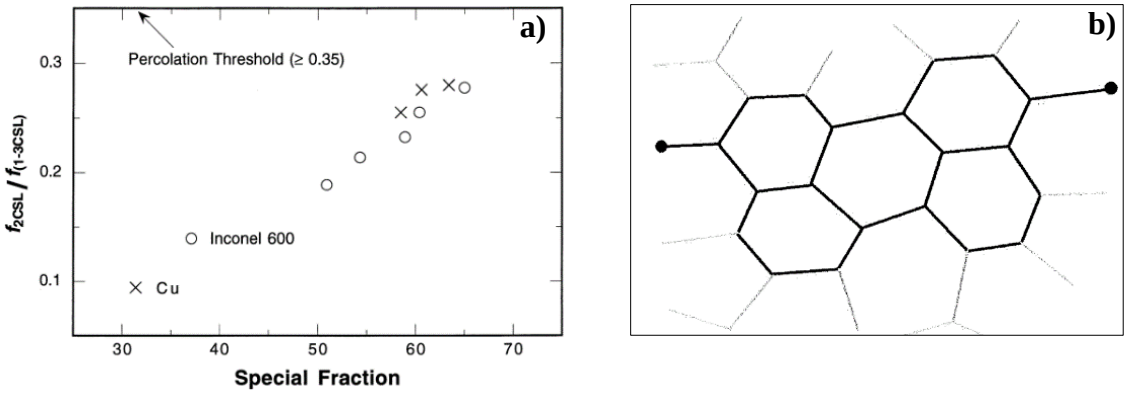

Figure 2.64. a) Discontinuity evaluation in the HAGB network by using triple junction distribution as an indicator (M Kumar, Schwartz, and King 1999), b) Demonstration of path of least resistance (in dark) by dangling branches in cluster analysis (D. Drabble 2010)

junctions are resistant. Here, f_{2CSL} are the fraction of crack resistant triple junctions whereas $f_{(1-3CSL)}$ indicates total number of active unit triple junctions in the microstructure (Valerie Randle 2004; Mukul Kumar, King, and Schwartz 2000). The percolative threshold was calculated plotted for Inconel and ofe-copper (Figure 2.64. a).

It was observed that with increase in 3-CSL fraction, the inequality criterion is close to being achieved. By extrapolating the data in above figure, the special fraction is noticeable higher while considering triple junctions over special boundaries. This highlights that although connectivity disruption is underway, still the percolation has not been stopped completely (M Kumar, Schwartz, and King 1999). Percolation theory indirectly correlates material properties through extracting mean free path that indicates intergranular damage.

Cluster analysis, which is directly related to connectivity measurements, considers 'interconnected cluster of each boundary type a "mass" based on the combined total length of grain boundary which is self-connected." This method is more of a direct way to quantify boundary connectivity. However, the limitation of this method was realized in case of diffusion controlled

Table 2.8. Summary of models for grain boundary connectivity measurement (D. Drabble 2010)

Model Type	Parameter Analysed	Comparison of Figure 5.1(b) with Figure 5.1(a) and Diffusion Rate Predictions
Neutral Twin Model	Special boundary fraction excluding neutral twins	(b) has a higher fraction of effective special boundaries than (a), and therefore would exhibit a lower diffusion rate
Triple Junction Distribution	Number fraction of triple junctions with 0,1,2 and 3 CSL boundaries	(b) has a higher fraction of 3-CSL triple junctions and a lower fraction of 0-CSL triple junctions, and therefore would exhibit a lower diffusion rate
Percolation Theory	"Mass" of connected HAB clusters	The HAB cluster is of equal mass in (a) and (b), and therefore both microstructures would exhibit equal diffusion properties
Effective Resistance Model	Grain boundary diffusion in a unit area of microstructure	The microstructure in (b) contains the original HAB network from (a), plus several other low-diffusivity parallel paths. Therefore, the diffusion rate in (b) would be slightly greater than (a).
Diffusion Theory	*Grain boundary diffusion*	*The diffusion rate of (b) cannot be less than that of (a), as the microstructure contains the original HAB network, plus the additional parallel paths. Therefore, the diffusion rate in (b) must be greater than (a). The magnitude of the difference is dependent on the ratio of diffusivity between special and general boundaries.*

properties for the usage of "dangling branches" treatment. In Figure 2.64. b, a simulated grain boundary network is being shown joining two points. The dark lines are the backbone of the cluster which are also path of least resistance or fast diffusion. These dark paths determine the rate of grain boundary transport. The loosely connected grey paths are also a part of the cluster. Although they are counted within the cluster mass, they offer resistance to diffusion.

This results into discrepancies while being attempted to correlate with certain type of materials property, like diffusion controlled regime of Coble creep (D. Drabble 2010).A brief description of all types of models for connectivity analysis is given in Table 2.8.

2.10.3 Mechanism of GBE:

From the discussion so far, it is clear that annealing twins are the key to engineer the grain boundary crystallography. When their proportion is high, interactions with other boundaries will result in multiple twinning and other beneficial special boundaries. This is governed by the rule of CSL joining or dissociation:

$$\sum A + \sum B \rightarrow \sum (A \; X \; B) \qquad \ldots\ldots\ldots \quad Eq\ 2.137$$

$$Or, \quad \sum A + \sum B \rightarrow \sum (A / B) \quad (\text{valid only when A/B is integer and A>B}) \quad \ldots\ldots \quad Eq\ 2.138$$

This indicates that when two ∑3 boundaries meet, a ∑9 is generated. Also, if a ∑9 meets a ∑3, the resulting boundary might be a ∑3 or ∑27 according to above two rules. The proportion of ∑9 was found to be one-fifth of that of ∑3 boundaries and ∑27 proportion is slightly higher than the random distribution proportion. However, GBE microstructure is mostly dominated by ∑3s (not only twin boundaries) and ∑9s (V. Randle 1999).

Now, although ∑3s in the form of annealing twins are not part of grain boundary network, they contribute to GBE indirectly. Other ∑3s like, incoherent twin boundaries (ITB), segments generated from reaction at triple junctions (Equations 2.137 and 2.138), are also factors to engineer grain boundaries. Twinning is believed to occur for two reasons: to decrease overall surface energy or to reorient the grain boundaries to a configuration suitable for dislocation absorption and mobility improvement during recrystallization (Gindraux and Form 1973). Although, the interfacial energy reduction criterion generates annealing twins during grain growth, strain-

induced boundary migration (SIBM) during recrystallization was found to be more responsible for twinning in low SFE microstructure.

A model, which is based on interaction between a mobile grain boundary and a twin, was proposed to capture the probable mechanism of GBE through enhancement of ∑3s. This was proposed by Randle in 1999. One of the assumptions made is that interaction between ∑9 and ∑3 will generates ∑3 rather than ∑27 which was observed to be true in reality from experimentally measured relatively low ∑27 fractions over ∑3 fraction. Even, preference of ∑3 incoherent interface formation was more than ∑27 as the former is associated with low energy and higher mobility. Similarly, interaction of a ∑27 with ∑9 should prefer ∑3 than ∑243 based on energy criterion. So, the method by which mobile ∑3 (ITBs and other segments) boundaries are introduced into the global boundary network is: $\sum 3^n + \sum 3^{n+1} \rightarrow \sum 3$ while the exponents added to give higher order ∑3 variants are ruled out (V. Randle 1999).

Figure 2.10.6 shows schematically the feature of the model which is known as "∑3 regeneration model'. This considers two recrystallized grains impinging on each other must have twins in order to produce more mobile boundary segments. The model also considers the grain on the left (Figure 2.65. a) has the comparatively faster moving boundary (marked by arrow) due to the twinned portion and it moves to hit the closest HAGB of the grain on right (Figure 2.65. b). On further proceeding, Figure 2.65. c shows its interaction with the first coherent twin boundary (CTB).

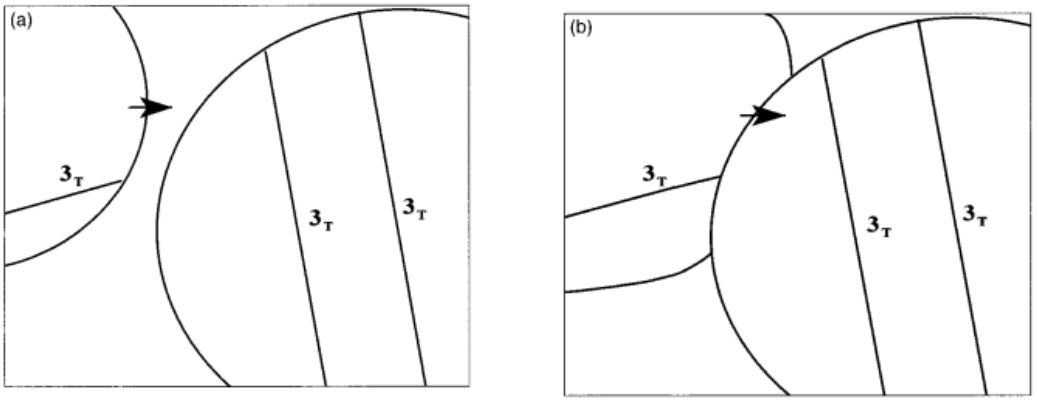

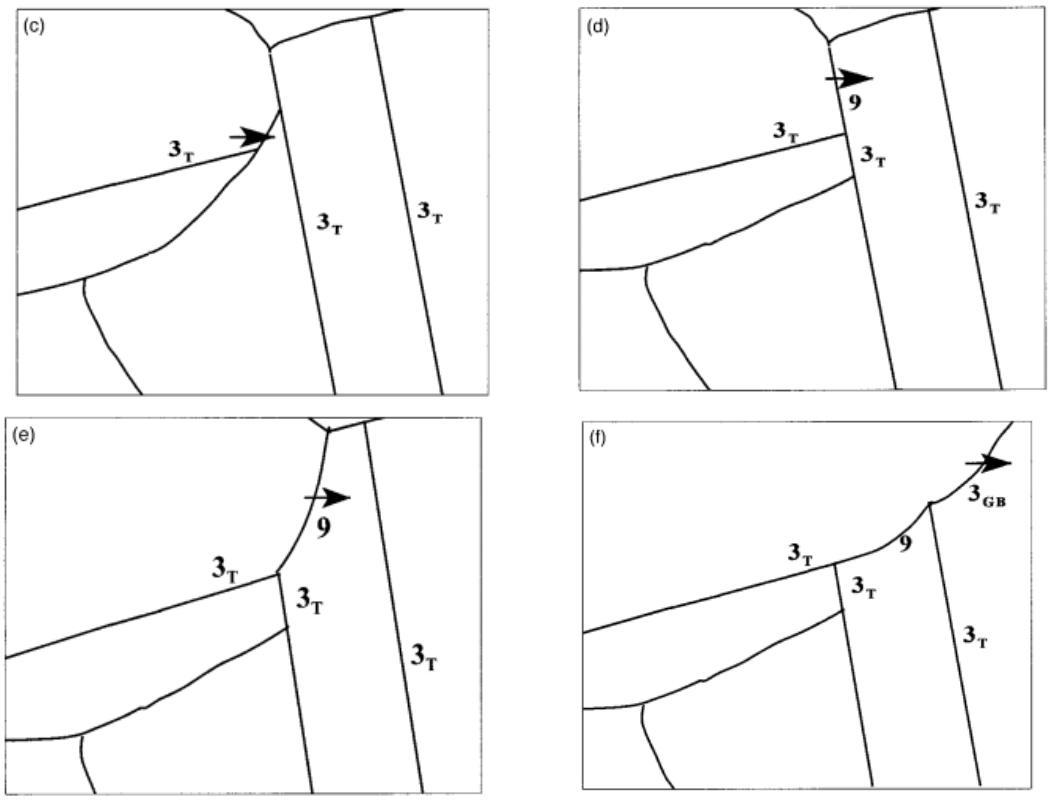

Figure 2.65.Schematic representation of generation of ∑3 boundary segments in the global boundary network by interaction amongst ∑3n variants, the "∑3 regeneration model" (V. Randle 1999)

This mobile boundary continues to sweep until the CTBs from left and right grains meet each other, resulting into a $\sum 3_T$-$\sum 3_T$-$\sum 9$ junctions (Figure 2.65. d). In this triple point, ∑9 is the most mobile segment other two being CTBs. Now, ∑9 continues to move which is being shown in Figure 2.65. e. On its way, it interacts with ∑3 from the other CTB of the grain on the right. Another triple junction reaction occurs leading to a new $\sum 3_G$-$\sum 3_T$-$\sum 9$ junction, where one of the ∑3s is formed as a mobile segment, not as CTB or ITB but as a part of the global boundary network (Figure 2.65. f). This mobile segment further sweeps through the microstructure as long as driving force is available or it doesn't interact other boundaries. This model got some strong experimental validation where the ∑3 (non-CTB) and ∑9 fractions were increased during strain annealing. Generation of ∑3 which is not a CTB was also observed in an experiment where ∑3s with planes away from {111} configuration and misorientations were found (V. Randle 1999). Thus, the

mechanism of GBE through "introduction and proliferation" of special ∑3 boundary segments was proposed.

2.10.4. GBE Techniques:

The technique of achieving GBE is by selective thermo-mechanical processing. Usually, different ranges of cold work followed by annealing and sometimes iteration of a particular deformation-annealing cycle is used to obtain desired grain boundary character distribution (GBCD) which determines a GBEd microstructures. Commonly used deformation methods, reported in the literature are rolling, mechanical compression, shot-peening, etc. Following deformation, annealing treatments are given to the deformed materials in box or tube furnaces for a broad range of time. An inert gas is sometimes used to ensure a protective atmosphere to prevent oxidation. Last step involves cooling either in air or in a quenching medium depending upon the purpose and the material (D. Drabble 2010).

GBE techniques can be broadly classified into two categories 'strain recrystallization' – involves higher amount of cold work and 'strain annealing'- involves lower strains. Later, TEM evidence showed that the term 'strain recovery' should be a best fit for what it was known to be 'strain recrystallization' as the recrystallization is not favored due to insufficient stored energy during short time annealing. With further research in this area, it was observed that repetition of some specific deformation- anneal cycle can even bring superior properties (Valerie Randle 2004). Finally, engineering grain boundaries can be achieved through one of the following four techniques:

a) ***Iterative recrystallization:*** Repeated recrystallization was found to result in small grain size (<30μm) with near-random texture along with desired GBCD. Usually, medium (20-30%) deformation per pass followed by high temperature annealing (around 0.6-0.8 T_m, where T_m is the absolute melting temperature) for short time is applied (Valerie Randle 2004) and this combination is repeated up to maximum 3-7 cycles. Due to iteration, considerable amount of broken paths are created in the HAGB network which can be attributed to increased density of special boundaries (∑3, ∑9 etc.). This method, therefore, exists somewhere between the grain growth regime, where strain energy has no influence and recrystallization which requires strain energy as driving force. Successful application

of this technique was done in a nickel based alloy (Ni-16Cr-9Fe) which was engineered using a 5-step iteration of 20% cold work followed short anneal (3 mins) at 1000°C. This results into increase in ∑3 fraction to 47% and ∑9 fraction to 10%, which was almost twice as in conventionally processed microstructure. In other low SFE systems like copper, a 3-step GBE using 30% compression followed by an anneal around 375°C for 10 mins yielded upto 58% of ∑3s in the GBCD. Another attempt with a 5 time iteration of the cycle of 20% deformation plus 5 min annealing at 750°C produced 45% ∑3 and 7% ∑9 (V. Randle 1999). Some more examples can be found from the observations (1,4,6,10,12,14,16,18) listed in table 2.7.

b) *One-step recrystallization:*

Medium levels of cold work is given in only one step which is ended by short anneal at high temperature in one-step recrystallization. This was also found to increase twin density alongwith grain refinement. This approach was adopted while engineering the boundaries in copper by using one step deformation of 50% followed by a 1 min annealing at 1000°C. Higher density of twins were achieved by this single step processing than iterative one. It is still an open area to research on which of iterative and one step recrystallization gives better properties (V. Randle 1999).

c) *Iterative strain annealing:*

Another variant of GBE techniques is iterative strain annealing which involves low amount of cold work (upto 6%) plus prolonged annealing at temperatures lower than that required for recrystallization. This pattern is repeated upto 2-3 times. Low temperature anneal ensures that recrystallization is stopped but reorients the grain boundaries to lower energy or low-∑ configurations. In alloy 600 (Ni-16Cr-9Fe), a 2-3 stage iterative treatment of 2-5% deformation followed by long duration (1-20h) annealing at 890-940°C resulted into almost doubling of ∑3s (from 6-12%) and ∑9s (5-12%) accompanied by improved creep strength. These figures compared to ∑ fractions reported in other variants seem less as the coherent twins are not considered in the calculation. Also, a 6% compression followed by a two-step annealing (14 h at 275°C and 7h at 375°C) increased ∑3 fraction upto 67% with an initial drop in twin density during the first anneal which was proved to be a requirement for final CSL fraction increase (V. Randle 1999).

d) *One- step strain annealing:*

Single annealing following small deformation or residual strain present after recrystallization was also found to be effective in bringing crystallographic modification of the HAGBs. Compressive

strain of 6-7% followed by single and two step annealing in the range of 500-750°C over a time range of 9-24h was given only once on 99.5% pure nickel (Ni200) specimens. Long annealing time improved $\sum 3^n$ densities with exact CSL configuration (Thomson and Randle 1997). In another study, 99.99% copper was cold rolled and annealed twice, 1 h at 900°C and 97h at 540°C in air. The first annealing treatment was given to increase the grain size upto 240μm to make the grain boundary plane measurement easy and to make profuse annealing twins. After annealing at low temperature, 68% of the ∑3 boundaries were found to have exact 111/111 symmetric tilt boundary plane, i.e., one with low energy configuration (an order of magnitude less energy than its asymmetric counterpart). Using this type of technique, in-situ grain boundary engineering through fine tuning the boundary plane orientation in addition to have ∑3 boundaries can be performed on finished parts under application (V Randle, Davies, and Hulm 1999). Some other types of GBE techniques can also be found from Table 2.7 where no or only one step deformation is applied.

2.10.5 Application of GBE:

Manipulation of relative fraction of special boundaries in global boundary network has significant impact on improving materials bulk properties. These include intergranular corrosion resistance, electromigration, dynamic embrittlement, cleavage cracking, plasticity, electrical conductivity, superconductivity, solute segregation, creep strength, etc. (Zelinski 2005). Some of the noticeable improvements were achieved in terms of increased yield strength and ultimate tensile strength in Ni-16Cr-9Fe, increased ductility in alpha brass with no significant decrease in tensile strength, increased fracture toughness of intermetallics materials Ni_3Al, Mo, etc., significant increase in high temperature fatigue resistance of ME3, a nickel based alloy (D. Drabble 2010).

Another area of improvement was creep strength. By increasing the low-Σ boundary fraction from 13% to 66%, secondary creep rate was decreased by a factor of 16 in as-cast nickel. A significant twenty fold sluggish secondary creep rate was achieved through GBE in Ni-16Cr-9Fe at 360°C. In superalloy V-57, 15-fold reduction in steady-state creep rate along with huge drop in primary creep strength, was achieved. Suppression of grain boundary carbide precipitation was possible through inclusion of low-∑ boundaries in alloy 617. Commercially pure nickel after GBE treatment was found to have enhanced resistance to hydrogen embrittlement as fraction of special boundaries increased from 46% to 75%. An addition 20-30% increase in fracture toughness was

also attributed to the presence of special boundaries resistant to segregation (D. Drabble 2010). Improvement in superalloy performance properties is given in Table 2.9 (Lehockey, Palumbo, and Lin 1998).

Even in corrosive environment of H_2SO_4, commercial lead-acid battery grids manufactured through GBE route was found to have higher longevity and better performance than a conventional one. Superalloys like Alloy 600, which is used in pressurized water reactors as nuclear-steam-generator tubing, also responded excellently after GBE treatment was given as magnitude and variance in intergranular crack depth decreased because of 70% special boundary in the microstructure. Sensitization in 304 stainless steel was found to be suppressed when twin–related low-energy boundaries in the microstructure ruled out chromium depletion. Thus, percolation of intergranular corrosion was arrested as chromium depletion was disrupted. Heat affected zone (HAZ) performance in 304 and high-nitrogen austenitic stainless steel was improved by making the boundaries resistant to sensitization and nitride precipitation respectively through GBE. Corrosion rate of 304, 316 stainless steel was found to be attenuated in corrosive environment after GBE was performed. Oxidation behavior of alloy 800H in supercritical water was changed and oxide spallation was reduced after GBE treatment was given (D. Drabble 2010).

Table 2.9. GBE benefits summarized for Ni- and Fe-based superalloys in terms of performance improvement (Lehockey, Palumbo, and Lin 1998)

Performance Property	Applicable Alloys	Improvement* (Pct)
Weldability	V-57, 738	up to 5000
Low-temperature corrosion	625, V-57, 738	40 to 50
High-temperature corrosion		
Pitting	738	90
Sulfide spiking		30 to 40
IGA		50
Creep		
Grain boundary sliding	625, V-57	>90
Power law		50
Fatigue	V-57, 738	50 to 75
Tensile properties		
Proof stress	625, V-57, 738	no significant change
UTS		
Ductility	V-57, 738	no significant change
	625	marginal increase

*This column represents improvement of GBE-processed alloys (*i.e.*, $F_{sp} > 50$ pct) over those conventionally processed (*i.e.*, $F_{sp} \sim 10$ to 20 pct).

The dreep drawability of Interstitial-Free steel components is dependent on ductility and cold-work embrittlement. Low-∑ boundaries were found to be a strong barrier to crack propagation thus improving their fracture strength which is of utmost importance during fabrication of autobody panels (Palumbo, Lehockey, and Lin 1998).

Further information on commercialization of GBE, patents filed and owned by different companies, processing analysis, market analysis, competition and cost analysis can be found in (Zelinski 2005).

2.11 Materials Selection:

Microstructure evolution during TMCR involves interaction among several metallurgical phenomena like recovery, recrystallization, grain growth and precipitation. Except for recovery, most of the processes are involved with movement of high angle grain boundaries (HAGB). In particular, when the steel is rolled at very high temperature, austenite grain size is a parameter that needs to be controlled with utmost care. This is one of the reasons of having significant importance to study the austenite grain boundary- their migration and character distribution. Also, the effect of solute microalloying elements, like niobium, to slow down austenite boundaries during grain growth has been a problem of scientific merit from the heart of advanced steel technology. As during TMCR, most of the commercial steels are water quenched after deformation which no more allows the austenite phase to be retained at room temperature. Phase transformation on slow cooling (producing ferrite) or fast cooling (producing martensite) obscures dislocation substructures created in austenite during processing. As some of the key objectives of this research work are to explore nature of austenite boundary movement, quantifying austenite growth kinetics, quantifying Nb solute drag on austenite grain boundaries and effect of different alloying elements on austenite growth, it is imperative to have them studied in austenite condition.

To study the effect of solute Nb on HAGB mobility by quantifying solute drag, it is necessary to look into austenite grain boundaries. Experiments performed on commercial microalloyed steels with low carbon (~0.05 wt%) suffer from inaccuracy due to occurrence of precipitates which consume the solute Nb dissolved in matrix. Yamamoto et al. decarburized commercial

microalloyed steels to bring the carbon down to ultra-low level (0.002 wt%) to rule out precipitate formation so that all the Nb remains dissolved in matrix as solute Nb (Yamamoto, Ouchi, and Osuka 1981). But, etching the prior austenite grain boundaries (PAGBs) with almost no carbon and out of ferritic microstructure was found to be a problem when this research work was started. In quest of a system where austenite phase can be retained at room temperature to observe the interaction of solute Nb with PAGBs, design of a new model alloy came into the picture.

The design of a system in which effect of Nb as solute and precipitate can be studied is really challenging as so many factors come into the picture. The first step is selecting conditions to come up with a room temperature austenitic alloy. To design such a model alloy, a number of systems were studied using TCFE6 database of Thermo-Calc in which Mn was added as austenite stabilizer. A considerable amount research of work on austenitic model alloys with Ni as stabilizer has been done by several researchers. Of them Fe-30%Ni, Fe-70%Ni were found to be used more (H. Zurob 2003; Nagarajan 2012; Rainforth et al. 2002). The current study aims at exploring grain growth in Mn- stabilized austenitic steels due to some attractive features. Firstly, Mn effectively stabilizes austenite which is better than Ni. Previous study with Ni stabilized austenitic model alloys (Fe- 70%Ni) showed that Ni increases the solubility of Nb to a huge extent for which solute drag effect dominates. The Mn stabilized alloys are particularly appropriate to study strain induced precipitation (SIP) which was one of the goals of this research (H. Zurob 2003). The advantage of using Mn is it doesn't increase the solubility of Nb that much and although it has attractive interaction with carbon, Nb has more strong carbide forming tendency leaving very little amount of carbon available for Mn. Although, this research work could not look into the precipitation aspect during TMCR, alloys designed for this purpose will be discussed in brief. Due to some interesting findings from the grain growth study, this research mostly preferred to focus on detailed exploration and understanding of the physics behind growth process in austenite phase and microstructural factors interacting with it. This fundamental study on high Mn model alloys might be considered as the first step to uncover some of the black boxes in the field of modern steel research, and the ideas extracted from it can also be extended to understanding grain growth feature in TWIP steels in near future.

Design considerations for model alloys to study strain induced precipitation are listed below:

- The alloy must be austenitic at room temperature with precipitates of NbX type only. The amount of Mn required to stabilize must be carefully balanced. Very high amount of Mn may lead to formation of some Mn-intermetallics while low Mn may make austenite phase very unstable at room temperature. As the microstructure observation requires some metallographic sample preparation, unstable austenite may generate numerous twins while cutting, mounting and polishing and even at lower temperature the unstable austenite may get transformed to martensite. At the same time, amount of carbon should also be more than 0.4 wt% so as to reduce the probability of austenite-to-martensite transformation.
- The precipitates must form on dislocations with cube –on-cube relationship. According to Kotval (H. Zurob 2003), the minimum stacking fault energy (SFE) of a system must be at least 50mJ/m^2 to get precipitation on grain boundaries and whole dislocations. Even, systems with SFE ranging from 20 to 50 mJ/m^2 show Nb precipitating on Frank partial dislocations. The objective of our alloy design includes judicial balance of between Mn, C and Nb as they have opposing effect on SFE. Apart from getting stabilization of austenite phase, high SFE would help dislocation cross slip and avoid twin deformation.
- The dissolution temperature of the precipitates is an important factor as it decides the maximum amount of Nb and C which can be kept in the chemistry. Amount must ensure complete dissolution of the precipitates at high temperature as coarse, undissolved particles play detrimental role during re-precipitation.

Considering above points, three model alloy chemistries were designed with a judicial balance of all the required criteria.

Design considerations for model alloys to study grain growth and solute drag are listed below:

- Like previous case, the system must have stable austenite phase retained at room temperature. As the interaction of solute Nb with moving HAGB is to be quantified, the study requires measurement of the austenite grain size through revealing austenite grain boundaries clearly. A Mn stabilized austenitic model alloy is therefore required for this.
- There should not be any precipitate as it decreases the matrix solute concentration. This will result in inaccurate assessment of solute drag. The amount of Mn must ensure proper solubility of Nb so as to detect its effect on HAGBs.

- To study the solute drag effect on HAGB movement during recrystallization, the SFE of the system must ensure dislocation slip or glide to be the only deformation mechanism. Despite having low SFE at room temperature, the high Mn austenitic steels are suitable candidate to study solute drag. This is because at very high temperature where solute drag is significant their SFE becomes very high to give slip as the deformation mechanism.

Based on above considerations, three model alloys were designed to study solute drag effect of Nb.

3 Experimental Details

3.1 Development of Materials:

Based on the discussion made in section 2.11 on design of materials, model alloy chemistries are finalized for studying solute drag effect. This particular series of alloys are termed as 'S-series'. Using the most current Thermo-Calc(Q) database generated by Nakano et al. (Nakano and Jacques 2010), the SFE is calculated in an equivalent series with addition of 0.5% carbon so as to get an idea of austenite stability.

The effect of different alloying elements on SFE is considered in detail as it dictates austenite stability. Nakano et al. found that SFE initially decreases with Mn content upto ~13 wt% and then increases (Figure 3.1. a). So, alloying with 30 wt% of Mn confirms higher value of SFE as required. Moreover,

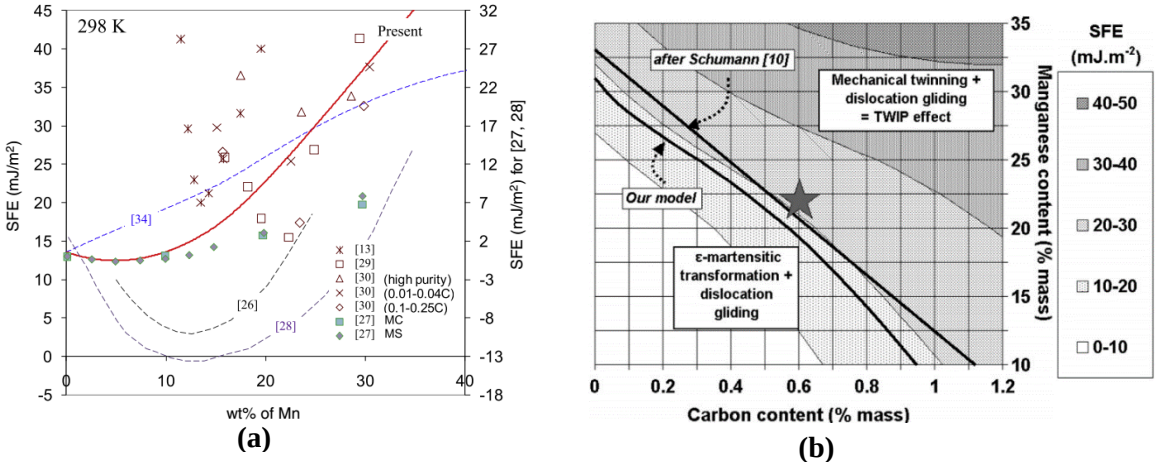

Figure 3.1. a) Composition dependence of SFE with wt% of Mn (Nakano and Jacques 2010), b) Phase-stability diagram in C-Mn plane at 300K with calculated SFE ranges (Scott et al. 2006)

probability of formation of ε-martensite from austenite is also reduced at high temperature based on the iso-SFE line calculated indicating austenite phase stability (Nakano and Jacques 2010; Allain et al. 2004). In addition to that, it was found 1%Nb addition to low carbon-low nitrogen Fe-Ni alloy lowers the SFE by 23 mJ/m^2 (Dulieu 2001). Keepin Nb level as low as 0.03, 0.05 and 0.07wt% doesn't really make significant reduction in SFE. The SFE achieved by the above design is reconfirmed from the research of Scott et al. (Scott et al. 2006) where composition dependence of SFE was analyzed by plotting the iso-SFE lines. As per Figure 3.1. b, the designed chemistry

offers SFE high enough to give dislocation slip as the only deformation mechanism and ensures stable austenite phase. At the same time, this design also satisfies the SFE of the model alloys at room temperature to be close to that of commercial microalloyed steel (~75mJ/m^2) (Nagarajan 2012).

The 3 model alloys designed for solute drag study are given in Table 3.1.

Table 3.1. Model alloy chemistry designed for Solute Drag (SD) study

ID	%Fe	%Mn	%Nb
S_1	bal	30	0.03
S_2	bal	30	0.05
S_3	bal	30	0.07

The above S-alloy series was melted and cast through the Resource for the Innovation of Engineered Materials (RIEM) program of CANMET Materials, Canada. A detailed ICP analysis of all the cast ingots was also provided which indicates very small amount of impurity present in terms of O, N. The achieved Mn level was shown in the ICP analysis to be very closed (29.07-29.29 wt%) to the target value. The cast ingots were then rolled using specific hot-rolling schedule. The final objective was to break the dendritic structure and achieve uniform grain size. There was a requirement of the final thickness to be within 13-15 mm so that further cold rolling, machining is possible on the hot rolled stock. The ingots were reheated at 1225°C for 1 hour followed by 3 passes of 14%, 18% and 17%. The S_1 ingot was then given 7 more passes with percentage reduction varying from 13-20%. Reduction during last two passes were kept around 13-17%. The plates were cooled in air to avoid quench stress build-up. After receiving the hot rolled plate of thickness 15mm, the microstructure was found to be somewhat coarse (~100 μm) with lots of bands present.

The next objective of preparing the S-series alloys for grain growth study was to apply specific cold rolling-annealing schedules to come up with uniform grain size, no bands in the microstructure and achieve mean grain size somewhere between 30-50 μm. Several trials were taken on 3 different Nb levels and optimized schedule found for achieving above target is given in Table 3.2.

Table 3.2. Final cold rolling-annealing process window optimized for S-alloy series

Alloys	%Cold Rolling	Annealing temperature (°C)	Annealing time (min)
S_1	50	950	120
S_2	45	1000	30
S_3	70	1000	30

It must be mentioned that the important aspect came across during above trials was existence of

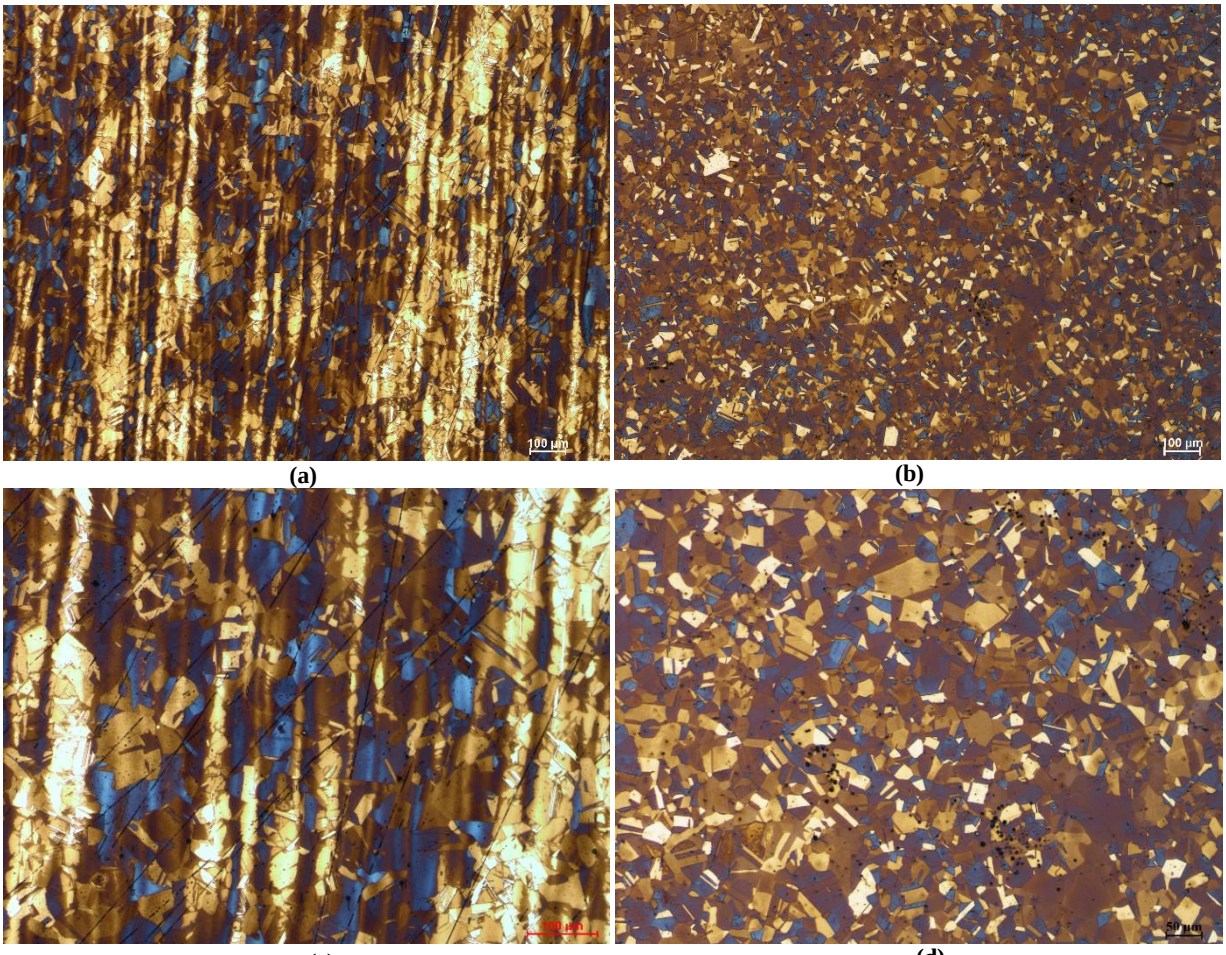

Figure 3.2. a) As-received microstructure of S2 (Fe-30Mn-0.05Nb) after hot rolling at 50-X magnification, c)100-X magnification, Microstructure of the same sample at b) 50-X , d) at 100X magnification after selective rolling-annealing treatment for refining the grain size.

some giant grains in the microstructure. Increasing the rolling reduction was not always a solution to avoid those big grains in the distribution. The nature of this type of giant grains still remains a mystery. It might stem from the cast structure that behave as big semi-rigid inclusions that follow the plastic flow of the adjacent surrounding smaller grains but leave themselves undeformed and un-recrystallized. Till date, complete removal of them from the microstructure has not been possible. Some suggestions on doing upset forging were made which might kill the giant grains. A comparison between as-hot rolled microstructure of S_2 is made with its counter-part which was undergone further deformation-annealing to improve its microstructure in terms of grain size and distribution. As it is seen from Figure 3.2. a, c, the average grain size is close to 100 μm and the microstructure has several bands with nearly a spacing of 50 μm. Improvement of grain refinement and nearly uniform grains are obtained by 45% cold rolling followed by 30min annealing at 1000°C as can be seen from Figure 3.2. b, d.

Another set of alloys were designed to study the effect of Mn on growth kinetics in absence of Nb. This study was aimed at correlating SFE with mobilities to elucidate their effect on grain growth. Variable Mn content resulted into systems with different SFE values (Table 3.3).

Table 3.3. Model alloy (M-series) chemistry designed for studying effect of Mn on grain growth

ID	%Fe	%Mn	%C
M_1	bal	30	0.5
M_2	bal	15	0.5
M_3	bal	6	0.5

Above alloys were melted and cast in Arcelor Mittal, France. After casting, the ingots were rolled in their pilot hot rolling mill. The rolling stand was equipped with pyrometers, on either side, to carefully monitor the temperature of the stock. The ingots were rolled into plates of 6 mm thickness in 4-5 passes. The final cooling was done with a mixture of air and water.

3.2 Grain Growth experiments:

The austenite grain growth experiments were carried out on Fe-30Mn and Fe-30Mn-0.5C alloys to get an idea of the nature of growth kinetics in the Fe-30Mn system. Following this, S-series alloys with varying niobium were chosen for next set of growth experiments. Another set of growth experiment was carried out with the M-series. For the grain growth experiments, the samples were cut from the stock whose thickness is more than 5mm. The samples used for this experiment are 10mm x 6mm x 6mm in dimension. The experiments were performed using a high temperature tube furnace capable of operating under different types of atmosphere. The samples were connected to a stainless steel rod at one end (Figure 3.3) and the rod is pushed into the heating zone once the tube atmosphere is purged with argon to completely remove air.

The temperatures of interest were 1000°C, 1100°C and 1200°C. The objective of choosing this particular window is to have some parity with industrial rough rolling process. When first few big deformation passes (roughing) are given, the temperature of the slab usually remains above 1000°C. At this high temperature, the grains are very prone to coarsening leading to poor final properties. The study of austenite boundary migration in the range of 1000-1200°C is, therefore,

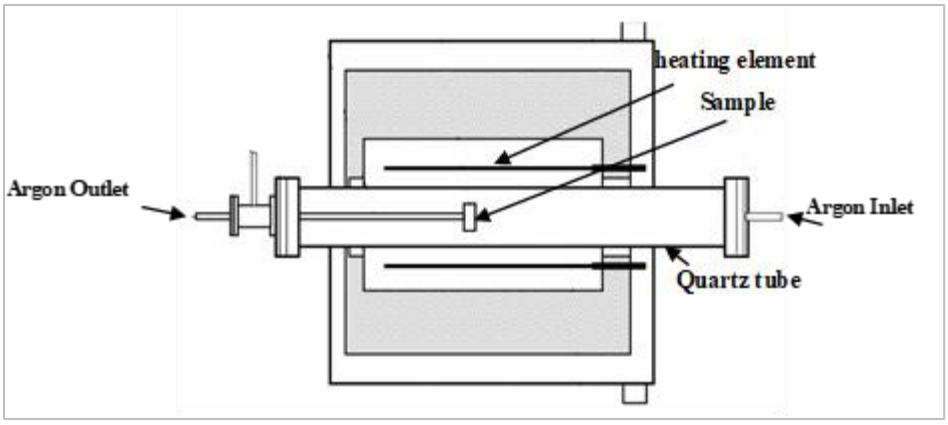

Figure 3.3. Experimental set up for austenite grain growth kinetics study (Zhou 2010)

expected to be helpful in controlling grain coarsening occurring between roughing and finishing passes. Although, in industrial scale the time available for this coarsening is found to be less than 2-3 minutes, for the purpose of understanding boundary migration process, the grain growth experiments are conducted for a wide time window depending on temperature. As the growth is expected to be faster at high temperature, the soaking time is kept limited within 24 hours at

1200°C while for 1100°C and 1000°C the soaking times were upto 4 days and 8 days respectively. In Figure 3.4, short schematics of the heating cycles used for studying grain growth in Fe-30Mn

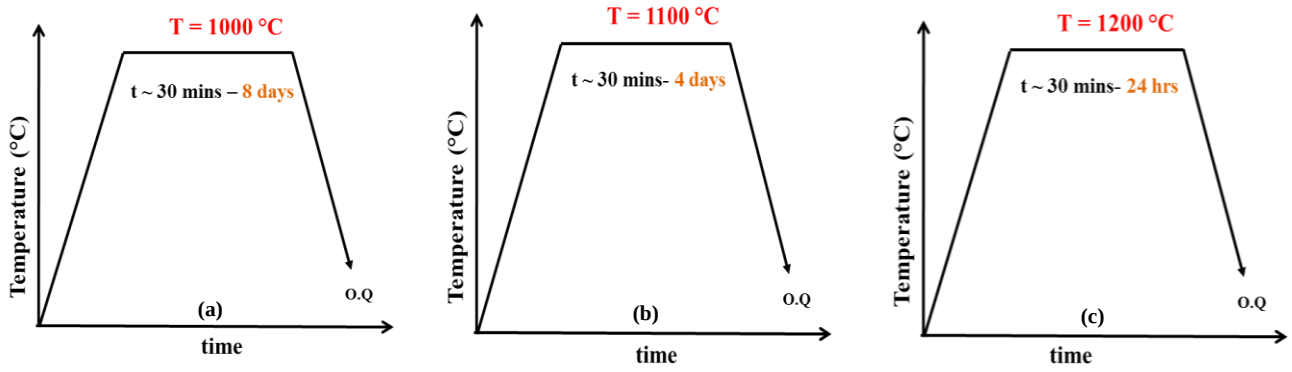

Figure 3.4.Graphical Illustration of the experimental scheme used to study grain growth in Fe-30Mn alloys with and without niobium at a) 1000°C, b) 1100°C and c) 1200°C

steel with and without Nb are given. The samples were finally quenched in oil bath. Different quenching media was tried to cool the sample. Of them, water quenching was found to give unreliable microstructure for grain growth study. Of air cooling and oil quenching, the second one performed the best and it also required less time. In terms of quench stress, oil quench is known to impart less stress on samples as was also observed in another work on Fe-24Mn steel (Liang 2008). For all the samples, utmost care was taken to transfer the sample to the oil bath very fast so

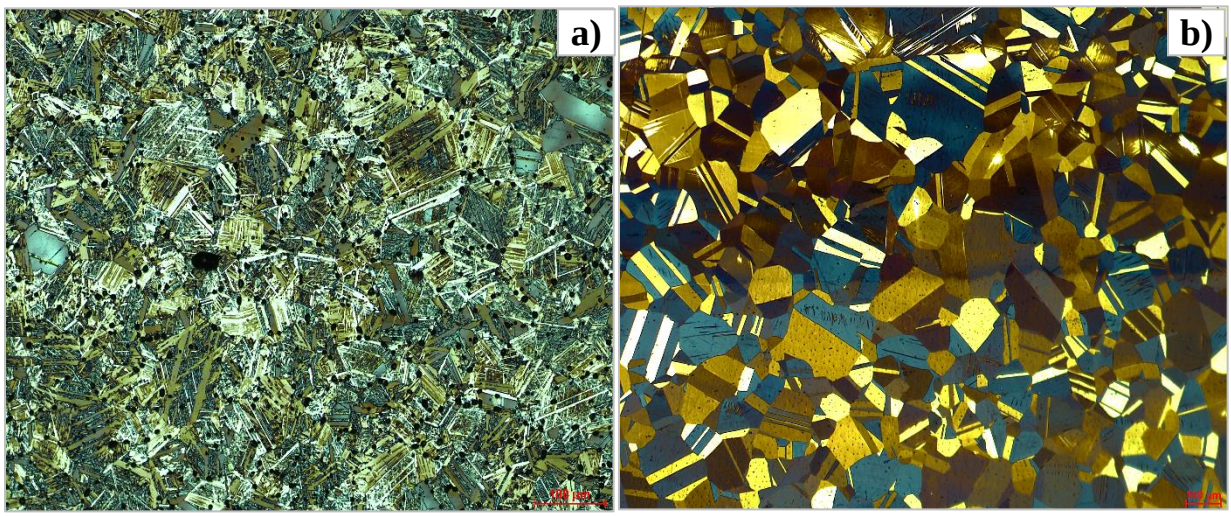

Figure 3.5.Microstructure of Fe-30Mn-0.03Nb samples after 8 day heat treatment at 1000°C after a) delayed transfer to oil bath showing transformed microstructure, b) quicker transfer to oil bath showing completely austenitic microstructure

that no undesirable microstructural change (in terms of ε-martensite formation) takes place. This is shown in Figure 3.5. a. A bad quenching resulted into formation of ε-martensite in one of the samples containing Fe-30Mn-0.03Nb after quenching from 1000°C. The same material when underwent a quicker transfer to oil bath from same temperature was found to have completely austenitic structure at room temperature with no distortion of the microstructure (Figure 3.5. b). However, this problem was encountered mostly in the S-series samples with no carbon and added niobium to Fe-30Mn base.

It must be mentioned that samples for long duration heat treatments and the ones at 1200°C were found to be internally oxidized very badly even in argon atmosphere. An attempt was taken to prevent this by using high purity argon gas and purging for a long time before inserting the sample. Not much improvement was achieved through it. Also, the damaged samples even after removing considerable amount of material from the surface, responded very bad during metallography and other characterization. The most effective way to avoid oxidation is to seal the samples in quartz tube. This was done in BIMR lab using a special vacuum system installed with a glass blowing facility. 10mm diameter quartz tube was cut into 10 cm long pieces with two ends open. One end was then fused using a glassblowing torch to make a closed end and quenched in water. After this, the small piece of the metal sample was put inside carefully so that it doesn't hit the sealed end to crack it. The tubing with the sample was then connected to the vacuum system and once the air pressure drops to a considerable extent, the other end is also fused to complete the capsuling of the sample. Theses capsules were pushed into the heating zone of the furnace by a specially designed rod during the high temperature or long duration heat treatments. During quenching, the same pusher rod is used to push the capsule to make them fall into the oil bath resting at the end of the furnace tube. Once it falls into the oil, a heavy bar was used to hit the capsule for breaking the sample out to quench in oil. Much expertise is required during quenching of the capsule samples which came after several trials. In terms of the M-series, the grain growth experiments were conducted only at 1200°C up to 24 hours.

3.3 Sample Preparation:

Under this section, a detailed description of the methods used for preparing samples for characterization will be provided.

3.3.1 Cutting and Mounting:

For the grain growth study, the samples were cut from the rolled plate using Struers® Accutome-5 precision cutter using resin bonded abrasive alumina blade. To avoid mechanical twin formation, delicate cutting parameters were chosen. The programming named as "ferrous-soft" was used with a feed rate of 0.01 mm/sec. This was found to be appropriate for having stable austenite microstructure at room temperature. The samples were cut along the Transverse Direction (TD/

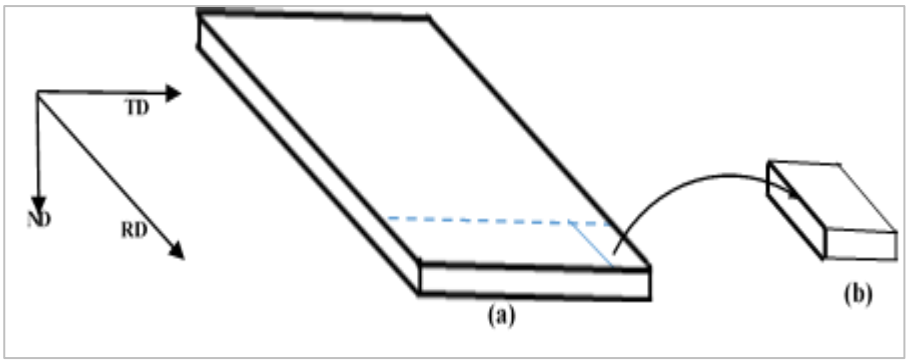

Figure 3.6. a) Configuration of grain growth samples with respect to rolled plate, b) grain growth sample with its surface of interest marked by arrow and enclosed by bold lines

ND) (blue dotted line in Figure 3.6. a) with an width of at least 10-12mm. Small pieces were then cut along the blue solid line parallel to the rolling direction. The surface of interest (RD/ND) is being shown by arrow in Figure 3.6. b. This surface was chosen so as to observe the growth of the recrystallized grains.

To avoid any kind of phase transformation, the samples were cold mounted. It was found that the hot mounting although works fast, the machine operates at temperature close to 180°C and applies high pressure to compact the bakelite powder. Therefore, although time consuming, cold mounting route was opted for all the samples. 25 grams of epoxy resin (Struers® epofix) was poured in a paper cup to which 3 grams of epofix hardener was added. The reason behind using epoxy resin is because of its good adhesion, high viscosity, ability of excellent infiltration and most importantly its resistance to etchants and solvents. Another advantage of using epoxy resins is its low linear shrinkage and transparency. The mixture was then stirred gently for at least 5 minutes to avoid lots of bubble formation. The whole cup was then placed inside a desiccator equipped with vacuum pump. The pump was turned on with the lid closing the top of the desiccator to make it completely air tight and the air suction was continued until almost all the bubbles come up to the surface of

the mixture and disappear. The pump was then turned off. The resin mixture was then slowly poured on the sample into black mold whose inner surface was lightly greased for making the removal process easy. It usually took 6 to 8 hours to cast the cold mount which is called ‘curing time’. Improper mixing or remaining bubbles at the bottom created a gap between the sample edge and the mount which later on had debris accumulation during polishing resulting into scratches on the sample surface.

3.3.2 Metallographic Preparation:

This method was primarily used to prepare samples for optical microscopy, electron back scatter diffraction, atom probe tomography and thermal etching. It is to emphasize again that being a low stacking fault energy material, all high Mn samples are very sensitive to deformation. While doing mechanical grinding or polishing, careful application of load must be practiced so as to avoid austenite-to-epsilon martensite transformation. Also, because of very soft matrix of the alloys, it is very difficult to remove scratches compared with any conventional steel sample. Any kind of particles (although, current samples are precipitate free) in the form of inclusion or debris embedded in the matrix may get loosened and come out resulting deep scratches on the surface during the polishing stage. Also, the samples were found to be extremely sensitive to water corrosion leaving rust stains on the surface. Another important aspect of sample preparation is to have a surface with as minimum as possible surface and sub-surface damage which actually makes EBSD pattern capture difficult.

Considering all the above, a specially designed grinding and polishing procedure was adopted for all high Mn samples to observe their microstructure. This was carried out in a Struers® Tegramin 25 Automatic Polisher.

Grinding:

1. The following SiC papers are used 500/ 800/ 1200/ 2400/ 4000-US. Each paper was placed down and the base turned on, using the wax block lightly coat the SiC paper (Do this for EVERY paper), this helps to prevent SiC particles from being pulled out and embedding into the sample.

2. Once the grinding is complete the samples were removed from the specimen holder and wiped with a paper towel (helps avoid oxidation). Then, the samples were rinsed with ethanol to remove any SiC particles which maybe on the sample. Also the specimen holder needs to be washed with water and dry before proceeding to the next step.

3. The loads and time are as follow:

SiC Paper	Load (Newton)	Time (Sec)	RPM (Base)	RPM (Head)	Direction
500	10	80	200	150	>>
800	10	80	180	120	>>
1200	10	70	150	110	>>
2400	10	90	150	100	>>
4000	15	70	150	100	>>

Polishing:

The polishing took quite a bit of time to end up with a scratch free sample. It was very important to look at the sample under the microscope after each polishing step to ensure the preparation is acceptable.

1. Between each step, the samples were washed by first rinsing it with ethanol. Then using a cotton ball soaked in ethanol, the surface was gently rubbed followed by another rinse in ethanol. Finally, the samples were dried in hot blow of air. This step was tried as quickly as possible to avoid corrosion. It was found that working with maximum 3 samples at a time made it possible to have corrosion free surface. Also, the samples for EBSD were not at all rinsed or treated with ethanol. Use of HPLC methanol for cleaning and rinsing was found to be extremely helpful to avoid corrosion.

2. The specimen holder needs to be cleaned with water and dried with paper towels before placing it back onto the polisher.

3. The cloths need to be cleaned by pressure washing the surface of the cloth and drying in front of the hair dryer (this is critical if a good polish is aimed for).

4. The last 2 steps are done manually using the spray bottle and usually when high quality surface finish is required e.g., during EBSD. The cloth was coated with the diamond suspension with spraying it every 30 seconds onto the cloth. For the last 30 seconds, the lubricant button in the polisher was manually pressed and held so that the polisher pump the lubricant onto the cloth. This helps to clean the samples and also avoids corrosion.

5. The polishing parameters are detailed in the following table.

Surface	Load (N)	Time (min)	Suspension	Lubricant	RPM (Base)	RPM (Head)	Direction
MD DAC	10	6	9 μm	Blue	130	100	>>
MD MOL	10	5	6 μm	Blue	130	90	>>
MD MOL	5	6	3 μm	Blue	100	80	>>
MD NAP	5	6	1 μm	Blue	100	80	>>
MD NAP	5	4	0.5 μm	Blue	90	50	>>
MD NAP	5	3	0.1 μm	Blue	80	60	>>

To get a better surface for EBSD, the samples were polished upto 1 μm step and were then manually oxide polished in 0.05 μm colloidal silica. As the sample was found to be prone to water corrosion, a 1:1 mixture of colloidal silica in propylene glycol was used on a neoprene cloth (MD-Chem) designed for oxide polishing. A load of 10 newton was used for 3 minutes followed by a short duration forced water cleaning and quick rinsing with methanol. The samples were dried using compressed air. Another 2 minutes of silica polishing followed cleaning was performed twice and the sample was observed under light microscope before it was taken for electropolishing. Due to slight etching effect of colloidal silica, some grain boundaries and annealing twins may be lightly visible on the scratch-free surface.

3.3.3 Etching:

As the primary objective of this thesis is related to grain size measurement, the most convenient method to visualize grain boundaries was etching. For different alloys, different types of etchants were used. For all of them, it was mandatory to have a clean, polished surface free of any artifacts. Etching is mainly a controlled corrosion process occurring due to electrolytic action between different surface parts of various potential. Usually a mirror polished surface reflects incident light

uniformly making the different surface features undistinguishable. Creating a contrast by difference in reflectivity is the primary objective of etching. Conventional 2% Nital did not perform well on the alloys. The presence of annealing twins make the etching process important to distinguish between grain and twin boundaries. 2% Nital can very lightly outline few of the High Angle boundaries and leave a microstructure which is unsuitable for grain size measurement. Of various etchants tried on the alloys, 5% Nital successfully etched all the grain boundaries including the twins particularly in Fe-15Mn-0.5C and Fe-30Mn-0.5C alloys. The Nital must be freshly prepared in high purity low carbon (HPLC) methanol before etching. Swabbing etching was not helpful. Therefore, a plastic wash bottle with an integrated spout on one side was used. The bottle was filled with 5% Nital and after closing the lid, it was pressed so that Nital comes out with pressure through the spout. This way, the samples were etched uniformly without any swabbing marks on the surface. The etching time usually varied between 10-15 seconds. For, Fe-30Mn-0.5C and Fe-15Mn-0.5C alloys, this etching while carried out for 20 seconds, produced a dark coloration (purple or coffee color) of the surface which was an indication of end time of etching. The samples were then force cleaned in methanol and dried in hot air. While using methanol by force cleaning, the dark coloration of the surface disappeared but returned while drying in hot air. The final color of the perfectly etched sample is light blue or coffee color. This color may vary based on the prior heat treatment of the sample.

For the Fe-30Mn alloys with and without niobium, however, above etching method was not sufficient to reveal the boundaries. This is probably because of absence of carbon in the alloys. A specially designed two-step etching was found to be excellent in creating contrast while imaging. At first the samples were etched in 5% Nital similar to what is described above except the duration. This Nital etching on the alloys should be done for 5-8 seconds. After this, the etched surface must be examined under light microscope. If the microstructural features are very faintly visible, the sample is ready for the second etching step. If the surface still looks like a mirror polished one, another 5 seconds of etching in 5% Nital was done. This happened particularly when the niobium content of the sample was increased. In particular, the pre-etching step helps to increase the sharpness of image. However, the second step of etching is known as color etching or tint etching. Of many tint etchants, Klemm's I etchant was found to be the most effective. A 50 ml aqueous saturated solution of sodium thiosulfate was prepared in distilled water. Normal tap water, once used, performed very bad in etching instead the sample got corroded extremely fast. To that 1 gram

of potassium metabisulfite was added. Usually, the mixing was done on a hot plate with a temperature around 60°C and continuously stirring with a glass rod. It is important to note that the final etching solution should not reach the boiling point and etching must be done once it reaches room temperature. It must be remembered that tint etching should not be performed by swabbing as it prevents film formation. The sample was dipped, with the polished surface up, in and out of the solution and this was continued until the Nital etched surface gets dark purple or violet coloration. In fact, during last few seconds of etching, the sample should remain motionless until the color development is prominent. The sample was then taken out and quickly washed in warm distilled water followed by rinsing in methanol and drying in hot air. For this type of etching on austenitic steels, it is always better to use plastic tongs rather than metallic ones.

Klemm's I is a complex type of tint etchant forming a complex film of sulfide, oxide and sulfate. The key ingredient of it is metabisulfite ion ($S_2O_5^{2-}$) present as potassium salt to which thiosulfate salt is added. This causes decomposition of metabisulfite in aqueous solution in presence of metal ions giving rise to SO_2, H_2S and H_2. Of them, SO_2 acts as a depassivating agent on passivated surfaces like stainless steels, H_2S acts a source of S^{2-} which forms the sulfide film of iron. The thiosulfate decomposition takes place in a similar manner. Correct proportion of chemicals mixed to form the etchant is important to control the stability of film by making the reaction (controlled corrosion) product deposit on the surface instead of getting redissolved and reverted to the etching solution. Once freshly prepared, Klemm's I etchant can be used upto 3-4 hours and then should be discarded.

The coloration is due to formation of a sulfide-based thin film of thickness 400-50000 Å which

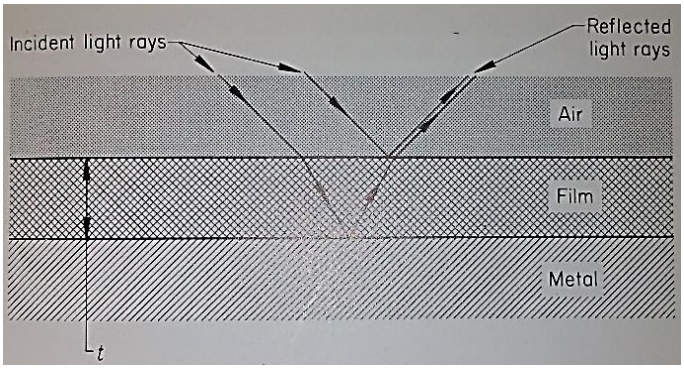

Figure 3.7. Demonstration of interference effect of light through air-film-metal causing coloration in image (Beraha and Shpigler 1977)

usually colors the grains and the twins completely through the effect of interference. The mechanism due to which interference produces color is shown in Figure 3.7. When incident light hits a metal surface coated with a film, it gets reflected from both film and metal surface. This introduces two competing reflected waves whose interference depends on wavelength of the light source in air (λ), film thickness (t) and refractive index of the film (n). Whenever, the effective path difference of the two rays is an even multiple of $\lambda/2$, constructive interference will occur. This path difference is proportional to twice the film thickness. Thereby, considering the effect of film causing the slowing down of the reflected wave, interference is favored at integral multiples of $\lambda/4$. In case of odd or even multiples, destructive (out of phase) or constructive (in phase) interference happens respectively. If white light gets reflected through such a metal-film-air system where the film thickness makes the green portion of the light reflected from metal surface out of phase with the same from film surface, then the resulting wave will have attenuating effect of destructive interference and will be of magenta color (complementary to green) appearing at thicknesses of 1, 3, 5… time(s) $\lambda_G/4n$ (λ_G is the wavelength of green light in air). This is how the coloration of different microstructural features happens.

The thickness of the film varies from one grain to other based on their orientation and this causes variation in color for different grains in the microstructure. If white light reflects from a progressively thickening film on the metal surface, no color will be observed initially because the film is too thin causing the interference occurring at ultraviolet region (~3500Å). Gradual thickening of the film makes the interference happen within blue-violet region (~ 4500 Å) and blue lights will undergo destructive interference giving rise to complementary yellow reflected light. Finally, a film thickening upto 5000 Å will cause green light interference as described above and results into magenta coloration. Gradually, the interference passes out of the visible range and belong to infrared domain as the film becomes thicker. It is worth mentioning that a very high quality surface finish is required before tint etching. Otherwise, most less prominent but existing scratches will be revealed by interference film (Beraha and Shpigler 1977; Vander Voort 1984).

3.3.4 Electropolishing:

Almost defect-free surfaces are required for electron backscatter diffraction (EBSD) studies to successfully capture and index Kikuchi patterns in annealed austenitic high manganese steel samples. In most cases, substantial amount of strain from previous coarse grinding is left as residue

up to subsurface are difficult to remove even by finest colloidal silica polishing. This makes the crystallographic information capture very erroneous, difficult and time consuming during EBSD. The most effective way to minimize above problems is eletropolishing. This method is a comparatively older one that came into practice before introducing diamond abrasive based mechanical polishing. Highest quality surface preparation was possible by this technique through controlled use of current and proper electrolytic medium.

In this work, almost all type of high manganese steel samples were prepared by eletropolishing whenever there was a need of performing EBSD or site specific atom probe experiments. The method involves the sample to be working as anode of an electrolytic cell with an appropriate electrolyte. Two different types of electrolytes were used. For Fe-30Mn, Fe-30Mn-0.5C and Fe-15Mn-0.5C alloys, a solution of 10% perchloric acid in HPLC methanol was used. For the samples containing niobium, especially Fe-30Mn-0.07Nb, a solution of 10% perchloric acid in acetic acid was used. At first the stainless steel pot which acts as cathode was placed on a stirrer plate with a magnet at the center. Based on requirement, acetic acid or HPLC methanol is poured into the pot. In all cases perchloric acid was added to the solvent as the reverse is harmful to do. Let the magnet stir the solution for 1-2 minutes to ensure a good mixing. To avoid any kind of heat generation due to chemical reaction, it is suggested to put a cooling system circulating around the steel pot throughout the time of electropolishing. Once the mixing is done, it is suggested to remove the

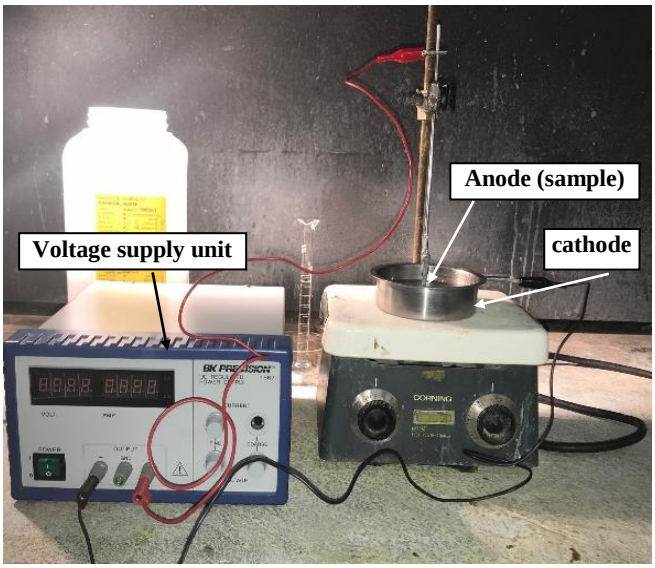

Figure 3.8. The experiment set-up used for electropolishing the samples prior doing EBSD

magnet as it otherwise prefers to stick to the sample during the electropolishing. The sample was then connected to an alligator clip with its surface of interest down. The steel pot is connected via black and the sample alligator via red wire to the rectified power supply which was a BK PRECISION ® DC regulated power supply (model 1667) (Figure 3.8). Finally, the sample rod is lowered into the solution and the power in turned on.

For most of our electropolishing, voltage around 25-40 V was used and the first run was continued for 1 minute. After this, the power is turned off and the sample was quickly removed from the clip with tongs and vigorously shaken into a beaker containing methanol to clean the residue. A slow cleaning will result into reaction product build up on the electropolished surface manifested by rusty appearance. In that case, the sample must be re-electropolished for 1 minute to clean the surface by removing the product layer. For niobium containing samples, irrespective of anything, a second run for another 30-45 seconds was practiced to get best result. After cleaning the samples were dried in compressed air to ensure no methanol residue causing any stain on the surface. It must be mentioned that all these operations must be done in a highly powerful fumehood. In almost all the alloys, a light etching effect was observed under light microscope after electropolishing. In case of no niobium alloys, acetic acid and perchloric acid solution was found to create cloudy patterns at the surface. This is why a second type of solution containing perchloric acid in methanol was used. Also, with very high voltage around 40 V, surface waviness became prominent which made some parts during EBSD out of focus. In addition to that, high voltage makes the flow lines of the cold rolled –annealed samples highly visible. Considering all above difficulties, it should be mentioned that, a universally applicable electropolishing scheme for all samples is not possible to design. The quality of electropolishing depends on many factors like polishing area, current density, voltage, time, orientation of sample and cathode, cathode-to-anode area ratio, depth of sample under the solution, cathode material, bath temperature, degree of prior mechanical treatment, washing technique. Once the eletropolished surface is achieved no further contact should be made with it and can be preserved inside a good vacuum desiccator for at least a week.

3.4 Characterization:

To characterize the samples, mostly optical microscopy and EBSD were used. For sample preparation of atom probe study, focused ion beam milling was used. In this section, a brief description of the modes of operation will be given.

3.4.1 Optical Microscopy:

Grain size measurement of the samples particularly requires a very good optical image taken by

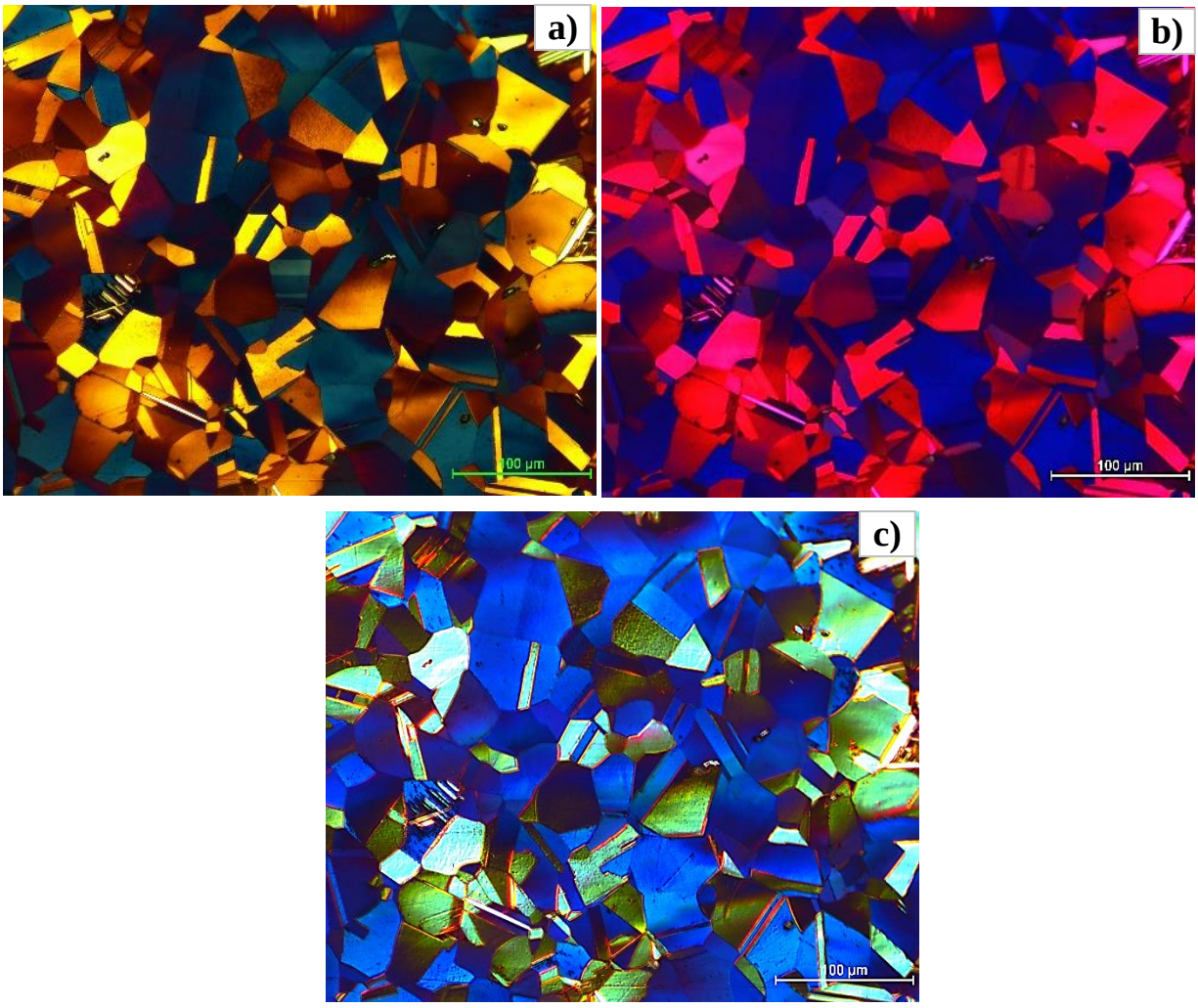

Figure 3.9. Microstructure of Fe-30Mn-0.03Nb in a) Bright field illumination, b) Polarized light microscopy and c) Differential Interference contrast (DIC) microscopy

the microscope. Observations were carried out on a Nikon Eclipse LV100 microscope. The image was acquired by NIS Element (advanced research version) software. First a bright field image was taken for every micrograph. Despite coloration in this type of image, certain features are not distinguishable. As for example an annealing twin lamella colored as brown sitting in a magenta colored grain is difficult to detect. Similarly, two neighboring grains with light or almost similar colors have a separating grain boundary which is also very faint in appearance (Figure 3.9. a). In this case, as contrast-enhancing mechanism, polarized light microscopy was used to detect grain

and twin boundaries. For this, the microscope was equipped with a polarizer that sits in the light path ahead of light source and polarizes the incident light on the sample surface, an analyzer that sits between objective and eyepiece to examine the reflected light from the sample surface. In modern microscope these are made of synthetic Polaroid sheet material that shows dichroism. As light is considered as a wave vibrating in all planes normal to its direction of propagation. After passing through the polarizer, the wave vibration occurs only in one plane. When this type of light hits the sample surface and the reflected light is made to pass through analyzer placed 90° to the polarizer, it is known as "crossed" position. With this configuration, 4 successive rotations of reflected light by 90° causes contrast by adjusting the light intensity. Sometimes an optical plate, known as sensitive tint plate, is inserted between the polarizer and analyzer which creates color contrast and detects the annealing twins easily (Figure 3.9. b). Thus color difference created on either side of the grain boundary makes it prominent and polarized light microscopy became a useful aid for grain size measurement.

For attaining further contrast of the boundaries, Differential Interference contrast (DIC) imaging technique was used. This technique is particularly helpful to reveal those microstructural features which otherwise don't show any intensity contrast. This One plane polarized light is split into two (ordinary and extraordinary) within which a path difference is created using a Wollastan prism. Upon re-uniting the two rays will produce an interference effect in the form of fringes. Path differences created by the surface features between the rays causes phase difference which is rendered as difference in brightness causing significant image contrast. When the distance between two fringes become greater than the field of view, single fringe covers the whole area of interest. This ultimately leads to a three-dimensional appearance of some of the microstructural features due to some shadow effect. Compared to Figure 3.9. a, interference contrast images have higher resolution, better contrast (Figure 3.9. c). French physicist, Georges Nomarski, later on changed the Wollaston prisms and modified difference in intensity making this technique of microscopy known as Nomarski Interference contrast microscopy (Lang, n.d.; Allen and David 1969). The grain size measurement was done by switching between three different types of a particular microstructure taken in above three modes.

3.4.2 Electron Backscattered Diffraction (EBSD):

Electron Backscatter Diffraction (EBSD) was used mainly to acquire crystallographic information of the grain boundaries by enabling individual grain orientation detection, point-to-point orientation correlations. This was carried out on a JEOL JSEM-7000F FEG-SEM instrument which is equipped with a Charge-Couple-Device (CCD) detector. Wide availability of Scanning Electron Microscopes (SEM), high speed data acquisition, ability to explain microstructural condition on a submicron scale make EBSD technique a convenient and highly accepting one for gathering information regarding the crystallographic microstructure. Being a surface sensitive technique, the samples used for this must have a damage free top layer (5-50nm) to ensure good data collection. This includes avoiding any residual damage from cutting, grinding stages and also formation of oxide layers as the high manganese samples are prone to surface oxidation when left open in air. As the backscattered electrons carry information from the lower part of the interaction volume away from the surface, a high angle tilt makes the backscattered electrons closer to the surface. For our experiments, a tilt of 70° was used with respect to the horizontal to ensure maximum number of signal capture with minimum effect of surface topography. The samples used were mostly taken out of the cold mount to electropolish. As mentioned before, a good electropolished surface without etching worked better than 0.1μm silica polished surface for EBSD.

The samples used for EBSD were of same dimensions as used in grain growth experiments except the height. The type of specimen holder used allowed up to 5mm of sample height for our measurement. The sample was mounted on a stub with nickel paint around it ensuring a good conducting path to avoid charge build up. To avoid a thin film of oxide formation at the surface, the samples were baked in an oven for exactly 30 minutes before putting into the SEM sample chamber. The baking step is necessary to dry the nickel paint and to make sure the sample is tightly fixed on the stub. It must be mentioned that using a carbon tape underneath the sample was not successful as it caused sample drift during the tilted condition especially when the EBSD scans were long duration. Before putting the sample into the specimen chamber, a quick blow of compressed air was done to remove any kind of debris on the surface.

Finally, the 10mm (X) x 6mm (Y) x 5mm (Z) sample (X,Y and Z are the sample axes inside the specimen chamber) on the stub was aligned in the 12.5 mm holder with the rolling direction

perpendicular to the arrow carved in the holder. This configuration will match the X-direction of the electron image on the screen to match with the rolling direction even after tilting. Basic instruction of SEM was followed while inserting the sample into the specimen chamber so that the vacuum is maintained inside the electron column. Once the air pressure hits around $5x10^{-4}$ Pascal inside the column, the gun valve was turned on. For most of our EBSD, a sample distance of 15 mm, accelerating voltage of 20KV and 15nA of probe current were used. Once the beam alignment and stigmation was done properly, the sample stage was lowered to 30 mm (using Z-control) and tilted to 70°.

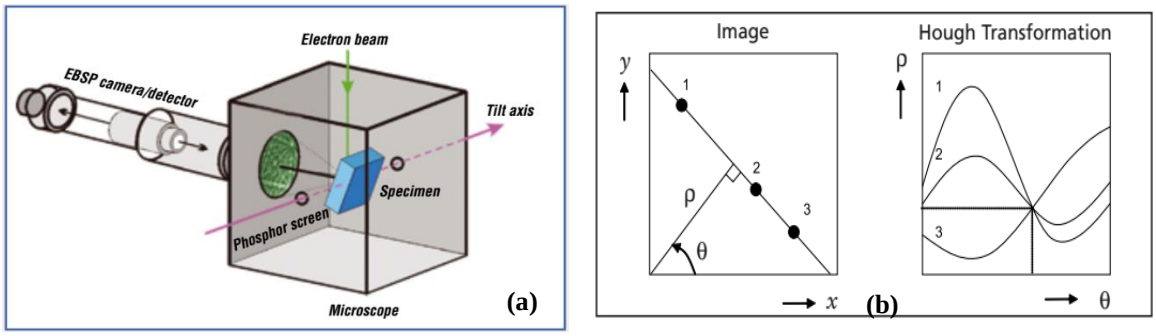

Figure 3.10. a) Demonstrating a typical EBSD setup highlighting tilted sample inside the specimen chamber b) Hough transformation principle for automated indexing of Kikuchi bands (Instruments, n.d.)

The EBSD scan was then run using Aztec that allows the insertion of the NORDLYS EBSD detector which is a camera with its CCD chip illuminated by a transparent phosphor screen. Upon interaction of primary electron beam with the atomic planes inside the specimen, diffraction happens due to inelastic scattering once Bragg condition is satisfied. The diffracted electrons form a set of paired large angle cones for every diffracting atomic plane. Intersection of these cones with the phosphor screen sitting 2 cm away from sample yields bands which form the characteristic Kikuchi pattern for a particular unit cell or grain orientation. Once the pattern is captured, the CCD camera views them as light of suitable wavelength through a lead glass screen and CHANNEL 5 software detects and indexes the bands based on matching with possible established patterns and finally project on computer screen. The automated indexing is based on Hough transformation. A point or pixel can actually belong to an infinite set of Kikuchi lines. The Kikuchi line passing through a particular point or pixel in(X,Y) system can be transformed to (ρ,θ) coordinate according to ρ= xcosθ +ysin θ where ρ and θ parametrize the Kikuchi line by a single point (Figure 3.10. b).

A pixel in image (X,Y) plane transforms to a sinusoidal wave in Hough space. Different points on a Kikuchi line therefore gives different sinusoidal waves in Hough space. Intersection of these waves gives a point of particular (ρ,θ) which gives the inclination of the Kikuchi line and this how the lines are reconstructed from Hough space. Then by matching the angular difference from a lookup table, the Kikuchi lines are indexed. The scan parameters were set by optimizing the quality of pattern capture and scan time which came after several trials. For camera setting, a binning level of 4x4 was found to be satisfactory with a gain level around 10 and a dwell/exposure time around 4-5 ms to compromise between signal and noise. The number of bands detection was set to be 12 with a Hough resolution 70°. Finally, scan was done with a step size of 1-3 microns on the area at 200X magnification.

The post-EBSD analysis was done using the "Tango" program in HKL software which produced

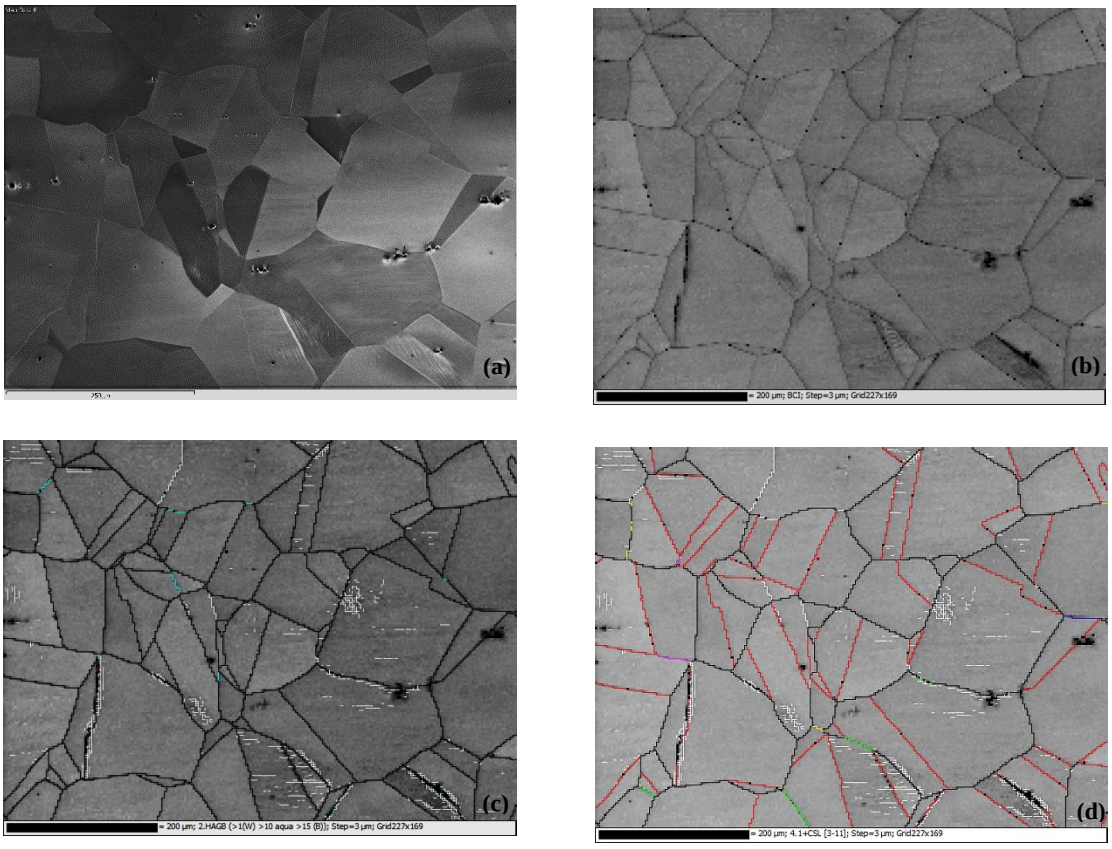

Figure 3.11. Fe-15Mn-0.5C sample EBSD details: a) Secondary Electron (SE) image, b) Band contrast image, Boundaries mapped based on c) misorientation angle ranges, d) CSL criteria from Σ = 3-11

the band contrast image (Figure 3.11. b). For all analyses, noise reduction was done using the in-built program in Tango. The main objective of EBSD was to characterize the crystallography of the boundaries in the microstructure. For this, the map was reconstructed with grain boundaries defined by different angle ranges. As for example, Figure 3.11. c was reconstructed based on the condition that boundaries greater than 15° are black, 10° are aqua and 1° are white in color. When the CSL criteria for different boundaries were added to impose over above HAGB condition, the boundaries with CSL geometry were characterized. It can be viewed from Figure 3.11. d color of Σ3 –red, Σ5-green, Σ7-blue, Σ9-magenta and Σ11-yellow. From this type of map, distribution of different CSL boundaries can be measured as the software calculates the length fraction of each type. Because of reconstruction, the calculated boundaries are of jagged type otherwise the SE image shows the original boundaries.

3.4.3 Focused Ion Beam (FIB) – Atom Probe Tomography (APT):

Atom Probe Tomography (APT) was used for studying segregation of solute elements at high angle grain boundary (HAGB). As will be discussed later, around 50% grain boundaries in the samples were diagnosed as special boundaries. Secondary electron imaging in the focused ion beam (FIB) microscope cannot indicate the crystallography of the boundary. For this purpose, samples were taken for a quick EBSD scan to identify a straight HAGB (e.g. the boundary marked by an arrow in Figure 3.12. a. This was done in an area near a previously-created microhardness

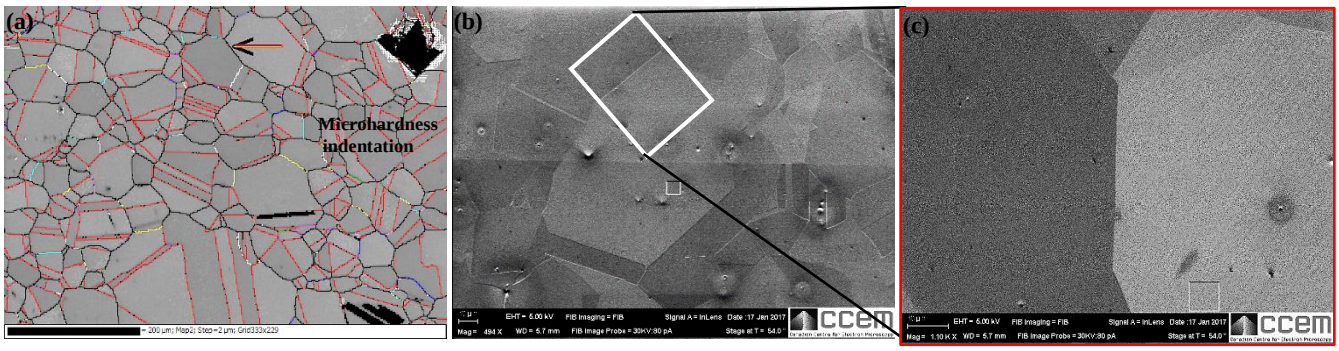

Figure 3.12. Site specific atom probe for segregation study, a) Identification of a high angle grain boundary from EBSD GBCD maps, b) re-imaging of the particular HAGB in FIB microscope in SE mode, c) rotated HAGB ready for FIB lift out

indentation which served as a landmark.

The same area with the boundary of interest could then be imaged in the FIB (Figure 3.12. b) and the boundary was extracted for APT sample preparation. APT requires the feature of interest to be located near the apex of a sharp needle-shaped sample. Use of FIB based technique has enabled the fabrication of site- specific atom probe samples (e.g. those containing grain boundaries) from bulk solid materials, thus avoiding the rigorous conventional electropolishing route. For this

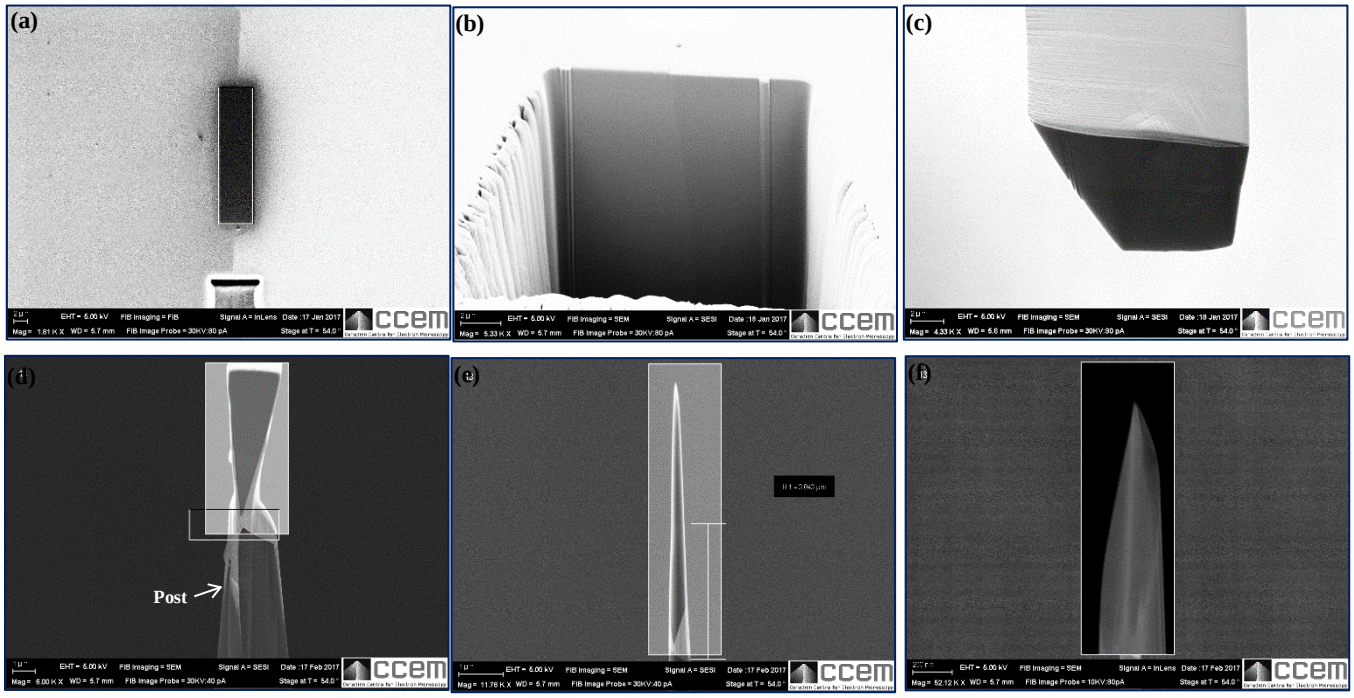

Figure 3.13. Sequence of atom probe sample preparation through the lift-out procedure using FIB-SEM route, a) Tungsten deposited on HAGB that is being shown in Figure 3.12. c, b) trench milled to check the boundary plane inclination, c) cross-sectional view of the lift-out specimen following extraction and 90° rotation, d) lift-out after trimming and attaching to pre sharpened post, e) needle following gradual thinning by annular milling, f) final APT specimen following final low kV sharpening

current study, "lift out" method was adopted (Peter Johann Felfer et al. 2012; Thompson et al. 2007) for sample preparation using a Zeiss NVision 40 (Carl Zeiss, Jena, Germany) dual-beam FIB-SEM. The FIB lift-out method for APT sample preparation involves separating the feature of interest (i.e. the HAGB for this study) by cutting it free from the surface of the bulk specimen. To start, the feature of interest was protected by tungsten (W) deposition (Figure 3.13. a). Meanwhile, it was ensured that the HAGB of interest has its inclination plane almost perpendicular to the specimen surface (Figure 3.13. b) as this configuration allows for a 90° rotation of the lift-out

(Figure 3.13. c) to orient the HAGB approximately normal to tip axis. Following rotation, cross-sections of the lift-out were mounted to pre-sharpened Si posts (Figure 3.13. d) by affixing them with additional W deposition. Roughly, 4-5 needles were prepared from a single lift-out. Sharpening the end of the needle-shaped samples was done by annular milling with a 30kV Gallium (Ga) ion beam and progressively smaller probe current, starting from 150 pA and ranging down to 40pA (Figure 3.13. e). Final sharpening of the needles, performed to clean away ion damage and position the HAGB at the tip apex was done using a defocused Ga ion beam at 10 kV with a probe current of 80 pA (Figure 3.13. f).

Atom probe analysis used a CAMECA local electrode atom probe (LEAP, CAMECA Instruments Inc., Madison, WI, USA) 4000X HR. For each HAGB extracted, at least 3 tips were run to measure segregation of atoms across the boundary. All the runs were performed at a stage temperature close to 47-59 K and under ultrahigh vacuum of approximately $3x10^{-11}$ Torr. Field evaporation was induced by laser pulsing (LP) using a UV laser (λ=355nm) at 60 pJ pulse energy coupled with a 250 kHz pulse rate. An evaporation rate of either 0.005 or 0.01 ions/pulse (0.5% or 1% respectively) was achieved by controlling the DC voltage applied to the tip. This voltage usually ranged between of 2 and 8 kV. Data reconstruction and analysis was performed using the Integrated Visualization and Analysis Software (IVAS) v3.6.14 established reconstruction algorithm (Gault et al. 2012).

3.5 Grain growth Study in Fe-6Mn-0.5C system:

The reason for having the grain growth study of Fe-6Mn-0.5C discussed in a separate section is its ambiguous response to optical metallography while attempting to reveal the prior austenite grain boundaries. Like other samples, heat treatment following the conventional scheme was done. Upon oil quenching, Fe-6Mn-0.5C samples show a microstructure containing Martensite (α') and retained austenite. All possible etchants and etching procedures were tried to reveal prior austenite grain boundaries (PAGB) for grain size measurement using linear intercept method. The appearance of the PAGBs was less prominent than the martensite plates at the grain interior. In conventional, low Manganese steel, hot picric acid etching with Teepol (wetting agent) added reveals the PAGBs clearly after a light backpolish following etching. The backpolish actually fades the grain interior in etching contrast and highlights the PAGBs (Figure 3.14. a) in as-quenched microstructure. For Fe-6Mn-0.5C samples, all possible variants of etchant chemistry was tried and

neither of 1-15 minute etching revealed the PAGBs. Neither a light backpolishing nor a darkfield optical microscopy could reveal the PAGBs. Instead, the long time etched samples started having deep pits which made them unsuitable for metallography (Figure 3.14. b). Another, way of

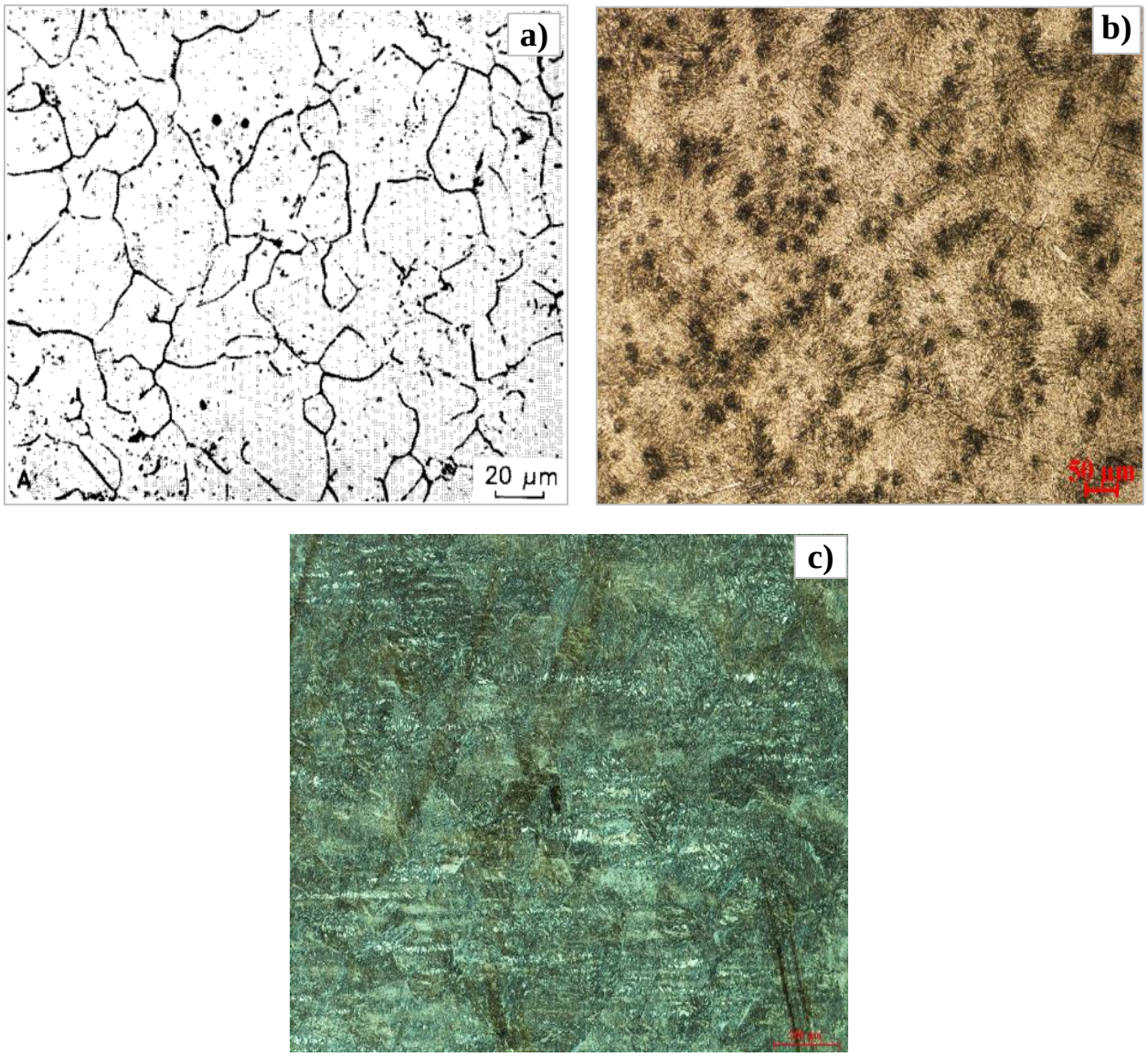

Figure 3.14. Microstructure of a) tempered Fe-0.22C-0.88Mn steels etched with saturated solution of picric acid with wetting agent and HCl delineating PAGBs with faded martensite inside the grains(Brewer, Erven, and Krauss 1991), b) Fe-6MN-0.5C steel in as-quenched condition etched by same etchant colored the martensite packets which on light backpolish disappears quickly leaving no trace of the PAGBs and rigorous pitting, c) Fe-6MN-0.5C steel tempered at 592°C for 1 hour shows no significant pro-eutectoid ferrite formation to decorate the grain boundary, instead amount of RA phase increased inside the grain.

revealing PAGBs was also tried by performing a short duration holding under the para-equilibrium temperature of 592°C for 1 hour with the intent of having a thin layer of pro-eutectoid ferrite forming along the PAGBs. However, this approach was also not successful as it increased the RA islands in the microstructure with no significant pro-eutectoid ferrite formed decorating the PAGBs (Figure 3.14. c). With all these approaches not having succeeded to produce a microstructure with clearly highlighting the PAGBs made the conventional line intercept method of grain size measurement extremely challenging, unreliable and time consuming. In search of a new method for grain growth study in Fe-6Mn-0.5C system, the current study delved into possible other methods grain size measurement. As one of the options, a comparatively new Laser ultrasonics for Metallurgy (LuMet) technology was used. The other option chosen was to use thermal etching technique for revealing PAGBs in Fe-6Mn-0.5C samples. Next, a brief description of the two techniques will be given.

3.5.1 Laser Ultrasonics for Metallurgy (LUMet):

This novel Canadian technology was developed at the National Research Council of Canada in Boucherville (QC,Canada) to a commercial sensor stage. This is a non-destructive and non-contact technique which involves application of lasers to generate and detect ultrasound pulse in the specimen. The attenuation and velocity of the output ultrasonic signal is measured and related to microstructural parameters.

Grain growth experiments for Fe-6Mn-0.5C samples (Figure 3.15) were conducted in a Gleeble 3500 thermomechanical simulator (Dynamic System Inc. Poestenkill, NY) equipped with a Laser Ultrasonics for Metallurgy (LUMet) sensor. To the rear door of the Gleeble chamber, LUMet sensor is attached. In this sensor, a frequency-doubled Q-switched Nd:YAG laser with a wavelength of 532 nm is used for the generation of a wide band compressive ultrasound pulse. The pulse duration is approximately of 6 ns, with a maximum energy of 72 mJ and up to 50 pulses/second rate of generation. A broadband ultrasound pulse is produced by the laser pulse (through vaporizing a small quantity of material at the surface of the order of a micrometer per hundred laser pulses) which propagates back and forth through the thickness of the sample. As it interacts with microstructure, its amplitude comes down. A frequency-stabilized Nd:YAG pulsed laser detects successive arrivals of the ultrasound pulse at the generation surface. This detection is indicated by infrared (λ-1064 μm, pulse duration-90 μs) illumination of the surface 50 times per

second. Through an active interferometer approach, the Infrared light reflected on the surface undergoes a demodulation inside a photo-refractive crystal. The measured properties represent average of the material properties corresponding to a volume expressed as the surface of the laser spot (about 2 mm) times the sample thickness. Center length of the sample is chosen for collinear alignment of both generation and detection laser beams. The ultrasound waveform is then analyzed by software CTOME v2.14 and its frequency dependent attenuation measured in-situ during grain growth experiment is finally correlated with average grain size variation upto 60 minutes of

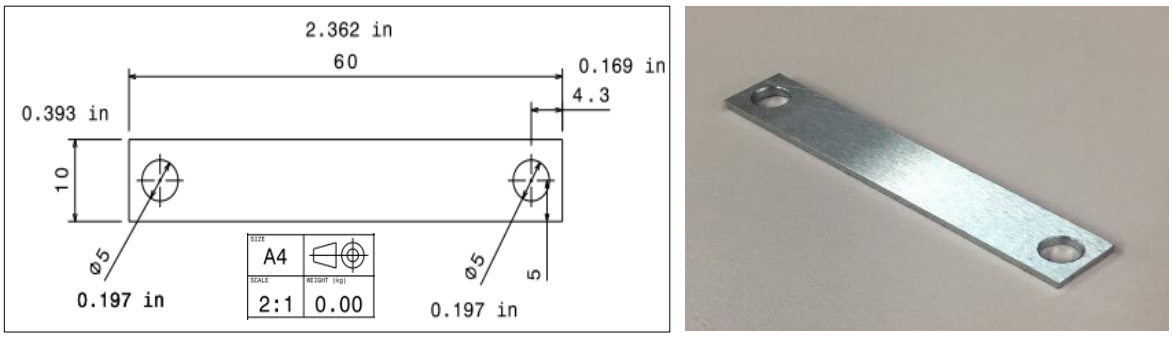

Figure 3.15. a) Specimen geometry used for LuMet grain growth measurement, b) final machined LuMet samples of Fe-6Mn-0.5 of 3 mm thickness [courtesy T.Garcin, UBC]

holding time. The signal attenuation due to scattering by grains is separated from the same by other factors. After this, the attenuation can be expressed in terms of a grain size dependent parameter 'b' as follows:

$$\alpha_{Sc} = a + bf^n$$

where, a represents non-grain size contribution of ultrasound attenuation (e.g., internal friction, magnetic damping etc.). Average grain diameter $\overline{D}$ can be related to b as

$$b = K(T)r\overline{D}^{n-1}$$

where, $K(T)$ is a temperature dependent calibration term and n is used as 3. Samples of steels, nickel and cobalt were used to set the precision in the measurement of 'b' by computing the distribution of measured values over 60 acquisitions conducted at the same position in the sample at room temperature (Matthias Militzer, Garcin, and Poole 2013).

The parameter b (grain size parameter) is calculated by the processing of the ultrasound waveforms measured during grain growth treatment. The analysis consists of several steps. At each step, the waveform (representing the signal measured a specific time of the treatment) is accepted or rejected according to 5 criteria. The testing sequence ensures that i) satisfactory amount of light collection, ii) acceptable signal to noise ratio, iii) the selected bandwidth, min and max frequency considered are resolved given the signal to noise conditions, iv) the quality (or standard error) of the least square fitting on the attenuation spectrum is acceptable and v) the measurement of grain size parameter falls in the range of applicability for the selected grain size calibration.

3.5.2 Thermal Etching (TE):

The method of thermal etching is based on preferential material transfer away from HAGBs upon heating the sample at very high temperature. It is a commonly known technique of developing grooves at emerging HAGBs. The mechanism requires a free surface and grain boundary where material transfer away from boundary results into an equilibrium groove angle at the triple junction between (mobile or stationary) boundary and surface. To achieve this, samples of same dimensions (10mm x 6mm x 6mm) as used for other grain growth experiments, were cut from the base plate of Fe-6Mn-0.5C steel following the same convention as depicted in Figure 3.6. The samples were in tube furnace. It took only 2-3 minutes for the sample to reach 1200°C. The holding time for

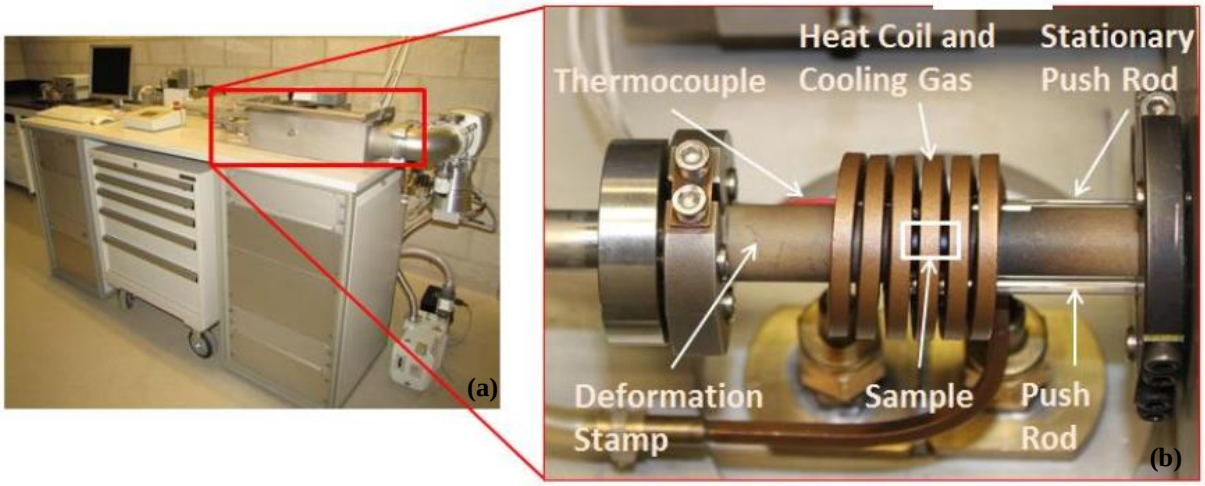

Figure 3.16. a) Bähr DIL 805 dilatometer used for grain growth cum thermal etching experiment for Fe-60Mn-0.5C steel, b) an interior view of the sample chamber with all necessary attachments labelled (Saragosa 2015)

then taken for routine metallographic preparation with finishing step as 1 µm diamond paste polishing. Before, loading the samples for heat treatment, a quick 0.04 µm oxide polishing was performed to ensure removal of potential oxide layer that might have formed when the samples were resting in a desiccator. The grain growth cum thermal etching experiment was carried out in a Bähr DIL 805 dilatometer at CanmetMATERIALS, Hamilton, Ontario (Figure 3.16. a). An S-type thermocouple (reliable over K-type at temperature higher than 1000°C) was spot welded to the sample surface to monitor and control the temperature inside the chamber (Figure 3.16. b). The ramp was set in such a way so as to simulate the heating rate same as the one used for other experiments this series of experiment ranges from 5-30 minutes. The experiments were conducted under vacuum to avoid oxidation of the polished sample surface. After the holding was over, the sample was quenched to room temperature using helium jet quenching. The specimen was then imaged using an Olympus PMG3 light microscope under bright field and Interference contrast mode.

3.6 Grain Boundary Engineering (GBE):

The objective of performing some experiments on grain boundary engineering (GBE) is to explore its effect on grain growth. Also, to the researcher's knowledge, no research work has been published to date on GBE of high Mn or TWIP steels. This attempt is also directed towards the generation of a database on GBE of high Mn/TWIP steels. For this experiment, two different types of alloy systems were chosen to be engineered. Also, both the methods of GBE were attempted.

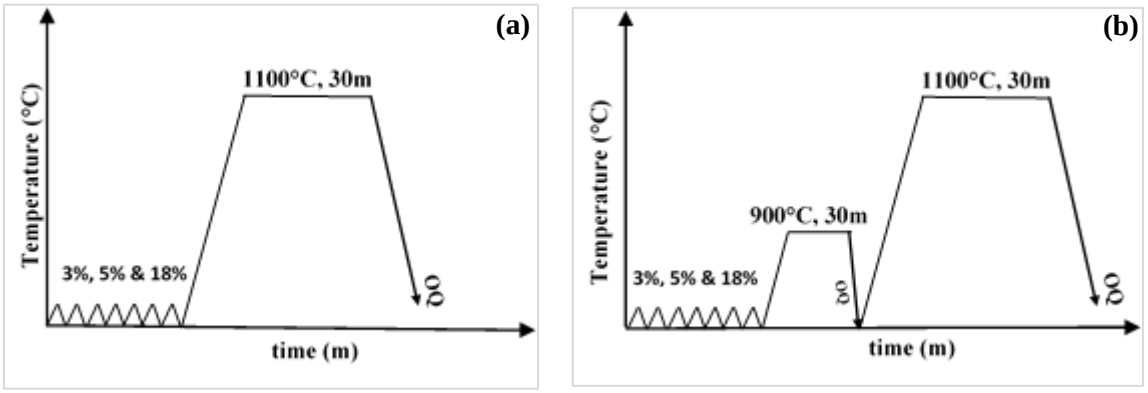

Figure 3.17. SA-GBE scheme for Fe-30Mn-0.5C a) without and b) with an intermediate annealing at 900°C, 30min before final grain growth experiment at 1100°C,30min

For, strain annealing grain boundary engineering (SA-GBE) experiments, Fe-30Mn-0.5C samples were chosen. Fe-30Mn-0.03Nb samples were used for strain recrystallization grain boundary engineering (SR-GBE) experiments. In addition to that, effect of amount of cold work, intermediate annealing before grain growth experiment and rolling iterations (in both Fe-30Mn-0.03Nb and Fe-30Mn-0.5C) were also explored.

For SA-GBE, Fe-30Mn-0.5C samples were cut from the base plate parallel to the rolling direction. The samples were divided into two different sets. One set of sample was taken for grain growth experiment direct after rolling (Figure 3.17. a) while the other set was given an intermediate annealing before the grain growth experiment (Figure 3.17. b). Three different cold reduction passes of 3%, 5% and 18% were applied to the samples. Then final grain growth experiment was done at 1100°C for 30 minutes with and without the intermediate annealing step. For each case, the same furnace and set up were used as was used in grain growth experiments. The final samples were taken for metallography and grain sizes were measured using linear intercept method on a tint etched microstructure. Grain boundary character distribution (GBCD) was measured in each type of intermediate annealed sample to correlate amount of cold deformation with special boundary fraction. Grain size of these samples were compared to a sample which underwent grain growth at 1100°C for 30 minutes without any GBE treatment.

To explore the effect of iterative processing on special boundary evolution and thereby its effect on grain growth, a 4-step rolling was conducted on one of the Fe-30Mn-0.5C samples following

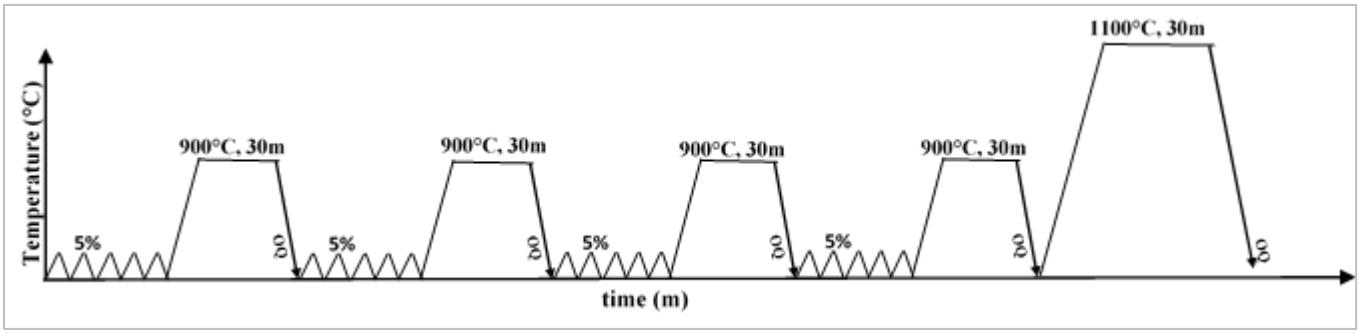

Figure 3.18. Schematic of iterative SA-GBE treatment performed on Fe-30Mn-0.5C before final grain growth experiment at 1100°C for 30 minutes

the SA-GBE route. Each step consists of 5% cold rolling followed by an annealing at 900°C for 30 minutes. After the 4 step GBE treatment, the sample was taken for a final grain growth experiment as specified in Figure 3.18.

For SR-GBE, 15 mm thickness pieces of material were cut from the base plate parallel to rolling direction. One piece was rolled from 15mm to 5 mm in one pass and then it was taken for grain growth experiment at 1100°C for 4 hours. To compare the effect of iterative processing by strain

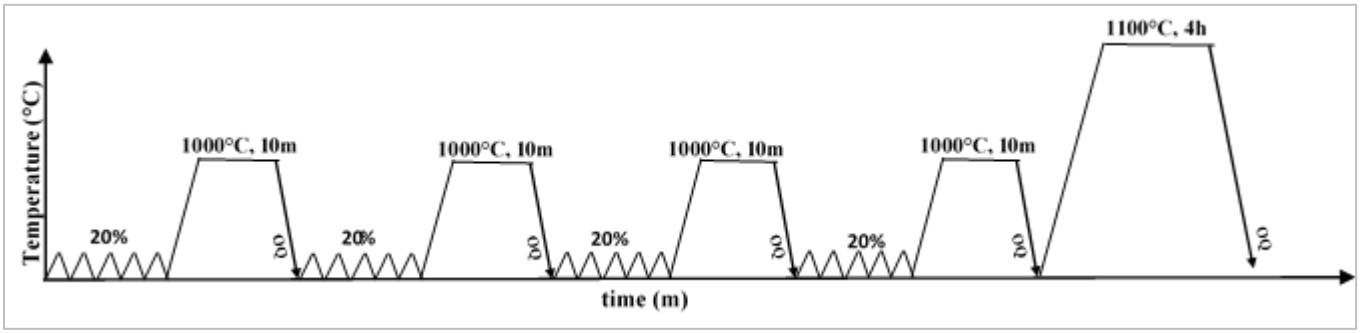

Figure 3.19. Schematic of iterative SR-GBE treatment performed on Fe-30Mn-0.03Nb before final grain growth experiment at 1100°C for 4 hours

recrystallization route, a 4 step GBE treatment was performed as described in Figure 3.19. The treated sample was then taken for final growth experiment for 4 hours. Final, grain size measurement was performed using the conventional linear intercept method.

4 Results:

Under this section, the results regarding grain growth kinetics will be shown for Fe-30Mn system with and without carbon at two different temperatures. The growth kinetics under the presence of two different levels of niobium will then be given at three different temperatures. Corresponding calculations on determination of mobilities will be shown thereafter with highlighting the temperature and solute dependence of mobility in the alloys. Effect of Mn on grain growth kinetics will be shown next from which mobility will be extracted in systems with different levels of Nb at one temperature. Next to this, atom probe results on segregation study will be given for different alloys to highlight segregation of elements. The chapter will end with the results obtained from grain boundary engineering experiments performed on Fe-30Mn-0.03Nb and Fe-30Mn-0.5C alloys and their impact on grain growth.

4.1 Grain growth kinetics in Fe-30Mn and Fe-30Mn-0.5C:

Austenite grain growth kinetics in absence of carbon was measured at three different temperatures,

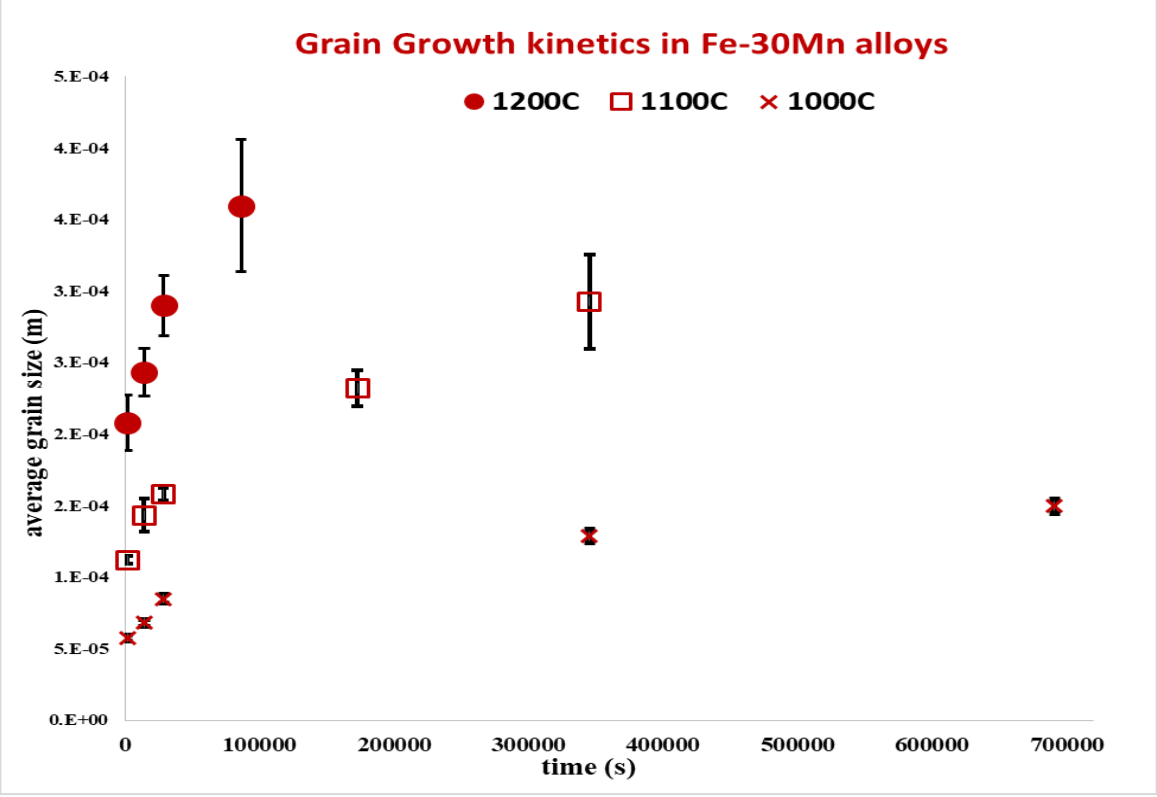

Figure 4.1. Austenite grain growth kinetics at three different temperatures in Fe-30Mn alloys

1000°C, 1100°C and 1200°C using Fe-30Mn alloys. The grain growth kinetics data are provided in Figure 4.1.

Austenite grain growth kinetics in presence of carbon was measured at two different temperatures, 1100°C and 1200°C, using Fe-30Mn-0.5C alloys. The results are being shown in Figure 4.2.

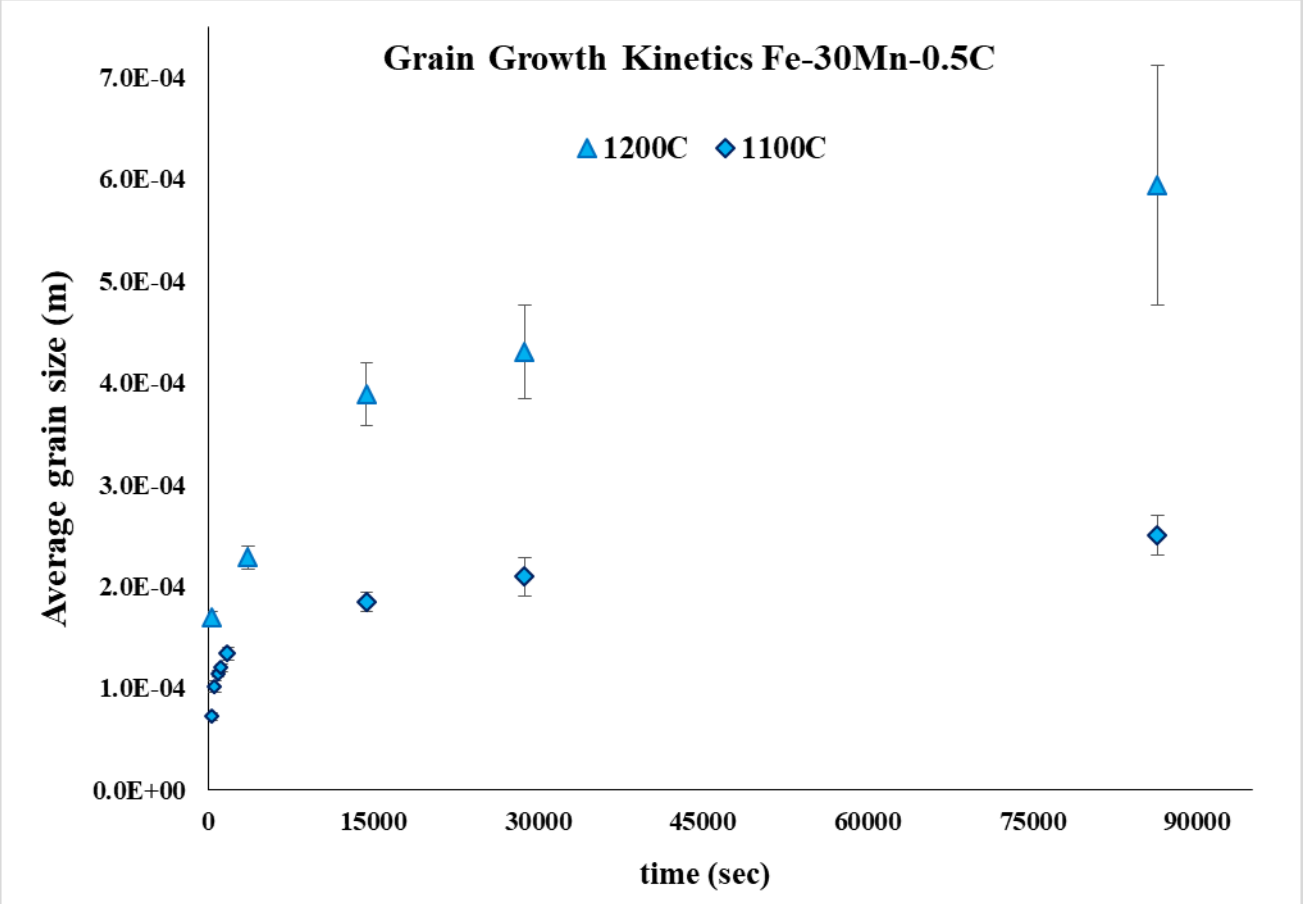

Figure 4.2. Austenite grain growth kinetics in Fe-30Mn-0.5C alloys at two different temperatures

Austenite grain growth kinetics in Fe-30Mn and Fe-30Mn-0.5C are compared at two different temperatures as shown in Figure 4.3 and Figure 4.4.

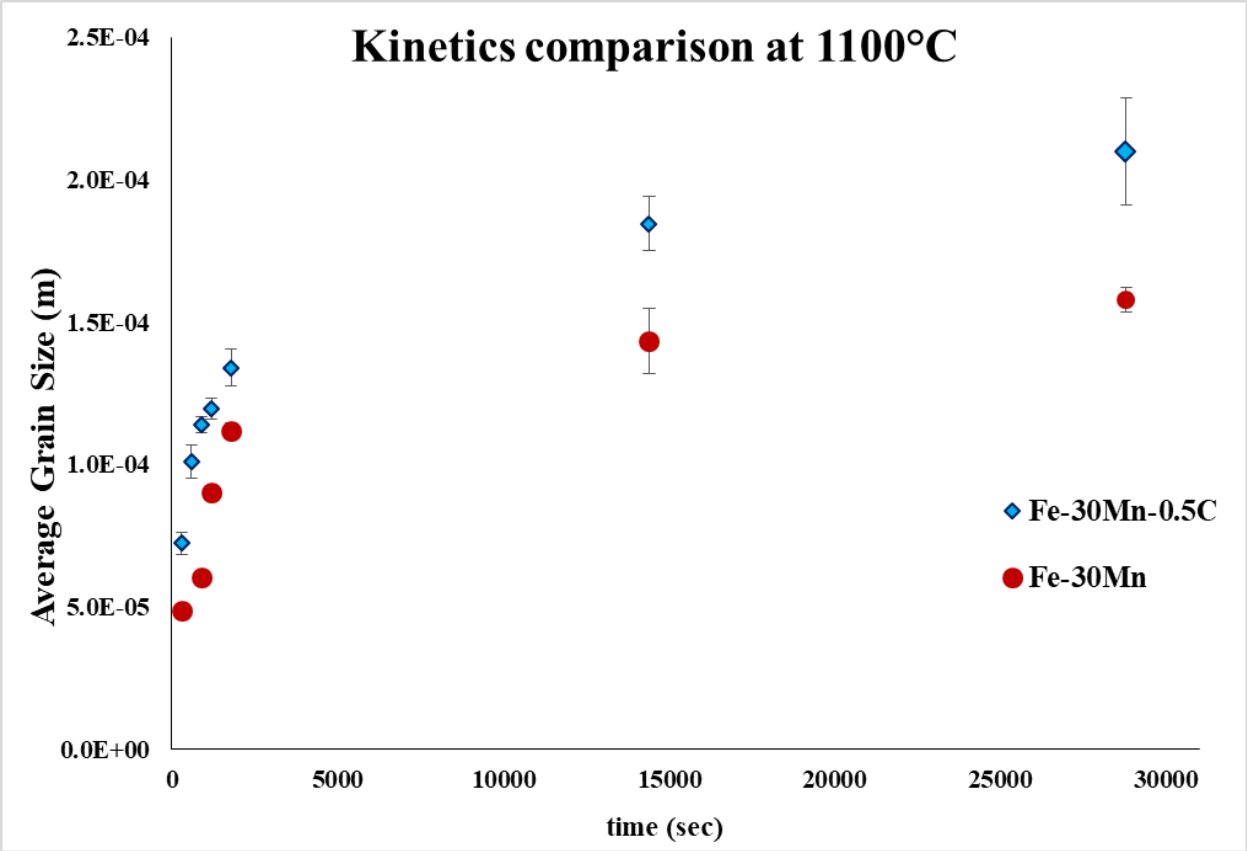

Figure 4.3. Comparison of grain growth kinetics at 1100°C with and without carbon

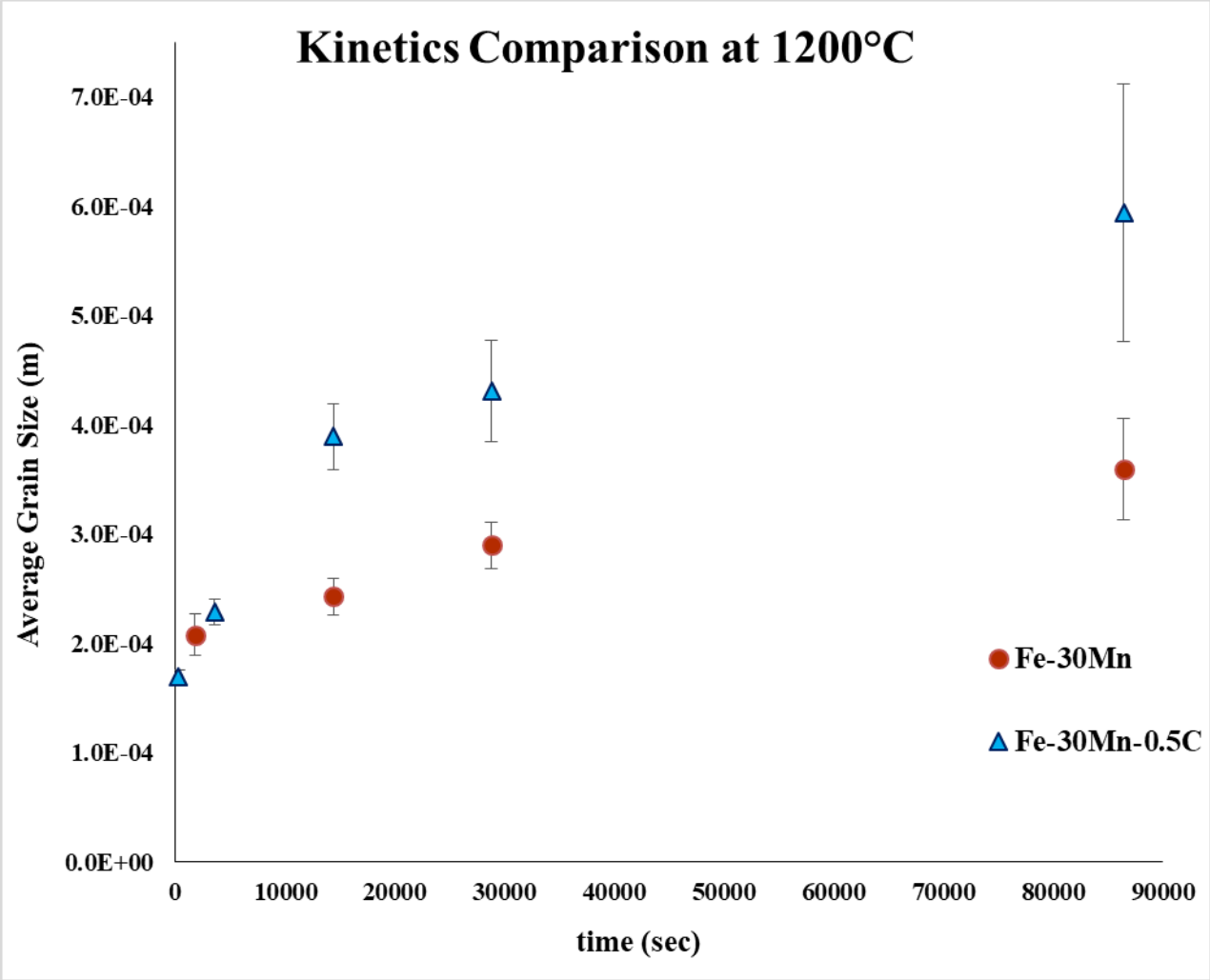

Figure 4.4. Comparison of grain growth kinetics at 1200°C with and without carbon

4.2 Grain growth kinetics in Fe-30Mn system in presence of Nb:

The grain growth kinetics in presence of niobium is measured at three different temperatures for

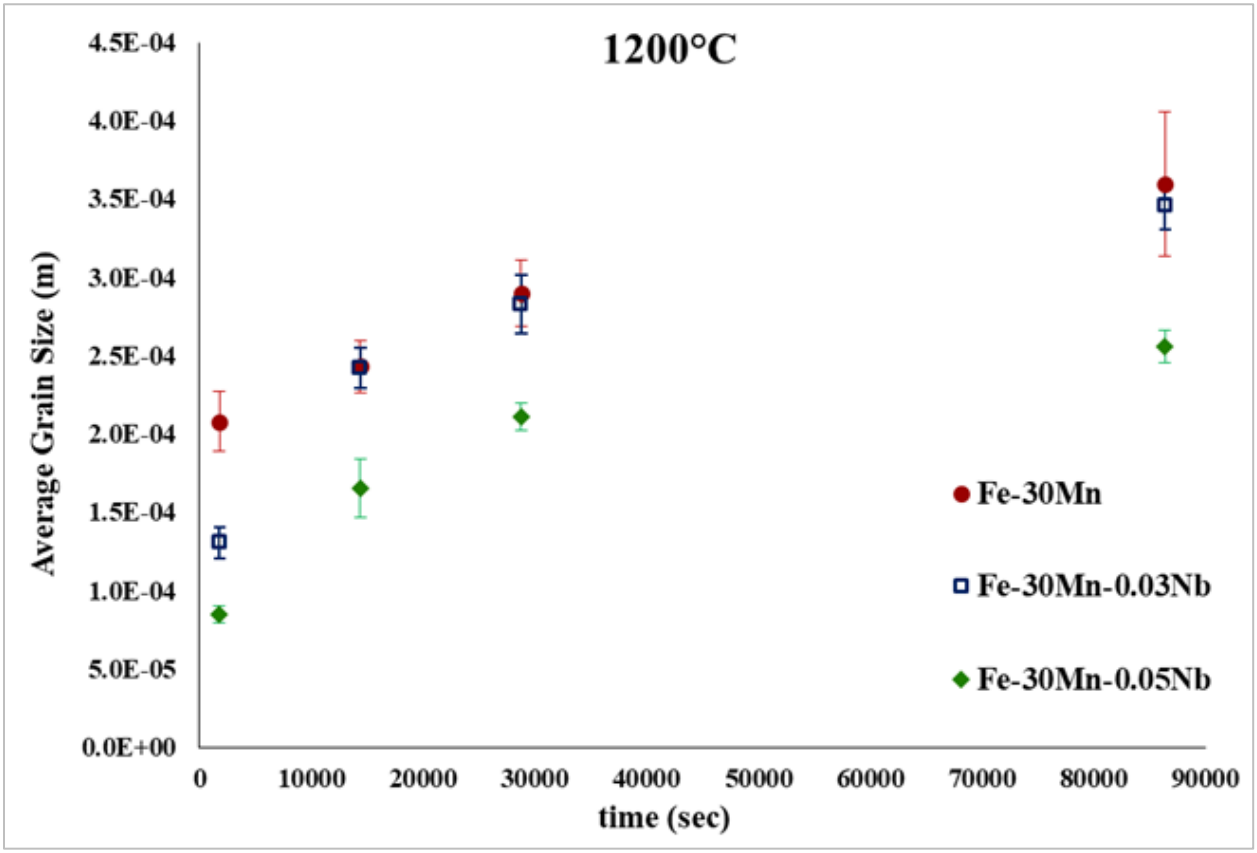

Figure 4.5. Comparison of grain growth kinetics plot in Fe-30Mn system with and without Nb at 1200°C

varying range of times. To highlight the difference in each case, the results are compared with the

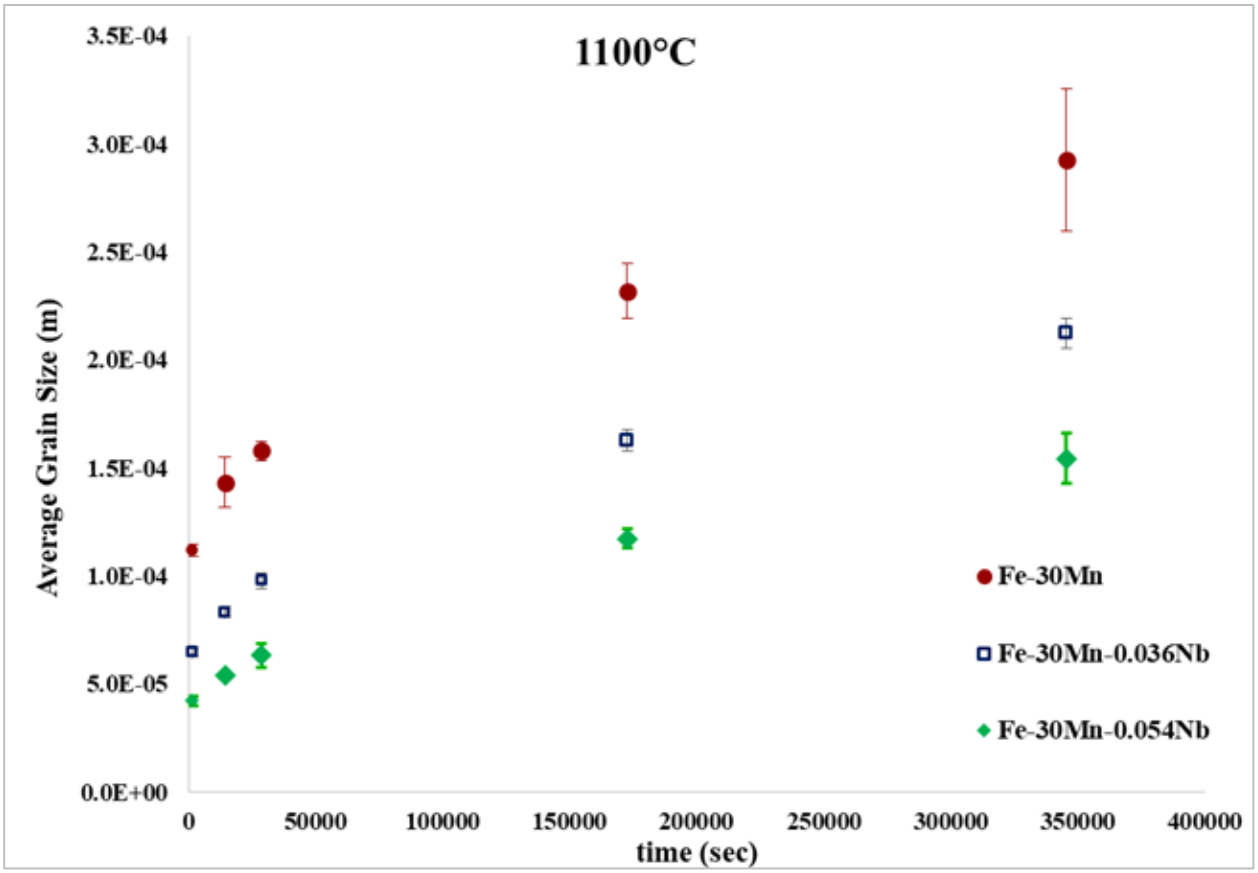

Figure 4.6. Comparison of grain growth kinetics plot in Fe-30Mn system with and without Nb at 1100°C

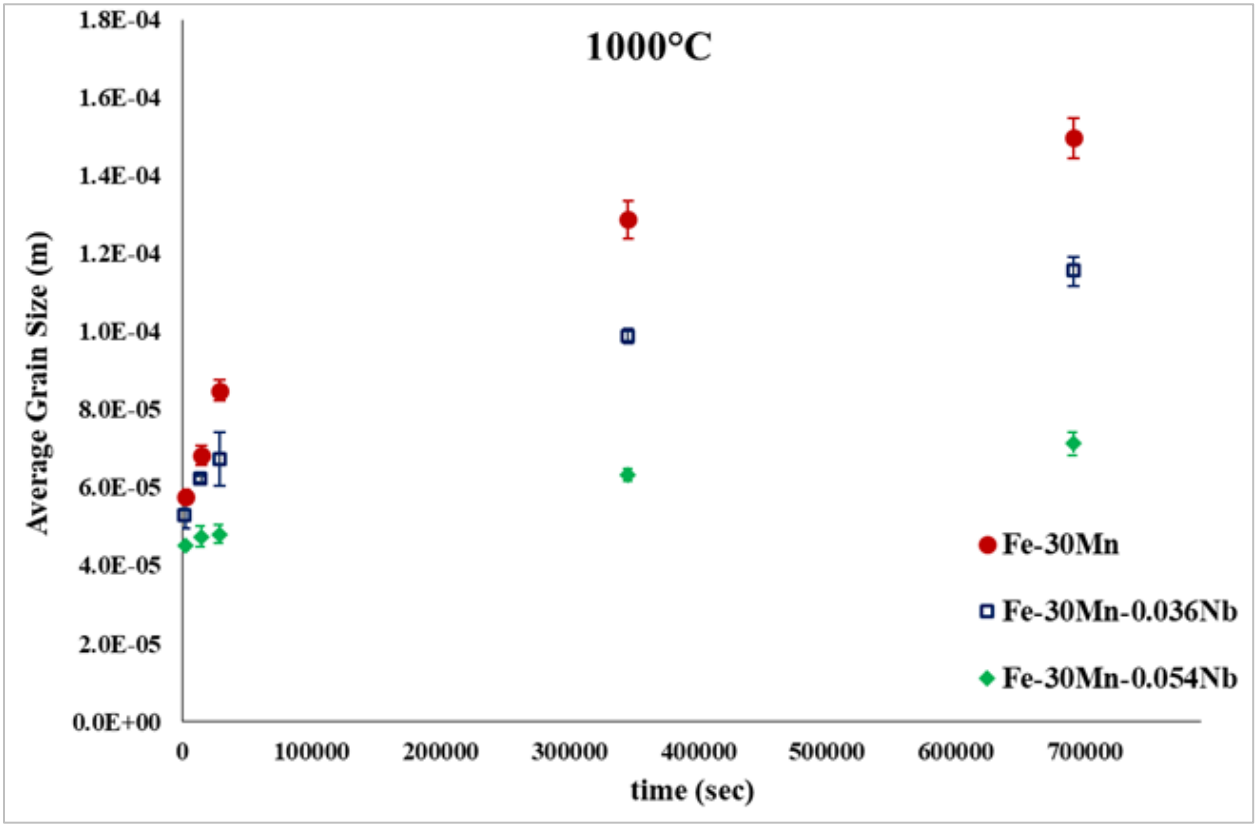

Figure 4.7.Comparison of grain growth kinetics plot in Fe-30Mn system with and without Nb at 1000°C

growth kinetics plot of Fe-30Mn data with no niobium added. Figures Figure 4.5, Figure 4.6 and Figure 4.7 show the comparison in austenite growth kinetics at 1200°C, 1100°C and 1000°C. For further elaboration, microstructure evolution in Fe-30Mn system with and without Nb was compared at 1000°C (Figure 4.8).

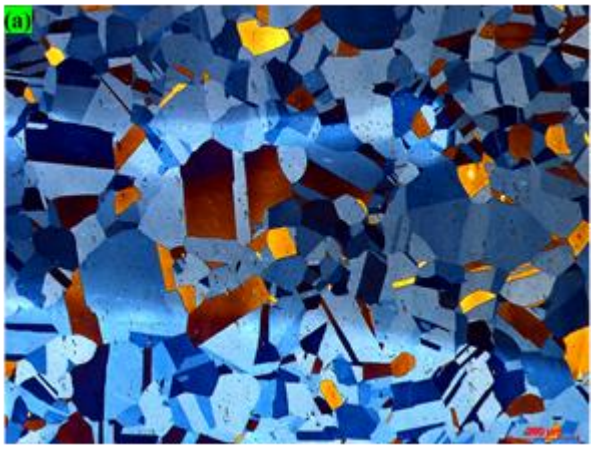

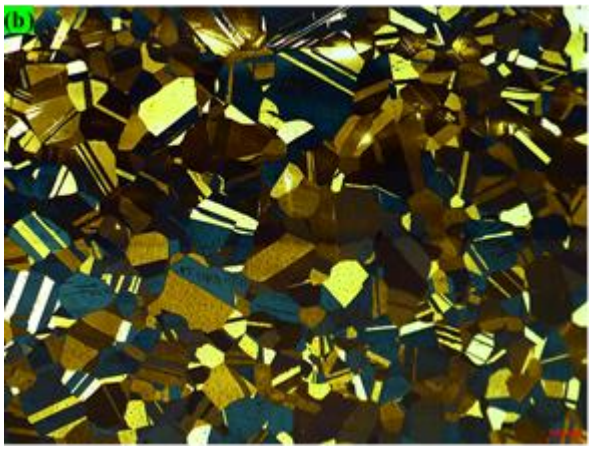

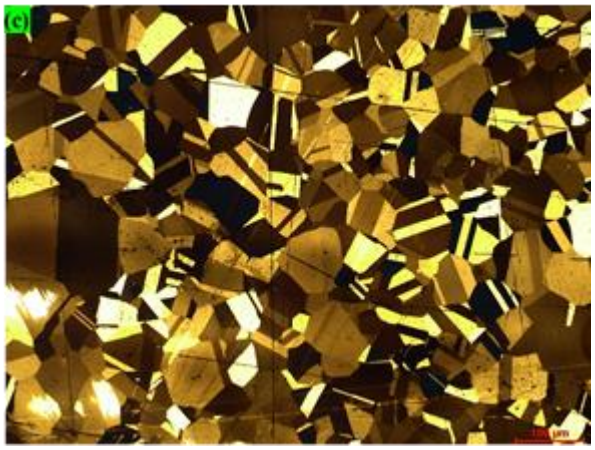

Figure 4.8. Grain size evolution in samples of a) Fe-30Mn, b)Fe-30Mn-0.03Nb and c)Fe-30Mn-0.05Nb after holding for 8 days at 1000°C

4.3 Estimation of Boundary mobility (M):

To estimate boundary mobility, two key equations were used. The growth rate equation proposed for normal grain growth is given in terms of critical grain size (R_{crit}) as follows:

$$\frac{dR_{crit}^2}{dt} = \frac{1}{2}\alpha M\gamma \qquad \text{..... Eq 4.1}$$

where, α is a geometrical factor as discussed in chapter 2.6, γ is the energy of high angle grain boundaries and M is the boundary mobility. To correlate, critical grain size with average grain size ($\bar{R}$) following equation was used (M Hillert 1965).

$$\bar{R} = \frac{8}{9}R_{crit}^2 \qquad \text{..... Eq 4.2}$$

Integrating equation 4.1 and using equation 4.2, the final equation to represent normal grain growth took the following form.

$$\bar{D}_f^2 - \bar{D}_i^2 = 1.58M\gamma\,(t_f - t_0) \qquad \text{..... Eq 4.3}$$

where, $\overline{D_f}$ and $\overline{D_i}$ are the initial and final value of the average grain diameter. The average grain diameters measured by linear intercept method on the optical microstructures are given in Figure 4.1 to 4.7 for different systems. A plot between $(\overline{D}_f^2 - \overline{D}_i^2)$ and (t_f - t_0) would therefore give a straight line whose

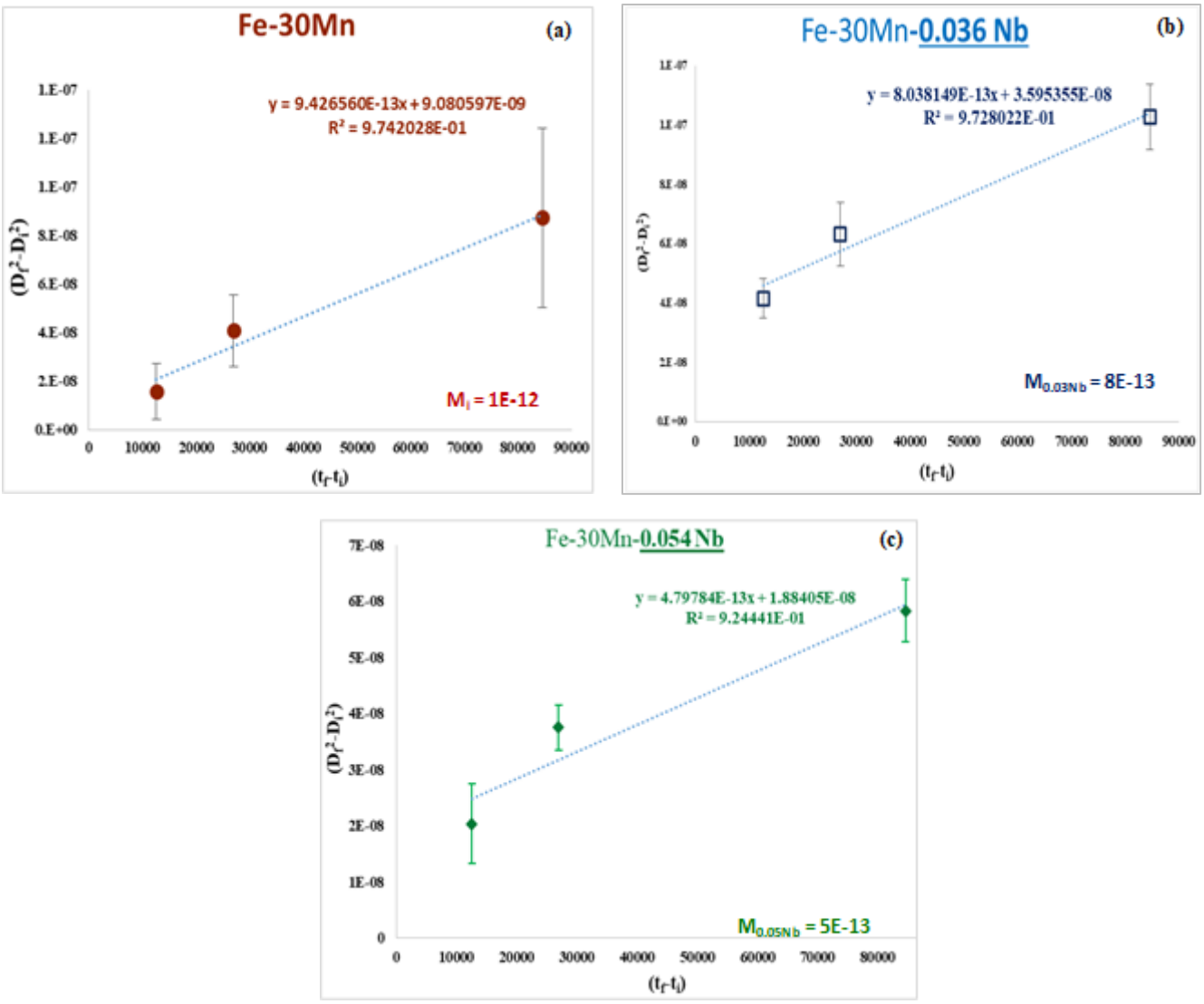

Figure 4.9. Extraction of mobility (M) from the grain growth data at 1200°C for a) Fe-30Mn, b) Fe-30Mn-0.036Nb and c) Fe-30Mn-0.054Nb

slope will be equal to the factor $1.58M\gamma$ (γ considered to be 0.625 J/m^2) in equation 4.3. Equating the two will determine the value of mobility, M. Mobility calculated from system without Nb is designated as, intrinsic mobility M_i. Next, a comparison between intrinsic mobility

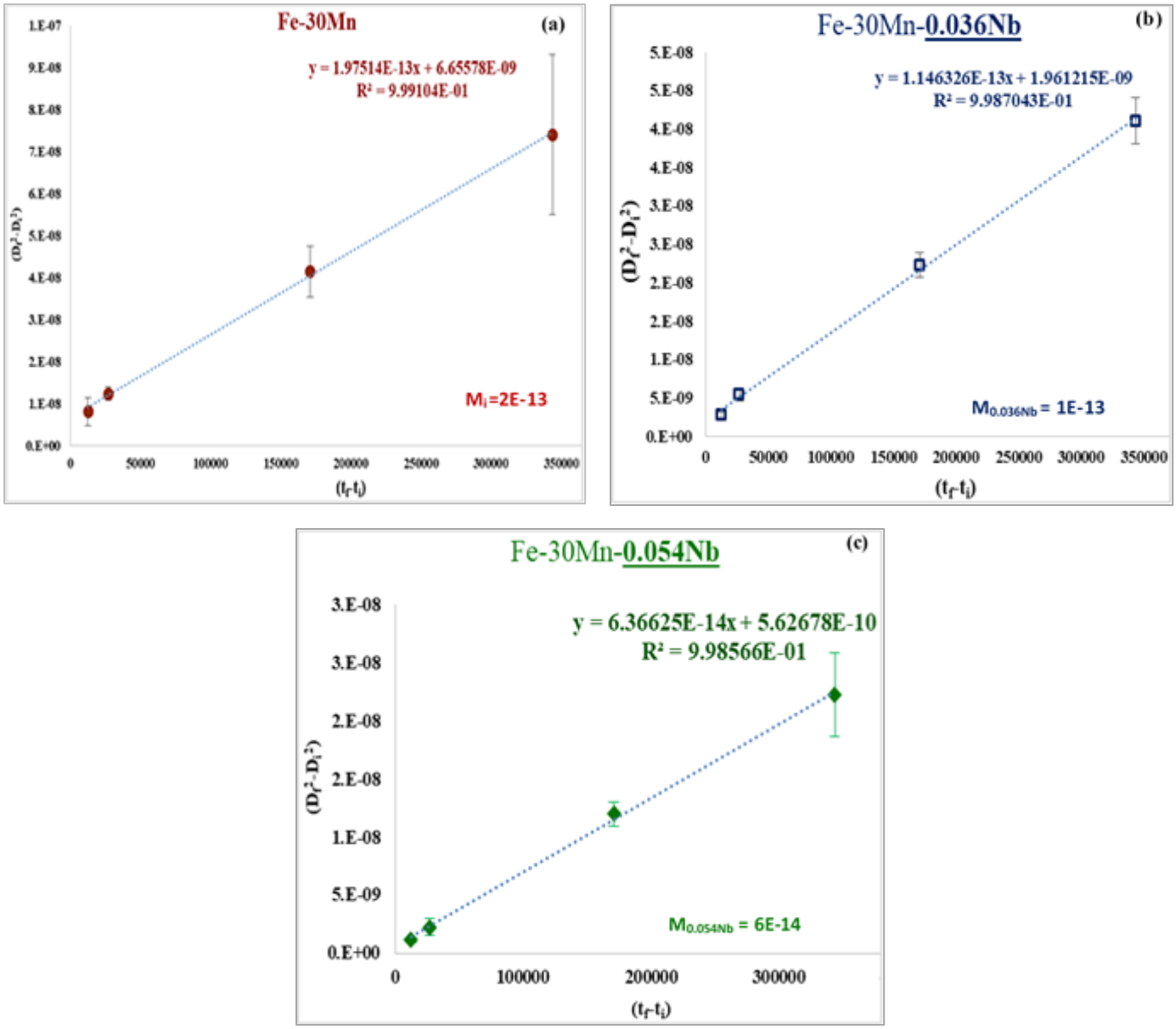

Figure 4.10. Extraction of mobility (M) from the grain growth data at 1100°C for a) Fe-30Mn, b) Fe-30Mn-0.036Nb and c) Fe-30Mn-0.054Nb

and the boundary mobility (*M*) in presence of different levels of Nb will be given at three different temperatures. Figures 4.9, 4.10 and 4.11 show the mobility extraction from grain growth data at 1200°C, 1100°C and 1000°C.

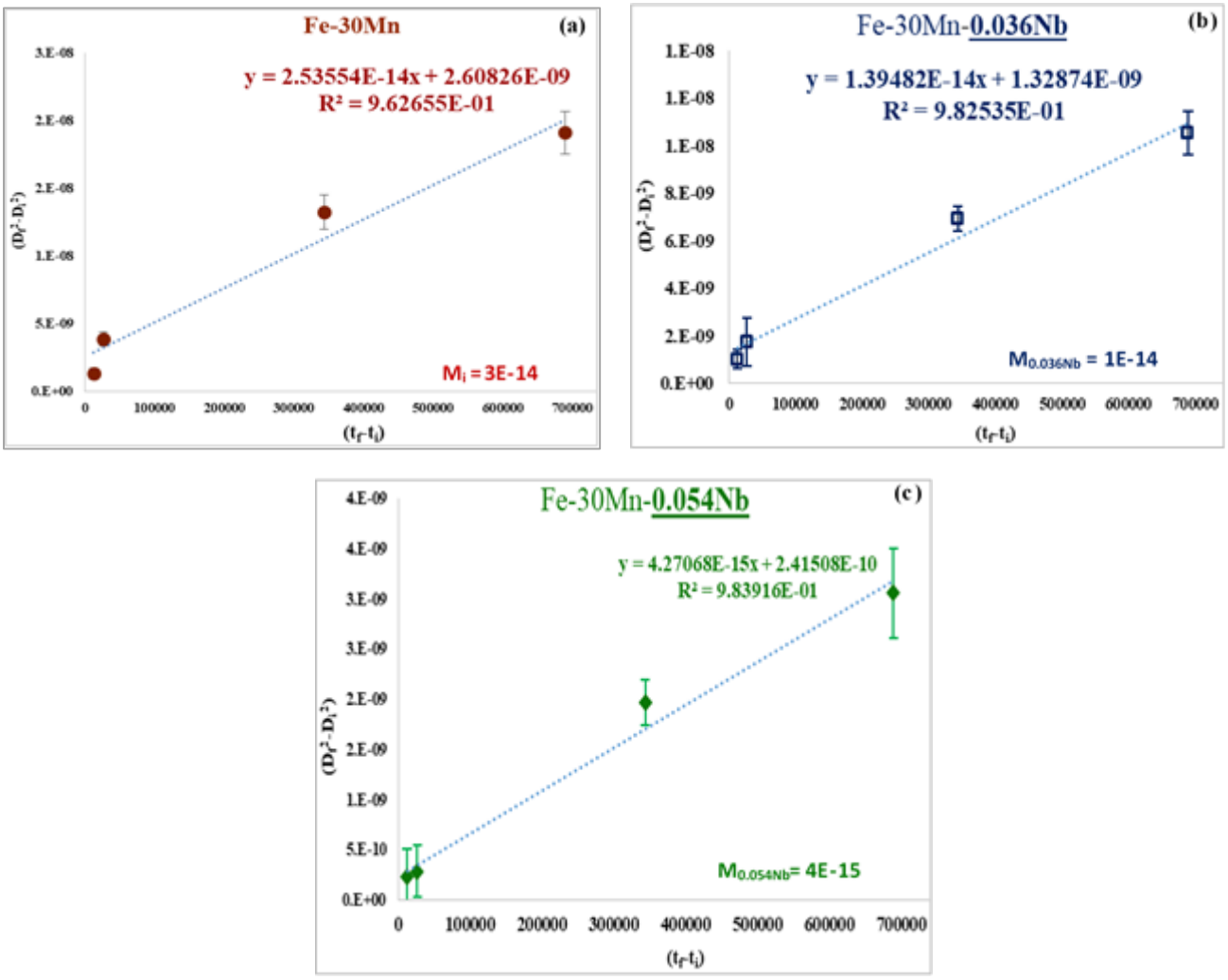

Figure 4.11. Extraction of mobility (M) from the grain growth data at 1000°C for a) Fe-30Mn, b) Fe-30Mn-0.036Nb and c) Fe-30Mn-0.054Nb

Next, difference in mobilities in presence and absence of carbon was calculated in a similar manner from the grain growth data of Fe-30-0.5C and Fe-30Mn alloys respectively. Figures 4.12 and 4.13 show the experimentally measured mobilities at 1200°C and 1100°C respectively.

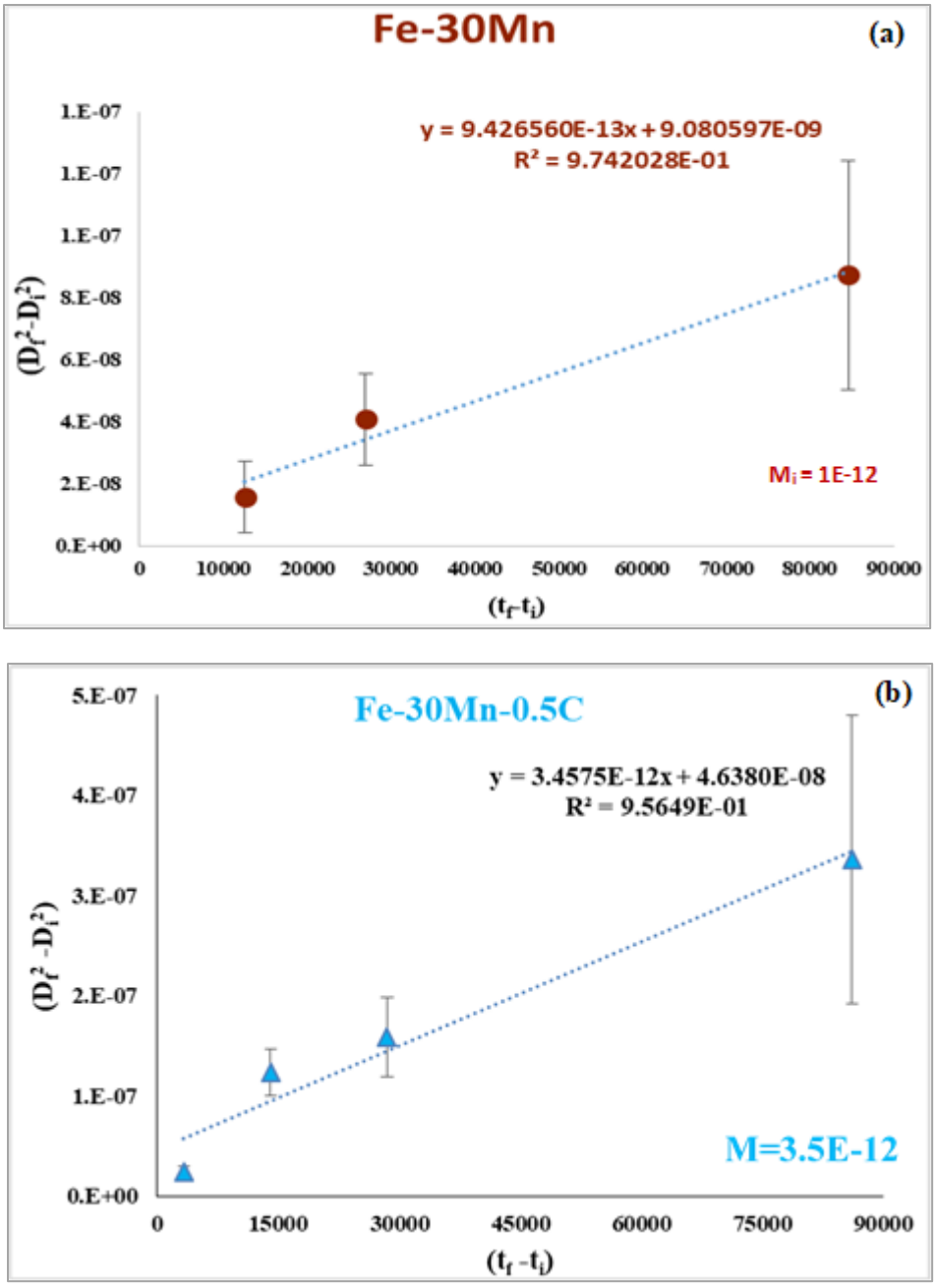

Figure 4.12. Extraction of mobility (M) from the grain growth data at 1200°C for a) Fe-30Mn, b) Fe-30Mn -0.5C

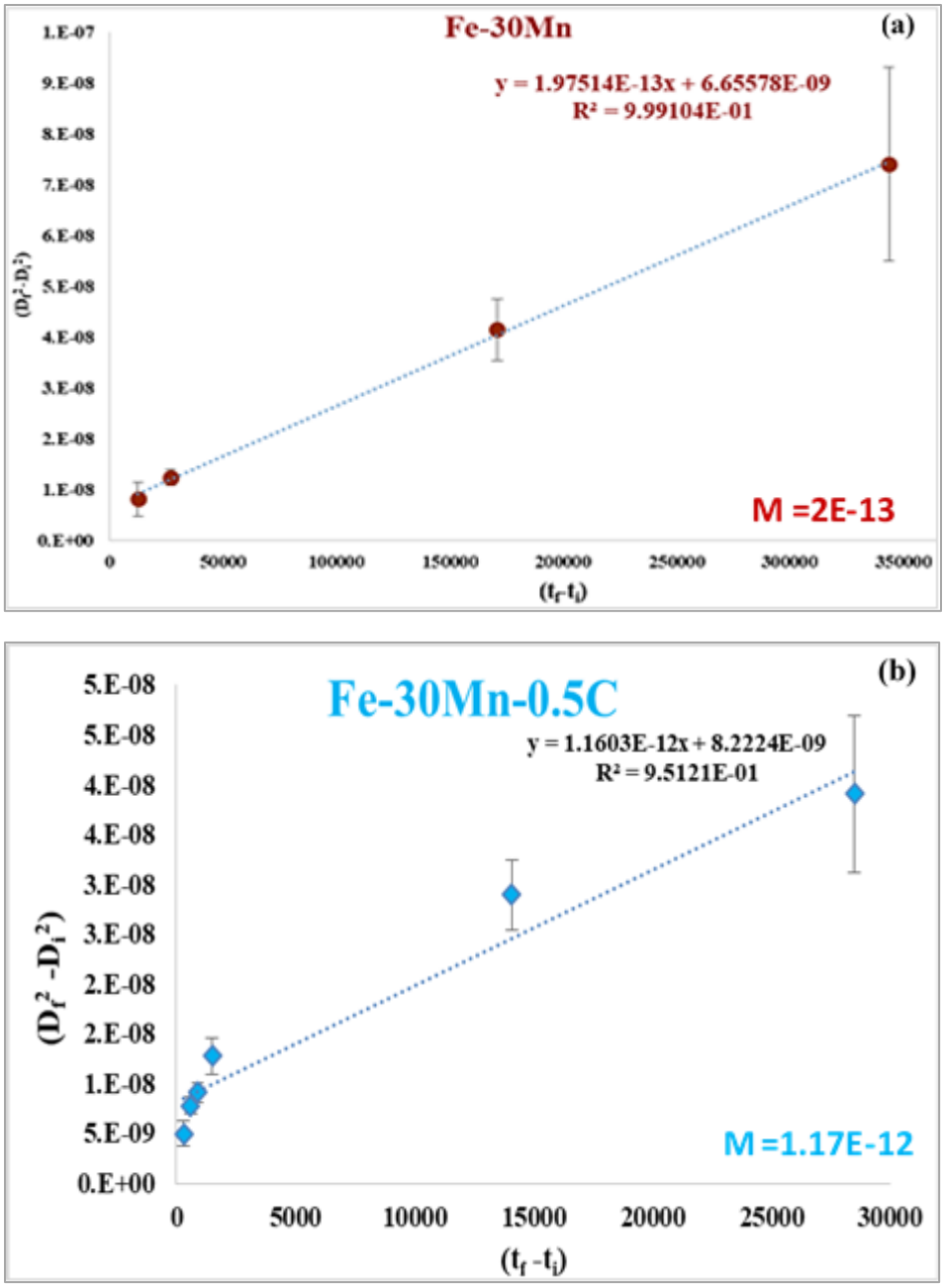

Figure 4.13. Extraction of mobility (M) from the grain growth data at 1100°C for a) Fe-30Mn, b) Fe-30Mn-0.5C

4.4 Temperature and Concentration correlation of Mobility:

The boundary mobility obtained from previous section was found to vary with temperature. In Figure 4.14. a, logarithm of mobility is plotted with respect to inverse of temperature for Fe-30Mn,

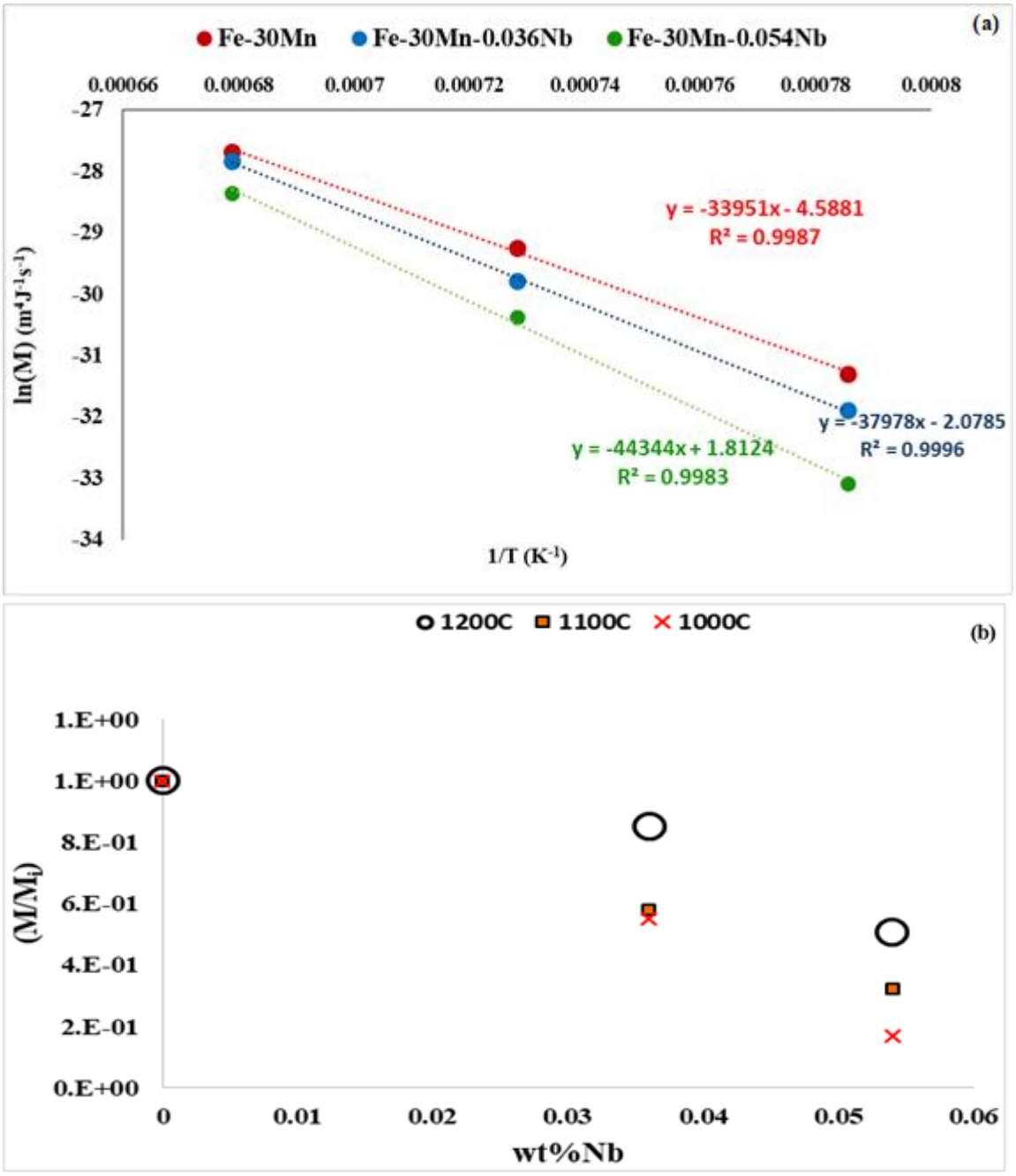

Figure 4.14. a) Temperature dependence of mobility for Fe-30Mn system in presence and absence of Nb, b) Solute Nb concentration dependence of (normalized) mobility at three different temperatures

Fe-30Mn-0.036Nb and Fe-30Mn-0.054Nb alloys. The trend obtained is in agreement with the one predicted by equation 2.32. From this plot, the slope of the line can be equated with (Q/R) which determines the value of the activation energy 'Q' of atomic jumps across the interface. At a fixed temperature, highest Nb condition offers the lowest mobility. In Figure 4.14.b, effect of solute

concentration on normalized mobility is plotted at three different temperatures. As shown, the effect of Nb solute drag increases as its concentration goes up in the solution resulting into gradual decrease in the boundary mobility. The concentration dependence is more pronounced at 1000°C.

4.5 GBCD of Fe-30Mn & Fe-30Mn-0.5C:

Evolution and distribution of Σ boundaries was obtained from Orientation Imaging Microscopy using EBSD. Figure 4.15 and 4.16 show evolution of CSL boundaries in Fe-30Mn and Fe-30Mn-0.5C alloys for varying time at 1100°C.

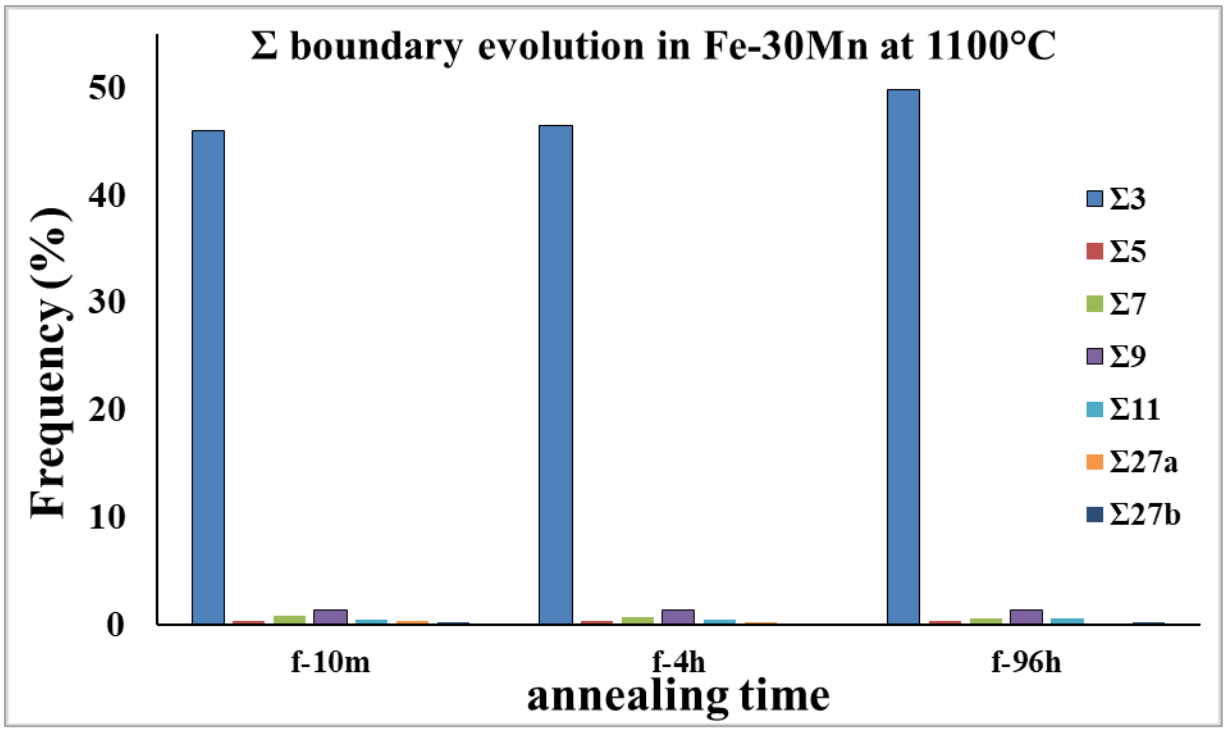

Figure 4.15. Time evolution of various Σ boundaries in Fe-30Mn system at 1100°C

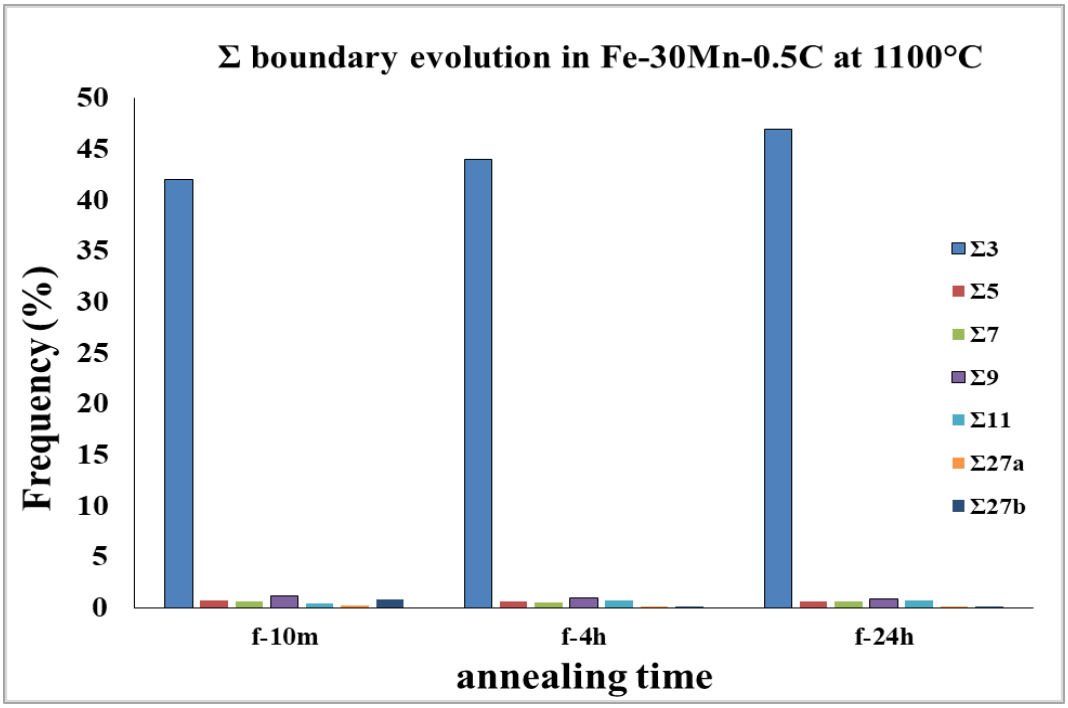

Figure 4.16. Time evolution of various Σ boundaries in Fe-30Mn-0.5C system at 1100°C

4.6 Effect of Mn on Grain Growth Kinetics:

Under this section the grain growth kinetics for alloys with varying Mn level and nearly fixed carbon will be reported. For, Fe-6Mn-0.5C alloys, grain growth kinetics was obtained by LUMet

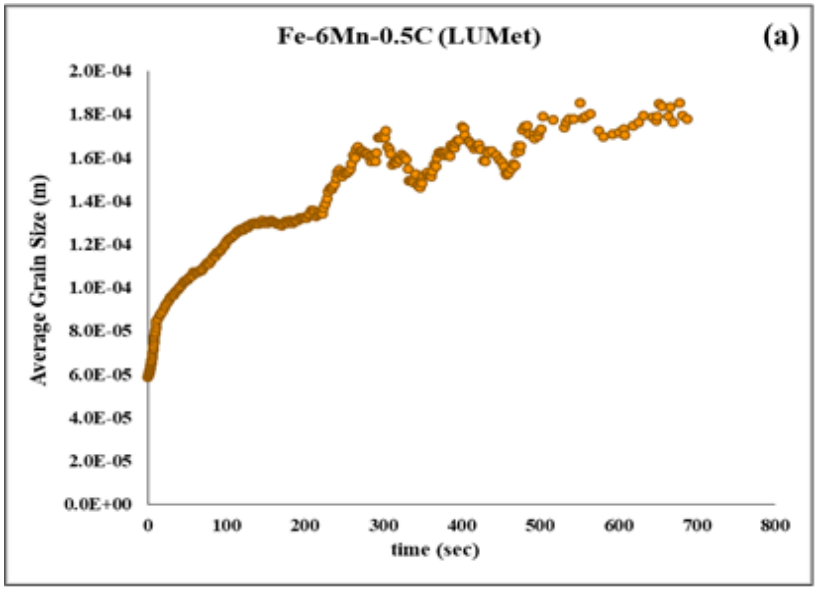

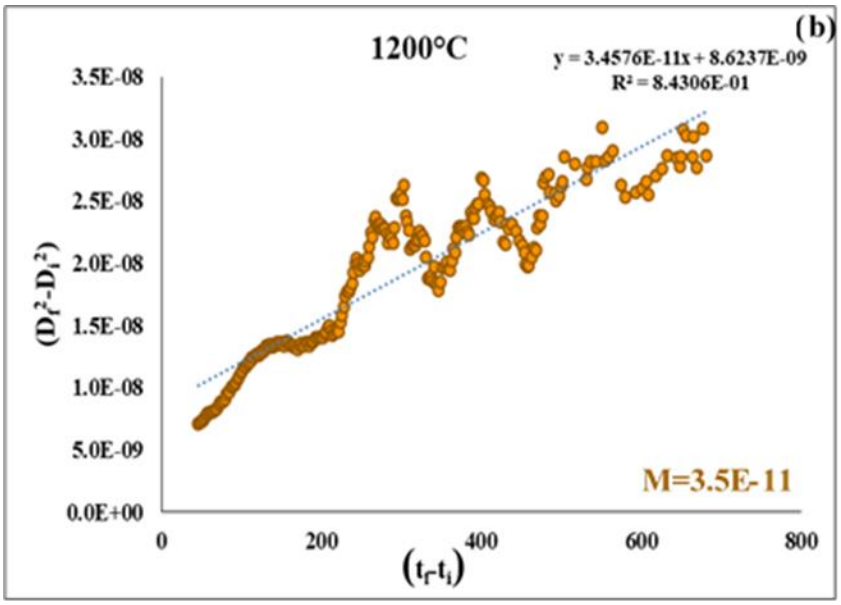

Figure 4.17. a) Grain growth kinetics plot in Fe-6Mn-0.5C system measured by LUMet , b) Extraction of mobility (M) from the grain growth data at 1200°C

and Thermal etching method. Figure 4.17. a shows the grain growth kinetics at 1200°C obtained by LUMet and similar method of mobility extraction is being shown in Figure 4.17. b. The reported data came after satisfactory noise reduction of the raw data obtained from LUMet measurement. On the other hand, the grain growth kinetics obtained from thermal etching and mobility extraction

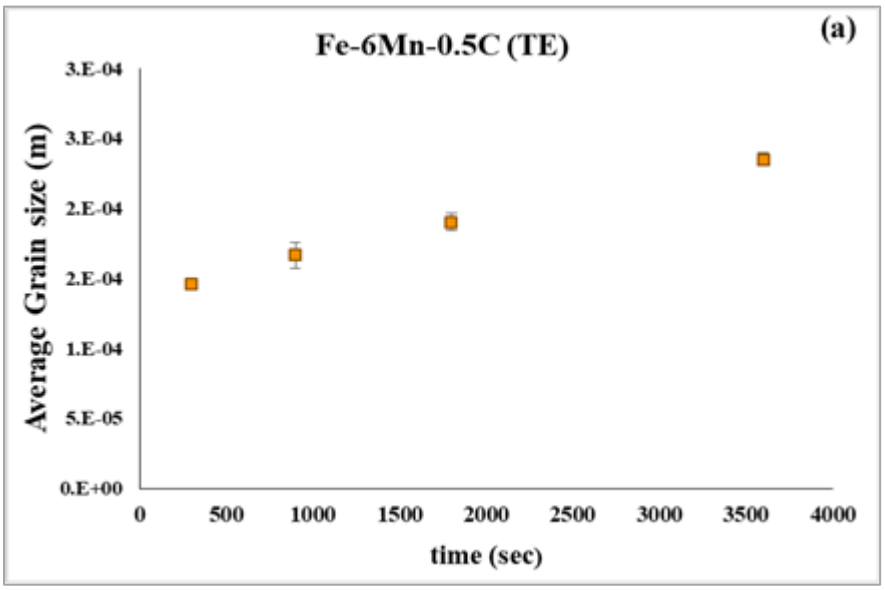

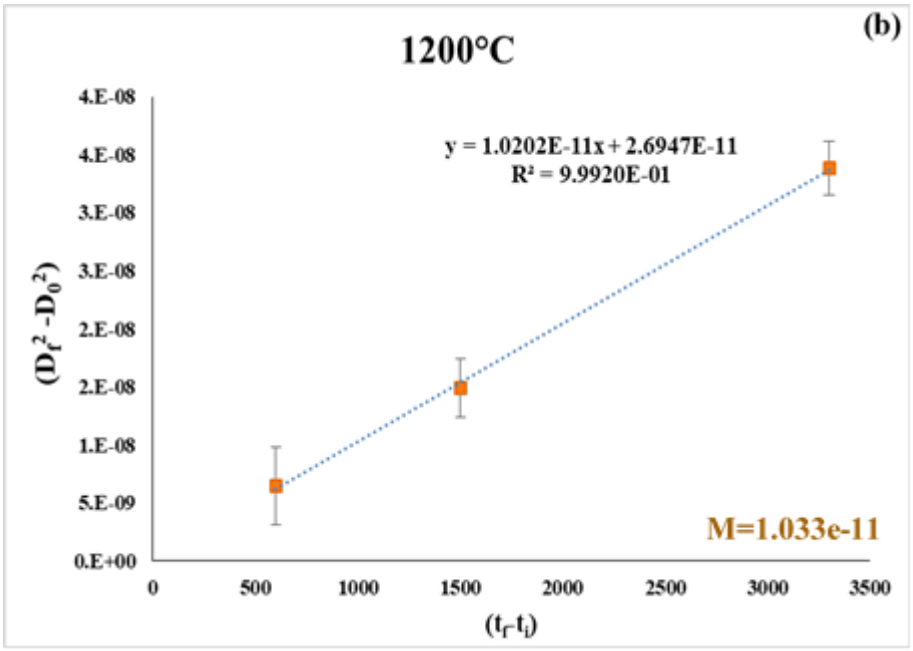

Figure 4.18. a) Grain growth kinetics plot in Fe-6Mn-0.5C system measured by Thermal Etching method, b) Extraction of mobility (M) from the grain growth data at 1200°C

are being shown in Figure 4.18. a and b respectively. Each data point corresponds to average of atleast 3 measurement values of grain size.

For Fe-15Mn-0.5C system, grain growth kinetics was determined using the annealing experiment at 1200°C for time ranging from 5 minutes to 24 hours. For this particular system, all the samples were sealed in quartz capsule as even for the shortest annealing time, the sample underwent huge amount of internal oxidation and the sample had to be discarded. Also, for Fe-15Mn-0.5C steel, following grain growth experiments water quenching gave better microstructure than oil quenching. So, unlike Fe-30Mn system, all the samples containing 15wt% Mn were water quenched. The grain growth kinetics at 1200°C for Fe-15Mn-0.5C is given in Figure 4.19. a and mobility extraction is shown in Figure 4.19. b.

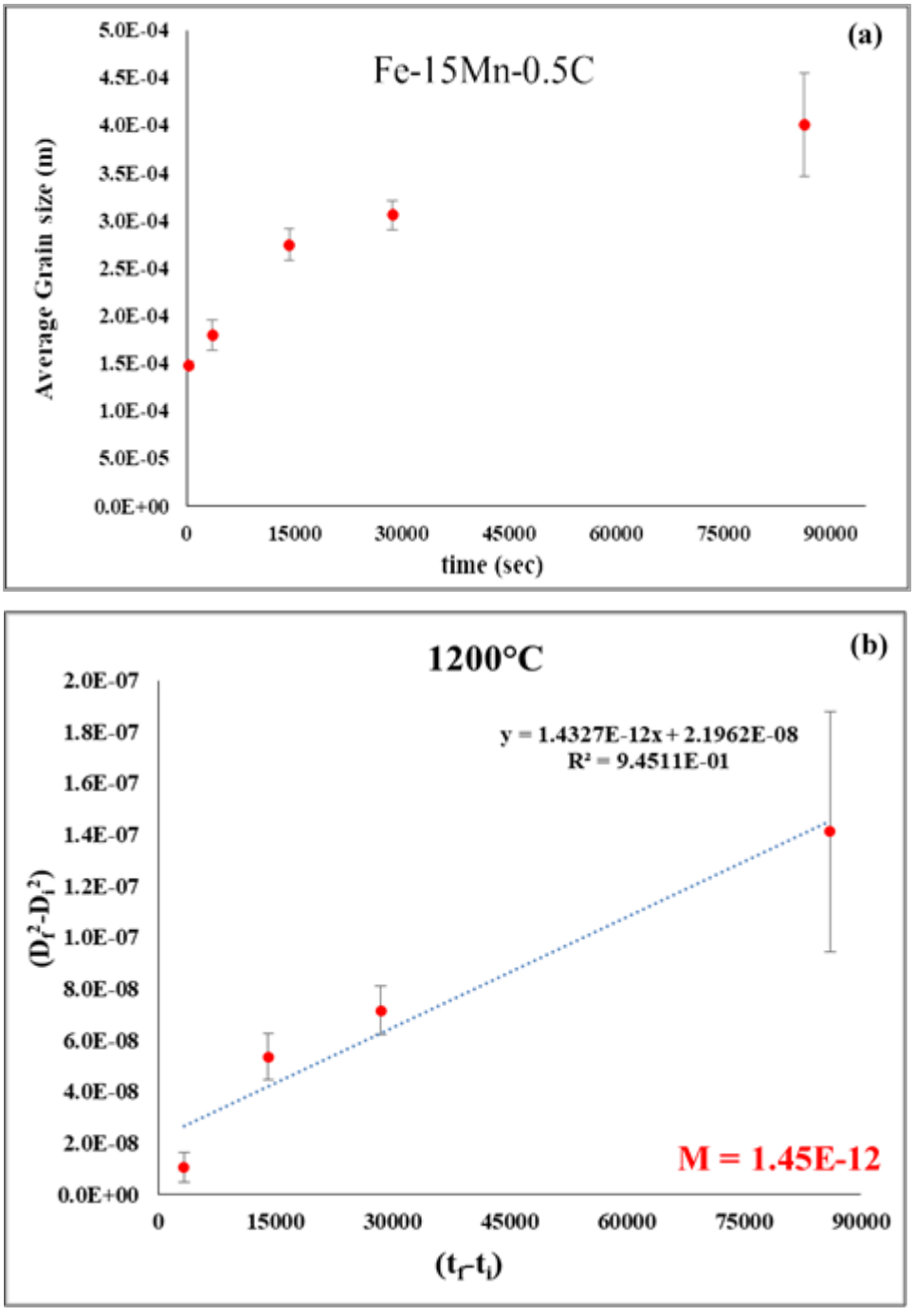

Figure 4.19. Grain growth kinetics plot in Fe-15Mn-0.5C system measured by isothermal annealing experiment, b) Extraction of mobility (M) from the grain growth data at 1200°C

For, Fe-22Mn-0.6C system, grain growth kinetics was calculated from the equation obtained from the data on annealing experiments performed with Fe-22Mn-0.6C (Ferraiuolo et al. 2009). The equation used was as follows:

$$D(\mu m)^{3.8894} = 2.2516 \cdot 10^{16} t(s) \cdot exp\left(\frac{-363\ (kJ/\ mol)}{RT}\right) \qquad \ldots\ldots\ldots\ Eq\ 4.4$$

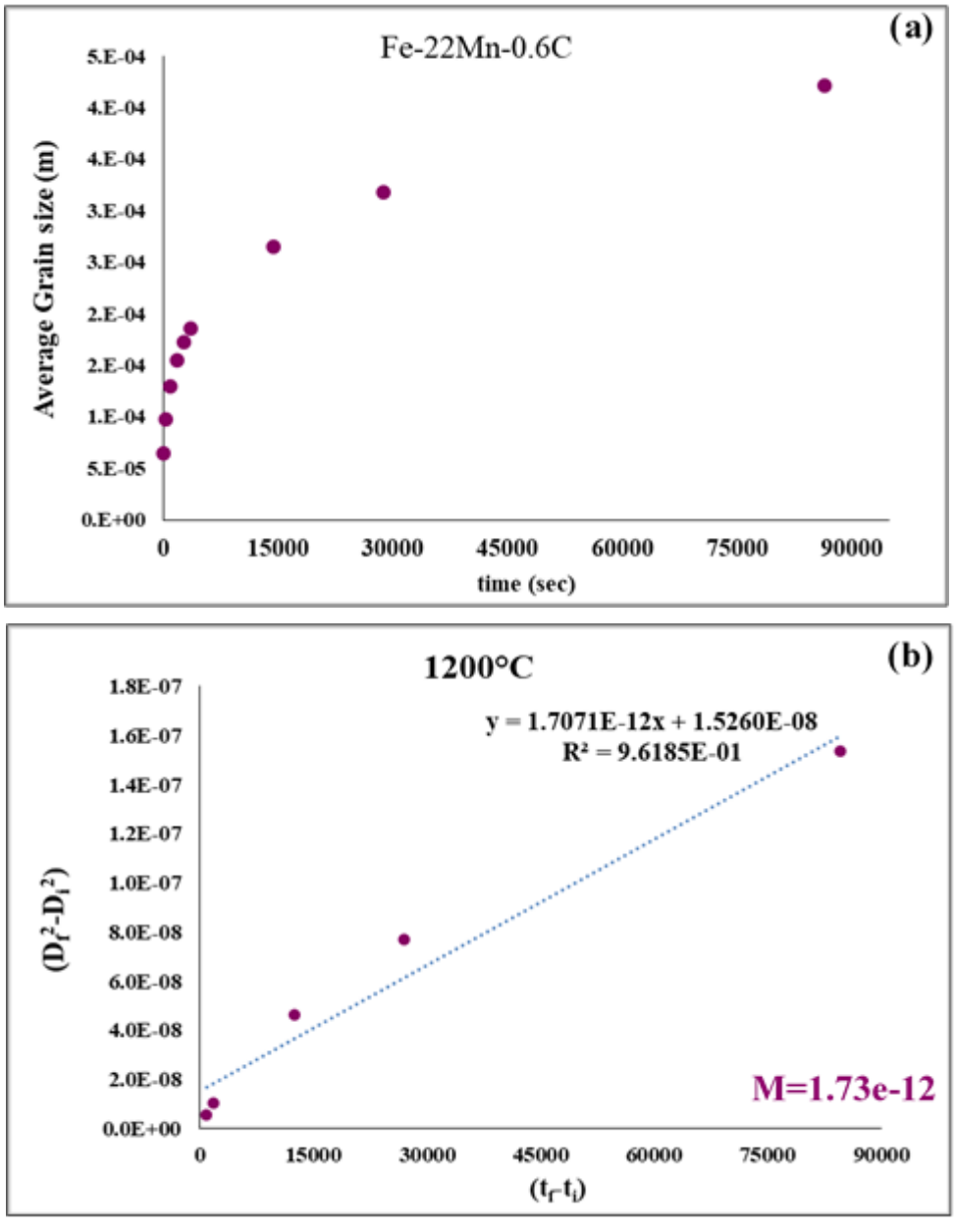

Figure 4.20. a) Grain growth kinetics plot in Fe-22Mn-0.6C system, b) Extraction of mobility (M) from the grain growth data at 1200°C

The kinetics obtained from above equation is being shown in Figure 4.20. a and similar approach was followed to obtained mobility value in Fe-22Mn-0.6C system at 1200°C (Figure 4.20. b).

4.7 Atom Probe Results:

3-D Atom Probe experiments were performed on alloys containing different levels of C, Mn and Nb. The first result was obtained from a sample of Fe-30Mn-0.077Nb after being heat treated at

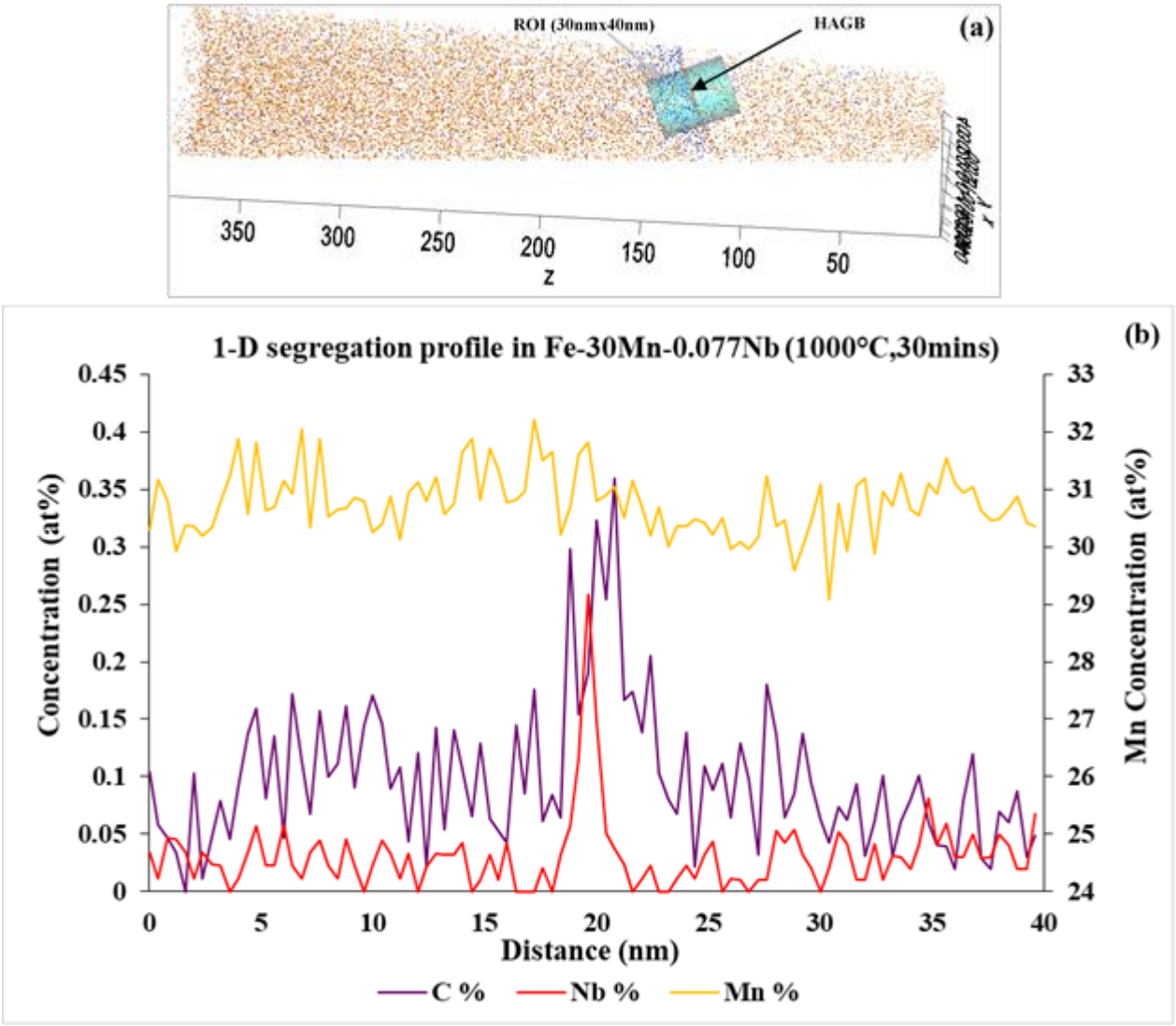

Figure 4.21. a) Construction of ROI perpendicular to the HAGB of interest, b) 1-D segregation profile of elements in Fe-30Mn-0.077Nb after a heat treatment at 1000°C for 30 minutes.

1000°C for 30 mins. The 1-D segregation profile (Figure 4.21. b) of the elements were done using a cylindrical ROI (Region of Interest, a volume normal to the boundary as shown in Figure 4.21.a of 30 nm diameter and 40nm length. The data was sampled using a constant bin width of 0.4nm. To verify reproducibility of the atom probe results, another tip from the same sample was run and

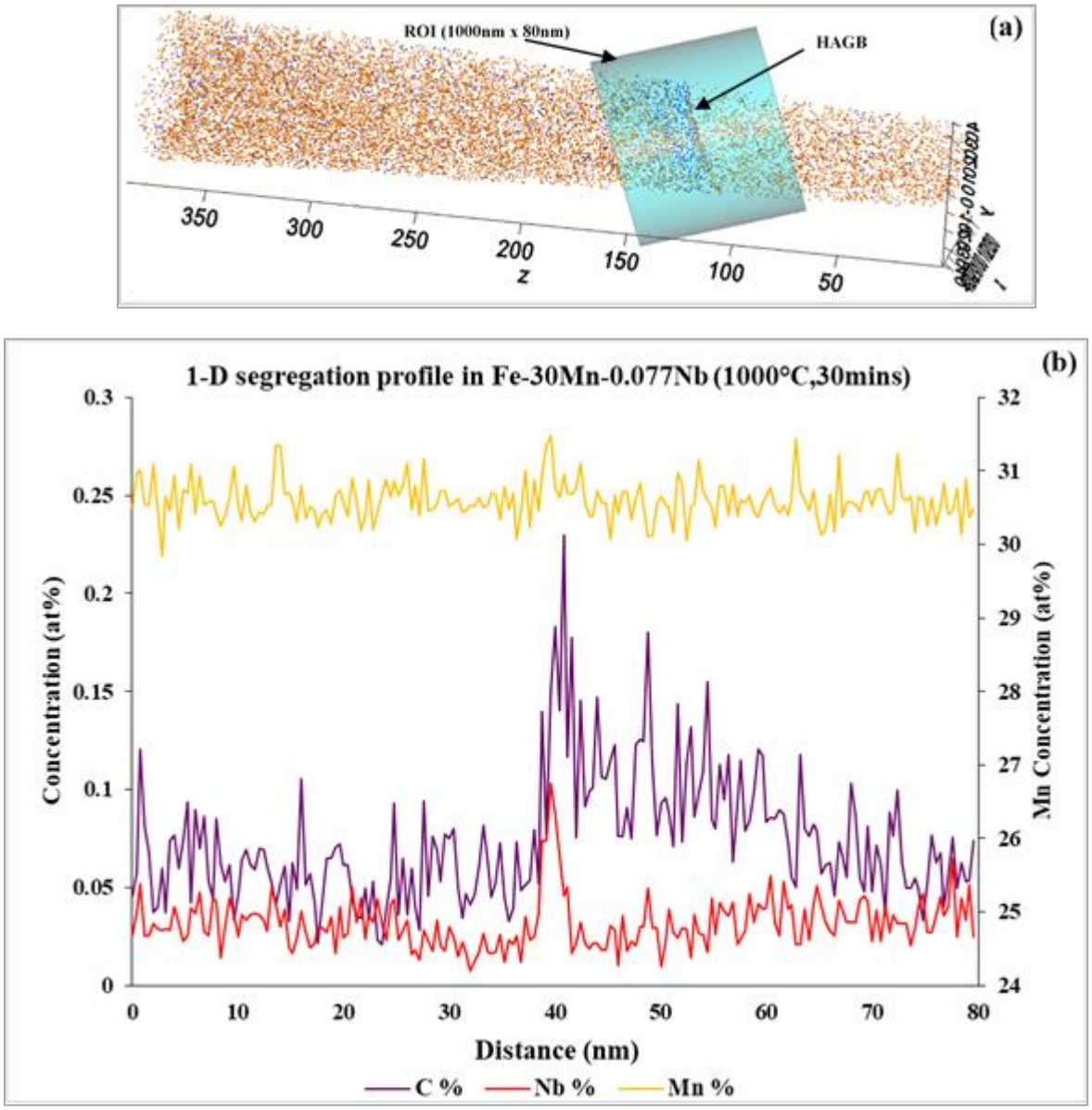

Figure 4.22. a) Construction of bigger ROI perpendicular to the HAGB of interest, b) 1-D segregation profile of elements in Fe-30Mn-0.077Nb after a heat treatment at 1000°C for 30 minutes

a larger ROI of 100nm diameter and 80nm length (Figure.4.22. a) was used to calculate 1-D segregation profile of elements across the HAGB of interest (Figure.4.22. b). Constant bin width of 0.4 mm was used for data sampling.

Another set of atom probe experiment was performed on an HAGB of Fe-30Mn-0.054Nb to verify the trend of segregation of Nb and Mn. The sample was soaked at 1000°C for 8 days. This was done with the intent of verifying the effect of annealing time on the segregation behavior of the elements mentioned above. A 1-D profile (Figure.4.23) across the HAGB of the segregants was calculated using a ROI of 30nm x 30nm cross section.

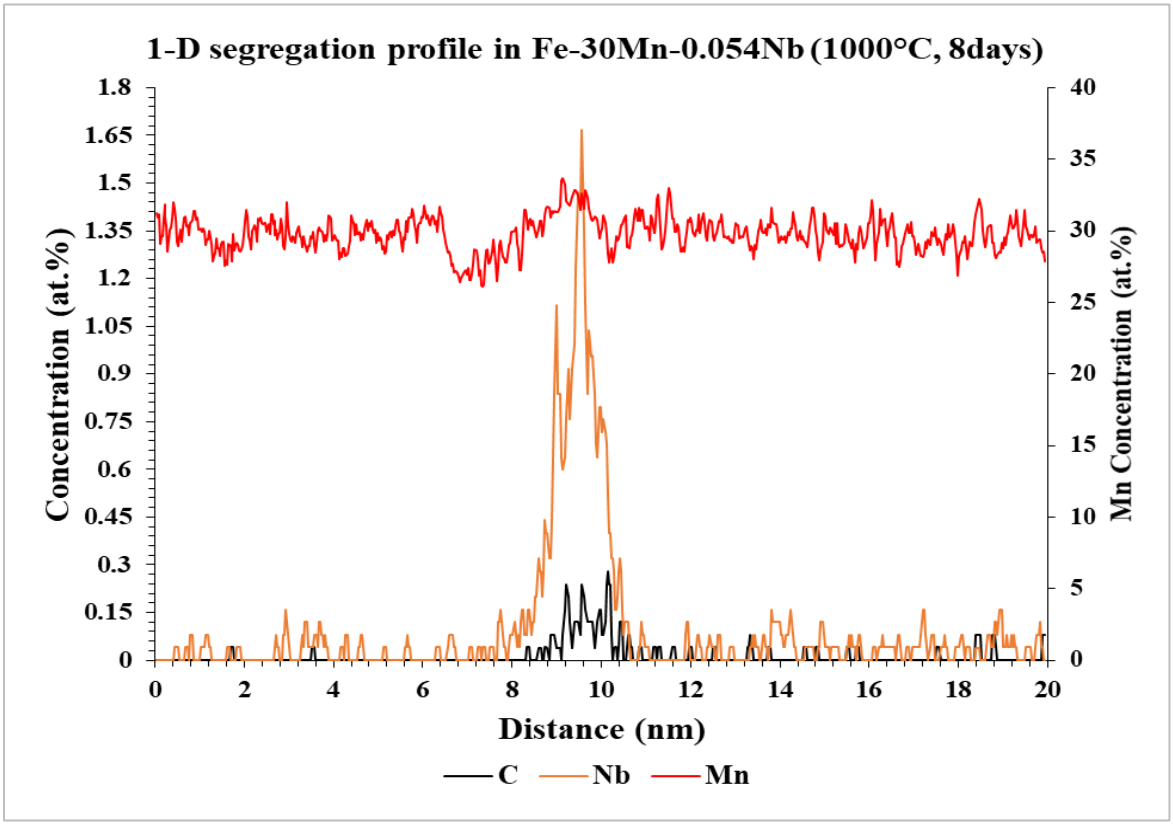

Figure 4.23.1-D segregation profile of elements in Fe-30Mn-0.054Nb after a heat treatment at 1000°C for 8 days using ROI of 30nm x 30nm cross-section

Next, atom probe experiment was performed on a tip from Fe-30Mn (with very low carbon) steel which was soaked for 8 days at 1000°C. The 1-D concentration profile of Mn (Figure.4.24) shows a very weak segregation at the HAGB of interest.

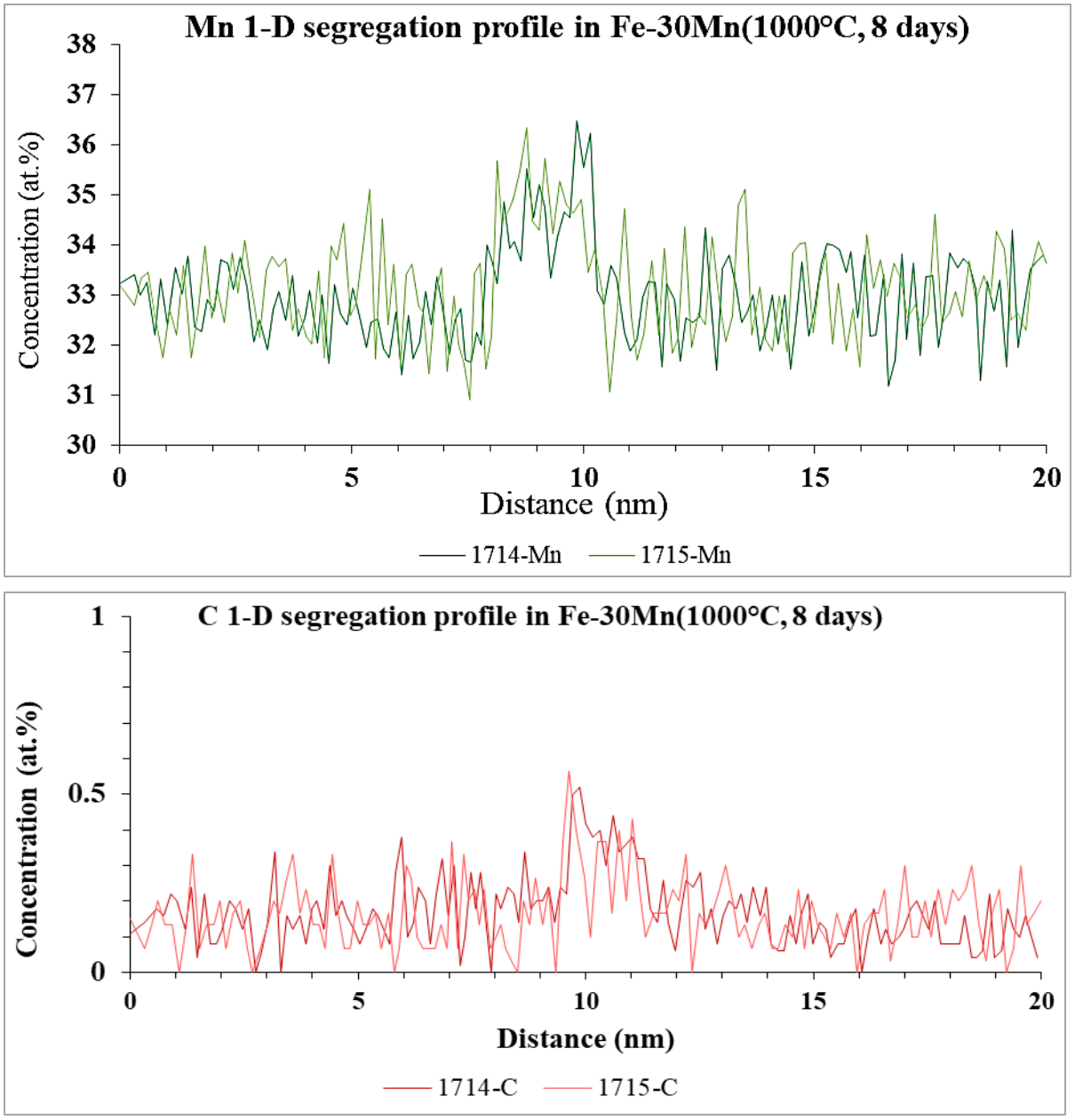

Figure 4.24.Two 1-D segregation profile measured in Fe-30Mn (very low carbon) sample for 8 days at 1000°C for a) Mn, b) carbon

Next set of atom probe experiment was performed to focus upon segregation of Mn across a HAGB. For this, two different compositions were chosen by varying Mn concentration and including carbon. First, a sample of Fe-30Mn-0.5C was chosen and it was soaked at 1000°C for 8 days. 1-D profile of segregants concentration across the grain boundary was calculated based on

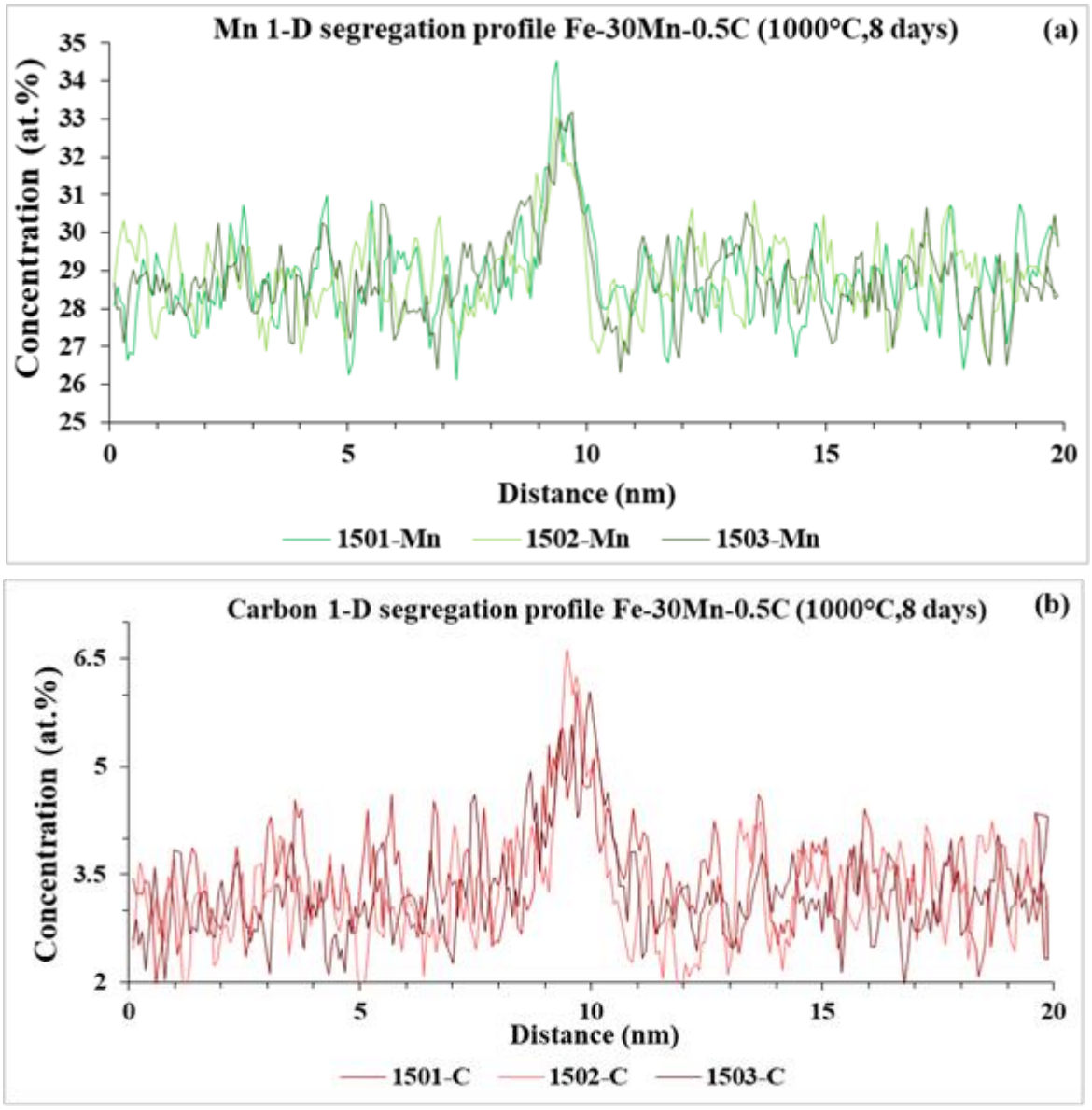

Figure 4.25.Three 1-D segregation profiles measured using 25nm cross section ROI of a) Mn, b) C segregation in a sample of Fe-30Mn-0.5C soaked for 8 days at 1000°C

25nm diameter ROI taken normal to the HAGB of interest. 3 tips were run to verify the reproducibility of the atom probe data for 3 different runs (1501, 1502 and 1503) which shows excellent agreement among three datasets (Figure 4.25. a, b).

Effect of Mn concentration of segregation profile was verified using a sample of chemistry Fe-15Mn-0.5C which was also soaked for 8 days at 1000°C. Similar to the last runs, 2 tips of Fe-

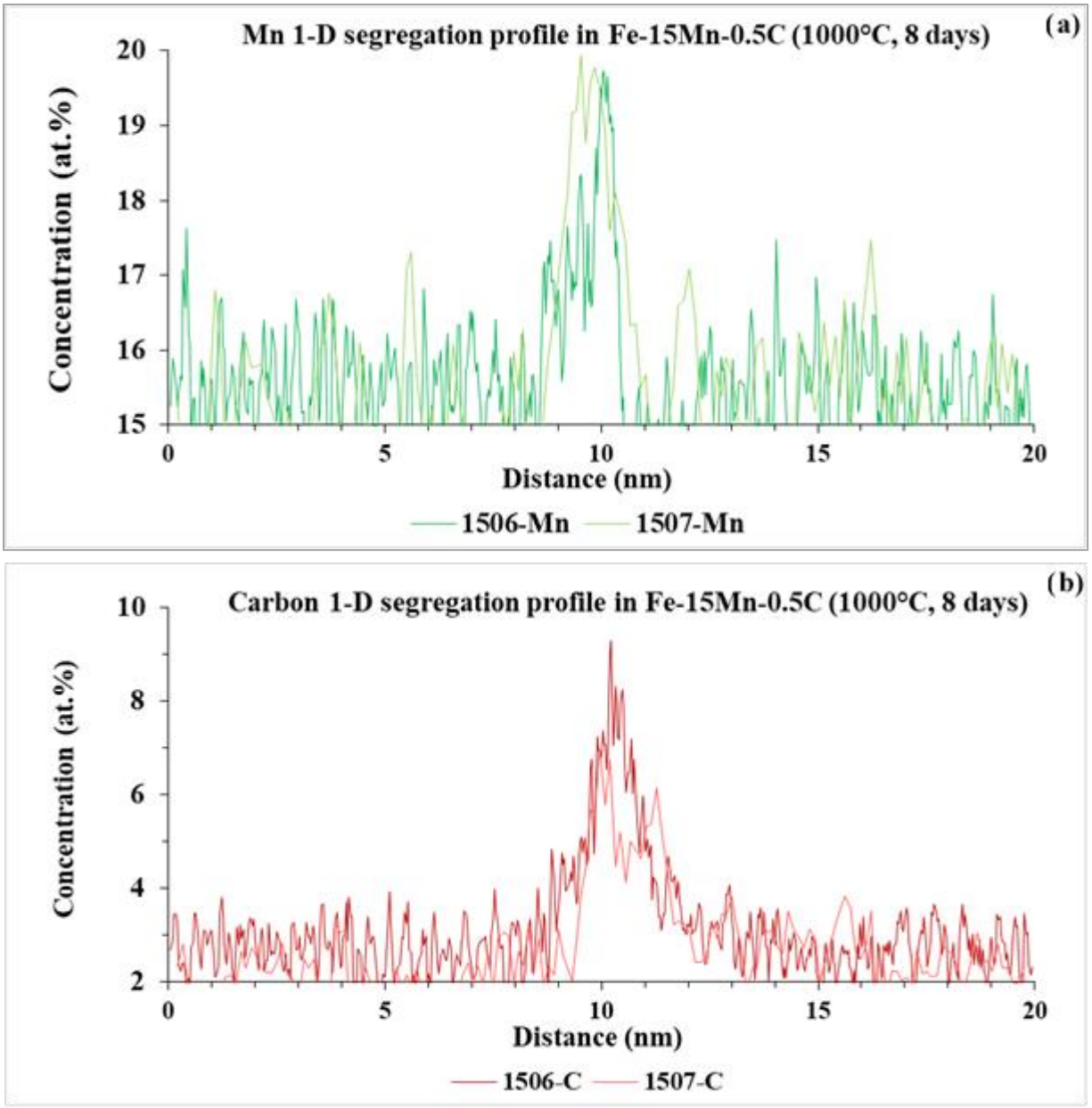

Figure 4.26. Two 1-D segregation profiles measured using 25nm cross section ROI of a) Mn, b) C segregation in a sample of Fe-15Mn-0.5C soaked for 8 days at 1000°C

15Mn-0.5C samples (1506, 1507) were run in the atom probe and ROI of 35nm diameter cross section was used to calculate 1-D segregation profile across the HAGB of interest. Figure 4.26. a and b show the concentration profile across HAGB of interest for segregants Mn and C.

4.8 Grain Boundary Engineering:

The purpose of performing Grain Boundary Engineering experiments was twofold. First of all, it was found that there is not much hard data on grain boundary engineering of high manganese steel, especially steels containing 30% Mn. Next to that, it was interesting to know if Grain Boundary Engineering helps to control grain growth kinetics. Under this section, the results of strain recrystallization treatment on Fe-30Mn-0.036Nb and strain annealing on Fe-30Mn-0.5C are described.

For the iterative strain recrystallization experiments on Fe-30Mn-0.03Nb, it was found that the grain boundary engineered sample after a grain growth experiment at 1100°C for 4 hours, the average grain size measured was 52 μm. Another sample of Fe-30Mn-0.03Nb steel was taken for a different grain boundary engineering route where the sample was given same amount of thickness reduction as achieved in iterative strain recrystallization, but in one step and then it was annealed in a similar way. When this sample was taken for a grain growth experiment at 1100°C for 4 hours, it was found that the average grain size was 51 μm. So, iterative strain recrystallization treatment was not effective to reduce the grain size as compared to single step strain recrystallization treatment. Possible reason for this will be given under the discussion section.

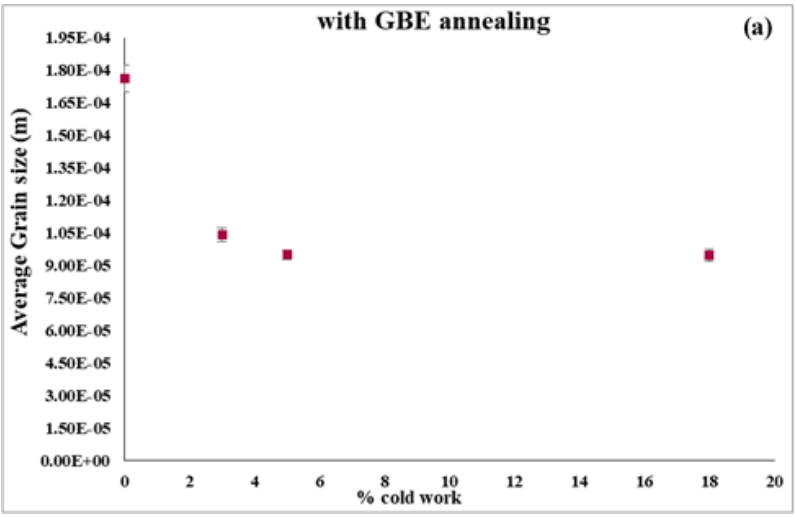

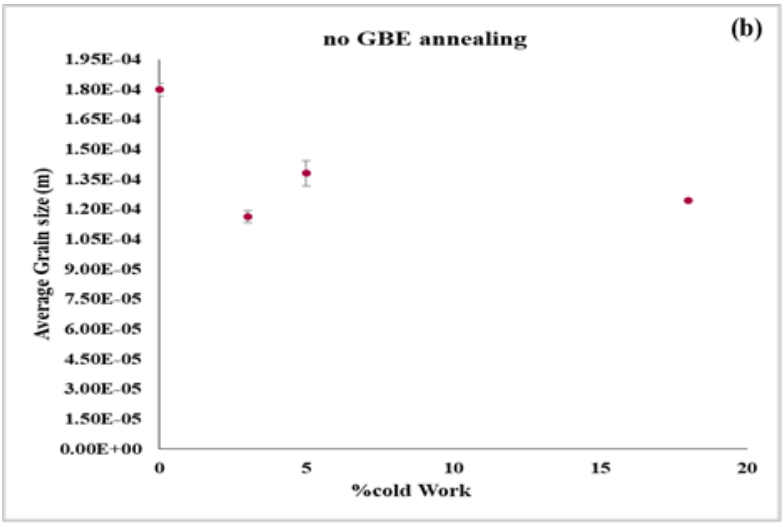

Figure 4.27. Grain size variation (at 1100°C after soaking for 30 minutes) with amount of cold work a) followed by annealing at 900°C for 30 minutes, b) followed by no annealing prior to growth experiment

For the strain annealing experiments, the grain boundary engineered samples were of Fe-30Mn-0.5C composition. After the grain boundary engineering treatment was performed, samples of each deformation set underwent grain growth experiment at 1100°C for 30 minutes. The average grain size was compared with a base sample which was not given any grain boundary engineering treatment prior to the grain growth experiment at 1100°C for 30 minutes. In Figure 4.27. a and b, variation of average grain size (after soaking at 1100°C for 30 minutes) with the amount of deformation followed by annealing and no annealing prior to growth experiment are given. Also, microstructure evolution for different GBE is given in Figure 4.28. a-d.

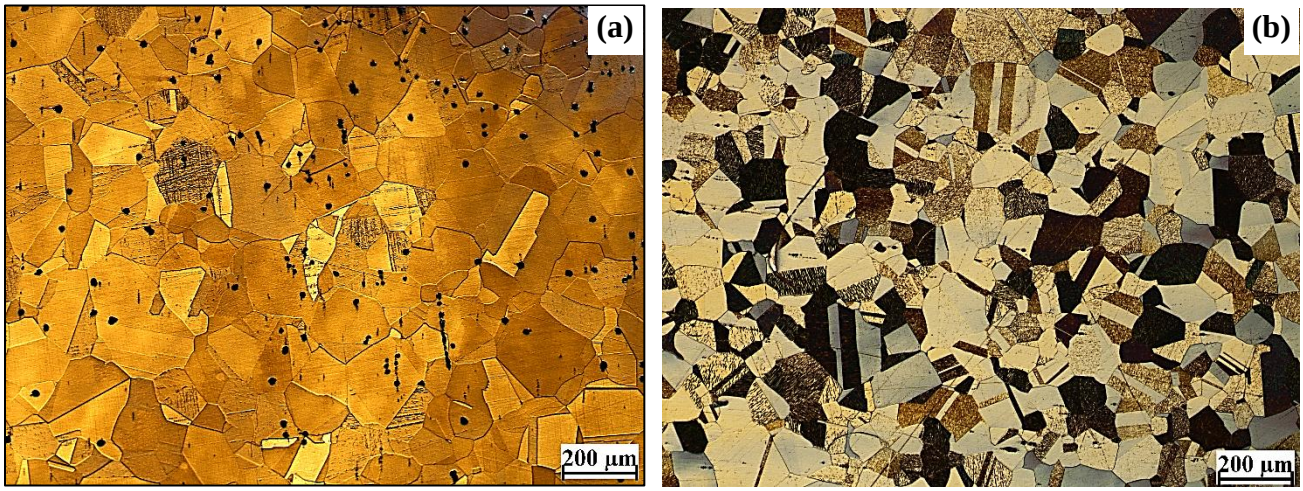

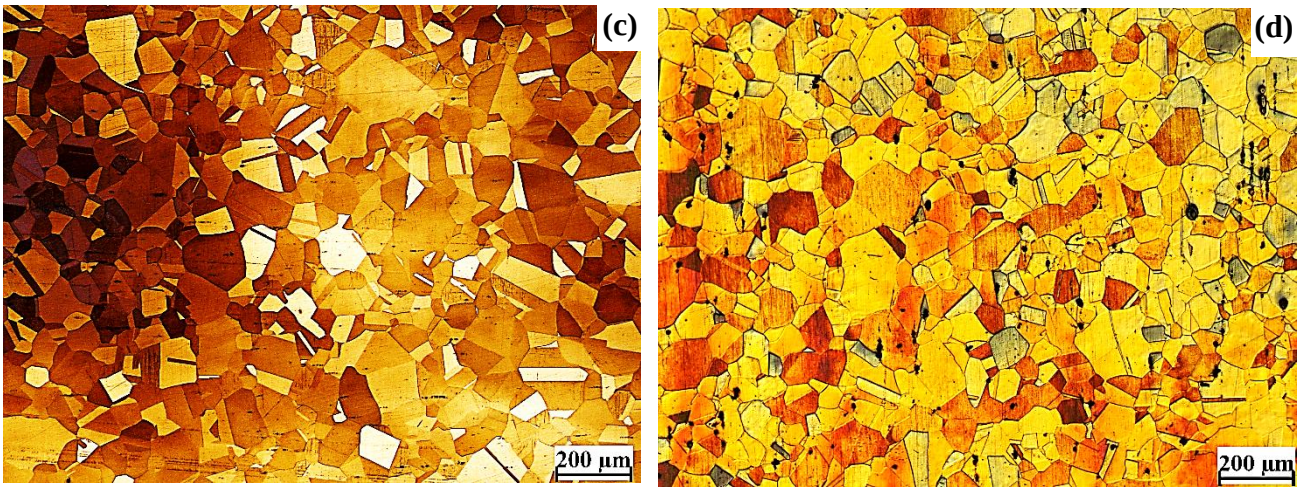

Figure 4.28.Microstructure of Fe-30Mn-0.5C samples after 1100°C,30 minute grain growth experiment following a) no GBE and b) 3%, c) 5%, d)18% cold work followed by 900°C,30 minute annealing treatment (as per Figure 3.17)

In Figure 4.29. a, b and c, evolution of special boundaries, particularly Σ3, 9 and 27 is given.

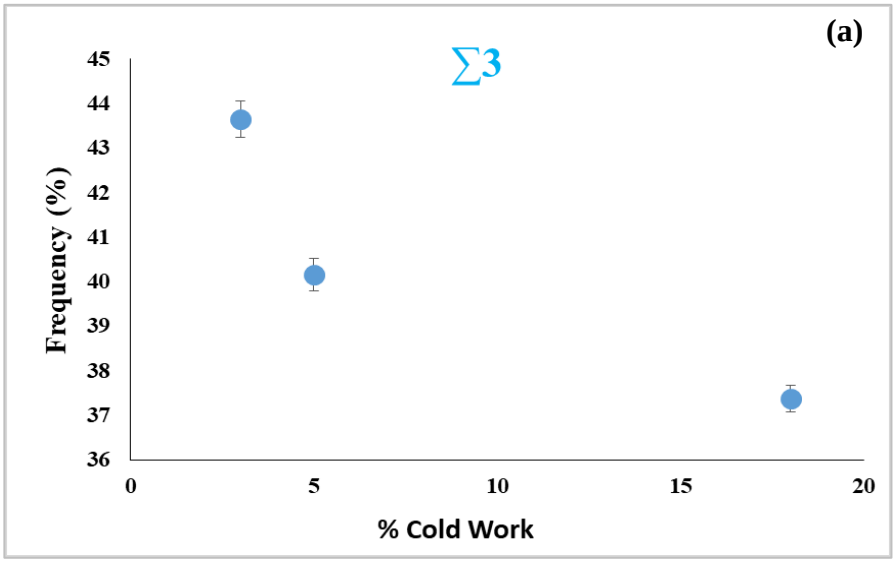

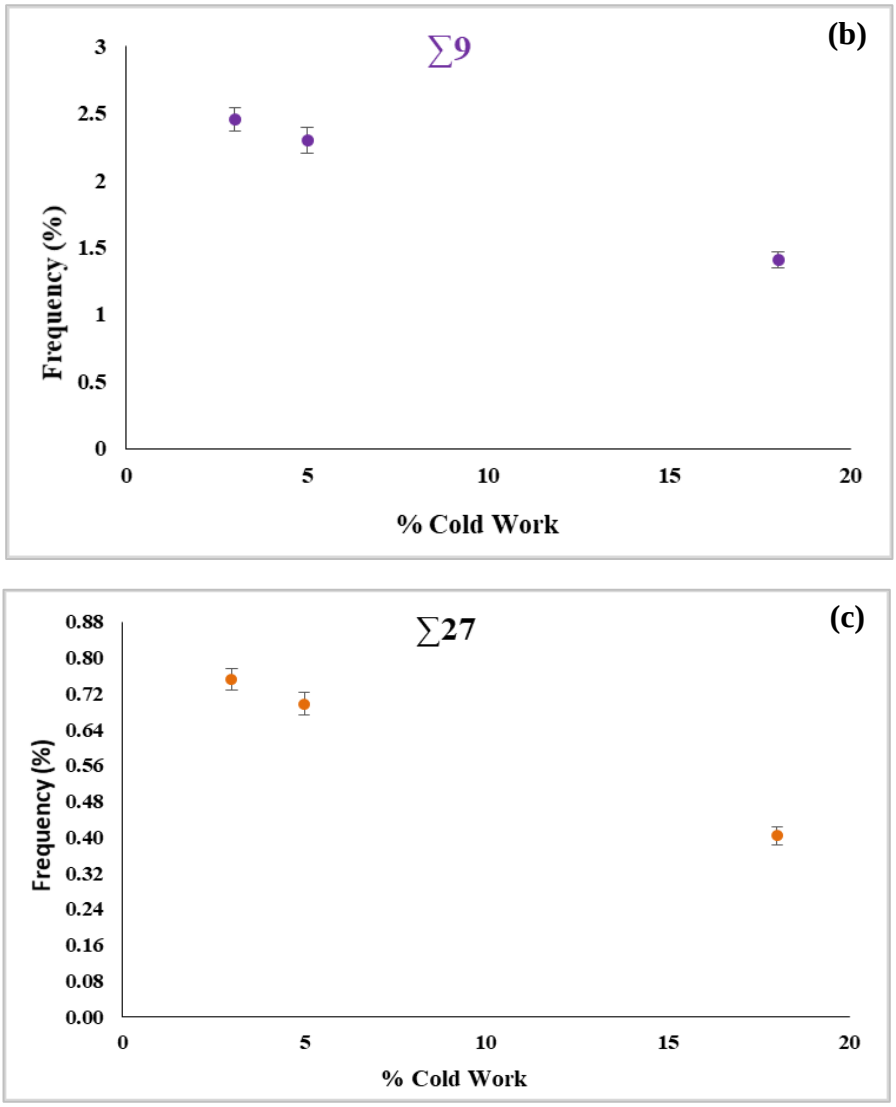

Figure 4.29. Grain Boundary Character Distribution (GBCD) of a) Σ3, b) Σ9 and c) Σ27 CSL boundaries after different amount of GBE reduction (as per figure 3.17)

The frequency percentage is indicative of length fraction of a particular boundary type in the global boundary network. The variation of other CSL boundaries are given in brief for reference as they don't directly belong to the Σ3 variant family (Figure 4.30).

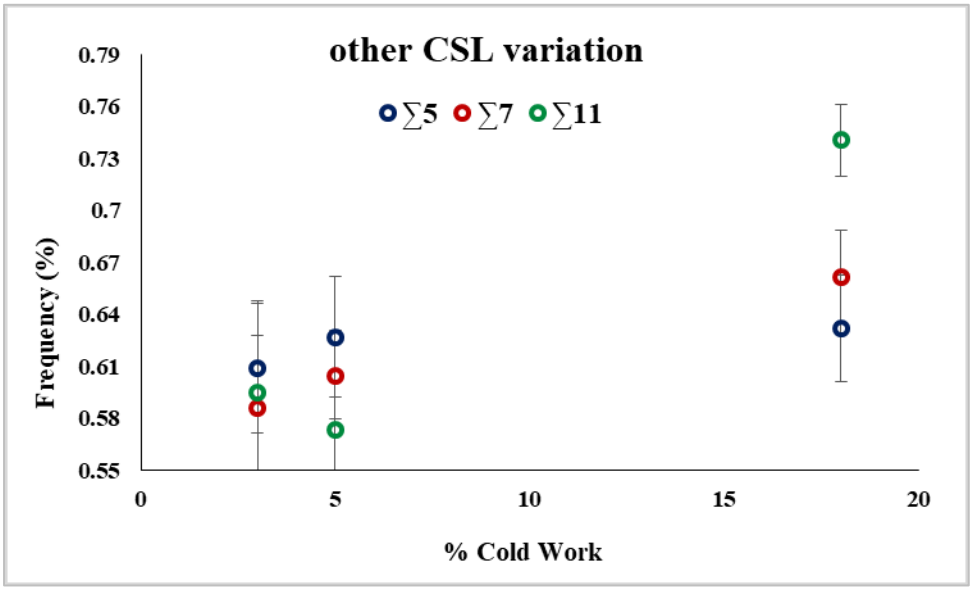

Figure 4.30. Change in GBCD of Σ5, 7 and 11 with varying amount of cold work (as per figure 3.17)

To further verify the effect of rolling iterations to special boundary evolution, GBCD was calculated from EBSD data of Fe-30Mn-0.5C samples after each cycle of GBE treatment depicted in Figure 3.18. It must be mentioned that in Figure 4.31. a, b and c, the GBCD of Σ3 and its

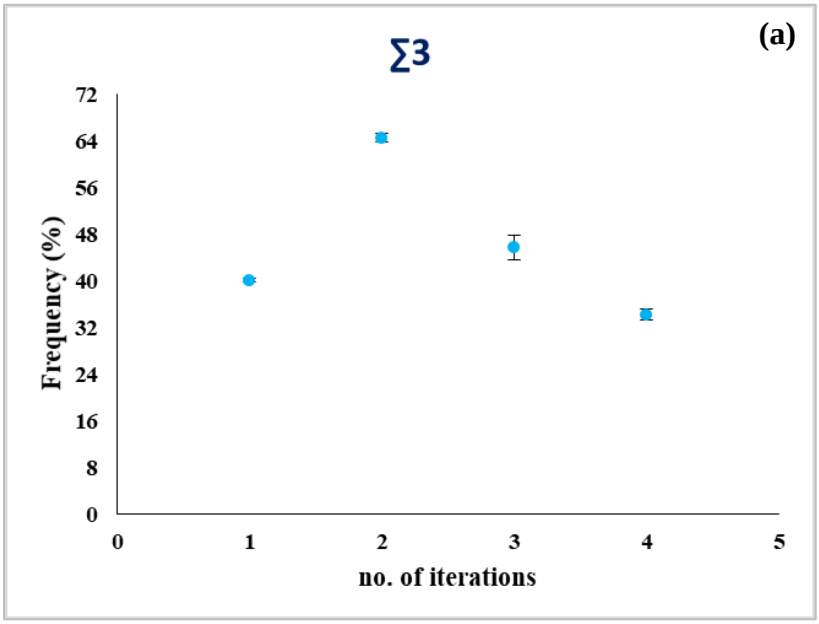

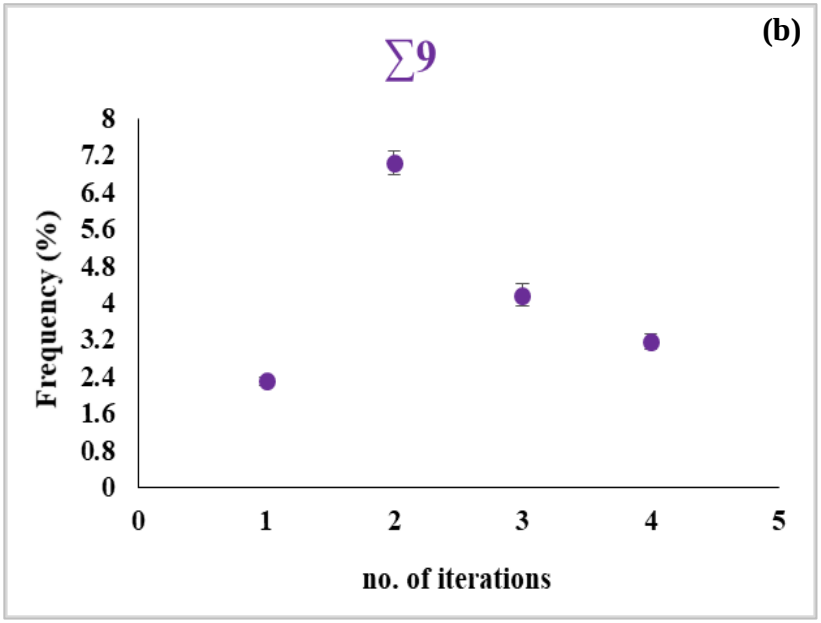

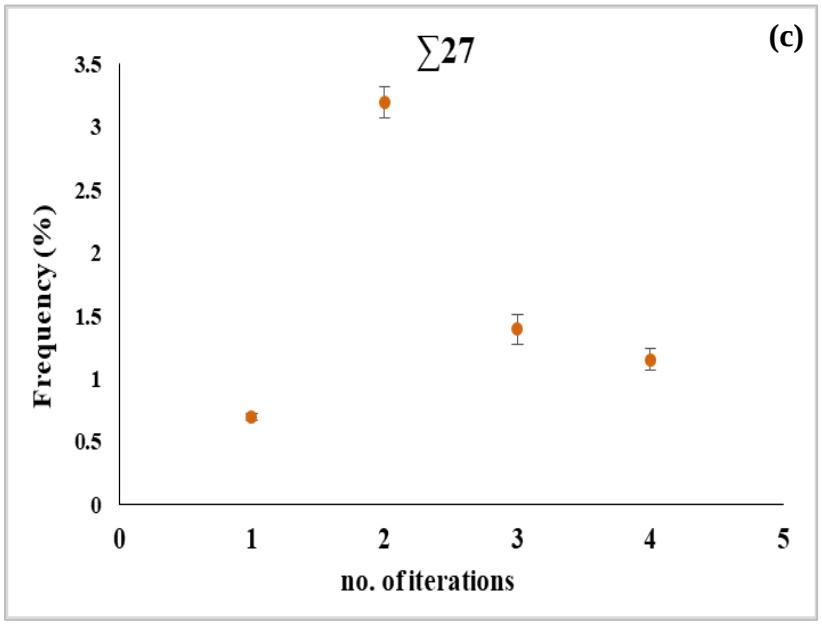

Figure 4.31. Grain Boundary Character Distribution (GBCD) of a) Σ3, b) Σ9 and c) Σ27 CSL boundaries after each iteration in the 4 step GBE (as per figure 3.18)

variants are given and the EBSD was performed on a sample after each iteration consisting of 5% cold rolling followed by half an hour of annealing at 900°C for 30 minutes.

In Figure 4.32, variation of frequency of Σ5, 7 and 11 is given altogether after each iteration of the 4 step GBE treatment mentioned in figure 3.18.

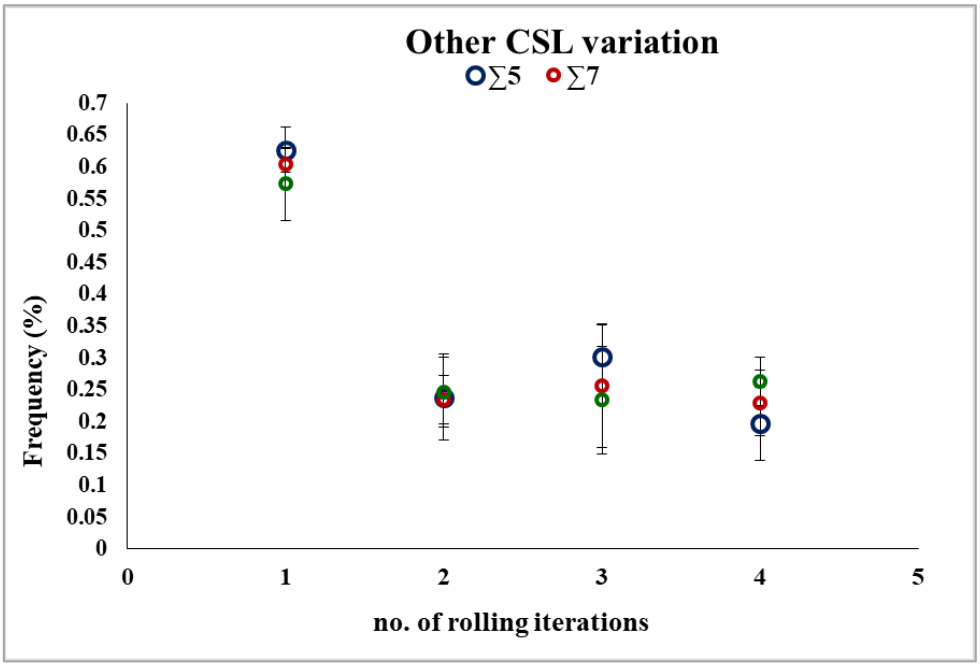

Figure 4.32. Change in GBCD of Σ5, 7 and 11 after each iteration in the 4 step GBE (as per figure 3.18)

5 Discussion

Under this section, a detailed discussion of the results obtained in the grain growth experiments of different steels will be given. In addition to that, the effect of Nb as a microalloying element to impart solute drag will be discussed. The new findings will be explained with various possibilities. The effect of alloying elements such as Mn and C on growth kinetics and segregation behavior will be included during the discussion of the atom probe results. This section will also present a modified form of a physically based model of twin inhibited grain growth kinetics. The chapter will end with a brief discussion on grain boundary engineering results obtained in Fe-30Mn systems.

5.1 Grain growth kinetics in Fe-30Mn system:

Under this section, growth kinetics of both the Fe-30Mn and Fe-30Mn-0.5C system will be discussed. As given in Figure 4.1, the grain growth kinetics in Fe-30Mn system within the temperature range of 1200°C-1100°C shows a parabolic trend. The growth kinetics is faster at higher temperature and it decreases as the temperature drops. When the grain size evolution in Fe-30Mn system was compared with commercial low Mn steels, it was found that growth kinetics is very slow in the 30Mn system. For example, a steel containing 1%Mn (Furumai, Zurob, and Phillion 2018) has mobilities 2 orders of magnitude higher than that of Fe-30Mn steel (Table 5.1).

Table 5.1. Comparison of Mobility at three different temperatures

Temperature (°C)	**Mobility (Fe-1%Mn) * ($m^4\ J^{-1}s^{-1}$)**	**Mobility (Fe-30%Mn) ($m^4\ J^{-1}s^{-1}$)**	$\frac{\mathbf{M\ (Fe-1\%Mn)}}{\mathbf{M\ (Fe-30\%Mn)}}$
1200	1e-10	1e-12	1e+2
1100	5e-11	2e-13	2.5 e+2
1000	1e-11	3e-14	3.33 e+2

* (Furumai, Zurob, and Phillion 2018)

When the mobility is plotted against inverse of temperature, it showed a linear trend (Figure 5.1). This indicates that mobility of Fe-1Mn and Fe-30Mn, both, follow Arrhenius equation as given by

Equation 2.32. When the activation energy is calculated from the slope, $Q_{Fe\text{-}1Mn}$ was found to be 162 kJ/mol whereas the activation energy for $Q_{Fe\text{-}30Mn}$ was 282 kJ/mol (Table 5.2). Interestingly, the value for 1%Mn is consistent with the activation energy for grain boundary diffusion which is

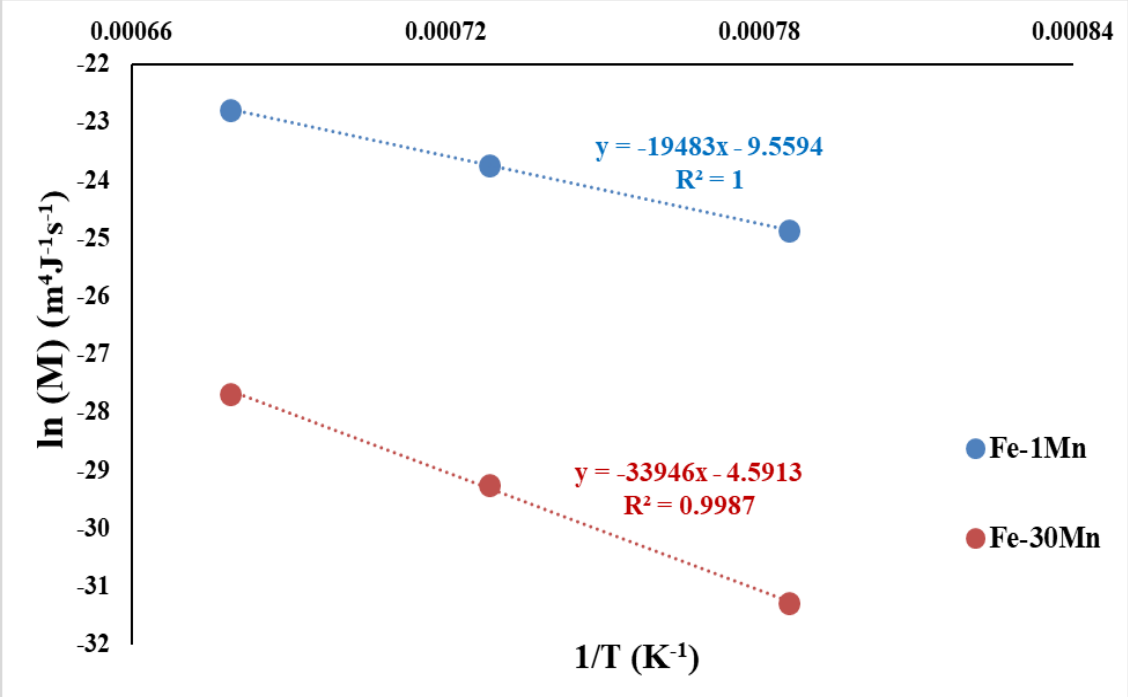

Figure 5.1. Temperature dependence of Mobility in Fe-1Mn and Fe-30Mn system (Fe- 1Mn data taken from (Furumai, Zurob, and Phillion 2018))

consistent with the simple model of Turnbull as well as a large volume of experimental data (Turnbull 1951; Zhou 2010; Furumai, Zurob, and Phillion 2018). The activation energy for the migration of grain boundaries in Fe-30%Mn is comparable to that for bulk self-diffusion in Fe.

Table 5.2. Activation energy (Q) of grain boundary migration calculated from grain growth data

Composition	**Activation Energy (Q), kJ/mol**	**($Q_{Fe\text{-}30Mn}$)/($Q_{Fe\text{-}1Mn}$)**
Fe-1Mn *	162	1.7
Fe-30Mn	282	

* (Furumai, Zurob, and Phillion 2018)

This unusual behavior has not often been reported in the literature. One exception is the report by Winning et al. which showed that some Low Angle Grain Boundaries (LAGB) have Q similar to

that of bulk diffusion (Winning et al. 2010). This comparison already points to a possible difference in the mechanism of migration of boundaries in 1%Mn and 30%Mn system.

The 2 orders of magnitude lower mobility in Fe-30Mn steels was initially thought to be due to the presence of high Mn content which might impede the grain boundary migration in the form of solute drag after segregating to high angle grain boundaries (HAGBs). The 3-D atom probe study across the HAGB of interest shows that the Mn profile is absolutely flat. The results obtained from two different tips of the same steel (Fe-30Mn-0.077Nb (very low carbon)) show similar segregation profile (Figure.4.21.b and Figure 4.22.b). This is a clear indication of Mn not segregating at HAGB as given by the flat profile (yellow lines). Another attempt to check Mn segregation was made using a different sample of high Mn steel by lowering Nb content from 0.077 to 0.054 to see if higher content of Nb interferes with Mn segregation. So, the second atom probe experiment was performed on a sample of composition Fe-30Mn-0.054Nb (very low carbon). Another objective of this experiment was to investigate if annealing time has an effect on segregation behavior of Mn. Some researchers have found that increasing annealing time helps to increase the concentration of segregants at HAGBs in commercially pure nickel (Welsh et al. 2016). So, the annealing parameters were chosen to be 1000°C and 8 days. As shown in Figure 4.23, even in presence of 0.054wt% Nb, Mn concentration profile across the HAGB is absolutely flat. However, another atom probe study was performed with a sample of Fe- 30Mn steel where a very weak segregation of Mn was observed (Figure 4.24.a). These results from the atom probe study confidently rule out the strong segregation possibility of Mn to HAGBs indicating the fact that in Fe-30Mn system, the grain growth is not slowed down because of Mn solute drag.

Next step to investigate the reason behind the slow kinetics in Fe-30Mn system was to examine the microstructure in detail. The EBSD performed on Fe-30Mn samples annealed at 1100°C for various time periods showed that the grain boundaries present in the microstructure belong to two different categories, 50% of the boundaries were characterized as random HAGBs which possess high mobility. Crystallography of remaining 50% boundaries indicated them to belong to low mobility special boundaries which can be described by various Coincidence Site Lattice criteria. Most of the special boundaries appeared as Σ3 CSL boundaries, primarily in the form of annealing twins (48%). Some, grain boundary/ boundary segments were also found to be of Σ3 CSL type (as

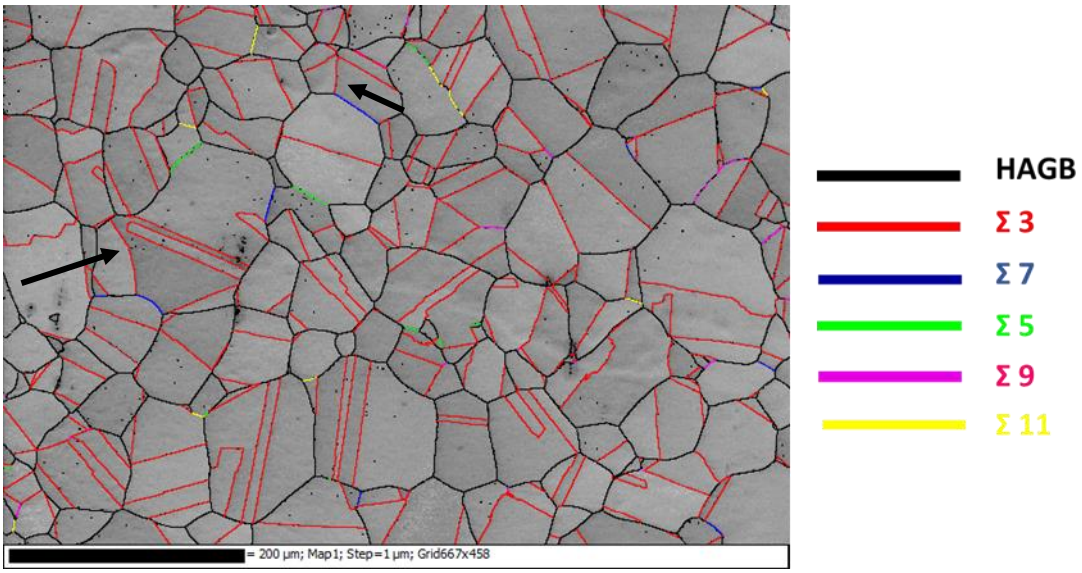

Figure 5.2. Grain boundary character distribution (GBCD) in Fe-30Mn steel after being annealed at1100°C for 10 minutes (CSL boundaries are identified based on Brandon Criterion)

indicated by arrows in Figure 5.2). The remaining special boundaries are mostly variants of Σ3 (Σ9 and Σ27(a, b)) or Σ5,7 and 11. As described in section 2.4.3.3, the special nature of these CSL boundaries are mainly due to highly ordered atomic structure at the boundary plane which results in low energy as well as low mobility. In connection to the slow grain growth process, the presence of special boundaries in the global boundary network could control the migration process. FCC materials with low stacking fault energy (SFE) are prone to annealing twin formation as discussed in section 2.9 and 2.10. In Fe-30Mn microstructure, plenty of annealing twins are present which contribute predominantly to the special boundary fraction.

A study on a low SFE electronic material, Ag-8Au-3Pd, showed that with increasing aging time, the grains grew very fast (Figure 5.3) in a conventional wire (with lower annealing twin density) than in its counterpart which was fabricated in such a way that the microstructure contains a larger amount of annealing twins (T. H. Chuang et al. 2012). In case of Fe-30Mn grain growth, annealing twins are the most pronounced factors to slow down boundary migration. The intercepts created on the HAGBs by parallel sided twins can leave low mobility boundary segments and this might be the reason of slow growth kinetics. This is also supported by Dash and Brown model of twin formation as being shown in Figure 2.53. a (section 2.9.3.3) (Dash, S., Brown 1963). The curvature of the HAGB segments intersected by coherent twin boundaries is smaller than the HAGB segment

associated with no annealing twins. Flatter segments move very slowly as the driving force becomes small according to equation 2.53. Uniform distribution of special boundaries thus changes the crystallography of HAGBs and introduces a significant amount of low mobility

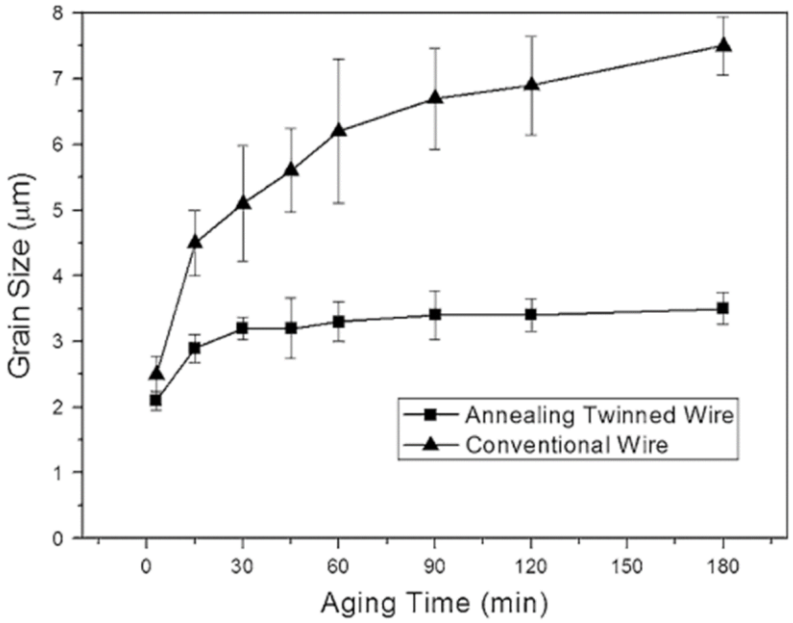

Figure 5.3. Growth Kinetics in Ag-8Au-3Pd bonding wires in presence of high and low (conventional) annealing twin density at 600°C (T. H. Chuang et al. 2012)

segments which result into slow grain growth kinetics.

5.2 Twin Inhibited Grain Growth Model:

Previous section highlights that in Fe-30Mn system, a completely different mechanism controls the grain boundary migration. In normal low Mn (Fe-1Mn) system, grain growth is controlled by all the high mobility random HAGBs. However, in high Mn system, annealing twins control the overall grain growth as the random HAGB migration is dictated by twin-related low mobility segments. Therefore, two different population of boundaries come into the picture. Under this scenario, normal grain growth model is therefore not appropriate to use for predicting the growth kinetics in high Mn system as it considers only one type of mobility similar to that of random HAGBs. One of the ways to model the twin controlled grain growth in high Mn system is through numerical modelling which is, in a way, very difficult to perform and time consuming as multiple variables are involed whose interrelation is not clearly established. Therefore, a very simple approach through physically based modelling is adopted. The approach introduces a simple idea

of the relative contribution of the annealing twin boundaries over random HAGBs to affect its migration. A detailed description of this model will be given next.

It has already been shown that the presence of annealing twins slows down austenite boundary migration at high temperature (T. H. Chuang et al. 2012). Twins considered in this model are in the form of complete parallel sided ones whereas in the current Fe-30Mn microstructure annealing twins of other morphologies are also present. As a very basic attempt to model grain growth in Fe-30Mn system, all the twins are considered to be parallel sided ones. A parallel sided twin of width '*d*' is considered to encircle a spherical austenite

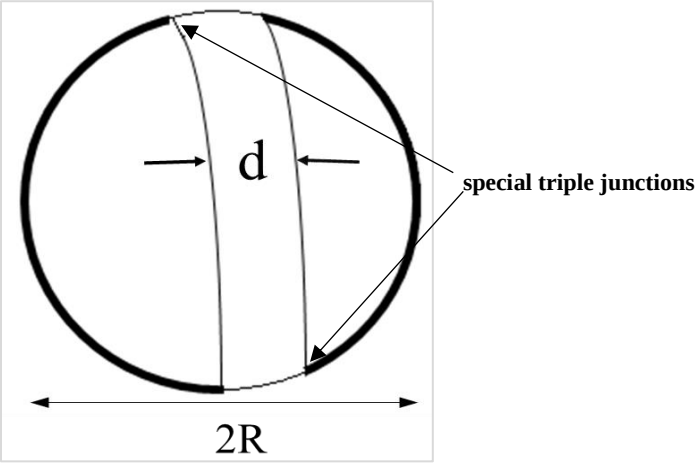

Figure 5.4. Parallel sided annealing twin encircling an austenite grain in the form of a ribbon

grain of diameter 2R in the form of ribbon (Figure 5.4). Under this condition, relative area taken by twin can be written as d/2R. This factor is a measure of the length of HAGB being modified by the annealing twin and possess low mobility pointing towards slowing down effect of the annealing twin on grain growth. Applying this term as a pinning factor to equation 4.1 for grain growth and using equation 4.2, we can write as follows:

$$\frac{d}{dt}\left(\frac{9}{8}\bar{R}\right)^2 = \frac{1}{2}M\gamma\left(1 - \frac{knd}{2\bar{R}}\right) \qquad \text{..... } Eq\ 5.1$$

In above equation, '*k*' is an adjustable parameter that captures the effectiveness of twin pinning, '*n*' represents number of twins per grain and '*d*' is twin width, *M* is the mobility of a random HAGB in Fe-30Mn system at 1100°C.

Rearranging above equation, we can express the final form of the equation that was used for calculating model predicted grain growth as follows:

$$\frac{81}{16}\frac{d\bar{R}}{dt} = M\frac{\gamma}{\bar{R}}\left(1 - \frac{knd}{2\bar{R}}\right) \qquad \ldots\ldots\ldots \text{ Eq 5.2}$$

Equation 5.2 can be integrated to obtain:

$$t = \frac{81}{32}\frac{Rknd}{M\gamma} + \frac{81}{32}\frac{R^2}{M\gamma} + \frac{81}{64}\frac{k^2n^2d^2\,ln(2R-knd)}{M\gamma} - \frac{81}{32}\frac{R_0knd}{M\gamma} + \frac{81}{32}\frac{R_0^2}{M\gamma} - \frac{81}{64}\frac{k^2n^2d^2\,ln(2R_0-knd)}{M\gamma} \qquad \ldots. \text{ Eq 5.3}$$

where, R_0 is the initial average grain size.

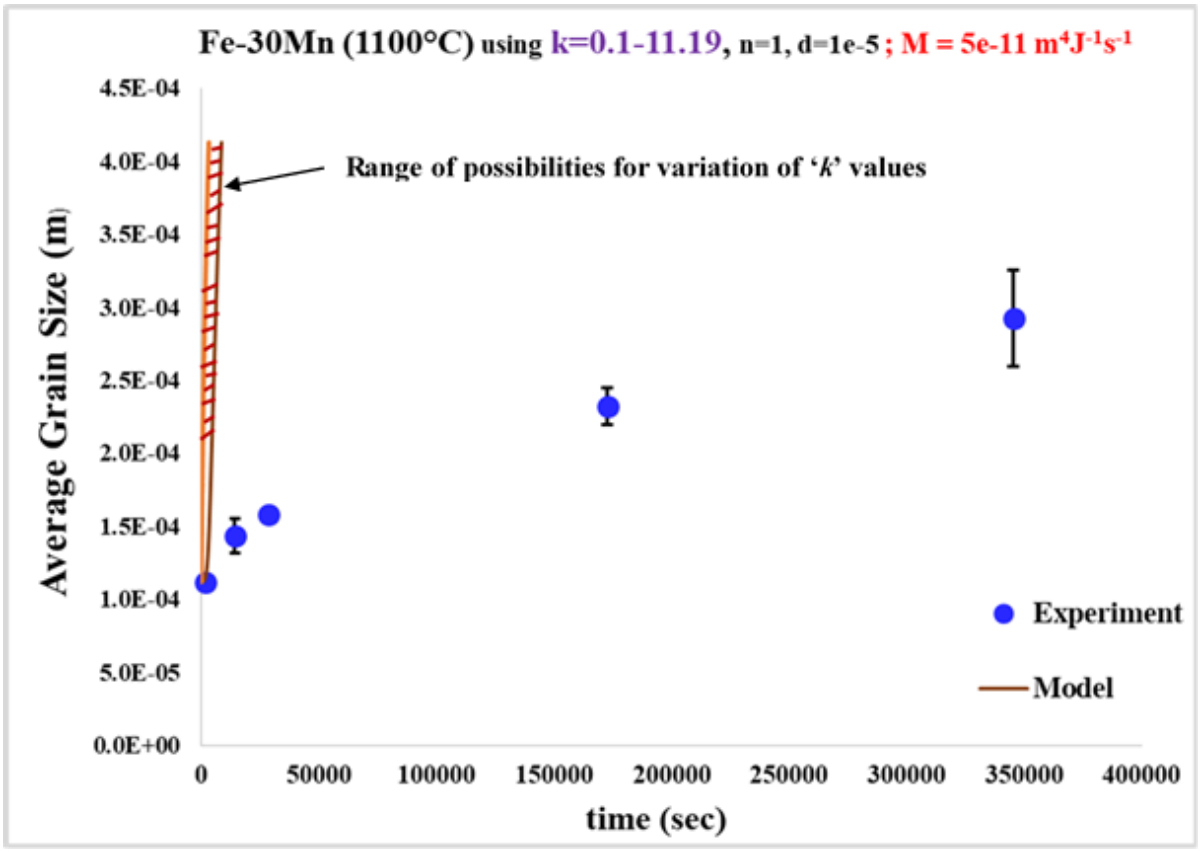

Figure 5.5.Model predicted growth kinetics plots for a range of possible k values with other conditions remaining constant

As was mentioned before, the Fe-30Mn microstructure comprises two different population of grain boundaries in terms of their mobility values. To predict growth kinetics based on above model, a very high mobility value (M =5e-11 $m^4J^{-1}s^{-1}$) was first used to represent HAGB mobilities similar

to that in Fe-1%Mn steel at 1100°C (Table 5.1). The influence of the low mobility boundaries is captured through the pinning term due to twins. In Figure 5.5, the range of possibilities for the variation of '*k*' values from 0.1 to 11.19 to predict growth kinetics is being shown with mobility value of 5e-11 $m^4J^{-1}s^{-1}$. This approach indicates that the use of mobility values similar to that of the HAGBs in Fe-1Mn system predicts a very fast growth kinetics for any *k* value within the range specified by hatched region in Figure 5.5.

Up to now, the twin width is assumed to be constant during grain growth for which the contribution from the pinning term gradually decreases over time. This can be fixed by making the ratio d/2R constant. So, in the next approach, it was considered that as the grains grow, the twin width also increases so that relative area fraction occupied by the twin remains constant over time, i.e., d/2R= 1/10. Using this assumption, equation 5.2 can be simplified as follows:

$$\frac{81}{16}\frac{d\bar{R}}{dt} = M\frac{\gamma}{\bar{R}}(1 - 0.1kn) \qquad \text{..... } Eq\ 5.4$$

Upon integration, another simplified form of equation 5.5 is obtained which will predict the growth kinetics according to new model assumption d/2R=0.1 and can be written as follows:

$$t = \frac{\left(\boldsymbol{D_f^2 - D_0^2}\right)}{\boldsymbol{1.58M\gamma(1 - 0.1kn)}} \qquad \text{..... } Eq\ 5.5$$

This approach captures the twin pinning in an efficient way. As can be seen from Figure 5.6, even though high boundary mobility value (M= 5e-11 $m^4J^{-1}s^{-1}$) is considered, the model shows a good fit with experimental data with k =9.95. Therefore, this approach ensures that the effectiveness of twin pinning is not lost over long time of holding.This approach is a clear indication of the presence of low energy and low mobility boundary segment to be rate controlling factor during grain growth in Fe-30Mn steel. These low mobility segments are generated through the interaction of annealing twins with the HAGBs.

There is a considerable amount of research work that highlights the fact that twinning is the primary process which is followed by twin interaction with HAGBs to generate other variants of

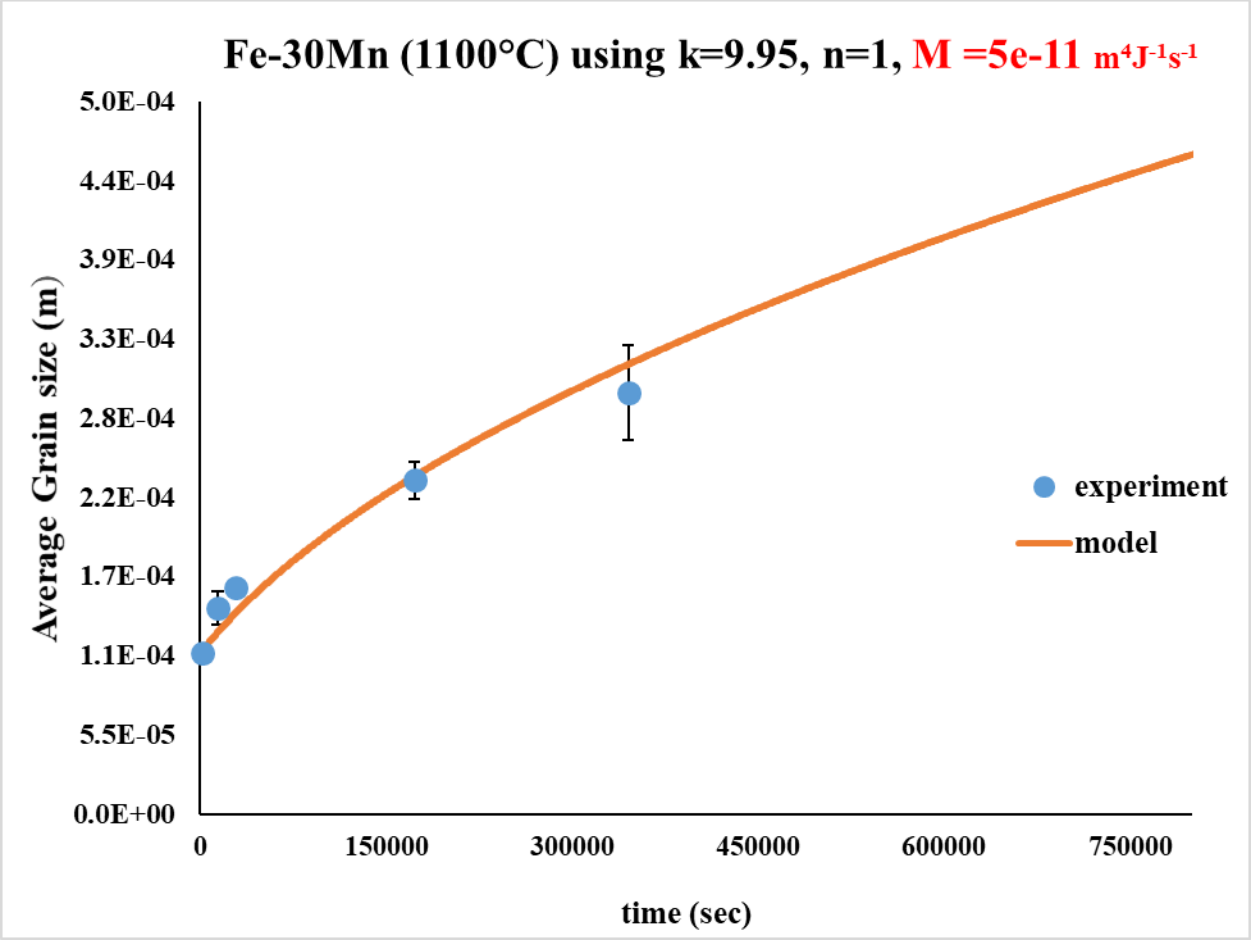

Figure 5.6. Comparison of model predicted and experimentally obtained grain growth kinetics in Fe-30Mn steel at 1100°C for d/2R=0.1, k=9.95, n=1 and M = 5e-11 $m^4J^{-1}s^{-1}$

Σ3 boundary according to Σ3 regeneration model (V. Randle 1999). All these $\Sigma 3^n$ (n=1, 2, 3) related boundaries introduce low mobility boundary segments in the global boundary network. Another study shows that, in pure copper foils, after introducing high density of nanotwins by pulsed electrodeposition, the annealing twins change the HAGB structure. An in-situ TEM study revealed that it is the triple junction created by the coherent twin boundary and the grain boundary intersection (as shown in Figure 5.4) that slows atom movement on the HAGB plane. The explanation given was in the light of highly ordered atomic structure at those triple junctions (TJ) which do not prefer any kind of structural changes required for atom migration to happen across the junction.

The atom migration mechanism was by the formation of a kink or step which is less likely to occur at the triple junctions (Chen et al. 2008). Similar to this concept, during grain growth, HAGB migration also takes place by the formation of steps or ledges. Due to the presence of special boundary segments, these structural changes are not favored because of highly ordered structure of the annealing twins, twin modified Σ3 and other low-CSL boundaries. So, there originates a structure-specific mobility difference on the twin intercepted HAGB segments which move slower than the free part (dark solid line in Figure 5.7) resulting into sluggish grain growth.

The constraint imposed on HAGBs by the intersecting twin boundaries was also explained in light of the degrees of freedom (Figure 5.7). Before the twin intersects the HAGB, the whole length

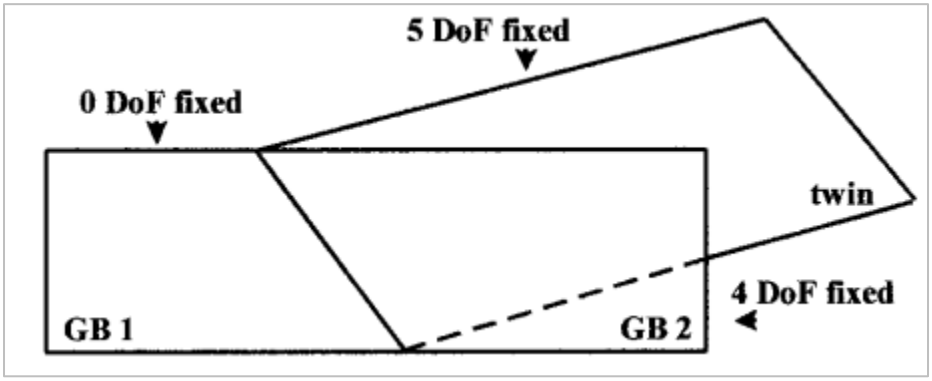

Figure 5.7. Constraint imposition on HAGBs due to intersection of annealing twins (V. Randle 1999)

of the HAGB was GB1, for which none of the 5 degrees of freedom (DOF) were fixed. The annealing twin shown on the other hand has fixed orientation and boundary plane resulting in all its DOF being fixed. Upon intersecting the HAGB, the twin creates a new boundary segment, GB2, which has 4 of its DOF fixed. Also, interaction of special boundaries with each other, results in other Σ boundaries of low mobility according to equations 2.137, 2.138. This justifies, how the annealing twins, introduce special low energy and low mobility boundary segments which ultimately slow down the grain growth kinetics in Fe-30Mn system. A similar idea was also reported by Thomas et al. where they performed large scale Molecular-Dynamics (MD) simulations to show boundary migration during grain growth of nano-scale grains in polycrystalline nickel gets significantly retarded because of different forms of twin-HAGB triple junctions in the microstructure (Thomas, King, and Srolovitz 2016).

5.3 Triple junction approach of justifying Fe-30Mn grain growth:

Based on discussion from previous section, it is clear that the low mobility boundary segments or the triple junctions (TJ) generated in the microstructure (because of intersection of annealing twins with HAGBs) are the key features responsible for the slow grain growth in Fe-30Mn steels. In this section, an attempt to justify the slow growth kinetics will be presented in the light of percolation theory.

As described in section 2.10.2.3c, percolation theory is mostly used to estimate continuous path length available in a microstructure for propagation of any intergranular phenomenon, e.g., corrosion cracks, fatigue cracks etc. Although, grain growth is not a percolative phenomenon, it advances through the migration of well-coordinated HAGBs. Using the different types of triple junction frequency into percolation theory, several researchers have estimated the threshold at which interfacial degradation starts diminishing because of discontinuity in their pathway (Mukul Kumar, King, and Schwartz 2000; Tsurekawa, Nakamichi, and Watanabe 2006). Following their approach, four different types of special triple junctions are found in the EBSD OIM maps on Fe-30Mn steels annealed at 1100°C for 10 minutes. They are 0-CSL (all three boundaries are HAGBs), 1-CSL (1 is a CSL and other 2 are HAGBs), 2-CSL (2 CSL and 1 HAGB) and 3-CSL (all three are CSL) triple junctions. Of them, 3-CSL TJ's are the inactive ones for propagation of any kind of degradation phenomenon. A parameter, $f_{2CSL}/f_{(1\text{-}3CSL)}$, is used to estimate the amount of continuous path available in a microstructure along the HAGBs. $f_{(1\text{-}3CSL)}$ indicates the frequency of active TJs that allow propagation and f_{2CSL} is the frequency of 2-CSL TJs. The term $f_{2CSL}/f_{(1\text{-}3CSL)}$ when reaches 0.35 is indicative of the percolation threshold for crack propagation. This also indicate that if more than 35% of TJs in the global boundary network are special in nature, percolative path along HAGBs starts getting disconnected making crack propagation gradually difficult. Using the above percolation term, $f_{2CSL}/f_{(1\text{-}3CSL)}$, the amount of continuous well connected HAGB path available in the microstructure can also be evaluated.

Using the MTex toolbox codes for triple junction calculation on EBSD orientation data file, a total of 584 triple junctions were found in the microstructure. Of them, f_{2CSL} was found to be 0.1095 and f_{3CSL} was calculated to be 0.0205. For, Fe-30Mn system, the value of $f_{2CSL}/f_{(1\text{-}3CSL)}$ came to be 0.111. This is very small compared to the threshold value of 0.35 mentioned above. With $f_{2CSL}/f_{(1\text{-}3CSL)}$ =0.111, it can be assumed that the HAGBs are still well connected as compared to the

threshold case. However, as grain growth is not a percolative phenomenon, this threshold value might not be an ideal parameter to quantify the extent of slow growth kinetics in Fe-30Mn steel. The term $f_{2CSL}/f_{(1\text{-}3CSL)}$ has been used with the sole intent to quantify the extent of unbroken, continuous HAGB length. Compared to Fe-30Mn system, because of scarcely present annealing twins and related resistant triple junctions, the HAGBs are better connected in Fe-1Mn microstructure resulting in $f_{2CSL}/f_{(1\text{-}3CSL)}$ to be very small. Therefore, the grains grow faster in Fe-1Mn steel as almost negligible frequency of resistant triple junctions makes the HAGBs less broken. This would probably lead to very well connected, mobile HAGBs with 1-2 orders higher mobility than that of Fe-30Mn. But, because of profuse twinning and its interaction with HAGBs in Fe-30Mn system during grain growth, the HAGBs get disconnected in good extent that makes the grain growth sluggish. The purpose of doing grain boundary engineering is to make the value of $f_{2CSL}/f_{(1\text{-}3CSL)}$ reach a very high value past the threshold. In the next section, discussion on this will be provided.

5.4 Effect of Mn on grain growth:

As reported in section 4.6, addition of various amounts of Mn was found to have an interesting impact on the grain growth kinetics. The reported mobility values are plotted with respect to Mn concentration in Figure 5.8. For 1%Mn, the mobility was calculated from the equation which gave the best fit of the grain growth kinetics data from Fe-1Mn as reported by Furumai et al., 2017 and as follows:

$$M = \frac{0.26}{T} exp\left(-\frac{20837}{T}\right) \qquad \ldots\ldots\ldots \text{Eq 5.6}$$

For Fe-6Mn steel, an upper and lower bounds of mobility value are reported. The upper bound was

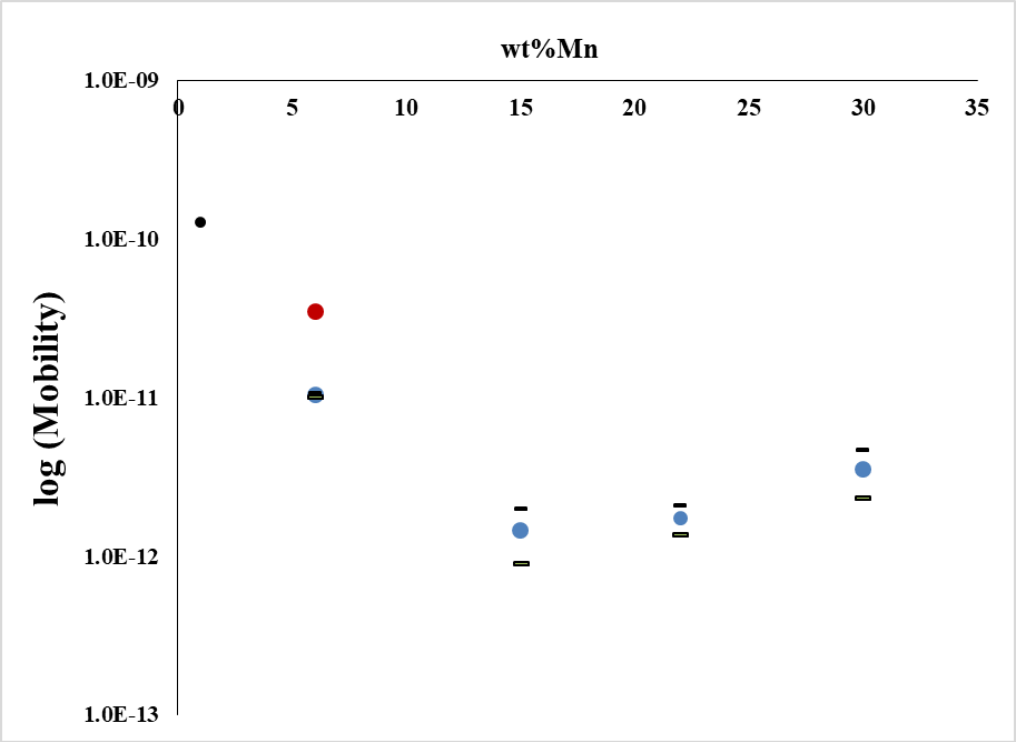

Figure 5.8. Dependence of austenite grain boundary mobility on concentration of Mn (Blue dots represent mobility obtained from isothermal grain growth data in the current work, maroon dot indicates mobility data obtained from LUMet method, black dot indicates mobility data from (Furumai, Zurob, and Phillion 2018))

calculated from the LUMet measurement and shown as maroon dot. Thermal etching method for revealing austenite grain boundaries offered the lower bound of the mobility and the data point is being shown in blue. When Mn content reaches 15%, minimum value of mobility is achieved.

Increasing Mn beyond 15% leads to slight increase in boundary mobility. The trend is quite similar to what is obtained for stacking fault energy (SFE) variation with respect to Mn concentration (Nakano and Jacques 2010). Figure 5.9 shows SFE variation with respect to Mn concentration as reported from different sources. Experimentally determined minima were reported to be 15 mJ/m^2 at 22wt% Mn by Volosovich et al. (open square symbols),15-20 mJ/m^2 at 13wt%Mn by Schumann et al. (given by ✶), 3 mJ/m^2 at 13 wt% Mn by Kim et al. (ref 26) and 13 mJ/m^2 at 12wt% Mn by Saeed-Akbari *et.al* (ref 28) (Ghasri Khouzani 2015; Nakano and Jacques 2010). The trend indicated by Nakano's model and the reference 26 and 28 of the same paper is closely similar to that of the mobility variation shown in Figure 5.8.

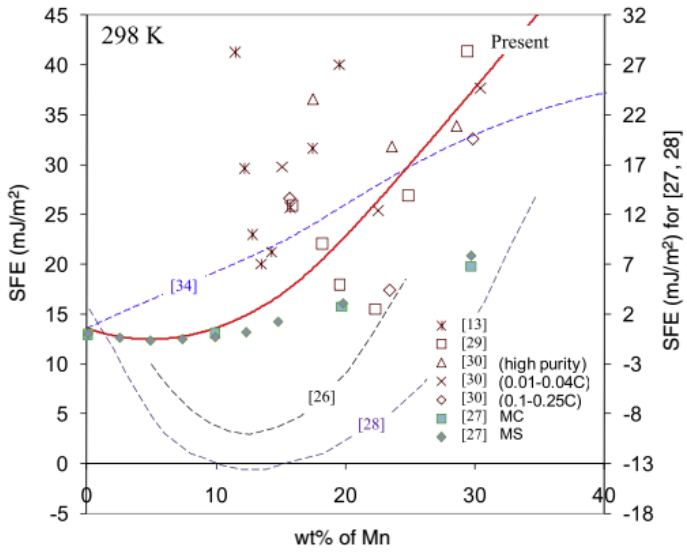

Figure 5.9. Variation in stacking fault energy (SFE) with respect to Mn concentration as indicated by the maroon line (Nakano and Jacques 2010) (Redline indicates the model output proposed by Nakano et al., all the other lines correspond to the references listed in the bottom-right of the picture and can be found in (Nakano and Jacques 2010))

This can be explained in terms of the effect of Mn on annealing twin frequency through changing the stacking fault energy (SFE).

Variation of annealing twin frequency with the change in Stacking Fault Energy (SFE) was studied

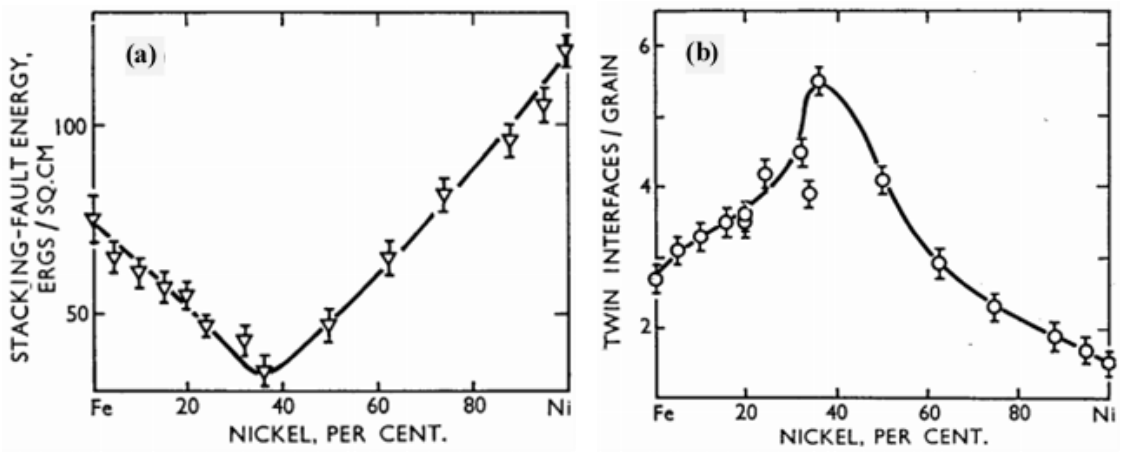

Figure 5.10. a) Concentration dependence of SFE, b) corresponding variation of twin frequency for a range of Nickel concentrations in a series of Fe-Ni alloys after annealing at 1100°C for 3 hours (Charnock and Nutting 1967)

in Fe-Ni system by Charnock and Nutting. It was found that as the nickel content increases, it changes the SFE (Figure.5.10.a) of the system as well as the twin frequency as shown in Figure.5.10.b for a broad range of concentration. Initially, the SFE decreases with the increase in annealing twin frequency. The trends then get reversed with further increase in nickel concentration leaving a minimum around 36% Ni. They assumed that the grain boundary energy increases linearly with the nickel content (Charnock and Nutting 1967).

In Figure 5.11, microstructures of alloys with varying Mn levels are being shown. A close inspection reveals the following facts:

- Fe-1Mn- As Stacking fault energy is highest because of small Mn concentration, twinning frequency is very small (Furumai, Zurob, and Phillion 2018). Qualitatively, it can be said that a very few grains in 1Mn steel, contain twin lamellae (Figure 5.11. a). As Mn concentration reaches 6wt%, the occurrence of annealing twins increases a little bit as indicated by Figure 5.11.b. This results in almost an order of magnitude drop in mobility. Compared to the 1% Mn microstructures shown in Figure 5.11. a, addition of 15 wt% Mn results in high density of annealing twins in the microstructure (Figure 5.11.c). A GBCD

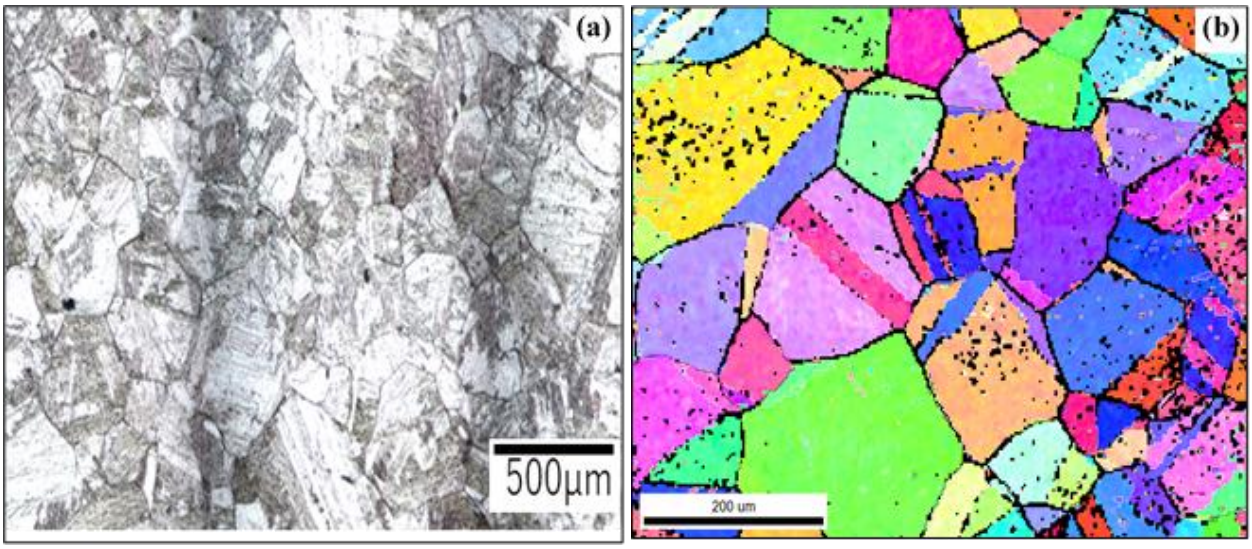

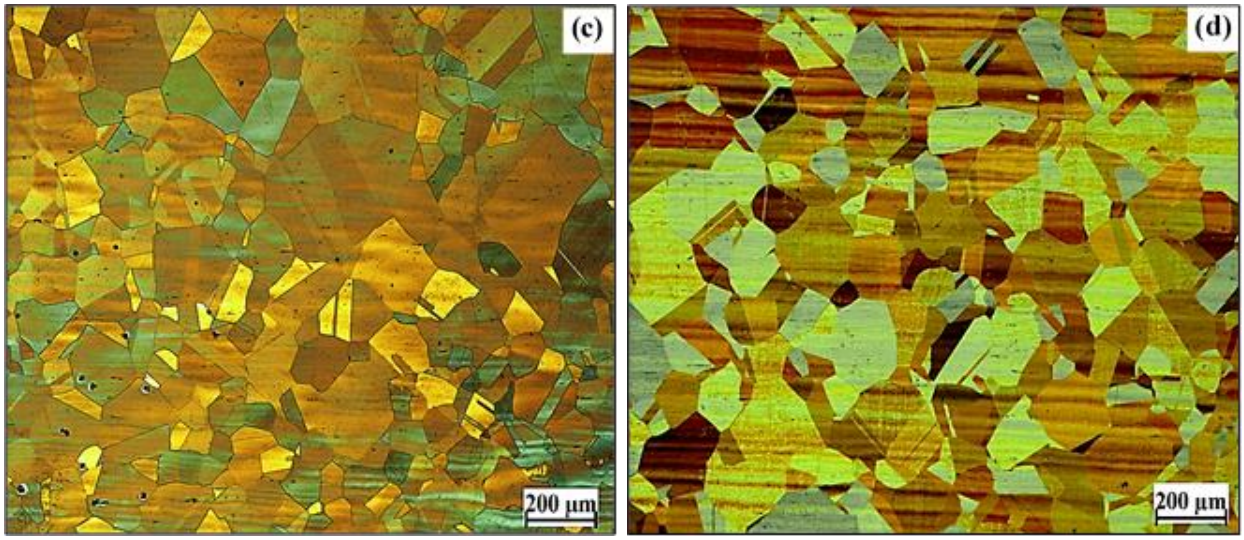

Figure 5.11. Microstructure with varying annealing twin density in a) Fe-1Mn, b)Fe-6Mn, c)Fe-15Mn and Fe-30Mn after being soaked at 1200C for 5 minutes

analysis of a Fe-15Mn-0.5C sample soaked at 1200°C for 1 hour shows that 30% of the grain boundaries are in the form of Σ3 CSL boundaries, with the majority of these in the form of annealing twins. It can be said that once the Mn concentration reaches 15%, the number of grains containing at least one annealing twin per grain increases significantly and that leads to very high frequency (30%) of Σ3 CSL boundary dominantly in the form of annealing twin boundaries. This significant increase in twin frequency due to 15 wt% Mn addition is indicative of the 2 orders of magnitude decrease in mobility and slow grain growth kinetics.

- In Fe-30Mn-0.5C system (Figure 5.11. d), although the frequency of Σ3 boundaries was found to reach 45%, not a significant drop in mobility was observed. This might be an indication of the fact that the twin frequency probably does not influence mobility variation through a simple, linear relation. Once again, twin morphology and detwinning kinetics might play some important role in controlling the overall mobility during grain growth in high Mn steels.
- Based on the observations shown in Figure 5.10, a correlation between SFE and twin frequency can be established which indicates that twinning frequency is inversely proportional to the SFE. So, as the SFE is decreased because of Mn addtion, formation of more annealing twin related Σ3 boundaries takes place in the microstructure which control

the HAGB migration. Therefore, the variation of boundary mobility during grain growth in a series of Fe-Mn steels is expected to be dictated by low mobility special boundaries generated by annealing twins in the microstructure.

- Atom probe results on Fe-15Mn-0.5C and Fe-30Mn-0.5C, indicate that there is a small enrichment of Mn at HAGBs. But, in Fe-30Mn-0.5C, 4 times higher mobility is reported (in next section) as compared to that in Fe-30Mn system at 1200°C. This indicates that although Mn segregates to austenite HAGBs, its solute drag effect seems to be weak. Herbig et al., performed atom probe tomography on fully recrystallized Fe-28Mn-0.3C samples and observed no Mn segregation at HAGBs (Herbig et al. 2015). An atom probe study on a fully recrystallized sample from Fe-9Mn steel revealed no Mn segregation took place at high angle prior austenite grain boundaries in as-quenched condition (Kuzmina, Ponge, and Raabe 2015). Another 3D-APT study on Fe-8Mn steel, revealed no appreciable Mn segregation to HAGBs (Kwon et al. 2013). An Auger Electron Spectroscopy (AES) study on Fe-8Mn steels, also did not reveal any HAGB enhancement of Mn (Nikbakht et al. 2010) in as-quenched condition. AES study also revealed no significant Mn segregation to HAGBs in Fe-12Mn system (Heo et al. 2013). All these strongly point toward the fact that with the increase in Mn content, its solute drag does not become significant as segregation of Mn to γ-HAGBs does not occur. This finally highlights that the effect of Mn on variation of boundary mobility during grain growth is not because of its solute drag, rather it is attributed to the presence of annealing twins generating low energy-low mobility boundary/ boundary segments in the microstructure during the course of grain growth.
- Effect of Mn as a solute on the grain boundary migration in steels containing varying level of Mn was also calculated. The steps followed to capture the effect of Mn in slowing down growth kinetics as a solute are as follows:
    - **Step I**- The driving force (P_d) for grain growth in Fe-1%Mn steel at 1200°C was calculated using equation 2.52 for a grain size of, $\bar{R} = 50\mu m$, grain boundary energy of 0.625 J/m^2. With these assumptions, the driving force was calculated as 25000 J/m^4.
    - Now, we calculate the velocity of boundary migration corresponding to above calculated driving force using the relation, V = M_i *P_d. M_i is the intrinsic mobility

which was considered to be 1.27e-10 $m^4J^{-1}s^{-1}$, similar to that of Fe-1%Mn system. This velocity is termed as V_{cal}.

- **Step-II** -The measurement of effect of Mn as a solute on boundary velocity was attempted to measure. For a constant grain size of 50 μm, the grain boundary velocity will be estimated in 6%Mn system using the following relation:

$$P_d = \frac{V_{guess}}{M_i} + P_{SD} \qquad \ldots\ldots\ldots\ldots \text{Eq 5.7}$$

In above equation, the left hand side is the measure of driving force for grain growth in Fe-6Mn steel for 50 μm average initial grain size which is a constant and similar to that used in calculating P_d in Step-I for Fe-1%Mn steel, M_i is the intrinsic mobility, P_{SD} is the Mn solute drag which will be calculated from the dissipation of free energy approach using Hillert's model (Mats Hillert and Sundman 1976). To calculate, P_{SD}, first the concentration profiles are calculated for three different zones of the grain boundary using equation 28 of the original paper. In this calculation, the cross boundary diffusion coefficient (D_x) was considered to be three times of that for bulk diffusion (D_{bulk}). A constant boundary width of 1nm, binding energy of 4000 J/mol for Mn and a square well grain boundary energy profile was chosen. Once the concentration profiles are calculated for the three distinct zones, dissipation values corresponding to the three zones were calculated using equation 2.125 from section 2.8.2. The calculated dissipation value is a measure of the Mn solute drag (P_{SD}) on moving boundaries. The same calculation was performed for 15% and 30% Mn steel considering similar average initial grain size of 50 μm to calculate corresponding P_{SD} values.

- **Step III**- A grain boundary velocity (V_{guess}) was then assumed to make the right hand side of the equation 5.7 match with the left hand side.i.e. P_d. The estimation of V_{guess} was done in iteration. So, for a constant driving force, Fe-6Mn system was found to have a lower V_{guess} because of the effect of solute Mn on boundary migration in Fe-6Mn steel. Similar calculation was performed for 15% and 30% Mn steels.
- **Step IV**- For estimating the effect of solute Mn on boundary migration, boundary velocity for any Mn concentration was assumed to be in the form of $V = k\sqrt{t}$

indicating parabolic growth, where k is a constant that takes into account the mobility of HAGBs. Under this condition, the change in velocity due to solute Mn can be estimated for time, '*t*', using the ratio of the V_{guess} for any Mn content to that in 1%Mn. Effect of solute Mn in slowing down the velocity of the boundary migration, as well as growth kinetics, can be assessed from the ratio between the *k* values as,

$$\frac{V_{guess}^{6Mn}}{V_{guess}^{1Mn}} = \frac{\bar{R}_{6Mn}}{\bar{R}_{1Mn}} = \frac{k_{6Mn}}{k_{1Mn}} \qquad \text{…….. } Eq\ 5.8$$

So, relative growth kinetics was used to estimate the effect of Mn solute drag on grain growth as shown in Figure 5.12. The trend shows that the effect of solute Mn

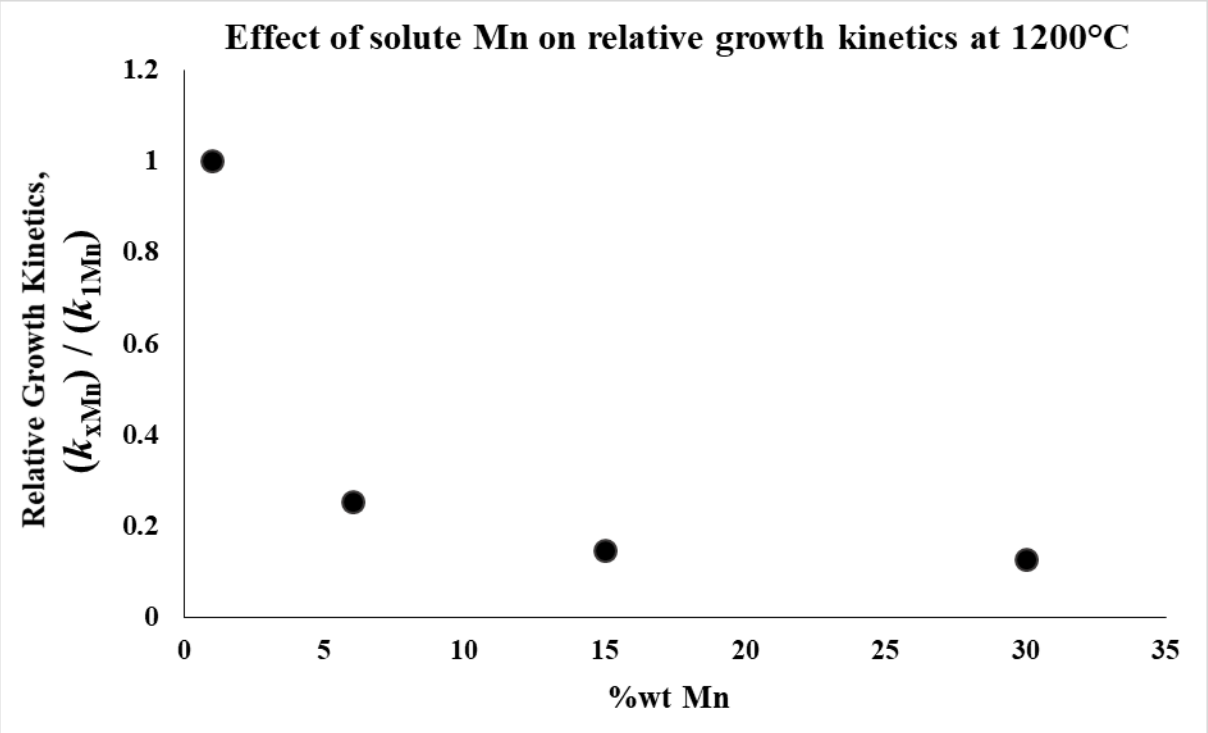

Figure 5.12. Estimation of solute Mn effect in slowing down the growth kinetics at 1200°C

in slowing down the growth kinetics decreases as the Mn concentration is increased beyond 6%. The important thing to note from the above figure is that, although the Mn solute drag can reduce '*k*' in Fe-30Mn by a factor of 8 compared to Fe-1Mn steel, it is still incompatible with the minimum mobility reported at 15% Mn as shown in Figure 5.8. It can be said that as the Mn concentration increases beyond 6%, the effect of Mn in slowing down grain

growth kinetics is primarily governed by the formation of annealing twins as its solute drag effect seems to be weak which can be seen from Figure 5.12.

5.5 Effect of carbon on grain growth:

Presence of carbon was found to have some effect on grain growth kinetics of Fe-30Mn system at both 1100°C and 1200°C. The mobility values extracted from the grain growth data in presence and absence of carbon are given in Table 5.3. The presence of carbon makes the growth kinetics faster by 6 times at 1100°C. However, this effect is less pronounce at 1200°C as only 4 times faster kinetics is obtained. Although, there is not a huge difference (in terms of orders of magnitude) in the mobility values obtained, the presence of carbon possibly interacts with grain growth process

Table 5.3. Comparison of grain boundary mobility of 30Mn system in presence and absence of carbon

Temperature (°C)	**M (Fe-30Mn) ($m^4 J^{-1}s^{-1}$)**	**M (Fe-30Mn-0.5C) ($m^4 J^{-1}s^{-1}$)**	$\frac{\mathbf{M\ (Fe-30Mn-0.5C)}}{\mathbf{M\ (Fe-30Mn)}}$
1200	9.54e-13	3.5e-12	4
1100	2e-13	1.17e-12	6

in two different ways. EBSD study reveals the grain boundary character distribution (GBCD) in both the alloys. The Fe-30Mn system has a little higher frequency of Σ3 boundaries (Figure 4.15) compared to Fe-30Mn-0.5C (Figure 4.16). At any time, Σ3 frequency is 2-3% less than that in Fe-30Mn. This is in agreement with the fact that carbon increases stacking fault energy (SFE). As an example, the addition of 0.5 wt% carbon was found to increase SFE by 8 mJ/m^2 (Nakano and Jacques 2010). The increase in stacking fault energy results in lower frequency of annealing twins in the microstrucutre. Also, the morphology of the annealing twins in presence of carbon varies from that in absence of carbon (Figure 5.13). In presence of carbon, not only the twinning frequency decreases, but also the presence of parallel sided twins (expected to be most effective HAGB pinning entity) decreases as can be seen from Figure 5.13.b. Also, the frequency of multiple twins in one grain decreases in presence of carbon. Atom Probe Tomography (APT) results also indicate that with the presence of 0.5 wt% carbon, some segregation of Mn to γ-HAGBs takes

place in Fe-15Mn and Fe-30Mn (Figure 4.25 and Figure 4.26) alloys. But, in presence of very low carbon, Mn does not segregate to γ-HAGBs (Figures 4.21.b, 4.22. b and4.23). It is worth mentioning that although in presence of carbon, Mn segregates to γ-HAGBs in Fe-30Mn-0.5C and its faster growth kinetics (Table 5.3) is indicative of grain growth being dictated by contribution of Mn through annealing twin formation, not Mn solute drag. There has always been a decraese in Σ3 boundary frequency (Figure 4.15 and Figure 4.16) by 3% in Fe-30Mn-0.5C compared to its counter part without any carbon. Addition of carbon increases Stacking Fault Energy (SFE) which lowers annealing twin frequency.

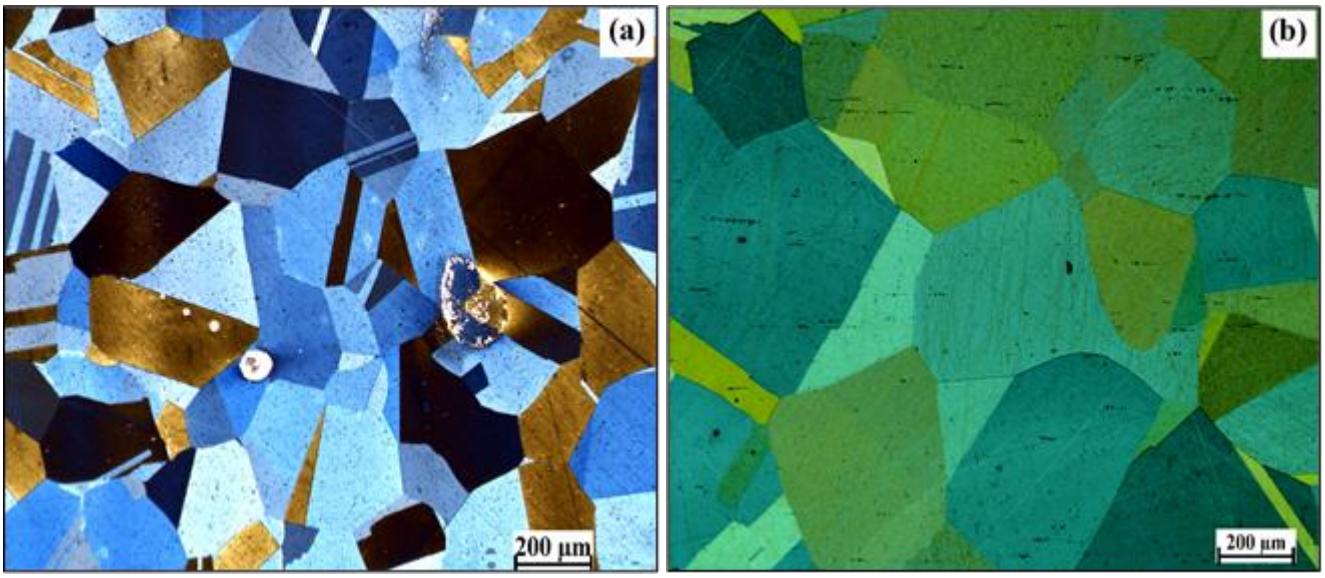

Figure 5.13. Difference in twin morphology after annealing at 1200°C for 24 hours a) Fe-30Mn, b)Fe-30Mn-0.5C

This might be one of the factors behind fast growth kinetics in Fe-30Mn system in presence of carbon. Also, the morphology of annealing twins and the detwinning frequency during grain growth in presence of carbon might play some role towards the faster growth kinetics in Fe-30Mn-0.5C.

5.6 Grain Boundary Engineering (GBE) and Grain Growth:

Grain boundary engineering of Fe-30Mn system was performed in two different ways, strain recrystallization (iterative) and strain annealing (both one step and iterative strain annealing). As

can be seen from the results obtained, iterative strain recrystallization treatment did not seem to have any effect on grain growth of Fe-30Mn-0.03Nb steel at 1100°C up to 4 hours. There may be two reasons behind GBE not working on Fe-30Mn-0.03Nb alloy during grain growth. The annealing performed during each cycle was at 1000°C for 10mins which seemed to very high for the nucleation of low-Σ CSL boundaries. To invoke complete recrystallization overcoming Nb solute drag after each 20% cold rolling in every cycle, annealing temperature of 1000°C was opted for. The faster grain boundary migration during high temperature recrystallization actually increased the random boundary fraction reducing the probability of nucleation of Σ3 and other variants (Shimada et al. 2002; T. Liu et al. 2013; Owen and Randle 2006). Another reason for GBE not having worked to control grain growth might be due to the presence of solute Nb. Because of solute Nb as substitutional alloying element with a strong tendency to segregate to grain boundaries, the chance of nucleation of low-Σ boundaries gets reduced. Because of Nb, ordered structure at boundary plane is disturbed resulting into almost no improvement in the special boundary fraction. These are possibly the reasons behind GBE having no benefit on grain growth of Fe-30Mn-0.03Nb. This requires further research to confirm the effect of annealing temperature, time and effect of solute Nb on it.

Single step strain annealing treatment performed on Fe-30Mn-0.5C was found to control grain size during growth experiment at 1100°C for 30 minutes. The cold rolling followed by an annealing before the final grain growth experiment was found to be more effective (Figure 4.27. a) to bring the grain size down during the growth experiment than the samples that were cold rolled and directly taken for growth experiment as shown in Figure 4.27. b. The second case rather showed an irregular drop in grain size with increased cold work. But, the grain size is still smaller (75-85 μm) than the no-GBE sample (110 μm) after grain growth at 1100°C for 30 minutes. A prior annealing before growth experiment rather showed a regular trend of bringing grain size down. As the amount of cold work is increased from 0 to 3%, the amount of Σ3 boundary is increased which probably brings the grain size down as shown in Figure 4.27 a. Further, increasing cold work to 5-18% although reduced Σ3, Σ9 and Σ27 frequencies (Fig 4.29. a, b, c), grain size after growth experiment was found be smaller. This is probably because of higher deformation resulting into smaller initial grain size which lead to smaller final grain size compared to the no-GBE case.

To explain the effect of amount of cold work on Σ3, Σ9 and Σ27 evolution, it can be said that with more deformation, higher driving force is available for boundary migration during recrystallization resulting in formation of more random HAGBs than low- Σ CSL boundaries. Similar trend of special boundary evolution was found during GBE of 304 stainless steel where maximum CSL frequency was obtained by 5% cold work. Increasing cold work actually resulted in lower frequency of CSL boundaries (Shimada et al. 2002).

With application of iterative strain annealing, the frequency of Σ3, 9 and 27 was increased during the second iteration and then it drops during third and fourth iteration as shown in Figure 4.31. a, b and c respectively. The initial increase of Σ fraction is because of the fact that after the first iteration 40% Σ3 frequency was obtained compared to very low frequency in the 0-GBE sample. From 0-GBE case, the first iteration introduced strain which on annealing gave 40% Σ3 boundary. During the deformation of second iteration, some strain gets retained in the form of dislocation pile-ups at twin boundaries. However, as twin (Σ3) fraction is not too high, still smaller driving force of grain boundary migration is available which results into boundary moving with an optimal velocity triggering more Σ3 generation. This corresponds to the jump in Σ3 frequency from 40 to 65%. With the increase in Σ3, according to regeneration model, frequency of Σ9 and Σ27 also peaks from 2% to 7% and 0.7% to 3% respectively. As more Σ3 is present, probability of occurrence of CSL joining or dissociation reaction (Equations 2.137 and 2.138) also increases which ultimately causes maximum Σ9 and Σ27 frequencies as can be seen from Figure 4.31. b and c respectively. After the second iteration, the cold work during third iteration results more retained strain at higher frequency of annealing twin boundaries. Thus introduces higher driving force for boundary migration

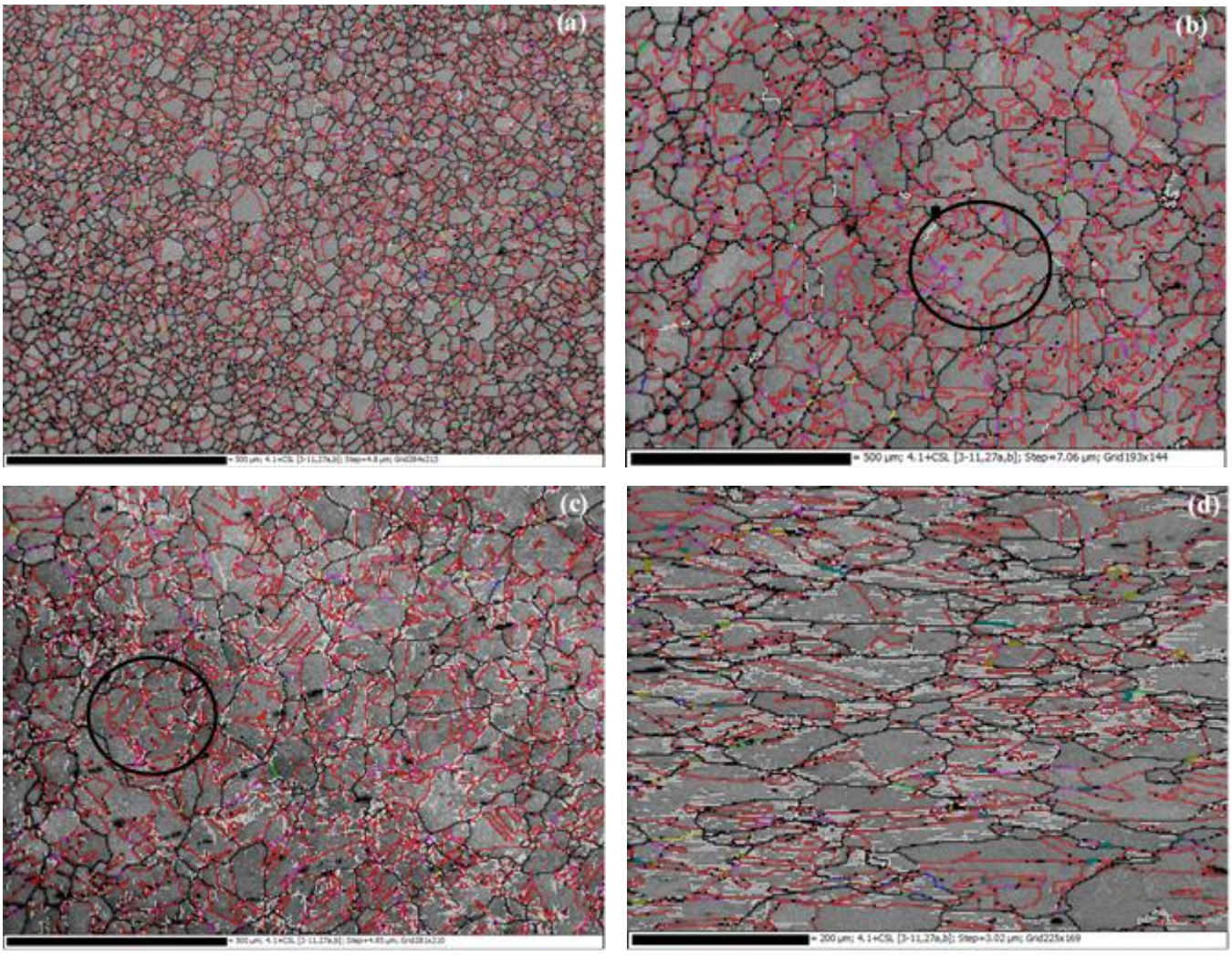

Figure 5.14. Grain boundary character distribution in Fe-30Mn-0.5C steel during iterative strain annealing after a) first, b) second (circle shows big grain cluster), c)third and d) fourth iteration of 5% deformation followedby annealing at 900°C for 30 minutes each.(Σ3-red, Σ5-green, Σ7-blue, Σ9-pink, Σ11-yellow, Σ27a &b-dark green and light red respectively, bold black boundaries are random HAGBs, white are LAGBs)

and recrystallization occurs with HAGBs sweeping through the microstructure destroying ordered Σ3 boundaries. This is the reason behind the drop in Σ3 frequency after third iteration. Also, third iteration onwards, formation of low angle subgrains were also detected as white boundaries in the EBSD images (Figure 5.14. c and d) which also causes the Σ3, 9 and 27 fractions to drop. So, after the second iteration, cumulative strain retention causes lowering in special boundary frequency. During the first iteration step, this retained strain is almost negligible as Σ3 boundaries just begin

Figure 5.15. Microstructure of no-GBE sample of Fe-30Mn-0.5C

to form from a no-GBE microstructure (Figure.5.15). Amount of retained strain only becomes significant once the Σ frequency becomes maximum after second iteration step and gradually reduces the Σ frequency.

The effect of iterative grain boundary engineering on grain growth at 1100°C after 30 minutes did

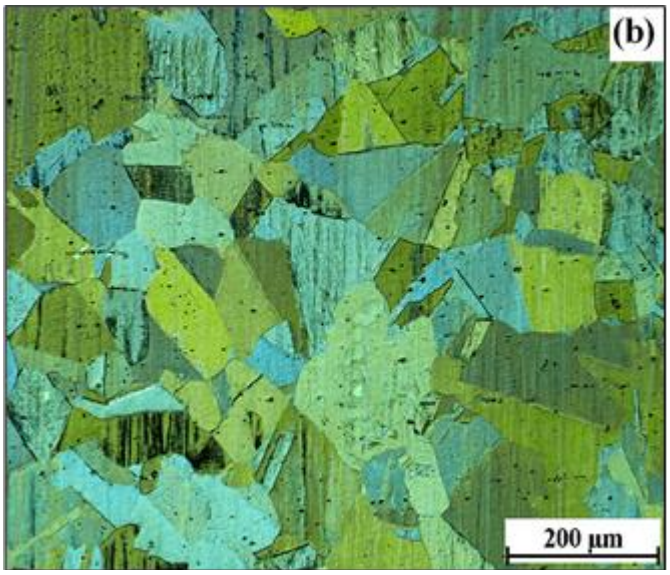

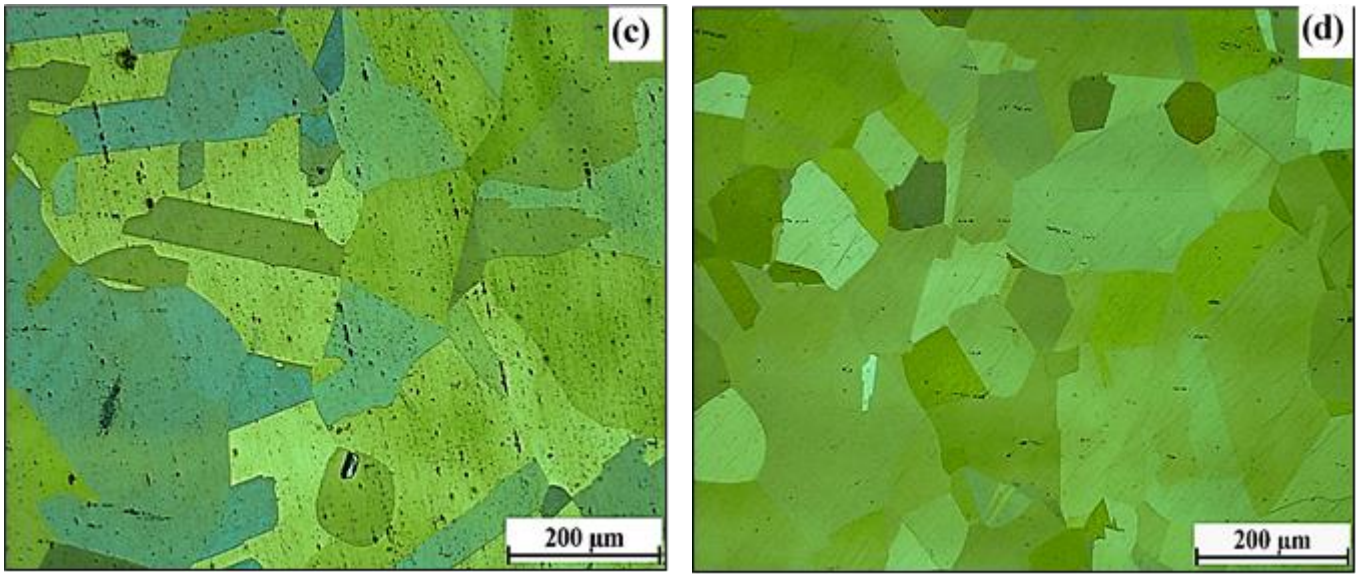

Figure 5.16. Microstructure of Fe-30Mn-0.5C samples after grain growth at 1100°C for 30 minutes after, a) one, b) two, c) three and d) four iterations followed by annealing at 900°C for 30 mins prior to growth experiment

not occur as expected. After the second iteration, although Σ3 frequency peaked around 64%, after grain growth experiment, the grains grew to more than 100 µm with a non-equiaxed shape (Figure 5.16.b). No further grain size control after 30 minutes of growth at 1100°C was observed in case of the samples that underwent third and fourth iteration of GBE (Figure.5.16. c, d). Compared to the three and four iteration samples, the one step sample after the growth experiment (Figure.5.16.a), showed a considerable extent of grain size control through GBE as can also be seen from Figure 4.27. a. Although the frequency of special boundaries increased with more iterations, the formation of big grain clusters (shown by circles in Figure 5.14. b, c) increased the average grain size after the final grain growth experiment. Further research work is needed to understand the origin and suppression of the cluster grains.

5.7 Binding Energy of Niobium:

Under this section segregation of Nb to HAGBs will be quantified by calculating its binding energy. The atom probe results given in Figures 4.21.b, 4.22.b and 4.23 shows 1-D concentration

Table 5.4. Binding energy comparison in Fe-30Mn system in presence different levels of Nb

parameters	Fe-30Mn-0.07Nb (Figure 4.21.b)	Fe-30Mn-0.07Nb (Figure 4.22. b)	Fe-30Mn-0.054Nb (Figure 4.23)
Boundary concentration, C (atom%)	0.26	0.1	1.7
Equilibrium Concentration, C_0 (atom%)	0.03	0.03	0.03
Enrichment factor, C/C_0	10	3.4	56.5
Binding energy, E_b, kJ/mol	-25	-13	-43

profiles of the segregants. Using equation 2.106, binding energy, E_b, can be calculated. The values extracted from the segregation profiles alongwith calculated binding energy values are given in Table 5.4. The average binding energy, E_b, of Nb based on the above measurements can be averaged as 27 kJ/mol with austenite grain boundaries. The variation in binding energy might be because of HAGB structure as within a particular boundary sites of different segregation potential exist which might result in varying E_b of solute niobium (H. Zurob 2003). The data reported on binding energy of niobium in the literature is mostly associated with ferrite boundary or during austenite-to-ferrite transformation and ranges between 24-38 kJ/mol (H. Zurob 2003; Maruyama, Smith, and Cerezo 2003). The calculated Nb binding energy values for austenite grain boundaries are in satisfactory agreement with the range predicted in the literature.

5.8 Effect of solute Nb on grain growth:

Niobium (Nb) as a microalloying element is expected to impart solute drag. The growth kinetics shown in figures 4.5-4.7 is a clear indication of the fact that various amounts of Nb addition to Fe-30Mn base steel indeed slowed down the growth of the grains. This is attributed to the solute drag effect of niobium although the exact mechanism may differ from the classical treatments (Cahn 1962). The effective mobility values calculated from the grain growth data are given in Figures 4.9-4.11.

Table 5.5. Effect of Nb solute drag on the mobility of HAGBs in Fe-30Mn system

Temperature (°C)	M_i (Fe-30Mn)	M_{S1} (Fe-30Mn-0.03Nb)	(M_i / M_{S1})	M_{S2} (Fe-30Mn-0.05Nb)	(M_i / M_{S2})
1200	1e-12	8e-13	1.1	5e-13	2
1100	2e-13	1e-13	2	6e-14	3
1000	3e-14	1e-14	3	4e-15	6

To highlight the solute drag effect at different temperatures, the mobility of Fe-30Mn system with and without Nb is given in Table 5.5. The addition of solute Nb does not affect the mobility of special boundaries, but most certainly reduces that of high mobility boundaries, e.g. HAGBs. This effect is more pronounced at lower temperature. So, up to 6 times less boundary mobility was achieved through addition of 0.05wt% Nb to Fe-30Mn base at 1000°C. Decreasing the Nb content decreases the solute drag effect as in case of 0.03wt% Nb addition lowers the mobility by only a factor of 1.8 compared to that of the base alloy (Fe-30Mn). As the temperature is increased, solute drag effect becomes less effective which is indicated by only 1.7 and 3 times mobility drop after 0.03 and 0.05 wt% Nb addition respectively in comparison to intrinsic mobility M_i (mobility of Fe-30Mn). Nb solute drag becomes even more inadequate at 1200°C as almost insignificant change in mobility is found due to Nb addition.

Effect of Nb solute drag at different temperatures is also being shown in Figure 4.14.b where normalized mobility is plotted again wt% of Nb. The trend indicates that the solute drag effect of Nb is more pronounced at 1000°C in case of 0.05wt% Nb addition. The general trend is also indicative of the fact that Nb addition slows down the growth kinetics within the temperature window of 1000°C -1200°C by decreasing boundary mobility. Addition of Nb also changes stacking fault energy, thereby, changes annealing twin formation kinetics which might also affect the growth kinetics. In Figure 4.14. a, the same phenomenon is explained in a different way. As the temperature decreases, the mobility is also decreased and this effect is strongly achieved as gradual increment in Nb addition is made. The activation energy (Q) values obtained by equating slope of the lines to (Q/R), where R is universal gas constant are given in Table 5.6. As we increase

Table 5.6. Apparent Activation energy (Q) of grain boundary migration calculated from grain growth data

Composition	Apparent Activation Energy (Q) kJ/mol
Fe-30Mn	282
Fe-30Mn-0.03Nb	315
Fe-30Mn-0.05Nb	368

the Nb content, the solute pins the boundary more and the boundary requires to perform more work to keep moving forward as indicated by higher activation energy.

Next, an attempt is made to use the twin inhibited grain growth model to predict the growth kinetics of Fe-30Mn steel in presence of two different levels of Nb at 1100°C. Using Cahn's solute drag theory for dilute Nb condition, first the mobility of Fe-30Mn-0.03Nb steel (M_{S1}) was calculated by rearranging equation 2.113 as:

$$\frac{1}{M_{S1}} - \frac{1}{M_i} = \alpha * C_{Nb} \qquad \ldots\ldots\ldots\ldots \quad Eq\ 5.9$$

To calculate 'α' (equation 2.110), a boundary width (δ) of 1nm, binding energy (E_b) of 30 kJ/mol and a cross boundary diffusion co-efficient, $D_x = 3*D_{bulk}$, were chosen. The intrinsic mobility, M_i, was taken as 5e-11 $m^4J^{-1}s^{-1}$ (Table 5.1) which is similar to that of Fe-1%Mn at 1100°C. Using these values, M_{S1} was calculated as 2.15e-11 $m^4J^{-1}s^{-1}$ .This value of M_{S1} was finally used in equation 5.4 to predict the growth kinetics in Fe-30Mn-0.03Nb steel at 1100°C. The model prediction is being

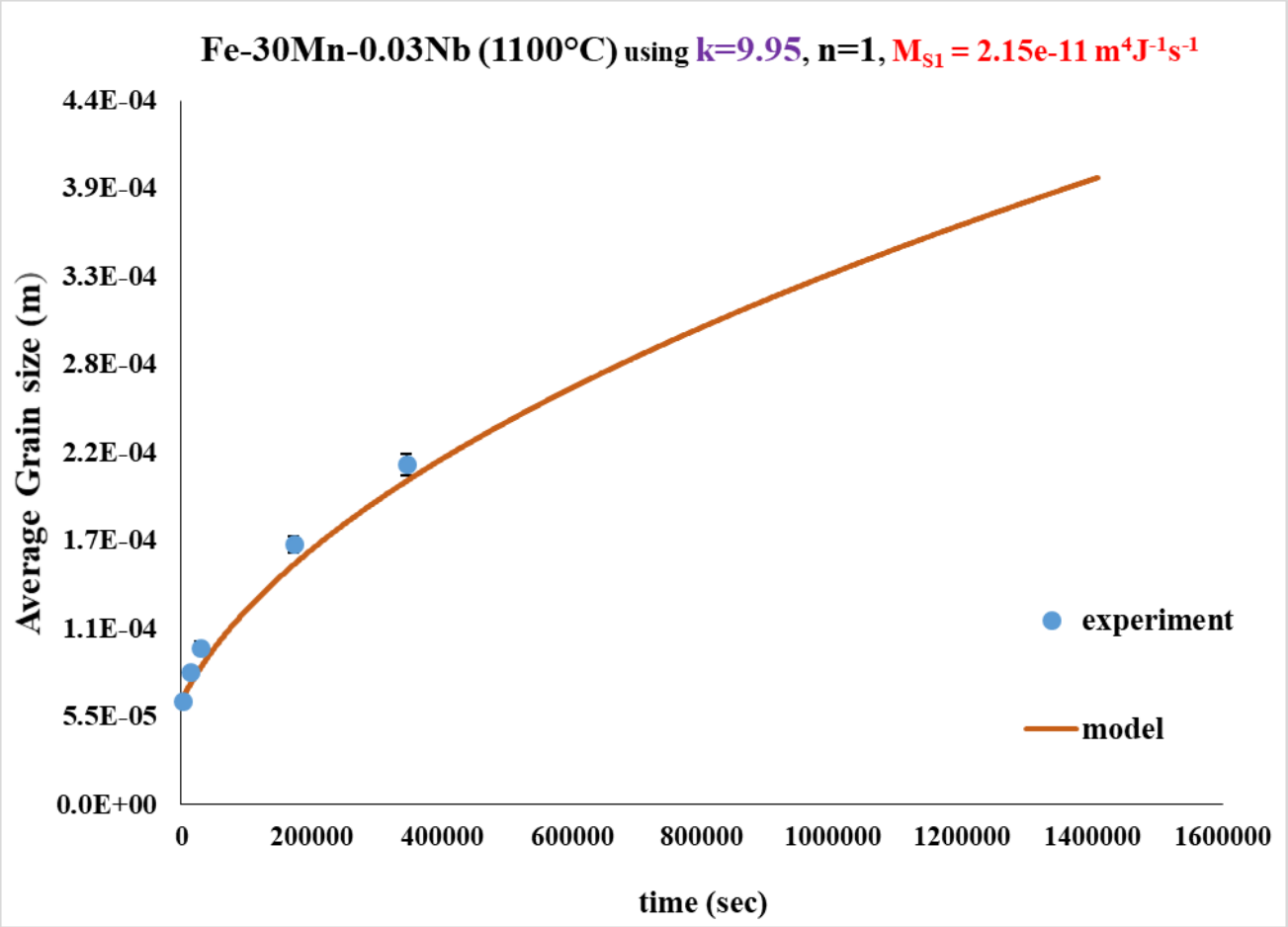

Figure 5.17. Comparison of model predicted and experimentally obtained grain growth kinetics in Fe-30Mn-0.03Nb steel at 1100°C for d/2R=0.1, k=9.95, n=1 and M = 2.15e-11 $m^4J^{-1}s^{-1}$

shown in Figure 5.17. A very good fit obtained by the model indicates that during the grain growth in Fe-30Mn-0.03Nb system, the effect of Nb solute drag on HAGBs was accurately captured through Cahn's equation alongwith the twin pinning effect captured by the pinning term. This strongly indicates the validity of the twin inhibited growth model proposed in section 5.2 for predicting grain growth in Fe-30Mn-0.03Nb steel.

Similar calculation was performed for predicting grain growth in Fe-30Mn-0.054Nb steel (S_2) at 1100°C. The model predicted grain growth in Fe-30Mn-0.05Nb steel is being shown in Figure 5.18.

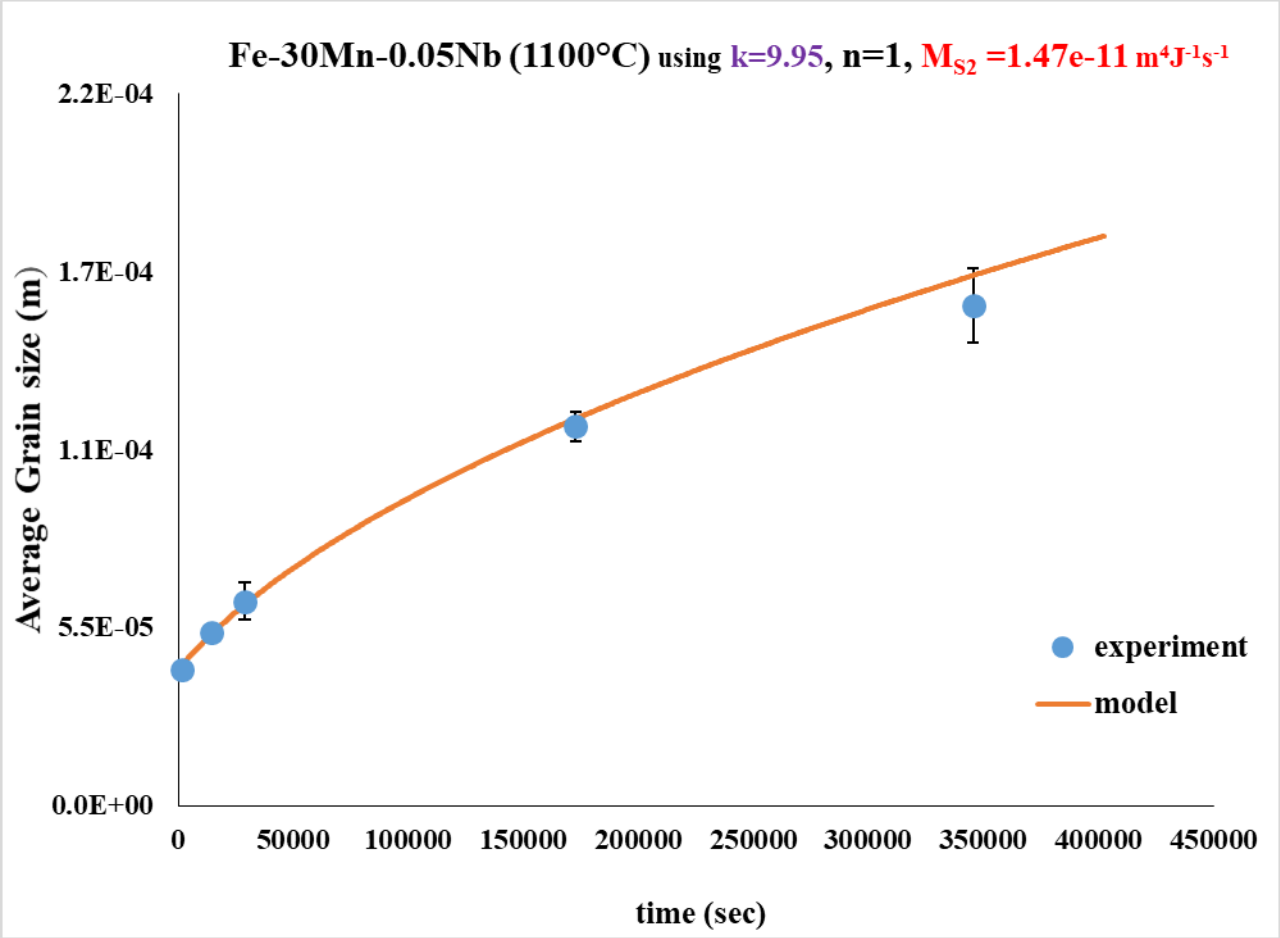

Figure 5.18. Comparison of model predicted and experimentally obtained grain growth kinetics in Fe-30Mn-0.05Nb steel at 1100°C for d/2R=0.1, k=9.95, n=1 and M = 1.47e-11 $m^4J^{-1}s^{-1}$

The obtained good fit once again proves the validity of the twin inhibited growth model for prediciting Fe-30Mn-0.05 growth kinetics.

Effect of Nb on lowering grain boundary mobility in Fe-30Mn-0.03Nb and Fe-30Mn-0.05 Nb system can be attributed solely to its effect on the mobility of HAGBs present in the microstructure. As already discussed, the presence of annealing twins and their intersection with HAGBs generate low mobility boundary segments. If an HAGB travels a distance 'λ' in time 't', the velocity (V), as well as the overall mobility can be expressed as follows:

$$V \propto M \propto \frac{\lambda}{t} \qquad \ldots\ldots\ldots \text{Eq 5.10}$$

Now, the total travel time can be assumed to consist of two different parts. One part is related to the time taken by the low mobility segments (thin lines in Figure 5.19) to get unpinned to move forward (t_{LAGB}). The other part comes from the time taken by the normal HAGBs (bold line, which has high mobility compared to the twin related segment) to advance (t_{HAGB}). Considering this,

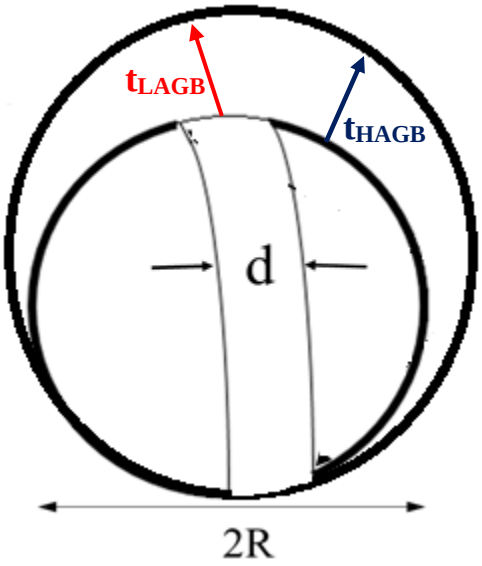

Figure 5.19. Effect of Nb solute drag on lowering the overall mobility through their influence on only the high mobility-HAGB segments (Nb solute drag increases the time to traverl along the blue arrow)

equation 5.10 can be rewritten as

$$V \propto M \propto \frac{\lambda}{t_{HAGB}+t_{LAGB}} \qquad \ldots\ldots\ldots \text{Eq 5.11}$$

Solute Nb can only segregate to HAGBs because of the higher free volume associated with their boundary plane and impart solute drag only on the HAGBs present in the microstructure. This increases the term 't_{HAGB}' in the denominator of equation 5.11. Thus, a decrease in mobility is obtained through solute drag effect of Nb on high angle-high mobility austenite grain boundaries.

6 Conclusions:

Grain growth in high manganese steel is explored in this research work. Study on austenite grain boundary migration is performed using a low stacking fault energy system which has a stable austenitic microstructure at room temperature. Several alloy design attempts finally led to the development of a steel with 30wt% Mn. Extensive experimental work was performed to facilitate the suitability of the alloy for grain growth study. Effect of solute Nb on austenite grain boundary migration at high temperature was also explored during grain growth in a series of second generation Fe-30%Mn TWIP steels alloyed with various levels of Nb. A series of atom probe experiments were performed to calculate binding energy values of Nb. Effect of Mn and C on growth kinetics was also explored and their segregation profiles were measured by 3-D atom probe tomography (APT). Detailed analysis of the microstructure including determination of crystallography of the boundaries was made using electron back scatter diffraction (EBSD). A 'twin inhibited growth' model was proposed for predicting grain growth in Fe-30Mn steel at 1100°C. The same model was also found to provide a good prediction of growth kinetics in case of Nb alloyed Fe-30Mn steels at 1100°C. A very basic attempt was also made to engineer the boundary crystallography to observe its effect on grain growth. Following are the conclusions obtained from this research work.

1. An alloy system was designed to come up with a stable austenitic microstructure at room temperature to study γ-grain boundary migration during grain growth at high temperatures.

2. Grain growth experiments were performed on Fe-30Mn base steel and a series of Nb alloyed Fe-30Mn steels within a temperature window of 1200-1000°C. This range of temperature simulates the condition a steel undergoes before the onset of finish rolling during the Thermo-Mechanically Controlled Processing (TMCP). The delay time between rough and finish rolling is a potential situation where coarsening of austenite grains take place resulting in poor mechanical properties. Understanding grain growth is therefore important from the perspective of refining grain size at high temperature to ensure excellent mechanical properties.

3. When the growth kinetics of the Fe-30Mn steels without Nb were compared with a low Mn (Fe-1%Mn) steel, the high Mn steel was found to have slower kinetics compared to the Fe-1Mn steel. A comparison of the boundary mobility values within the temperature range of 1200-1000°C showed that the Fe-30Mn steel has 2 orders of magnitude lower mobility than Fe-1Mn steel. Slow growth was not supported by solute drag effect of Mn as atom probe results obtained Mn segregation profile across the HAGB showing no significant boundary enrichment of manganese.

4. EBSD study revealed that almost 50% of the grain boundaries present in the global boundary network are of special type. Their specialness was expressed in terms of having a very good atomic fit at the boundary plane and can be described using coincidence site lattice (CSL) model. These boundaries possess low energy and low mobility compared to random high angle grain boundaries (HAGBs). Out of the 50% special boundaries, 46% appeared in the form of only Σ3 which came because of the presence of numerous annealing twins in the microstructure.

5. Presence of annealing twins and their interaction with other random HAGBs in the microstructure results in other special boundaries which are variants of Σ3. The annealing twins, upon intersecting the HAGBs, create low energy intercepts/segments on HAGBs which are low energy-low mobility parts interfering with the fast moving segments of HAGBs and reduce the boundary migration rate.Thus, it was revealed that the microstructure of Fe-30Mn system consists of two distinct population of grain boundaries, e.g., high energy HAGBs with higher mobility and twin-related special boundary/boundary segments with low mobility.

6. A modified grain growth model in presence of annealing twins was presented for Fe-30Mn system at 1100°C. Initially, the model predicted a very fast growth kinetics considering boundary mobility (M =5e-11 $m^4J^{-1}s^{-1}$) similar to the HAGBs in Fe-1Mn system. Inspite of changing the adjustable parameter, *k*, within a broad range from 0.5-11.195, no good fit was obtained by the model. This was an indication of the inability of this approach to capture the twin pinning effect over time. Another important aspect revealed from this approach was that

the mobility of HAGBs seems to be playing a secondary role in controlling the final growth kinetics.

7. The second approach made by the model was in the form of constant twin pinning over the complete time period of grain growth by assuming a constant ratio of twin width to grain diameter. With this approach, even using high mobility similar to that of HAGBs (used in first approach. i.e. M =5e-11 $m^4J^{-1}s^{-1}$), a good fit between model predicted and experimentally observed growth kinetics was obtained. This, once again, highlights the fact that the presence of the annealing twins controls the overall growth kinetics because of their pinning effect on comparatively fast moving HAGBs.

8. Another approach of using frequency of special triple junctions (TJ) showed that presence of annealing twins, special boundaries and boundary segments, actually makes the HAGB network disconnected in many places. With the increased special boundary frequency, in the light of percolation theory, the extent of continuous HAGB path available was shown to be decreased. Therefore, slow grain growth in Fe-30Mn steel can be attributed to the presence of annealing twins and twin modified HAGBs segments.

9. Effect of Mn on the grain growth kinetics was determined using a series of steels containing fixed level of C and varying level of Mn. It was found that with increased Mn content, mobility decreases and reaches a minima around 15 wt% Mn. Almost, two orders of decrease in boundary mobility is obtained as Mn concetration is changed from 1 to 15%. This is mainly attributed to the increase in the annealing twin related Σ3 boundary frequency from almost zero to 30% as Mn is increased to 15%. Atom probe study revealed that Mn segregates to austenite HAGBs in presence of carbon. In Fe-30Mn-0.5C and Fe-15Mn-0.5C, slight grain boundary enrichment of Mn is observed. In presence of very low carbon, weak Mn segregation was also observed in atom probe studies of Fe-30Mn steels. However, all the Fe-30Mn steels containing Nb showed an absolutely flat Mn segregation profile.

10. Effect of Mn on lowering grain boundary mobility was found to come primarily through the formation of the annealing twins. As the Mn content increases, stacking fault energy (SFE) decreases resulting in the increase in annealing twin frequency in the microstructure. Grain boundary character distribution (GBCD) showed that as the Mn content increases from 1% to 15%, huge frequency of special boundaries are introduced which mostly came from annealing twin nucleation and their interaction with the HAGBs. These are the key factors in slowing down the HAGB migration. A calculation was performed to estimate the effect of Mn solute drag in slowing down growth kinetics. This also highlighted that with the increase in Mn concentration beyond 6%, Mn solute drag effect is no more significant to slow down the overall growth kinetics compared to its slowing down effect through the twin pinning. Some atom probe results from various research works also showed that Mn segregation to γ-HAGBs becomes weak as Mn content is increased beyond 6%. Above evidences clearly indicates that Mn solute drag effect is not significant in slowing down the growth kinetics in high Mn steels.

11. Effect of carbon on the growth kinetics was determined and it was found that at 1100°C, mobility in Fe-30Mn-0.5C system is 6 times higher than that in Fe-30Mn-0C. At 1200°C, the presence of carbon increased the mobility of Fe-30Mn-0.5C by a factor of 4 compared with Fe-30Mn-0C. A decrease in annealing twin related Σ3 boundary frequency by 3% in presence of carbon was observed which occurred as SFE was increased due to the presence of carbon. This might have been one reason behind faster growth kinetics in Fe-30Mn-0.5C. Along with this, morphology of the annealing twins and detwinning kinetics might have played some role to increase the mobility in presence of carbon.
12. Addition of Nb was found to have some impact on grain growth kinetics through its solute drag effect on only the fast moving HAGBs. At 1200°C, austenite grain boundary mobility was decreased by factors of 1.2 and 2 with the addition of 0.03 wt% and 0.05wt% Nb respectively. As the temperature was decreased to 1100°C, addition of 0.03wt% Nb reduced boundary mobility by 2 times and 0.05 wt% Nb lowered mobility by 3 times compared to Fe-30Mn mobility. Effect of solute Nb was a little more pronounced at 1000°C when factors of 2 and 6 reductions in mobility were achieved through the addition of 0.03 wt% and 0.05 wt% Nb respectively. All these mobility reduction was because of Nb solute drag affecting the movement of only the HAGBs present in the microstructure.

13. Cahn's model was used to predict the mobility values of the HAGBs in Fe-30Mn steels in presence of two different levels of Nb. This mobility, when used in the 'twin inhibited grain growth model', a very good fit was obtained by the model with the experimentally obtained growth kinetics in Fe-30Mn-0.03Nb and Fe-30Mn-0.05Nb steels. This approach clearly indicates that the Nb solute drag effectively decreases the mobility of only the HAGBs in the microstructure. The mobility of all the twin related low mobility special boundaries remain unaffected by the solute Nb as Nb segregation is not possible to those boundary planes because of their low excess volume. Therefore, the effect of solute Nb in slowing down the growth kinetics in Nb-alloyed Fe-30Mn steels came through its solute drag effect on only the HAGBs in the microstructure which was nicely captured by Cahn's solute drag approach. Combining this with the twin pinning approach, it was found that the proposed 'twin inhibited grain growth' model can also be extended to predict grain growth in Nb alloyed Fe-30 Mn systems at 1100°C.

14. A very basic study on grain boundary engineering of Fe-30Mn-0.5C system was presented where it was seen that one-step strain annealing effectively slows down the grain growth at 1100°C till 30 minutes. Effect of various strain levels in single step processing and effect of iterative strain annealing were also determined in terms of evolution of grain boundary character distribution (GBCD). The outcome of grain boundary engineering also reflects the fact that the grain boundary crystallography can be changed to a very high percentage (64%) of Σ3 CSL boundary. However, because of big cluster grain formation, the samples that underwent iterative GBE grew very fast during the final growth experiment at 1100°C up to 30 minutes resulting very big average grain size compared to no GBE microstructure.

7 Future Plans

Although this research work offers many important findings, a few things still remain unclear. In future, some smart work towards the following directions can be considered to pursue to uncover many of the black boxes in this area. A list of future work is as follows:

1. The cross boundary and bulk diffusion coefficient in high manganese system (Fe-30Mn) needs to be determined experimentally.

2. Incorporation of twin nucleation as well as annihilation kinetics during grain growth is one of the aspects, some research work should be performed on.
3. The exact energy of the special boundaries including annealing twins need to be determined for Fe-30Mn system using TEM or other techniques. This can be directly used in the grain growth model.
4. Amount of continuous HAGB path available in the microstructure needs to be determined which might be used as a twin pinning parameter to control grain growth.
5. Low temperature strain annealing treatments need to be performed before doing grain growth experiments in Fe-30Mn-0.5C steels with the sole intent of increasing special boundary frequency upto the maximum limit.
6. Effect of cross-rolling during grain boundary engineering on evolution of special boundary fraction needs to be examined. Also effect of magnetic field during, grain boundary engineering is another direction to explore GBE of high Mn steel.

8 References

Akhiani, Hamed, Majid Nezakat, Mohsen Sanayei, and Jerzy Szpunar. 2015. “The Effect of Thermo-Mechanical Processing on Grain Boundary Character Distribution in Incoloy 800H/HT.” *Materials Science and Engineering A* 626. Elsevier: 51–60. doi:10.1016/j.msea.2014.12.046.

Allain, S, J Chateau, O Bouaziz, S Migot, and N Guelton. 2004. “Correlations between the Calculated Stacking Fault Energy and the Plasticity Mechanisms in Fe – Mn – C Alloys.” *Materials Science and Engineering: A* 37: 158–62. doi:10.1016/j.msea.2004.01.059.

Allen, RD, and GB David. 1969. “The Zeiss-Nomarski Differential Interference Equipment for Transmitted-Light Microscopy.” *Zeitschrift Für Metallkunder Wissenschaftliche Mikroskopie Und Mikroskopische Technik* 69 (4): 193–221.

Aoki, Makoto, Yet-Ming Chiang, Igor Kosacki, L Lee, Harry Tuller, and Yaping Liu. 1996. “Solute Segregation and Grain-Boundary Impedance in High-Purity Stabilized Zirconia.” *Journal of the American Ceramic Society* 79 (5): 1169–80.

Aust, K T. 1994. “Grain Boundary Engineering*.” *Canadian Metallurgical Quarterly* 33 (4): 265–74.

Bäcke, Linda. 2010. “Modeling the Effect of Solute Drag on Recovery and Recrystallization during Hot Deformation of Nb Microalloyed Steels.” *ISIJ International* 50 (2): 239–47.

Bai, Qin, Qing Zhao, Shuang Xia, Baoshun Wang, Bangxin Zhou, and Cheng Su. 2017. “Evolution of Grain Boundary Character Distributions in Alloy 825 Tubes during High Temperature Annealing: Is Grain Boundary Engineering Achieved through Recrystallization or Grain Growth?” *Materials Characterization* 123. Elsevier Inc.: 178–88. doi:10.1016/j.matchar.2016.11.016.

Bai Qi, Deng. 1993. “Effect of Rolling Parameters on the No-Recryst Allization Temperature (TNR) in Nb-Bearing Steels.” McGill University, Montreal,Canada.

Bailey, JE, and PB Hirsch. 1962. “The Recrystallization Process in Some Polycrystalline Metals.” In *Proceedings of the Royal Society of London A: Mathematical, Physical and Engineering Sciences*, 267:11–30.

Bainbridge, Douglas W, Hsien Li Choh, and Eugene H Edwards. 1954. “Recent Observations on the Motion of Small Angle Dislocation Boundaries.” *Acta Metallurgica* 2 (2): 322–33.

Bate, Peter, and Bevis Hutchinson. 1997. “A Re-Evaluation of the Mechanism of SIBM.” *Scripta Materialia* 36 (2): 195–98.

Beck, Paul A, and Philip R Sperry. 1950. “Strain Induced Grain Boundary Migration in High Purity Aluminum Strain Induced Grain Boundary Migration in High Purity Aluminum.” *Journal of Applied Physics* 21 (2): 150–52.

Beraha, Emanuel, and Bilu Shpigler. 1977. *Color Metallography*. American Society for Metals.

Bouaziz, O, S Allain, C P Scott, P Cugy, and D Barbier. 2011. “High Manganese Austenitic Twinning Induced Plasticity Steels : A Review of the Microstructure Properties Relationships.” *Current Opinion in Solid State and Materials Science* 15 (4): 141–68. doi:10.1016/j.cossms.2011.04.002.

Brewer, A W, K A Erven, and G Krauss. 1991. “Etching and Image Analysis of Prior Austenite Grain Boundaries in Hardened Steels.” *Materials Characterization* 27 (1): 53–56.

Brofman, PJ and Ansell, GS. 1978. “On the Effect of Carbon on the Stacking Fault Energy of Austenitic Stainless Steels.” *Metallurgical and Materials Transactions A* 9 (6): 879–80.

Burke, JE, and D Turnbull. 1952. “Recrystallization and Grain Growth.” *Progress in Metal Physics* 3: 220–44.

Cahn, J W. 1962. “The Impurity-Drag Effect in Grain Boundary Motion.” *Acta Metallurgica* 10 (9): 789–98.

Cahoon, J. R., Qiangyong Li, and N. L. Richards. 2009. “Microstructural and Processing Factors Influencing the Formation of Annealing Twins.” *Materials Science and Engineering A* 526 (1–2): 56–61. doi:10.1016/j.msea.2009.07.021.

Carpenter, H . C . H . , Tamura, S . 1926. “The Formation of Twinned Metallic Crystals Source : Proceedings of the Royal Society of London . Series A , Containing Papers of a Published by : Royal Society Stable URL : http://www.jstor.org/stable/94588 REFERENCES Linked References Are Available on JS.” *Mathematical and Physical Character*. 113 (763): 161–82.

Charnock, W, and J Nutting. 1967. “The Effect of Carbon and Nickel upon the Stacking-Fault Energy of Iron.” *Metal Science Journal* 1 (1): 123–27.

Chen, Kuan-chia, Wen-wei Wu, Chien-neng Liao, Lih-juann Chen, and K N Tu. 2008. “Observation of Atomic Diffusion at Twin-Modified Grain Boundaries in Copper.” *Science* 321 (5892): 1066–69.

Cho, J R, H S Jeong, D J Cha, W B Bae, and J W Lee. 2005. “Prediction of Microstructural Evolution and Recrystallization Behaviors of a Hot Working Die Steel by FEM.” *Journal of Materials Processing Technology* 160 (1): 1–8. doi:10.1016/j.jmatprotec.2004.01.001.

Cho, Sang-hyun, Ki-bong Kang, and John J Jonas. 2001. “The Dynamic, Static and Metadynamic Recrystallization of a Nb-Microalloyed Steel.” *ISIJ International* 41 (1): 63–69.

Chuang, Tung-han, Hsin-jung Lin, Chien-hsun Chuang, Yu-yun Shiue, Fuh-sheng Shieu, Yen-lin Huang, Po-chun Hsu, Jun-der Lee, and Hsing-hua Tsai. 2014. “Thermal Stability of Grain Structure and Material Properties in an Annealing Twinned Ag – 4Pd Alloy Wire.” *Journal of Alloys and Compounds* 615. Elsevier B.V.: 891–98. doi:10.1016/j.jallcom.2014.07.057.

Chuang, Tung-han, Hsi-ching Wang, Chien-hsun Chuang, Jun-der Lee, and Hsing-hua Tsai. 2013. “Effect of Annealing Twins on Electromigration in Ag-8Au-3Pd Bonding Wires.” *Journal of Electronic Materials* 42 (3): 545–51. doi:10.1007/s11664-012-2381-2.

Chuang, Tung Han, Chih Hsin Tsai, Hsi Ching Wang, Che Cheng Chang, Chien Hsun Chuang, Jun Der Lee, and Hsing Hua Tsai. 2012. “Effects of Annealing Twins on the Grain Growth and Mechanical Properties of Ag-8Au-3Pd Bonding Wires.” *Journal of Electronic Materials* 41 (11): 3215–22. doi:10.1007/s11664-012-2225-0.

Cole, J I, D S Gelles, and J J Hoyt. 1992. “Phase Stability of Reduced-Activation Mn-Stabilized Austenitic Steels.” *Journal of Nuclear Materials* 191: 657–61.

Cooman, B C De, Kwang-geun Chin, and Jinkyung Kim. 2011. “High Mn TWIP Steels for Automotive Applications.” In *New Trends and Developments in Automotive System Engineering*, 101–28.

Curtze, S, V Kuokkala, A Oikari, J Talonen, and H Ha. 2011. “Thermodynamic Modeling of the Stacking Fault Energy of Austenitic Steels.” *Acta Materialia* 59 (3): 1068–76. doi:10.1016/j.actamat.2010.10.037.

Dash, S., Brown, N. 1963. “An Investigation of the Origin and Growth of Annealing Twins.” *Acta Metallurgica* 11 (9): 1067–75.

Dobrzański, L A, and W Borek. 2011. “Hot Deformation and Recrystallization of Advanced High-Manganese Austenitic TWIP Steels.” *Journal of Achievements in Materials and Manfacturing Engineering* 46 (1): 71–78.

Doherty, R D, D A Hughes, F J Humphreys, J J Jonas, D Juul Jensen, M E Kassner, W E King, T R Mcnelley, H J Mcqueen, and A D Rollett. 1997. “Current Issues in Recrystallization : A Review.” *Materials Science and Engineering: A* 238 (2): 219–74.

Drabble, Daniel. 2010. “The Effect of Grain Boundary Engineering on the Properties of Incoloy 800H/HT.” University of Canterbury. Mechanical Engineering.

Drabble, Daniel J., Catherine M. Bishop, and Milo V. Kral. 2011. "A Microstructural Study of Grain Boundary Engineered Alloy 800H." *Metallurgical and Materials Transactions A: Physical Metallurgy and Materials Science* 42 (3): 763–72. doi:10.1007/s11661-010-0447-4.

Dulieu, David. 2001. "The Role of Niobium in Austenitic and Duplex Stainless Steels." In *International Symposium on Niobium 2001*, 975–99.

Dumay, A, J Chateau, S Allain, S Migot, and O Bouaziz. 2008. "Influence of Addition Elements on the Stacking-Fault Energy and Mechanical Properties of an Austenitic Fe – Mn – C Steel." *Materials Science and Engineering: A* 483: 184–87. doi:10.1016/j.msea.2006.12.170.

Dunlop, J W C, Y J M Brechet, L. Legras, and H S Zurob. 2007. "Modelling Isothermal and Non-Isothermal Recrystallisation Kinetics : Application to Zircaloy-4." *Journal of Nuclear Materials* 366 (1): 178–86. doi:10.1016/j.jnucmat.2006.12.074.

Engl, Bernhard. 2011. "Advanced High-Strength Sheet Steels with High Manganese." *Journal of Steel and Related Materials* 9.

Fang, Xiaoying, Kun Zhang, Hong Guo, Weiguo Wang, and Bangxin Zhou. 2008. "Twin-Induced Grain Boundary Engineering in 304 Stainless Steel." *Materials Science and Engineering A* 487 (1–2): 7–13. doi:10.1016/j.msea.2007.09.075.

Felfer, Peter J, Chris R Killmore, Jim G Williams, Kristin R Carpenter, Simon P Ringer, and Julie M Cairney. 2012. "A Quantitative Atom Probe Study of the Nb Excess at Prior Austenite Grain Boundaries in a Nb Microalloyed Strip-Cast Steel." *Acta Materialia* 60 (13–14). Acta Materialia Inc.: 5049–55. doi:10.1016/j.actamat.2012.06.013.

Felfer, Peter Johann, Talukder Alam, Simon Peter Ringer, and Julie Marie Cairney. 2012. "A Reproducible Method for Damage-Free Site-Specific Preparation of Atom Probe Tips from Interfaces." *Microscopy Research and Technique* 75 (4): 484–91. doi:10.1002/jemt.21081.

Fernández, A I, P Uranga, B López, and JM Rodriguez-Ibabe. 2000. "Static Recrystallization Behaviour of a Wide Range of Austenite Grain Sizes in Microalloyed Steels." *ISIJ International* 40 (9): 893–901.

Ferraiuolo, A, A Smith, JG Sevillano, F de las Cuevas, G Pratolongo, H Gouveia, M Mendes Rodrigues, and P Karjalainen. 2009. "Metallurgical Design of High Strength Austenitic Fe-C-Mn Steels with Excellent Formability." *Contract RFSRCT-00030, Research Programme of the Research Fund for Coal and Steel, European Union (2005-2008)*.

Friedel, Jacques. 2013. *Dislocations: International Series of Monographs on Solid State Physics*.

Vol. 3. Elsevier.

Fullman, R. L., and J. C. Fisher. 1951. “Formation of Annealing Twins during Grain Growth.” *Journal of Applied Physics* 22 (11): 1350–55. doi:10.1063/1.1699865.

Furu, T, R Ørsund, and Erik Nes. 1995. “Subgrain Growth in Heavily Deformed Aluminium—experimental Investigation and Modelling Treatment.” *Acta Metallurgica Et Materialia* 43 (6): 2209–32.

Furumai, Kohei, Hatem Zurob, and A.B Phillion. 2018. “Evaluating the Competition between Nb(C,N) Precipitation and Grain Size Evolution on the Hot Ductility of Nb Containing Steels.” *ISIJ International (Under Review)*.

Gao, Yong, R. O. Ritchie, Mukul Kumar, and R. K. Nalla. 2005. “High-Cycle Fatigue of Nickel-Based Superalloy ME3 at Ambient and Elevated Temperatures: Role of Grain-Boundary Engineering.” *Metallurgical and Materials Transactions A* 36 (12): 3325–33. doi:10.1007/s11661-005-0007-5.

Gault, Baptiste, Michael P Moody, Julie M Cairney, and Simon P Ringer. 2012. *Atom Probe Microscopy*. Springer Science & Business Media.

Geoffrey, Tweedale. 1985. “Sir Robert Abbott Hadfield, F.R.S. (1858-1940), and the Discovery of Manganese Steel.” *Notes and Records of the Royal Society* 40 (1): 63–74.

Ghasri Khouzani, Morteza. 2015. “Homogenous and Carbon Graded High Manganese Steels.” McMaster University, Hamilton, Canada.

Gindraux, G., and W. Form. 1973. “New Concepts of Annealing-Twin Formation in FCC Metals.” *Journal of the Institute of Metals* 101: 85–93.

Gleiter, H. 1969a. “The Formation of Annealing Twins.” *Acta Metallurgica* 17 (12): 1421–28. doi:10.1016/0001-6160(69)90004-2.

Gleiter, H. 1969b. “The Mechanism of Grain Boundary Migration.” *Acta Metallurgica* 17 (5): 565–73.

Gomez, M, SF Medina, and P Valles. 2005. “Determination of Driving and Pinning Forces for Static Recrystallization during Hot Rolling of a Niobium Microalloyed Steel.” *ISIJ International* 45 (11): 1711–20.

Gondet, S, T Duffar, F Louchet, F Theodore, and N Van Den Bogaert. 2003. “A Visco-Plastic Model of the Deformation of InP during LEC Growth Taking into Account Dislocation Annihilation.” *Journal of Crystal Growth* 252 (1): 92–101. doi:10.1016/S0022-

0248(03)00839-X.

Goodhew, P J. 1979. “Annealing Twin Formation by Boundary Dissociation.” *Metal Science* 13 (April): 108–12. doi:10.1179/msc.1979.13.3-4.108.

Gottstein, G, and L S Shvindlerman. 1992. “On the Orientation Dependence of Grain Boundary Migration.” *Scripta Metallurgica et Materialia* 27 (11): 1515–20.

Gottstein, Gunter, and L S Shvindlerman. 2009. *Grain Boundary Migration in Metals: Thermodynamics, Kinetics, Applications*.

Grassel, O., Kruger, L., Frommeyer, G., Meyer, L.W. 2000. “High Strength Fe-Mn-(Al, Si) TRIP/TWIP Steels Development—properties—application.” *International Journal of Plasticity* 16 (10): 1391–1409.

Hansen, SS, JB Vander Sande, and Morris Cohen. 1980. “Niobium Carbonitride Precipitation and Austenite Recrystallization in Hot-Rolled Microalloyed Steels.” *Metallurgical Transactions A* 11 (3): 387–402.

Hatherly, M, and FJ Humphreys. 2012. *Recrystallization and Related Annealing Phenomena*.

Heo, N H, J W Nam, Y Heo, and S Kim. 2013. “Grain Boundary Embrittlement by Mn and Eutectoid Reaction in Binary Fe – 12Mn Steel.” *Acta Materialia* 61 (11): 4022–34.

Herbig, M, M Kuzmina, C Haase, R K W Marceau, I Gutierrez-urrutia, and D Haley. 2015. “Grain Boundary Segregation in Fe – Mn – C Twinning-Induced Plasticity Steels Studied by Correlative Electron Backscatter Diffraction and Atom Probe Tomography.” *Acta Materialia* 83. Acta Materialia Inc.: 37–47. doi:10.1016/j.actamat.2014.09.041.

Hillert, M. 1965. “On the Theory of Normal and Abnormal Grain Growth.” *Acta Metallurgica* 13 (3): 227–38.

Hillert, Mats, and B O Sundman. 1976. “A Treatment of the Solute Drag on Moving Grain Boundaries and Phase Interfaces in Binary Alloys.” *Acta Metallurgica* 24 (8): 731–43.

Hondros, ED. 1965. “The Influence of Phosphorus in Dilute Solid Solution on the Absolute Surface and Grain Boundary Energies of Iron.” In *Proceedings of the Royal Society of London A: Mathematical, Physical and Engineering Sciences*, 286:479–98.

Hondros, ED, and M P Seah. 1977. “Segregation to Interfaces.” *International Metals Reviews* 22 (1): 262–301.

Huang, Y, and F J Humphreys. 2000a. “The Annealing Behaviour of Deformed Cube-Oriented

Aluminium Single Crystals." *Acta Materialia* 48 (10): 2543–56.

Huang, Y, and FJ Humphreys. 2000b. "Subgrain Growth and Low Angle Boundary Mobility in Aluminium Crystals of Orientation {110}〈001〉." *Acta Materialia* 48 (8): 2017–30.

Humphreys, F J. 1997a. "A Unified Theory of Recovery, Recrystallization and Grain Growth, Based on the Stability and Growth of Cellular microstructures—I. The Basic Model." *Acta Materialia* 45 (10): 4231–40.

Humphreys, F J. 1997b. "A Unified Theory of Recovery, Recrystallization and Grain Growth, Based on the Stability and Growth of Cellular microstructures—II. The Effect of Second-Phase Particles." *Acta Materialia* 45 (12): 5031–39.

Humphreys, F J. 2004. "Nucleation in Recrystallization." *Materials Science Forum* 467: 107–16. doi:10.4028/www.scientific.net/MSF.467-470.107.

Hutchinson, Bevis, Stefan Jonsson, and Lena Ryde. 1989. "On the Kinetics of Recrystallisation in Cold Worked Metals." *Scripta Metallurgica* 23 (5): 671–76.

Janssens, Koenraad G F, David Olmsted, Elizabeth A Holm, Stephen M Foiles, Steven J Plimpton, and Peter M Derlet. 2006. "Computing the Mobility of Grain Boundaries." *Nature Materials* 5 (2): 124–27. doi:10.1038/nmat1559.

Jin, Y., B. Lin, M. Bernacki, G. S. Rohrer, A. D. Rollett, and N. Bozzolo. 2014. "Annealing Twin Development during Recrystallization and Grain Growth in Pure Nickel." *Materials Science and Engineering A* 597. Elsevier: 295–303. doi:10.1016/j.msea.2014.01.018.

Jin, Yuan. 2014. "Annealing Twin Formation Mechanism." Ecole Nationale Supérieure des Mines de Paris.

Jun, Joong-hwan, and Chong-sool Choi. 1998. "Variation of Stacking Fault Energy with Austenite Grain Size and Its Effect on the M S Temperature of $\gamma \rightarrow \varepsilon$ Martensitic Transformation in Fe – Mn Alloy." *Materials Science and Engineering: A* 257 (2): 353–56.

Kang, Singon, Yeon-seung Jung, Joong-hwan Jun, and Young-kook Lee. 2010. "Effects of Recrystallization Annealing Temperature on Carbide Precipitation , Microstructure , and Mechanical Properties in Fe – 18Mn – 0 . 6C – 1 . 5Al TWIP Steel." *Materials Science and Engineering: A* 527 (3): 745–51. doi:10.1016/j.msea.2009.08.048.

King, WE, and AJ Schwartz. 1998. "Toward Optimization of the Grain Boundary Character Distribution in OFE Copper." *Scripta Materialia* 38 (3): 449–55.

Kumar, B. Ravi, S. K. Das, B. Mahato, Arpan Das, and S. Ghosh Chowdhury. 2007. "Effect of

Large Strains on Grain Boundary Character Distribution in AISI 304L Austenitic Stainless Steel." *Materials Science and Engineering A* 454–455 (April 2007): 239–44. doi:10.1016/j.msea.2006.11.053.

Kumar, M, A J Schwartz, and W E King. 1999. "Modifications in the Grain Boundary Character Distribution in FCC Materials through Thermo-Mechanical Processing." In *Proc. Inter. Conf. on Texture of Materials*, 9–13.

Kumar, M, Adam J Schwartz, and Wayne E King. 2002. "Microstructural Evolution during Grain Boundary Engineering of Low to Medium Stacking Fault Energy in Fcc Metals." *Acta Materialia* 50: 2599–2612.

Kumar, Mukul, Wayne E King, and Adam J Schwartz. 2000. "Modifications to the Microstructural Topology in F.c.c. Materials through Thermomechanical Processing." *Acta Materialia* 48 (9): 2081–91. doi:http://dx.doi.org/10.1016/S1359-6454(00)00045-8.

Kuzmina, Margarita, Dirk Ponge, and Dierk Raabe. 2015. "Grain Boundary Segregation Engineering and Austenite Reversion Turn Embrittlement into Toughness : Example of a 9 Wt .% Medium Mn Steel." *Acta Materialia* 86: 182–92.

Kwon, K H, Y Ha, K Hono, and Nack J Kim. 2013. "Origin of Intergranular Fracture in Martensitic 8Mn Steel at Cryogenic Temperatures." *Scripta Materialia* 69 (5): 420–23. doi:10.1016/j.scriptamat.2013.05.042.

Lang, Walter. n.d. "Nomarski Differential Interference-Contrast Microscopy."

Lauridsen, E M, H F Poulsen, S F Nielsen, and D Juul Jensen. 2003. "Recrystallization Kinetics of Individual Bulk Grains in 90 % Cold-Rolled Aluminium." *Acta Materialia* 51 (15): 4423–35. doi:10.1016/S1359-6454(03)00278-7.

Lechuk, Steven John. 2000. "A Study of Austenite Grain Growth in a Ti-Nb HSLA Steel." University of British Columbia.

Lee, D. S., H. S. Ryoo, and S. K. Hwang. 2003. "A Grain Boundary Engineering Approach to Promote Special Boundaries in Pb-Base Alloy." *Materials Science and Engineering A* 354 (1–2): 106–11. doi:10.1016/S0921-5093(02)00919-X.

Lee, S. Y., Y. B. Chun, J. W. Han, and S. K. Hwang. 2003. "Effect of Thermomechanical Processing on Grain Boundary Characteristics in Two-Phase Brass." *Materials Science and Engineering A* 363 (1–2): 307–15. doi:10.1016/S0921-5093(03)00668-3.

Lehockey, E. M., G. Palumbo, and P. Lin. 1998. "Improving the Weldability and Service Performance of Nickel-and Iron-Based Superalloys by Grain Boundary Engineering."

Metallurgical and Materials Transactions A 29 (12): 3069–79. doi:10.1007/s11661-998-0214-y.

Lehockey, E M. 1999. “On Improving the Corrosion and Growth Resistance of Positive Pb-Acidbattery Grids by Grain Boundary Engineering.” *Journal of Power Sources* 78: 79–83.

Lejcek, Pavel. 2010. *Grain Boundary Segregation in Metals*.

Li, B., and Sammy Tin. 2014. “The Role of Deformation Temperature and Strain on Grain Boundary Engineering of Inconel 600.” *Materials Science and Engineering A* 603: 104–13. doi:10.1016/j.msea.2014.02.078.

Liang, Xin. 2008. “Structure and Mechanical Properties of Fe-Mn Alloys Structure and Mechanical Properties of Fe-Mn Alloys.” McMaster University.

Lin, Brian. 2015. “Investigating Annealing Twin Formation Mechanisms in Face-Centered Cubic Nickel.” Carnegie Mellon University.

Lin, P., G. Palumbo, U. Erb, and K. T. Aust. 1995. “Influence of Grain Boundary Character Distribution on Sensitization and Intergranular Corrosion of Alloy 600.” *Scripta Metallurgica et Materiala* 33 (9): 1387–92. doi:10.1016/0956-716X(95)00420-Z.

Lin, Peter Keng-yu. 1998. “Evolution of Grain Boundary Character Distributions in FCC and BCC Materials.” University of Toronto.

Liu, Tingguang, Shuang Xia, Hui Li, Bangxin Zhou, and Qin Bai. 2013. “Effect of Initial Grain Sizes on the Grain Boundary Network during Grain Boundary Engineering in Alloy 690.” *Journal of Materials Research* 28 (9): 1165–76. doi:10.1016/j.matchar.2014.02.011.

Liu, W J, and J J Jonas. 1988. “A Stress Relaxation Method for Following Carbonitride Precipitation in Austenite at Hot Working Temperatures.” *Metallurgical and Materials Transactions A* 19 (6): 1403–13.

Lo, K. H., C. H. Shek, and J. K L Lai. 2009. “Recent Developments in Stainless Steels.” *Materials Science and Engineering R: Reports* 65 (4–6): 39–104. doi:10.1016/j.mser.2009.03.001.

Lücke, K, and K Detert. 1957. “A Quantitative Theory of Grain-Boundary Motion and Recrystallization in Metals in the Presence of Impurities.” *Acta Metallurgica* 5 (11): 628–37.

Lücke, K, and H.P. Stüwe. 1971. “On the Theory of Impurity Controlled Grain Boundary Motion.” *Acta Metallurgica* 19 (10): 1087–99.

Mahajan, S, C.S. Pande, M.A Imam, and B.B. Rath. 1997. “Formation of Annealing Twins in Fcc Crystals.” *Acta Materialia* 45 (6): 2633–38.

Maruyama, Naoki, G D W Smith, and A Cerezo. 2003. “Interaction of the Solute Niobium or Molybdenum with Grain Boundaries in a -Iron.” *Materials Science and Engineering: A* 353 (1): 126–32. doi:10.1016/S0921-5093(02)00678-0.

Maruyama, Naoki, and George D W Smith. 2004. “3D Atom Probe Analysis on Nb and Mo Segregation during Recrystallisation of α -Fe.” In *Materials Science Forum*, 467:949–56. Trans Tech Publ. doi:10.4028/www.scientific.net/MSF.467-470.949.

Mecking, H, and U.F Kocks. 1981. “Kinetics of Flow and Strain-Hardening.” *Acta Metallurgica* 29 (11): 1865–75.

Medina, SF, and P Fabregue. 1991. “Activation Energy in the Static Recrystallization of Austenite.” *Journal of Materials Science* 26 (20): 5427–32. doi:10.1007/BF02403940.

Menyhard, M, Min Yan, and V Vitek. 1994. “Atomistic vs Phenomenological Approaches to Grain Boundary Segregation : Computer Modeling of Cu-Ag Alloys.” *Acta Metallurgica et Materialia* 42 (8): 2783–96.

Meyers, M.A., McCowan, C. 1984. “The Formation of Annealing Twins:overview & New Thoughts.” *Interface Migration and Control of Microstructure: Proceedings of an International Symposium Held in Conjunction with ASM’s Metals Congress and TMS/A*, 99–123.

Meyers, Marc A., and Lawrence E. Murr. 1978. “A Model for the Formation of Annealing Twins in F.C.C. Metals and Alloys.” *Acta Metallurgica* 26 (6): 951–62. doi:10.1016/0001-6160(78)90046-9.

Michiuchi, M., H. Kokawa, Z. J. Wang, Y. S. Sato, and K. Sakai. 2006. “Twin-Induced Grain Boundary Engineering for 316 Austenitic Stainless Steel.” *Acta Materialia* 54 (19): 5179–84. doi:10.1016/j.actamat.2006.06.030.

Militzer, M, E B Hawbolt, and T R Meadowcroft. 2000. “Microstructural Model for Hot Strip Rolling of High-Strength Low-Alloy Steels.” *Metallurgical and Materials Transactions A* 31 (4): 1247–59.

Militzer, Matthias, Thomas Garcin, and Warren J Poole. 2013. “In-Situ Measurements of Grain Growth and Recrystallization by Laser Ultrasonics.” *Materials Science Forum* 753: 25–30. doi:10.4028/www.scientific.net/MSF.753.25.

Momeni, Amir, Shahab Kazemi, Golam Ebrahimi, and Alireza Maldar. 2014. “Dynamic

Recrystallization and Precipitation in High Manganese Austenitic Stainless Steel during Hot Compression." *International Journal of Minerals, Metallurgy, and Materials* 21 (1): 36–45. doi:10.1007/s12613-014-0862-4.

Nagarajan, Vishwanathan. 2012. "A New Approach for Modelling Strain Induced Precipitation of Niobium Carbonitrides in Austenite during Multipass Hot Rolling." University of Sheffield.

Nakano, Jinichiro, and Pascal J Jacques. 2010. "Effects of the Thermodynamic Parameters of the Hcp Phase on the Stacking Fault Energy Calculations in the Fe – Mn and Fe – Mn – C Systems." *CALPHAD: Computer Coupling of Phase Diagrams\and Thermochemistry* 34 (2). Elsevier Ltd: 167–75. doi:10.1016/j.calphad.2010.02.001.

Nes, E. 1995. "Recovery Revisited." *Acta Metallurgica et Materialia* 43 (6): 2189–2207.

Nielsen, John P. 1967. "The Origin of Annealing Twins." *Acta Metallurgica* 15 (6): 1083–85. doi:http://dx.doi.org/10.1016/0001-6160(67)90277-5.

Nikbakht, F, M Nasim, C Davies, E A Wilson, and H Adrian. 2010. "Isothermal Embrittlement of Fe – 8Mn Alloys at 450°C." *Materials Science and Technology* 26 (5): 552–58. doi:10.1179/174328409X405616.

Owen, Gregory, and Valerie Randle. 2006. "On the Role of Iterative Processing in Grain Boundary Engineering." *Scripta Materialia* 55 (10): 959–62. doi:10.1016/j.scriptamat.2006.04.049.

Palumbo, G, EM Lehockey, and P Lin. 1998. "Applications for Grain Boundary Engineered Materials." *Jom Journal of the Minerals, Metals and Materials Society* 50 (2): 40–43.

Pande, C. S., M. a. Imam, and B. B. Rath. 1990. "Study of Annealing Twins in Fcc Metals and Alloys." *Metallurgical Transactions A* 21 (11): 2891–96. doi:10.1007/BF02647209.

Pereda, B, JM Rodriguez-Ibabe, and B López. 2008. "Improved Model of Kinetics of Strain Induced Precipitation and Microstructure Evolution of Nb Microalloyed Steels during Multipass Rolling." *ISIJ International* 48 (10): 1457–66.

Petrov, Yu N. 1993. "On the Carbon Distribution at Structural Imperfections in Manganese Austenite." *Scripta Metallurgica et Materialia* 29 (11): 1471–76.

Phiu-on. 2008. "Deformation Mechanisms and Mechanical Properties of Hot Rolled Fe-Mn-C-(Al)-(Si) Austenitic Steels."

Priester, Louisette. 2012. *Grain Boundaries: From Theory to Engineering*. Vol. 172. Springer

Science & Business Media.

Qiu, Cong. 2013. “The ‘ Solute - Drag ’ Effect on Migrating Interfaces during Solid-State Phase Transformations.” Monash University.

Rainforth, WM, MP Black, RL Higginson, EJ Palmiere, CM Sellars, I Prabst, P Warbichler, and F Hofer. 2002. “Precipitation of NbC in a Model Austenitic Steel.” *Acta Materialia* 50 (4): 735–47.

Randle, V. 1999. “Mechanism of Twinning-Induced Grain Boundary Engineering in Low Stacking-Fault Energy Materials.” *Acta Materialia* 47 (15): 4187–96. doi:10.1016/S1359-6454(99)00277-3.

Randle, V, P Davies, and B Hulm. 1999. “Grain-Boundary Plane Reorientation in Copper.” *Philosophical Magazine A* 79 (2): 305–16. doi:10.1080/01418619908210299.

Randle, Valerie. 2002. “Sigma-Boundary Statistics by Length and Number.” *Interface Science* 10 (4): 271–77. doi:10.1023/A:1020877528820.

Randle, Valerie. 2004. “Twinning-Related Grain Boundary Engineering.” *Acta Materialia* 52 (14): 4067–81. doi:10.1016/j.actamat.2004.05.031.

Randle, Valerie. 2010. “Grain Boundary Engineering: An Overview after 25 Years.” *Materials Science and Technology* 26 (3): 253–61. doi:10.1179/026708309X12601952777747.

Randle, Valerie, and Paul Davies. 1999. “Deviation from Reference Planes and Reference Misorientation for Σ3 Boundaries.” *Interface Science* 7 (7): 5–13.

Randle, V, P R Rios, and Y Hu. 2008. “Grain Growth and Twinning in Nickel.” *Scripta Materialia* 58: 130–33. doi:10.1016/j.scriptamat.2007.09.016.

Rehman, Md Kashif, and Hatem S Zurob. 2013. “A Novel Approach to Model Static Recrystallization of Austenite During Hot Rolling of Nb Microalloyed Steel . Part I : Precipitate-Free Case.” *Metallurgical and Materials Transactions A* 44 (4): 1862–71. doi:10.1007/s11661-012-1526-5.

Remy, L. 1977. “Temperature Variation of the Intrinsic Stacking Fault Energy of a High Manganese Austenitic Steel.” *Acta Metallurgica* 25 (2): 173–79.

Rémy, L, A Pineau, and B Thomas. 1978. “Temperature Dependence of Stacking Fault Energy in Close-Packed Metals and Alloys.” *Materials Science and Engineering* 36 (1): 47–63.

Rohrer, Gregory S, David M Saylor, Bassem El, Brent L Adams, Anthony D Rollett, and Paul

Wynblatt. 2004. “The Distribution of Internal Interfaces in Polycrystals.” *Zeitschrift Für Metallkunde* 95 (4): 197–214.

Schlegel, Scott M., Sharla Hopkins, and Megan Frary. 2009. “Effect of Grain Boundary Engineering on Microstructural Stability during Annealing.” *Scripta Materialia* 61 (1). Acta Materialia Inc.: 88–91. doi:10.1016/j.scriptamat.2009.03.013.

Schuh, C. A., M. Kumar, and W. E. King. 2005. “Universal Features of Grain Boundary Networks in FCC Materials.” *Journal of Materials Science* 40 (4): 847–52. doi:10.1007/s10853-005-6500-9.

Scott, C, S Allain, M Faral, and N Guelton. 2006. “The Development of a New Fe-Mn-C Austenitic Steel for Automotive Applications.” *La Revue de Métallurgie-CIT* 103 (6): 293–302.

Seah, M P. 1980. “Grain Boundary Segregation.” *Journal of Physics F: Metal Physics* 10 (6): 1043.

Sellars, C M. 1990. “Modelling Microstructural Development during Hot Rolling.” *Materials Science and Technology* 6 (11): 1072–81.

Setsuo Takaki, Hideshi Nakatsu, Youichi Tokunaga. 1993. “Effects of Austenite Grain Size on ε Martensitic Transformation in Fe-15mass% Mn Alloy.” *Materials Transactions, JIM* 34 (6): 489–95.

Shimada, M, H Kokawa, Z J Wang, Y S Sato, and I Karibe. 2002. “Optimization of Grain Boundary Character Distribution for Intergranular Corrosion Resistant 304 Stainless Steel by Twin- Induced Grain Boundary Engineering.” *Acta Materialia* 50 (9): 2331–41.

Stalheim, Douglas G, Keith R Barnes, and Dennis B Mccutcheon. 2006. “Alloy Designs for High Strength Oil and Gas Transmission Linepipe Steels.” In *Proceedings of the International Symposium Microalloyed Steels for the Oil and Gas Industry*, 73–108.

Subramanian, Sundaresa V, M Kashif Rehman, Hatem S Zurob, and Cheng Jia Shang. 2013. “Recrystallization and Grain Coarsening Control in Processing High Niobium Microalloyed Line Pipe Steels.” *Materials Science Forum* 753: 391–96. doi:10.4028/www.scientific.net/MSF.753.391.

Sun, W.P., and E.B. Hawbolt. 1997. “Comparison between Static and Metadynamic Recrystallization-an Application to the Hot Rolling of Steels.” *ISIJ International* 37 (10): 1000–1009.

Sunil Kumar, B., Balla Sai Prasad, Vivekanand Kain, and Jayanth Reddy. 2013. “Methods for

Making Alloy 600 Resistant to Sensitization and Intergranular Corrosion." *Corrosion Science* 70: 55–61. doi:10.1016/j.corsci.2012.12.021.

Tan, L., T. R. Allen, and J. T. Busby. 2013. "Grain Boundary Engineering for Structure Materials of Nuclear Reactors." *Journal of Nuclear Materials* 441 (1–3). Elsevier B.V.: 661–66. doi:10.1016/j.jnucmat.2013.03.050.

Tanaka, T. 1981. "Controlled Rolling of Steel Plate and Strip." *International Metals Reviews* 26 (1): 185–212.

Telang, Abhishek, Amrinder S. Gill, Mukul Kumar, Sebastien Teysseyre, Dong Qian, Seetha R. Mannava, and Vijay K. Vasudevan. 2016. "Iterative Thermomechanical Processing of Alloy 600 for Improved Resistance to Corrosion and Stress Corrosion Cracking." *Acta Materialia* 113. Elsevier Ltd: 180–93. doi:10.1016/j.actamat.2016.05.009.

Thaveeprungsriporn, V., P. Sinsrok, and D. Thong-Aram. 2001. "Effect of Iterative Strain Annealing on Grain Boundary Network of 304 Stainless Steel." *Scripta Materialia* 44 (1): 67–71. doi:10.1016/S1359-6462(00)00582-0.

Thomas, Spencer L, Alexander H King, and David J Srolovitz. 2016. "When Twins Collide : Twin Junctions in Nanocrystalline Nickel." *Acta Materialia* 113: 301–10.

Thompson, K, D Lawrence, D J Larson, J D Olson, T F Kelly, and B Gorman. 2007. "In Situ Site-Specific Specimen Preparation for Atom Probe Tomography." *Ultramicroscopy* 107 (2–3): 131–39. doi:10.1016/j.ultramic.2006.06.008.

Thomson, C.B., and V. Randle. 1996. "The Effects of Strain Annealing on Grain Boundary Distribution and Hardening in Superpure Nickel." *Texture, Stress, and Microstructure* 32 (1–2): 71–79. doi:10.1023/A:1018573327408.

Thomson, C.B., and V. Randle. 1997. "The Effects of Strain Annealing on Grain Boundaries and Secure Triple Junctions in Nickel 200." *Journal of Materials Science* 32 (7): 1909–14. doi:10.1023/A:1018573327408.

Tsurekawa, Sadahiro, Shinya Nakamichi, and Tadao Watanabe. 2006. "Correlation of Grain Boundary Connectivity with Grain Boundary Character Distribution in Austenitic Stainless Steel." *Acta Materialia* 54 (13): 3617–26. doi:10.1016/j.actamat.2006.03.048.

Turnbull, D. 1951. "Theory of Grain Boundary Migration Rates." *JOM* 3 (8): 661–65.

Verdier, M, Y Brechet, and P Guyot. 1998. "Recovery of AlMg Alloys : Flow Stress and Strain-Hardening Properties." *Acta Materialia* 47 (1): 127–34.

Verlinden, B, J Driver, I Samajdar, and Roger D Doherty. 2007. *Thermo-Mechanical Processing of Metallic Materials*.

Vervynckt, S, K Verbeken, P Thibaux, and Y Houbaert. 2010. "Characterization of the Austenite Recrystallization by Comparing Double Deformation and Stress Relaxation Tests." *Steel Research International* 81 (3): 234–44. doi:10.1002/srin.200900126.

Voort, George F Vander. 1984. *Metallography, Principles and Practice*. ASM International.

Wang, Wei Guo. 2007. "Grain Boundary Engineering: Progress and Challenges." *Materials Science Forum* 539–543: 3389–94. doi:10.4028/www.scientific.net/MSF.539-543.3389.

Wang, Xiaoyan, Arnaud Dallemagne, Yaqing Hou, and Sen Yang. 2016. "Effect of Thermomechanical Processing on Grain Boundary Character Distribution of Hastelloy X Alloy." *Materials Science and Engineering: A* 669. Elsevier: 95–102. doi:10.1016/j.jnucmat.2007.05.002.

Was, Gary S., Visit Thaveeprungsriporn, and Douglas C. Crawford. 1998. "Grain Boundary Misorientation Effects on Creep and Cracking in Ni-Based Alloys." *Jom Journal of the Minerals, Metals and Materials Society* 50 (2): 44–49. doi:10.1007/s11837-998-0249-y.

Wasnik, D. N., V. Kain, I. Samajdar, B. Verlinden, and P. K. De. 2002. "Resistance to Sensitization and Intergranular Corrosion through Extreme Randomization of Grain Boundaries." *Acta Materialia* 50 (18): 4587–4601. doi:10.1016/S1359-6454(02)00306-3.

Watanabe, Tadao. 1984. "An Approach to Grain Boundary Design for Strong and Ductile Polycrystals." *Res Mechanica* 11: 47–84.

Watanabe, Tadao. 1993. "Grain Boundary Design and Control for High Temperature Materials." *Materials Science and Engineering A* 166 (1–2): 11–28. doi:10.1016/0921-5093(93)90306-Y.

Watanabe, Tadao. 2011. "Grain Boundary Engineering : Historical Perspective and Future Prospects." *Journal of Materials Science* 46 (12): 4095–4115. doi:10.1007/s10853-011-5393-z.

Watanabe, Tadao, and Sadahiro Tsurekawa. 1999. "The Control of Brittleness and Development of Desirable Mechanical Properties in Polycrystalline Systems by Grain Boundary Engineering." *Acta Materialia* 47 (15): 4171–85. doi:10.1016/S1359-6454(99)00275-X.

Welsh, S. L., M. Kapoor, O. D. Underwood, R. L. Martens, G. B. Thompson, and J. L. Evans. 2016. "Influence of Grain Boundary Character and Anneal Time on Segregation in Commercially Pure Nickel." *Journal of Materials* 2016: 15.

http://dx.doi.org/10.1155/2016/4597271.

Winning, M, A D Rollett, G Gottstein, D J Srolovitz, and A Lim. 2010. “Mobility of Low-Angle Grain Boundaries in Pure Metals.” *Philosophical Magazine* 90 (22): 3107–28. doi:10.1080/14786435.2010.481272.

Wynblatt, Paul, and Dominique Chatain. 2006. “Anisotropy of Segregation at Grain Boundaries and Surfaces.” *Metallurgical and Materials Transactions A* 37 (9): 2595–2620.

Yamamoto, S, C Ouchi, and T Osuka. 1981. “The Effect of Microalloying Elements on the Recovery and Recrystallization in Deformed Austenite.” *Thermomechanical Processing of Microalloyed Austenite,* 613–39.

Yang, Wuqiang, Min Xu, Huanhuan Bai, Ye Meng, Litao Wang, Lifa Shi, and Yinghao Pei. 2015. “Concentration Depth Distribution of Grain Boundary Segregation Measured by Wavelength Dispersive X-Ray Spectroscopy.” *Ultramicroscopy* 159. Elsevier: 432–37. doi:10.1016/j.ultramic.2015.03.004.

Yoshie, Atsuhiko, Hirofumi Morikawa, Yasumitsu Onoe, and Kametaro Itoh. 1987. “Formulation of Static Recrystallization of Austenite in Hot Rolling Process of Steel Plate.” *Transactions of the Iron and Steel Institute of Japan* 27 (6): 425–31.

Zelinski, Jeffrey. 2005. “An Evaluation of Grain Boundary Engineering Technology and Processing Scale-Up.” Massachusetts Institute of Technology.

Zhang, Ming Xian, Bin Yang, Sheng Long Wang, and Huan Chun Wu. 2016. “Mechanisms of Thermo-Mechanical Process on Grain Boundary Character Distribution of 316L Austenitic Stainless Steel.” *Materials Science Forum* 850: 965–70. doi:10.4028/www.scientific.net/MSF.850.965.

Zhou, Tihe. 2010. “Control of Microstructure during Solidification & Homogenization of Thin-Slab Cast Direct-Rolling (TSCDR) Microalloyed Steels.” McMaster University.

Zurob, H S, Y Brechet, and G Purdy. 2001. “A Model for the Competition of Precipitation and Recrystallization in Deformed Austenite.” *Acta Materialia* 49 (20): 4183–90.

Zurob, H S, J Dunlop, and Y Brechet. 2006. “Quantitative Criterion for Recrystallization Nucleation in Single-Phase Alloys : Prediction of Critical Strains and Incubation Times.” *Acta Materialia* 54 (15): 3983–90. doi:10.1016/j.actamat.2006.04.028.

Zurob, H S, C R Hutchinson, Y Brechet, and G Purdy. 2002. “Modeling Recrystallization of Microalloyed Austenite: Effect of Coupling Recovery, Precipitation and Recrystallization.” *Acta Materialia* 50 (12): 3077–94.

Zurob, Hatem. 2003. “Effects of Precipitation, Recovery and Recrystallization on the Microstructural Evolution of Microalloyed Austenite.” McMaster University.

Zurob, Hatem S, G Zhu, SV Subramanian, Gary R Purdy, and Hutchinson, Christopher R, Brechet, Yves. 2005. “Analysis of Mn Effect on Recrystallization Kinetics in High Nb Steels.” *Materials Science Forum* 500: 123–30. doi:10.4028/www.scientific.net/MSF.500-501.123.